

Flow-Induced Vibration of Elastically Mounted Cylinder-Plate Assemblies

by

Ying Wu

A thesis
presented to the University of Waterloo
in fulfillment of the
thesis requirement for the degree of
Doctor of Philosophy
in
Mechanical and Mechatronics Engineering

Waterloo, Ontario, Canada, 2023

© Ying Wu 2023

Examining Committee Membership

The following served on the Examining Committee for this thesis. The decision of the Examining Committee is by majority vote.

External Examiner: Rajeev Jaiman
Professor, Dept. of Mechanical Engineering,
University of British Columbia

Supervisor(s): Fue-Sang Lien
Professor, Dept. of Mechanical and Mechatronics Engineering,
University of Waterloo

Internal Member: William Melek
Professor, Dept. of Mechanical and Mechatronics Engineering,
University of Waterloo

Xianguo Li
Professor, Dept. of Mechanical and Mechatronics Engineering,
University of Waterloo

Internal-External Member: Hans De Sterck
Professor, Dept. of Applied Mathematics,
University of Waterloo

Author's Declaration

I hereby declare that I am the sole author of this thesis. This is a true copy of the thesis, including any required final revisions, as accepted by my examiners.

I understand that my thesis may be made electronically available to the public.

Abstract

The transverse flow-induced vibration (FIV) of an elastically supported cylinder-plate assembly (viz., a rigid splitter-plate attached to the downstream side of a cylinder) is investigated deeply and systematically in this thesis, using the numerical simulation based on Computational Fluid Dynamics (CFD) and the mathematical wake-oscillator model.

To investigate the influence of splitter-plate length (L_{SP}), a circular cylinder-plate assembly is numerically simulated in laminar flow, involving extensive spans of plate length $L_{SP}/D = 0-4$ (where D is the cylinder diameter) and reduced velocity $U_r = 2-30$. The simulations demonstrate that L_{SP} substantially affects nearly every aspect of the assembly's FIV. For structural vibration, the self-limited FIV is induced for $L_{SP}/D \leq 0.5$, while a galloping-dominated FIV is triggered for $L_{SP}/D \geq 0.75$. For branching behavior, both odd- and even-multiple synchronizations between the structure oscillation and vortex shedding are supported in the assembly. In particular, two new branches (viz., initial galloping branch and still branch) are identified for $L_{SP}/D \geq 2.5$. For nonlinear dynamical characteristics, the beating phenomenon of FIV is closely related to some irregular vortices and wake modes unique to the assembly based on the flow analysis.

To investigate the synergy effect of the aspect ratio of cylinder (AR) and plate length, the transverse FIV of an elliptical cylinder-plate assembly is simulated under same conditions, involving various combinations of AR (0.5, 0.67, 0.75, 1, 1.5 and 2) and L_{SP}/D (0.5, 0.75 and 2.5). The two geometrical factors lay different emphasis in influencing the assembly's FIV. AR determines whether a FIV can be induced on the assembly, with a critical value occurring in the range $0.67 < AR_{cri} < 0.75$ at $Re = 100$. Once the FIV is triggered ($AR > AR_{cri}$), the fundamental vibration mode (limited or unlimited) depends on L_{SP} , and a change in AR only has a relatively limited impact on the vibration level.

To mathematically predict FIV, the coupled wake-oscillator models based on lift coefficient (C_L) and wake angular displacement (θ) are improved from different aspects. Then, a genetic algorithm (GA) optimized nonlinear grey-box estimation framework is proposed to determine free parameters. Based on this, various model structures are discussed in terms of the VIV of a circular cylinder and the galloping of a cylinder-plate assembly. The results suggest that the optimal model has six free parameters with the first-order polynomial expression for the prediction of VIV. While for the complex galloping occurred at larger U_r , more high-order polynomial terms are necessary to predict the non-sinusoidal oscillations, which leads to the optimal model with eight free parameters.

Overall, this thesis offers crucial new perspectives on the nature and physical mechanisms behind the complex transverse FIV response of a cylinder-plate assembly.

Acknowledgements

First and foremost I am extremely grateful to my supervisor Prof. Fue-Sang Lien and my co-author Prof. Eugene Yee for their invaluable advice, continuous support, and patience during my PhD study. Their immense knowledge and plentiful experience have encouraged me all the time of my academic research life. My gratitude extends to the China Scholarship Council (CSC) and the University of Waterloo for the funding opportunity to undertake my PhD study. I would also like to thank all the members in my research group. It is their kind help and support that have made my study and life in the Canada a wonderful time. Finally, I would like to express my appreciation to my parents, my grandparents and my boyfriend Mr. Ma Xiaolei. Without their tremendous understanding and encouragement in the past four years, it would be impossible for me to complete my PhD study.

I try to tell a complete research story during my PhD, and this is a long, challenging but rewarding process. There is still plenty of research that can be done about this topic and hope this thesis can give some insights and inspirations to the researchers in this area.

Table of Contents

Examining Committee	ii
Author's Declaration	iii
Abstract	iv
Acknowledgements	v
List of Figures	xi
List of Tables	xxvii
List of Abbreviations	xxix
List of Symbols	xxx
1 Introduction	1
1.1 Background	1
1.2 Fundamentals of FIV Phenomenon	3
1.2.1 Classification	3
1.2.2 Vortex-Induced Vibration	4
1.2.3 Buffeting	5
1.2.4 Galloping	5

1.2.5	Flutter	6
1.3	Important Parameters to FIV	6
1.3.1	The Reynolds Number (Re)	7
1.3.2	The Strouhal Number (St)	7
1.3.3	Natural Frequency of Structure	9
1.3.4	Mass and Damping of Structure	10
1.3.5	The Reduced Velocity (U_r)	11
2	Literature Review	12
2.1	Vibration Response and Flow Analysis of FIV	12
2.1.1	VIV of a Circular Cylinder	12
2.1.2	Influence of Cross-Sectional Shape on FIV	14
2.1.3	Flow Analysis of FIV	16
2.2	Branching Behavior of FIV	18
2.2.1	Branching of VIV for a Circular Cylinder	18
2.2.2	Branching of FIV for a Non-Circular Cylinder	19
2.3	Nonlinear Analysis of FIV	21
2.3.1	Beating Phenomenon of FIV	22
2.3.2	Nonlinear Dynamical Features of FIV	23
2.4	Wake-Oscillator Model of FIV	24
2.4.1	C_L -Based Wake Oscillator Model for VIV	25
2.4.2	θ -Based Wake Oscillator Model for VIV	27
2.4.3	Quasi-Steady Model for Galloping	29
2.4.4	Wake-Oscillator Model for FIV	31
2.5	FIV of Cylinder-Plate Assembly	32
2.5.1	Configuration of Cylinder-Plate Assembly	33
2.5.2	Effect of Splitter-Plate Length	34
2.6	Motivations and Novelties	35
2.7	Outline of Thesis	38

3	FIV of Circular Cylinder-Plate Assembly with Various Plate Lengths	39
3.1	Problem Description	39
3.2	Numerical Methodology	41
3.2.1	Simulation Set-Up	41
3.2.2	Numerical Techniques	42
3.2.3	Independence Study	45
3.2.4	Model Validation	48
3.3	Vibration Response	52
3.3.1	Vibration Characteristics	52
3.3.2	Fluid Force Characteristics	56
3.3.3	Components of Transverse Force	58
3.4	Branching Behavior	62
3.4.1	Branching Identification	62
3.4.2	Mechanism Analysis	77
3.4.3	A Further Discussion	90
3.5	Nonlinear Characteristics Analysis	93
3.5.1	Beating Phenomenon	95
3.5.2	Nonlinear Dynamical Characteristics	105
3.5.3	Wake Modes During Beating	114
3.6	Chapter Summary	121
4	FIV of Elliptical Cylinder-Plate Assembly with Various Aspect Ratios	125
4.1	Problem Description	125
4.2	FIV Occurred in a Limited Range of U_r	127
4.2.1	Vibration Characteristics	127
4.2.2	Branching Behavior	130
4.2.3	Periodic Oscillation in Synchronization Branch	134
4.2.4	Aperiodic Oscillation in Non-Synchronization Branch	143

4.3	FIV Occurred in an Unlimited Range of U_r	150
4.3.1	Vibration Characteristics	150
4.3.2	Branching Behavior	153
4.3.3	Periodic Oscillation in Synchronization Branch	157
4.3.4	Aperiodic Behavior in Non-Synchronization Branch	168
4.3.5	Elliptical Cylinder-Plate Assembly with a Longer Splitter-Plate	173
4.4	Mechanism Analysis	175
4.4.1	Why does an elliptical cylinder-plate assembly with $AR = 2$ and $L_{SP}/D = 0.5$ have a narrow FIV range?	175
4.4.2	Why is FIV inhibited in the elliptical cylinder-plate assembly with $AR < 0.75$?	179
4.5	Chapter Summary	181
5	GA–Optimized Nonlinear Grey-Box Model for FIV	184
5.1	Problem Description	184
5.2	Improved Mathematical Model	185
5.2.1	Improved Wake-Oscillator Model Based on C_L	185
5.2.2	Improved Wake-Oscillator Model Based on θ	189
5.3	GA–Optimized Nonlinear Grey-Box Model	190
5.3.1	The State-Space Model	191
5.3.2	Model Parameter Estimation	193
5.3.3	Parameter optimization based on genetic algorithm	195
5.4	Results and Discussions	197
5.4.1	Configuration of Model Parameters	197
5.4.2	VIV of a Circular Cylinder	203
5.4.3	Galloping of a Circular Cylinder-Plate Assembly	214
5.4.4	A Further Discussion	224
5.5	Chapter Summary	229

6 Conclusions and Future Works	231
References	236
APPENDICES	255
A Publications During PhD	256

List of Figures

1.1	Low-turbulence free surface water channel with (a) a single VIVACE converter and (b) a four-cylinder VIVACE converter [19].	2
1.2	(a) Bladeless wind turbine and (b) bladeless wind farm [163].	3
1.3	Comparison of amplitude-velocity and frequency-velocity of FIV phenomenon: (a) VIV; (b) instability like galloping and flutter; and, (c) wake galloping. .	4
1.4	Regimes of flow around a smooth, circular cylinder in steady current [127, 130].	8
1.5	Strouhal number versus Reynolds number for circular cylinders [85].	9
2.1	Vibration responses for VIV of a circular cylinder in air [41]. The dimensionless mass ratio defined as $n = \rho D^2 L / (2m_{osc}) = 0.00257$ in Feng's experiments is equivalent to $m^* = 4m_{osc} / (\rho \pi D^2 L) = 247.7$ in this thesis. The damping ratio $\beta = 0.00103$ in Feng's experiments has the same definition as Eq. (1.6).	13
2.2	Map of vortex modes near the fundamental lock-in region. The critical curve marks the transition from one mode of vortex formation to another [175]. .	17
2.3	Branch identification of VIV responses from different experimental studies: 1DOF VIV at $m^* = 247.7$ by Feng [41], 1DOF VIV at $m^* = 2.4$ by Khalak and Williamson [71, 72], and 2DOF VIV at $m^* = 2.6$ by Jauvtis and Williamson [67].	19
2.4	Classification of mathematical modelling of FIV.	25
2.5	Schematic and governing equations of static wake oscillators for (a)–(c) circular cylinder [21, 45, 156], (d) square cylinder [159] and (e) 3:2 rectangular cylinder [97].	28

3.1	Sketch of a splitter plate attached to an elastically-mounted circular cylinder constrained to oscillate in the transverse (y -) direction.	40
3.2	Sketch definition of computational domain and boundary conditions used in the numerical simulations.	41
3.3	Computational mesh used to discretize the computational domain. Mesh partitioning of whole domain and local mesh refinement close to the surface of the bare circular cylinder ((a), (c)) and the cylinder-plate assembly ((b), (d)).	43
3.4	Partitioning of the computational domain into three regions by the specification of two parameters (innerDistance and outerDistance) in the dynamic meshing methodology.	45
3.5	Comparison of numerical results between this thesis and previous numerical investigations (Ahn and Kallinderis [1], Borazjani and Sotiropoulos [24], Bao <i>et al.</i> [15], Zhao [197], and Wang <i>et al.</i> [169]): (a) normalized maximum transverse displacement Y_{max} as a function of U_r ; (b) root-mean-square lift coefficient $C_{L,rms}$ as a function of U_r ; and, (c) mean drag coefficient $C_{D,mean}$ as a function of U_r . The current numerical simulations are of the VIV response of a circular cylinder for $Re = 150$, $m^* = 2.5465$, and $\zeta = 0$. The resolution of U_r used in the present simulations is 0.5.	49
3.6	Comparison of numerical results between this thesis and previous numerical investigations (Bourguet and Jacono [25], Dorogi and Baranyi [38]) for the normalized maximum transverse displacement Y_{max} as a function of U_r . The current numerical simulations are of the VIV response of a circular cylinder for $Re = 100$, $m^* = 10$, and $\zeta = 0$. The resolution of U_r used in present simulations is 0.5.	50
3.7	Comparison of numerical results between this thesis and previous numerical investigations (Sun <i>et al.</i> [154], Zhang <i>et al.</i> [190]) for the normalized maximum transverse displacement Y_{max} as a function of U_r . The current numerical simulations are of the FIV response of a cylinder-plate assembly with various plate lengths L_{SP}/D for $Re = 100$, $m^* = 10$, and $\zeta = 0$	51
3.8	The normalized vibration amplitude plotted as a function of L_{SP} and U_r	52
3.9	The dominant vibration frequency normalized by structural natural frequency (f_Y^*/f_n) plotted as a function of L_{SP} and U_r	53

3.10	Plots of (a) the normalized vibration amplitude (Y_{max}) and (b) the normalized dominant vibration frequency (f_Y^*/f_n) as a function of the reduced velocity U_r stratified in terms of the splitter-plate length L_{SP}	54
3.11	Three-dimensional plot of (a) the root-mean-square lift coefficient $C_{L,rms}$ and (b) the time-averaged (mean) drag coefficient $C_{D,mean}$ as a function of L_{SP} and U_r	57
3.12	Three-dimensional plot of (a) the root-mean-square lift coefficient $C_{L,rms}$ and (b) the time-averaged (mean) drag coefficient $C_{D,mean}$ as a function of L_{SP} and U_r	58
3.13	Variation of aerodynamic fluid forces acting on a cylinder-plate assembly: (a) the root-mean-square lift coefficient $C_{L,rms}$ and (b) the time-averaged (mean) drag coefficient $C_{D,mean}$ as a function of the reduced velocity U_r and stratified with respect to the plate length L_{SP}	59
3.14	The maximum vibration amplitude Y_{max} , the root-mean-square lift force coefficient and the mean drag force coefficient acting on the cylinder ($C_{Lc,rms}$, $C_{Dc,mean}$) and splitter-plate ($C_{Lp,rms}$, $C_{Dp,mean}$) as a function of U_r for six plate lengths.	60
3.15	The branch identification of cylinder-plate assembly with $L_{SP}/D = 0.5$. (a) Dependence on U_r of Y_{max} and of the RMS lift coefficients ($C_{L,rms}$, $C_{Lc,rms}$, $C_{Lp,rms}$). Power spectral density isopleths of (b) Y , (c) C_L , (d) C_{Lc} and (e) C_{Lp} plotted against the associated normalized frequency and U_r . In (b)–(e), the diagonal and horizontal dashed lines represent the Strouhal frequency ($St = 0.148$) and the unit normalized frequency, respectively. The solid lines in (b) and (c) represent the phase differences between Y and C_L (square) and between C_{Lc} and C_{Lp} (diamond), respectively. The assembly undergoes an integrated VIV-galloping, with three synchronizations identified: namely, 1:1 at $U_r = 5.5$ –10, 1:2 at $U_r = 11$ –11.5, and 1:3 at $U_r = 19$ –19.5. “Kinks” (identified by red boxes) in the amplitude response signal the onset of synchronizations.	63

- 3.16 Dynamical characteristics of the cylinder-plate assembly with $L_{SP}/D = 0.5$ at three reduced velocities $U_r = 6, 11.5$ and 19 in (a)–(c), corresponding to the three synchronizations identified in Fig. 3.15. The dynamical characteristics are displayed in terms of the time series of Y and C_L (first column of panels), the phase portraits C'_L-C_L (second column of panels), the Lissajous figures C_L-Y (third column of panels), and the power spectra of Y and C_L (fourth column of panels). In all these plots, the results for Y and C_L are shown as the black and red curves, respectively. 65
- 3.17 Instantaneous vorticity fields in one oscillation cycle T of a cylinder-plate assembly with $L_{SP}/D = 0.5$ at three $U_r =$ for three synchronizations: (a) $U_r = 6$ for 1:1; (b) $U_r = 11.5$ for 1:2; and, (c) $U_r = 19$ for 1:3. The corresponding wake modes are “2S”, “T+S” and “ $3 \times (2S)$ ”, respectively. 66
- 3.18 The branch identification of cylinder-plate assembly with $L_{SP}/D = 0.75$. The notations used here have been described in Fig. 3.15. The assembly undergoes an unlimited galloping response, with three synchronizations identified: namely, 1:2 at $U_r = 11$ – 11.5 , 1:3 at $U_r = 15$ – 20 and 1:5 at $U_r = 29$ – 30 . The onset of synchronization is signalled by a “kink” in the amplitude response. 68
- 3.19 The branch identification of cylinder-plate assembly with $L_{SP}/D = 1.5$. The notations used here have been described in Fig. 3.15. Four synchronizations have been identified: namely, one lock-in branch (1:1 at $U_r = 5.25$ – 6.5) and three galloping synchronizations (beginning with a “kink”)—1:3 at $U_r = 11.5$ – 16.5 , 1:4 at $U_r = 18$, and 1:5 at $U_r = 22$ – 25 . The lift components C_{Lc} and C_{Lp} are out-of-phase at $U_r = 6.5$ – 8 70
- 3.20 The branch identification of cylinder-plate assembly with $L_{SP}/D = 2$. The notations used here have been described in Fig. 3.15. Five synchronizations are identified: namely, one lock-in (1:1 at $U_r = 3.5$ – 7) and four galloping synchronizations—1:3 at $U_r = 12$ – 18 , 1:5 at $U_r = 19$ – 20 , 1:6 at $U_r = 24$, and 1:7 at $U_r = 27$ – 29 . Only 1:5 and 1:7 synchronizations are signalled by a “kink” in the amplitude response. The lift components C_{Lc} and C_{Lp} are out-of-phase at $U_r = 7$ – 10 72
- 3.21 Instantaneous vorticity fields in one oscillation cycle T of a freely-vibrating cylinder-plate assembly with $L_{SP}/D = 2$ at five reduced velocities for five synchronizations: (a) $U_r = 4$ for 1:1; (b) $U_r = 17$ for 1:3; (c) $U_r = 19$ for 1:5; (d) $U_r = 24$ for 1:6; and, (e) $U_r = 28$ for 1:7. The corresponding wake modes are “2S”, “ $3 \times (2S)$ ”, “ $5 \times (2S)$ ”, “ $6 \times (2S)$ ” and “ $7 \times (2S)$ ”, respectively. 73

3.22	The branch identification of cylinder-plate assembly with $L_{SP}/D = 2.5$. The notations used here have been described in Fig. 3.15. An initial galloping branch (pink vertical strip) is identified at $U_r = 12$ –15. A still branch (gray vertical strip) is identified at $U_r = 2$ –3.5 and 10–12. Four synchronizations are identified: namely, one lock-in (1:1) at $U_r = 3.5$ –7.5 and three galloping synchronizations—1:3 at $U_r = 15$ –23, 1:5 at $U_r = 23$ –24, and 1:7 at $U_r = 24$ –25. Only the 1:5 synchronization is signalled by a “kink” in the amplitude response. The lift components C_{Lc} and C_{Lp} are out-of-phase at $U_r = 7.5$ –10.	75
3.23	Instantaneous vorticity fields in one oscillation cycle T of cylinder-plate assembly with $L_{SP}/D = 2.5$ at four reduced velocities for four synchronizations: (a) $U_r = 4$ for 1:1; (b) $U_r = 19$ for 1:3; (c) $U_r = 23$ for 1:5; and, (d) $U_r = 25$ for 1:7. The wake modes for the first two cases are “2S” and “ $2 \times (P+S)$ ”, respectively. There is no identifiable wake pattern for the third case. For the fourth case, the associated wake pattern is “ $7 \times (2S)$ ”.	76
3.24	Instantaneous interaction between the shear layers and the vortex behind moving body: (a) circular cylinder at $U_r = 5$ and 8; (b) assembly with $L_{SP}/D = 0.25$ at $U_r = 5, 8, 11$; and, (c) assembly with $L_{SP}/D = 0.5$ at $U_r = 11, 19.5$. Snapshots are obtained at oscillation maxima ($t = 0$ and $T/8$) and minima ($t = 4T/8$ and $5T/8$).	78
3.25	Vortex shedding mode in the range of reduced velocities that are close to the transition from VIV to galloping for cylinder-plate assembly with $L_{SP}/D = 0.5$. An oscillation cycle is divided into the (a) first and (b) second halves of the cycle. At $U_r = 10$, VIV response corresponds to a “2S” wake mode. At $U_r = 10.5$, three vortices are shed in total, whereas at $U_r = 11$, a galloping response is triggered with “ $2 \times (2S)$ ” wake mode.	79
3.26	Temporal evolution of instantaneous shear layers around a cylinder-plate assembly over one oscillation cycle at a time interval of $T/12$: (a) $L_{SP}/D = 1.5$ at $U_r = 4$; (b) $L_{SP}/D = 1.5$ at $U_r = 5.5$; (c) $L_{SP}/D = 2$ at $U_r = 4$; and, (d) $L_{SP}/D = 2$ at $U_r = 5.5$. Both values of U_r correspond to the VIV branch. The positive and negative peaks in the cycle occur at time $t = 0$ and $t = 6T/12$, respectively.	83
3.27	Time series of the instantaneous displacement (black curve) and lift coefficient (red curve) and the wake patterns within (a) quasi-steady regime for $L_{SP}/D = 2$ and (b) still branch for $L_{SP}/D = 2.5$ at two reduced velocities: namely, $U_r = 3$ (parts (i) and (iii)) and $U_r = 10$ (parts (ii) and (iv)).	86

3.28	Snapshots of the instantaneous vorticity fields in one oscillation period T for the initial galloping branch: (a) $L_{SP}/D = 2.5$ at $U_r = 14$; (b) $L_{SP}/D = 3$ at $U_r = 14$; and, (c) $L_{SP}/D = 3.5$ at $U_r = 30$	87
3.29	Temporal evolution of the instantaneous shear layer around cylinder-plate assembly over one oscillation cycle: (a) $L_{SP}/D = 2$ at $U_r = 30$; (b) $L_{SP}/D = 2.5$ at $U_r = 14$; (c) $L_{SP}/D = 2.5$ at $U_r = 30$; (d) $L_{SP}/D = 3$ at $U_r = 30$; and, (e) $L_{SP}/D = 3.5$ at $U_r = 30$	88
3.30	The identification and characterization of the branching behavior of a cylinder-plate assembly in the $(L_{SP}/D, U_r)$ plane. The assembly is undergoing a flow-induced vibration in a low-Reynolds number of $Re = 100$ with a mass ratio of $m^* = 10$ and a zero structural damping ($\zeta = 0$). The galloping regime is enclosed within the solid purple line. The synchronization branches are shaded in green (VIV regime), blue (odd-multiple synchronization in the galloping regime), and dark purple (even-multiple synchronization in the galloping regime). The initial galloping and the still (quiescent) branches are shaded in light purple and grey, respectively. The square symbols in the plane delineate various types of beating phenomena of the lift coefficient—Type 1 (red squares), Type 2 (green squares), Type 3 (yellow squares), Type 4 (blue squares) and Type 5 (unfilled squares).	94
3.31	Time series of Y (grey) and C_L (black) for various combinations of L_{SP}/D and U_r . These time series are superimposed on the time variations of the local frequency of lift coefficient f_{C_L} (red), the structural natural frequency f_n (blue) and the Strouhal frequency f_{St} (green). Five distinctive types of beating are classified: (a)–(e) Type 1–5.	97
3.32	The periodic beating behavior in the amplitude envelope of time history of a signal. The beating intensity is defined as the difference between largest peak value (high-peak) and lowest peak value (low-peak) over one beating period.	99
3.33	Time series of the transverse force coefficient C_L (black curves) and the corresponding amplitude envelopes (red curves) for a number of selected examples of beating in the galloping regime. The examples are characterized by the plate length L_{SP}/D of the cylinder-plate assembly and the reduced velocity U_r	101

3.34	(a) Isoleths of the energy transfer per unit length (in J/m) between the elastically-supported cylinder-plate assembly and surrounding flow shown as a function of the non-dimensional amplitude of the transverse displacement (Y_{max}) and the splitter-plate length (L_{SP}/D) at a fixed value of the reduced velocity $U_r = 6$ within the VIV regime. The black dashed line represents the condition of zero energy transfer. Time series of the transverse displacement $Y(t)$ at $U_r = 6$ for (b) a bare circular cylinder, (c) a cylinder-plate assembly with $L_{SP}/D = 0.75$, and (d) a cylinder-plate assembly with $L_{SP}/D = 4$. . .	103
3.35	(a) Time series of $Y(t)$ (dashed black lines) and the energy transferred per unit length over one oscillation cycle between the structure (cylinder-plate assembly) and the surrounding fluid (solid red lines). (b) Time series of the total net energy per unit length $P_{net,T}$ transferred to the cylinder-plate assembly, the energy per unit length transferred to the cylinder $P_{net,C}$ only, and the energy per unit length transferred to the splitter-plate $P_{net,SP}$ only. The examples shown here are selected values of the splitter-plate length L_{SP}/D and the reduced velocity U_r	104
3.36	Schematic depiction of the geometric visualization tools used to analyze the nonlinear dynamics of a dynamical system. A dynamical quantity of interest is q . The time series $q(t)$ is a periodic oscillation with a quasi-sinusoidal waveform, corresponding to the closed orbits in the three-dimensional phase space (q, q', q'') which start from the origin of the space, gradually spiral outward and finally converge to the stable limit cycle when a stationary state of the oscillatory motion is reached. The red points correspond to the intersections between closed orbits and the Poincaré section ($q'' = 0$). . . .	106
3.37	(a) Amplitude response of the cylinder-plate assembly with $L_{SP}/D = 0.5$. Dynamical characteristics of lift coefficient with respect to (b) time series $C_L(t)$, (c) power spectral density, (d) phase-plane portrait (C_L, C'_L), and (e) Poincaré section, at three representative reduced velocities: (i) $U_r = 13.5$, (ii) $U_r = 18$, (iii) $U_r = 19.5$	108
3.38	(a) Amplitude response of the cylinder-plate assembly with $L_{SP}/D = 0.75$. Dynamical characteristics of lift coefficient with respect to (b) time series $C_L(t)$, (c) power spectral density, (d) phase-plane portrait (C_L, C'_L), and (e) Poincaré section, at three representative reduced velocities: (i) $U_r = 6.5$, (ii) $U_r = 8.5$, (iii) $U_r = 13.5$	109

3.39	(a) Amplitude response of the cylinder-plate assembly with $L_{SP}/D = 1.5$. Dynamical characteristics of lift coefficient with respect to (b) time series $C_L(t)$, (c) power spectral density, (d) phase-plane portrait (C_L, C'_L) , and (e) Poincaré section, at three representative reduced velocities: (i) $U_r = 17$, (ii) $U_r = 20$, (iii) $U_r = 25$	110
3.40	(a) Amplitude response of the cylinder-plate assembly with $L_{SP}/D = 2.0$. Dynamical characteristics of lift coefficient with respect to (b) time series $C_L(t)$, (c) power spectral density, (d) phase-plane portrait (C_L, C'_L) , and (e) Poincaré section, at three representative reduced velocities: (i) $U_r = 11$, (ii) $U_r = 23$, (iii) $U_r = 26$	111
3.41	Division of consecutive oscillation cycles during beating.	114
3.42	Six consecutive oscillation cycles (C1–C6) for analyzing the wake modes of quasi-periodic beating, in terms of the time series of Y (black curve) and C_L (red curve). Blue curves connect multiple positive and negative peaks during beating of $C_L(t)$ and determine the amplitude envelope.	115
3.43	Snapshots of the instantaneous vorticity field over six consecutive oscillation cycles (each cycle with period T) for a cylinder-plate assembly with $L_{SP}/D = 0.75$ at $U_r = 10$. Each cycle includes eight vorticity snapshots equally spaced in time. The corresponding wake modes are “ $2 \times (2S)$ ”, “ $S + S_A$ ”, “ $G(S_B + 2S) + S$ ”, “ $2 \times (2S)$ ”, “ $S_A + G(S_B + 2S)$ ”, and “ $2 \times (2S)$ ”, respectively.	116
3.44	Eleven consecutive oscillation cycles (C1–C11) for analyzing the wake modes of aperiodic beating of the lift coefficient. Time series of the transverse displacement Y and lift coefficient C_L are shown as the black and red curves, respectively.	118
3.45	Snapshots of the instantaneous vorticity field over five selected oscillation cycles (C1, C5, C7, C9, and C11) for a cylinder-plate assembly with $L_{SP}/D = 0.5$ at $U_r = 14$. Each cycle includes eight snapshots of the vorticity equally spaced in time.	119
3.46	Temporal snapshots of the instantaneous vorticity field for the 1:5, 1:6 and 1:7 synchronization branches of a cylinder-plate assembly with $L_{SP}/D = 2$. In this example, C_L undergoes a periodic oscillation without beating.	121

4.1	A sketch of an elastically-mounted elliptical cylinder-plate assembly constrained to oscillate in the transverse direction. An equivalent circle (with diameter D) whose cross-sectional area is equal to that of an ellipse (with length a and width b) is plotted as the dashed curve.	126
4.2	The computational mesh used for the numerical simulation of the FIV of an elliptical cylinder-plate assembly: (a) entire domain; (b) in the vicinity of the elliptical cylinder and the splitter-plate.	127
4.3	(a) The non-dimensional maximum transverse displacement Y_{max} ; (b) the dominant frequency of oscillation f_Y^*/f_n ; (c) the root-mean-square lift coefficient $C_{L,rms}$; and, (d) the mean drag coefficient $C_{D,mean}$. All these quantities are plotted as a function of U_r for six values of elliptical ratio: $AR = 0.5, 0.67, 0.75, 1, 1.5$ and 2	129
4.4	The branch identification of the FIV for an elliptical cylinder-plate assembly with a fixed plate length $L_{SP}/D = 0.5$ and various aspect ratios: (a)–(d) $AR = 0.75, 1, 1.5$ and 2 . In each case, the maximum transverse displacement Y_{max} and the root-mean-square lift coefficient $C_{L,rms}$ are shown as function of U_r . The synchronization branches in the amplitude response are identified as the shaded regions with different colours. “Kinks” in the amplitude responses are marked by the red boxes.	131
4.5	(a) The maximum transverse displacement Y_{max} as a function of U_r for an elliptical cylinder-plate assembly with various aspect ratios. PSD of Y plotted against f_Y/f_n and U_r for (b)–(e) $AR = 0.75, 1, 1.5$ and 2 . In (b)–(e), the vertical, horizontal and diagonal dashed lines represent the boundaries of synchronization branches, the unit normalized frequency $f_Y/f_n = 1$ and the Strouhal frequency f_{St} , respectively. The solid line with squares represents the phase difference ϕ between the oscillations in Y and C_L	132
4.6	(a) The maximum transverse displacement Y_{max} as a function of U_r for an elliptical cylinder-plate assembly with various aspect ratios. PSD (logarithmic scale) of C_L plotted against f_Y/f_n and U_r for (b)–(e) $AR = 0.75, 1, 1.5$ and 2 . Other notations used here are the same as those in Fig. 4.5.	133

4.7	Dynamical characteristics in the 1:1 synchronization branch (viz., lock-in) for an elliptical cylinder-plate assembly with (a) $AR = 1$ and $U_r = 8$; (b) $AR = 1.5$ and $U_r = 8$; and, (c) $AR = 2$ and $U_r = 7$. The dynamical characteristics are displayed in terms of the time series of Y and C_L (first column of panels), the phase portraits $C_L-C'_L$ and $Y-Y'$ (second column of panels), the Lissajous figures $Y-C_L$ (third column of panels), and the normalized power spectra of Y and C_L (fourth column of panels). In all plots, the results for Y and C_L are presented as black and red curves, respectively.	135
4.8	Instantaneous vorticity fields in one oscillation cycle T within the 1:1 synchronization branch (viz., lock-in) for an elliptical cylinder-plate assembly with (a) $AR = 1$ and $U_r = 8$; (b) $AR = 1.5$ and $U_r = 8$; and, (c) $AR = 2$ and $U_r = 7$. The “2S” mode is observed for the three cases.	136
4.9	Dynamical characteristics in the 1:2 synchronization branch for an elliptical cylinder-plate assembly with (a) $AR = 1$ and $U_r = 11$; (b) $AR = 1.5$ and $U_r = 11$; and, (c) $AR = 2$ and $U_r = 11$. The notations used here are the same as those described in the caption of Fig. 4.7.	138
4.10	Instantaneous vorticity fields in one oscillation cycle within the 1:2 synchronization branch for an elliptical cylinder-plate assembly with (a) $AR = 1$ and $U_r = 11$; (b) $AR = 1.5$ and $U_r = 11$; (c) $AR = 2$ and $U_r = 8$; (d) $AR = 2$ and $U_r = 10$; and, (e) $AR = 2$ and $U_r = 11$. The wake modes are identified as “ $2 \times (2S)$ ”, “T+S”, “ $\pm(2S)$ ”, “ $2 \times (2S)$ ” and an irregular mode for the five cases, respectively.	139
4.11	Dynamical characteristics in the 1:3 synchronization branch for an elliptical cylinder-plate assembly with (a) $AR = 1$ and $U_r = 19$; (b) $AR = 1.5$ and $U_r = 19$; and, (c) $AR = 2$ and $U_r = 13$. The notations used here are the same as those described in the caption of Fig. 4.7	141
4.12	Instantaneous vorticity fields in one oscillation cycle within the 1:3 synchronization branch for an elliptical cylinder-plate assembly with (a) $AR = 1$ and $U_r = 19$; (b) $AR = 1.5$ and $U_r = 19$; and, (c) $AR = 2$ and $U_r = 13$. The wake modes are “ $3 \times (2S)$ ”, “ $3 \times (2S)$ ” and “ $2 \times (P+S)$ ”, respectively. . .	142
4.13	Quantities of interest associated with the non-synchronization branch for an elliptical cylinder-plate assembly with $AR = 0.75$. (a) Power spectra (normalized by the maximum power) of C_L over $U_r = 7-13$. (i) Time series of C_L ; (ii) phase portraits $C_L-C'_L$; and, (iii) Poincaré sections at three reduced velocities: namely, (b)–(d) $U_r = 11, 12$ and 13 . The amplitude envelopes of the time series are shown as red curves.	144

4.14	Quantities of interest associated with the non-synchronization branch for an elliptical cylinder-plate assembly with $AR = 1$. (a) Power spectra (normalized by the maximum power) of C_L over $U_r = 12$ –18. (i) Time series of C_L ; (ii) phase portraits C_L - C'_L ; and, (iii) Poincaré sections at two reduced velocities: namely, (b)–(c) $U_r = 14$ and 17. The amplitude envelopes of the time series are shown as red curves.	145
4.15	Quantities of interest associated with the non-synchronization branch for an elliptical cylinder-plate assembly with $AR = 1.5$. (a) Power spectra (normalized by the maximum power) of C_L over $U_r = 13$ –18. (i) Time series of C_L ; (ii) phase portraits C_L - C'_L ; and, (iii) Poincaré sections at two reduced velocities: namely, (b)–(c) $U_r = 14$ and 17. The amplitude envelopes of the time series are shown as the red curves.	146
4.16	Four consecutive oscillation cycles in the time series of Y (black curve) and C_L (red curve) for an elliptical cylinder-plate assembly with $AR = 1.5$ at $U_r = 14$. The red dashed curves delineate the amplitude envelope of C_L . . .	148
4.17	Instantaneous vorticity fields over four consecutive oscillation cycles (labelled cycle 1, 2, 3, and 4) used for the vortex-shedding analysis associated with the three-period beating in Fig. 4.16.	149
4.18	Effect of aspect ratio AR ($0.5 \leq AR \leq 2.5$) on the vibration response of an elliptical cylinder-plate assembly with $L_{SP}/D = 0.75$ and 2.5. (a) The maximum transverse displacement Y_{max} ; (b) the frequency ratio f_Y^*/f_n ; (c) the root-mean-square lift coefficient $C_{L,rms}$; and, (d) the mean drag coefficient $C_{D,mean}$ as a function of U_r	151
4.19	Branching behavior of an unlimited FIV response provoked on an elliptical cylinder-plate assembly of various aspect ratios and a fixed splitter-plate length $L_{SP}/D = 0.75$. The maximum transverse displacement Y_{max} (left vertical axis) and the root-mean-square lift coefficient $C_{L,rms}$ (right vertical axis) are plotted as a function of U_r for (a)–(d) $AR = 0.75, 1, 1.5$ and 2. The synchronization branches are shaded in different colours. “Kinks” in the amplitude response are delineated by red boxes.	154
4.20	(a) The maximum transverse displacement Y_{max} as a function of U_r for an elliptical cylinder-plate assembly with $AR = 0.75$ –2 and $L_{SP}/D = 0.75$. PSD (logarithmic scale) of Y exhibited as a function of f_Y/f_n and U_r for (b)–(e) $AR = 0.75, 1, 1.5$ and 2. Other notations used here are the same as that in Fig. 4.5.	155

4.21	(a) The normalized amplitude responses and (b)–(e) PSD of C_L for $AR = 0.75$ – 2 and $L_{SP}/D = 0.75$. Other notations used here are the same as that in Fig. 4.5.	156
4.22	Dynamical characteristics of the “lock-in” regime for an elliptical cylinder-plate assembly with (a) $AR = 1.5$ and (b) $AR = 2$ at $U_r = 6$ and of the transition regime between the 1:1 and 1:2 synchronizations for (c) $AR = 2$ at $U_r = 8$. The evolution of instantaneous vorticity fields during one oscillation cycle T is displayed for (d) $AR = 1.5$ at $U_r = 6$; (e) $AR = 2$ at $U_r = 6$; (f) $AR = 2$ at $U_r = 7$; and, (g) $AR = 2$ at $U_r = 8$. The “2S” and “quasi-2S” modes are identified in the “lock-in” and transition regimes, respectively.	159
4.23	Dynamical characteristics of the 1:3 synchronization branch for an elliptical cylinder-plate assembly with (a) $AR = 0.75$, (b) $AR = 1$, (c, d) $AR = 1.5$, and (e, f) $AR = 2$ at two values of reduced velocity (viz., $U_r = 16$ and 20).	161
4.24	Instantaneous vorticity field over one oscillation cycle T in the 1:3 synchronization branch for an elliptical cylinder-plate assembly with (a) $AR = 0.75$, (b) $AR = 1$, (c) $AR = 1.5$ and (d, e) $AR = 2$ at $U_r = 16$ and 20 . The 1:3 synchronization branch is associated with a “ $3 \times (2S)$ ” mode.	162
4.25	Dynamical characteristics of the 1:5 synchronization branch for an elliptical cylinder-plate assembly with (a)–(c) $AR = 1, 1.5$ and 2 at $U_r = 29$ and 30 . The vortex-shedding pattern over one oscillation cycle T is exhibited in (d)–(e) where a “ $5 \times (2S)$ ” mode is identified.	164
4.26	Dynamical characteristics of the 1:2 synchronization branch for an elliptical cylinder-plate assembly with (a)–(c) $AR = 1, 1.5$ and 2 at $U_r = 11$. The transition regime between the 1:2 and 1:3 synchronizations for the assembly with (d) $AR = 2$ at $U_r = 14$. Instantaneous vorticity field during one oscillation cycle for (e)–(g) $AR = 1, 1.5$ and 2 at $U_r = 11$; and, $AR = 2$ at (h)–(i) $U_r = 13$ and 14 . The “ $2 \times (2S)$ ” and “quasi- $2 \times (2S)$ ” modes are supported by the 1:2 synchronization and the transition regime, respectively.	165
4.27	Dynamical characteristics of the 1:4 synchronization branch for an elliptical cylinder-plate assembly with (a)–(b) $AR = 1.5$ and 2 at $U_r = 24$ (c)–(d) Instantaneous vorticity field during one oscillation cycle T . The 1:4 synchronization branch supports a “ $4 \times (2S)$ ” mode.	166
4.28	The normalized power spectra of the lift coefficient C_L for reduced velocities in the range from 6 to 30 for an elliptical cylinder-plate assembly with (a)–(d) $AR = 0.75, 1, 1.5$ and 2	169

4.29	Dynamical characteristics in the non-synchronization branches of an elliptical cylinder-plate assembly with $L_{SP}/D = 0.75$. The dynamical characteristics consist of (i) the time series of Y (grey lines) and C_L (blue lines); (ii) phase portrait $C_L-C'_L$; and, (iii) Poincaré section. The red dashed lines delineate the amplitude envelope of $C_L(t)$	171
4.30	The instantaneous vorticity field over five consecutive oscillation cycles for an elliptical cylinder-plate assembly with $L_{SP}/D = 0.75$ and $AR = 1.5$ at $U_r = 28$. This is a period-5 oscillation.	172
4.31	The unlimited FIV of an elliptical cylinder-plate assembly with $L_{SP}/D = 2.5$ for (a) $AR = 1$ and (b) 1.5, in terms of the branching behavior of amplitude response and PSD of Y and C_L . Other notations used here are the same as those in Figs. 4.19–4.21.	174
4.32	The branching behavior and wake mode for an elliptical cylinder-plate assembly with $L_{SP}/D = 0.5$ in the (AR, U_r) plane. The assembly's FIV response occurs over a limited U_r range.	176
4.33	The branching behavior and wake mode of an elliptical cylinder-plate assembly with $L_{SP}/D = 0.75$ in the (AR, U_r) plane. The assembly's FIV response occurs over an unlimited U_r range.	177
4.34	Power spectra of C_L obtained from an elliptical cylinder-plate assembly with $AR = 2$ and $L_{SP}/D = 0.5$ for $U_r = 6$ –14.	178
4.35	A comparison of the structural oscillations and the flow surrounding the elliptical cylinder-plate assembly with $AR = 0.5$ –1 and $L_{SP}/D = 0.5$ at $U_r = 6$. (a) Time series of Y (black) and C_L (red) for $AR = 0.5$ (left panel) and $AR = 0.67$ (right panel). (b) The flow patterns surrounding the assembly at time $t = T$ for (i)–(iv) $AR = 0.5, 0.67, 0.75$ and 1. Zoomed-in view of the instantaneous vorticity field around the assembly at times (c) $t = 3T/8$ and (d) $t = 7T/8$ for (i)–(iv) $AR = 0.5, 0.67, 0.75$ and 1.	180
5.1	A schematic model of an elastically mounted circular cylinder undergoing the cross-flow VIV due to the aerodynamic fluid force acting on the oscillating body.	186
5.2	A schematic of a bluff body experiencing transverse galloping.	187
5.3	The evolution of minimum and mean objective values as a function of iterations in one optimization procedure of genetic algorithm.	198

5.4	Flow chart of the GA-optimized grey-box estimation framework.	199
5.5	Time series of Y and C_L for VIV of circular cylinder at $U_r = 5$. The C_L -based model is identified when various even polynomial terms are free to estimate: Case 1—no even polynomial coefficient; Case 2— A_2 ; Case 3— A_2 and A_4 ; Case 4— A_2 , A_4 and A_6	200
5.6	Time series of Y and C_L for VIV of circular cylinder at $U_r = 5$. The C_L -based grey-box model is estimated when various odd and even polynomial terms are free to estimate: Case 5— A_1 ; Case 6— A_1 and A_2 ; Case 7— A_1 , A_2 and A_4 ; Case 8— A_1 , A_2 , A_4 and A_6	201
5.7	The VIV response of a circular cylinder in terms of the transverse displacement and lift coefficient as a function of U_r , surrounded by the time series of Y (black) and C_L (red) at eight representative values of U_r . Note that the periodic and beating oscillations are respectively marked by blue and red points in the amplitude response.	202
5.8	The time series of Y and C_L for VIV of a circular cylinder at $U_r = 6$ from estimation data and C_L -based wake-oscillator models. For Case 1-1, the estimated parameters are $C_{L0} = 0.1894$, $St = 0.1590$, $\epsilon = 2.6422$, $A_1 = 0.3976$ and $B_1 = 0.1737$. For Case 1-2, the estimated parameters are $C_{L0} = 0.0818$, $St = 0.1591$, $\epsilon = 0.7283$, $A_1 = 0.4380$, $B_1 = -0.3356$ and $B_2 = 0.8748$	204
5.9	The time series of Y and C_L for VIV of a circular cylinder at $U_r = 4.5$ from estimation data and C_L -based wake-oscillator models. For Case 1-1, the estimated parameters are $C_{L0} = 0.6$, $St = 0.1607$, $\epsilon = 0$, $A_1 = 0.2458$ and $B_1 = 1.8165$. For Case 1-2, the estimated parameters are $C_{L0} = 0.5715$, $St = 0.1589$, $\epsilon = 0.016$, $A_1 = 0.7711$, $B_1 = 1.8253$ and $B_2 = 1.1840$	205
5.10	Fitness of $Y(t)$ (top) and $C_L(t)$ (bottom) from Case 1-1 and Case 1-2 for VIV of a circular cylinder at different reduced velocities.	206
5.11	Estimated parameters of C_L -based wake oscillator model with an optimal structure for VIV of circular cylinder. (a)–(f) represent C_{L0} , St , ϵ , A_1 , B_1 and B_2 as a function of U_r	209
5.12	Estimated parameters of θ -based wake oscillator model with an optimal structure for VIV of circular cylinder. (a)–(f) represent C_{L0} , St , ζ_f , f_m , \bar{l}^* and A_1 as a function of U_r	213

5.13	The galloping response of a circular cylinder-plate assembly with $L_{SP}/D = 0.75$ in terms of Y and C_L as a function of U_r , surrounded by $Y(t)$ (black) and $C_L(t)$ (red) at eleven representative values of U_r . The periodic and beating oscillations are respectively marked by blue and red points in the amplitude response.	215
5.14	Fitness of $Y(t)$ (top) and $C_L(t)$ (bottom) from Case 1-1 and Case 1-6 for galloping of a circular cylinder-plate assembly at larger reduced velocity.	217
5.15	The time series of Y and C_L for galloping of a circular cylinder-plate assembly with $L_{SP}/D = 0.75$ at $U_r = 19$ from estimation data and C_L -based wake-oscillator models. For Case 1-1, the estimated parameters are $C_{L0} = 0.1553$, $St = 0.1563$, $\epsilon = 0.0007$, $A_1 = 0.0682$ and $B_1 = -6.1186$. For Case 1-6, the estimated parameters are $C_{L0} = 0.2073$, $St = 0.1563$, $\epsilon = 0.0025$, $A_1 = -0.8891$, $A_3 = 8.7814$ and $B_1 = -6.0558$. For Case 1-7, the estimated parameters are $C_{L0} = 0.3375$, $St = 0.1563$, $\epsilon = 0.0184$, $A_1 = 0.9373$, $A_3 = -163.4914$, $A_5 = 2572.8800$, $A_7 = -10073.8521$ and $B_1 = -5.5171$	219
5.16	The time series of Y and C_L for galloping of a circular cylinder-plate assembly with $L_{SP}/D = 0.75$ at $U_r = 29$ from estimation data and C_L -based wake-oscillator models. For Case 1-1, the estimated parameters are $C_{L0} = 0.1041$, $St = 0.1570$, $\epsilon = 0.0042$, $A_1 = 0.0378$ and $B_1 = -5.4993$. For Case 1-6, the estimated parameters are $C_{L0} = 0.2884$, $St = 0.1570$, $\epsilon = 0.0474$, $A_1 = -0.4622$, $A_3 = 5.1627$ and $B_1 = -5.4442$. For Case 1-7, the estimated parameters are $C_{L0} = 0.0492$, $St = 0.1570$, $\epsilon = 0.0010$, $A_1 = -1.1962$, $A_3 = -49.2549$, $A_5 = 1495.0582$, $A_7 = -8154.3825$ and $B_1 = -4.9050$	220
5.17	Estimated parameters of C_L -based wake oscillator model with optimal structure for the galloping of circular cylinder-plate assembly. (a)–(h) represent C_{L0} , St , ϵ , A_1 , A_3 , A_5 , A_7 and B_1 as a function of U_r	222
5.18	Time history of C_L from estimation data and estimated wake-oscillator models (Cases 2-1, 2-2, 2-3 and 2-4) at (a) $U_r = 19$ and (b) $U_r = 29$	223
5.19	Estimated parameters of θ -based wake oscillator model with optimal structure for the galloping of circular cylinder-plate assembly. (a)–(h) represent C_{L0} , St , ζ_f , f_m , \bar{l}^* , A_1 , A_3 and A_5 as a function of U_r	225
5.20	Fitness value of Y (up) and C_L (bottom) associated with the galloping of a circular cylinder-plate assembly with $L_{SP}/D = 0.75$ from the best-structured C_L -based (Case 1-7) and θ -based (Case 2-3) wake oscillator models.	226

5.21	Time history of lift coefficient and instantaneous vorticity field of a stationary circular cylinder at $Re = 100$	227
5.22	Time history of lift coefficient and instantaneous vorticity field of a stationary circular cylinder-plate assembly with $L_{SP}/D = 0.75$ at $Re = 100$	228

List of Tables

3.1	Boundary conditions and their corresponding mathematical expressions. . .	42
3.2	Dependence of numerical results on the size of the computational domain. All the numerical simulations were conducted at fixed values of $L_u/D = 15$, $Re = 150$, $m^* = 2.5465$, $\zeta = 0$, and $U_r = 6$	46
3.3	Dependence of numerical results on the grid resolution. All the numerical simulations were conducted at fixed values of $Re = 150$, $m^* = 2.5465$, $\zeta = 0$, and $U_r = 6$	47
3.4	Dependence of numerical results on the time step size. All the numerical simulations were conducted at fixed values of $Re = 150$, $m^* = 2.5465$, $\zeta = 0$, and $U_r = 6$	48
3.5	Summary of branching (synchronization) behaviors for cylinder-plate assemblies for $L_{SP}/D = 0-4$	80
3.6	Frequency content of the displacement (Y) and the transverse force coefficient (C_L) in the various galloping synchronization (GS) branches for cylinder-plate assemblies with $L_{SP}/D = 0.5-2.5$. The Arabic numbers in spectra column refer to the fundamental frequency (1) as well as the order of harmonics present in the frequency spectra.	91
5.1	Optimization properties of genetic algorithm.	196
5.2	Configurations of parameters for the wake-oscillator models based on C_L (Case 1-X) and θ (Case 2-X). 1–fixed to zero, 0–free.	203
5.3	Estimated C_L -based wake oscillator model with different odd polynomial terms. The estimation data is associated with the VIV of a circular cylinder at $U_r = 6$ and 7.	207

5.4	Estimated C_L -based wake oscillator model with different odd polynomial terms. The estimation data is associated with the VIV of a circular cylinder at $U_r = 4.5$ and 8.5	207
5.5	Estimated parameters for C_L -based wake oscillator model with (Case 1-2) and without (Case 1-5) the second-order polynomial term. The estimation data is associated with the quasi-periodic oscillation for VIV of a circular cylinder at $U_r = 6, 7, 4.5$ and 8.5	210
5.6	Estimated parameters of θ -based wake oscillator model with various combinations of even and odd polynomial terms. The estimation data is associated with the non-sinusoidal periodic oscillation for VIV of a circular cylinder at $U_r = 6$ and 7	211
5.7	Estimated parameters of θ -based wake oscillator model with various combinations of even and odd polynomial terms. The estimation data is associated with the quasi-periodic oscillation for VIV of a circular cylinder at $U_r = 4.5$ and 8.5	212
5.8	Estimated parameters for C_L -based wake oscillator model with (Case 1-2) and without (Case 1-5) the second-order polynomial term. The estimation data is associated with the quasi-periodic oscillation for VIV of a circular cylinder at $U_r = 9, 25, 27$ and 29	216
5.9	Estimated parameters and fitness of $Y(t)$ and $C_L(t)$ at $U_r = 13$. Invalid solutions from Case 1-1 (Solutions 1–3) and Case 1-2 (Solution 4), as well as a valid solution from Case 1-6 (Solution 5). The unreasonable parameter is marked in box.	218
5.10	Fitness value of Y (columns 2–3) and C_L (columns 4–5) associated with the VIV of circular cylinder from the best-structured C_L -based (Case 1-2) and θ -based (Case 2-1) wake oscillator models.	224

List of Abbreviations

XDOF = X-Degree-of-Freedom

ALE = Arbitrary Lagrangian Eulerian

CFD = Computational Fluid Dynamics

CFL = Courant-Friedrichs-Lewy

FIV = Flow Induced Vibration

FSI = Fluid Structure Interaction

GA = Genetic Algorithm

IB = Initial Branch

LB = Lower Branch

NRMSE = Normalized Root Mean Squared Error

NS = Navier-Stokes

ODE = Ordinary Differential Equation

PISO = Pressure Implicit with Splitting Operators

PSD = Power Spectral Density

PTC = Passive Turbulence Control

QS = Quasi-Steady

SIMPLE = Semi-Implicit Method for Pressure-Linked Equations

SU = Super-Upper Branch

UB = Upper Branch

VIV = Vortex Induced Vibration

VIR = Vortex-Induced Rotation

VIVACE = Vortex Induced Vibration Aquatic Clean Energy

List of Symbols

D	Characteristic length of structure	[m]
a	Length of an elliptical cylinder in the in-line direction	[m]
b	Length of an elliptical cylinder in the cross-flow direction	[m]
AR	Aspect ratio of an elliptical cylinder, $AR = b/a$	[-]
L_{SP}	Length of a splitter-plate	[m]
W_{SP}	Width of a splitter-plate	[m]
m_{osc}	Mass of oscillating system	[kg]
m_a	Added mass by fluid	[kg]
C_a	Added mass coefficient	[-]
m_d	Displaced fluid mass by structure	[kg]
m^*	Structural mass ratio	[-]
k	Spring stiffness	[N m ⁻¹]
c, c_{sys}	Structural damping coefficient	[N s m ⁻¹]
ζ	Structural damping ratio	[-]
Re	Reynolds number	[-]
St	Strouhal number	[-]
ρ	Density of fluid	[kg m ⁻³]

ν	Kinematic viscosity of fluid	$[\text{m}^2 \text{s}^{-1}]$
μ	Dynamic viscosity of fluid	$[\text{kg m}^{-1} \text{s}^{-1}]$
U	Freestream velocity	$[\text{m s}^{-1}]$
U_r	Reduced velocity	$[-]$
U_R	Resonance velocity	$[-]$
U_v	Onset velocity of vortex-induced vibration	$[-]$
α	Flow incidence angle	$[\circ]$
F_y	Fluid force in the cross-flow direction	$[\text{N}]$
F_x	Fluid force in the in-line direction	$[\text{N}]$
C_L	Lift coefficient	$[-]$
C_{Lc}	Lift coefficient on circular cylinder	$[-]$
C_{Lp}	Lift coefficient on splitter-plate	$[-]$
$C_{L,rms}$	Root-mean-square of lift coefficient	$[-]$
C_{L0}	Lift coefficient on a fixed structure subjected to vortex shedding	$[-]$
C_L^{QS}	Lift coefficient calculated from the quasi-steady hypothesis	$[-]$
C_D	Drag coefficient	$[-]$
C_{Dc}	Drag coefficient on circular cylinder	$[-]$
C_{Dp}	Drag coefficient on splitter-plate	$[-]$
$C_{D,mean}$	Mean drag coefficient	$[-]$
θ	Angular displacement of near-wake region	$[\circ]$
l	Half length of wake oscillator	$[\text{m}]$
h	Width of wake oscillator	$[\text{m}]$
ϵ	Van der Pol parameter	$[-]$

f_m	Magnus parameter	[–]
A_i	Fitting parameters ($i = 1, 2, \dots, 7$)	[–]
B_i	Fitting parameters ($i = 1, 2$)	[–]
t	Dimensional time	[s]
τ	Dimensionless time	[–]
y, \dot{y}, \ddot{y}	Transverse displacement, velocity and acceleration of structure	[m, m/s, m/s ²]
Y	Dimensionless transverse displacement of structure	[–]
Y_{max}	Dimensionless maximum transverse displacement of structure	[–]
T	One oscillation cycle	[–]
ϕ	Phase difference between two temporal signals	[°]
f_n	Structural natural frequency	[Hz]
$f_{n,air}$	Structural natural frequency in vacuum or air	[Hz]
$f_{n,water}$	Structural natural frequency in water	[Hz]
f_{St}	Vortex shedding frequency of flow past a stationary structure	[Hz]
f_{vs}	Vortex shedding frequency of flow past an oscillating structure	[Hz]
f_{osc}	Oscillation frequency of structure	[Hz]
f^*	Frequency ratio	[–]

Chapter 1

Introduction

1.1 Background

Flow-induced vibration (FIV) of bluff body refers to the alternate motion of body due to the aerodynamic force exerted by a moving fluid over the body surface. The flow regime is significantly affected by this structural motion—in consequence, FIV is a classical bidirectional flow–structure interaction (FSI) problem, which is linked to various fluid dynamics phenomena (e.g., boundary-layer separation, vortex formation and shedding, hydrodynamic loading on the structures) as well as structure vibrations. From this, flow-induced vibration is a very complex physical phenomenon consisting of highly non-linear dynamical characteristics. In real-world engineering, flow-induced vibrations occur widely in various applications exposed to wind, tidal wave, or river flow, including but not limited to bridges, transmission lines, marine cables, riser pipes, heat exchanger tubes, etc.

It should be noted that FIV is a general term encompassing various structure oscillations stimulated by the flowing fluid, such as vortex-induced vibration (VIV), galloping, flutter, buffeting, etc. Generally speaking, the inducing mechanisms and the response characteristics of these FIV phenomena are distinctive. Needless to say, intensified scientific research on the underlying mechanisms of FIV leads to improvements in our current understanding of this important physical phenomenon. The FIV of bluff body can be investigated by various methods, including wind-tunnel or water-channel experiments, numerical simulations, mathematical models and machine learning [177]. Furthermore, the complete analysis of FIV phenomenon include not only the structure’s oscillatory motions (e.g., displacement, frequency, phase angle) but also the complex flow dynamics around the structure (e.g., vortex shedding, wake evolution, boundary-layer separation and reattachment).

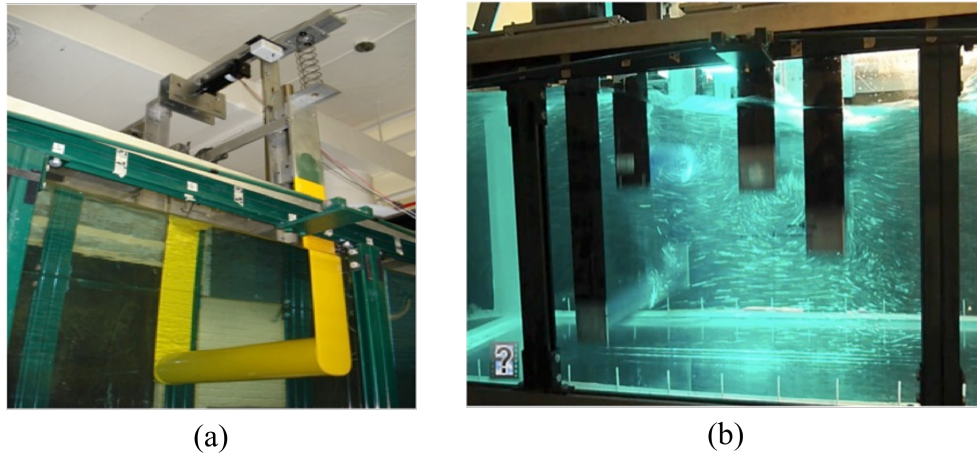


Figure 1.1: Low-turbulence free surface water channel with (a) a single VIVACE converter and (b) a four-cylinder VIVACE converter [19].

In terms of practical applications, the suppression of FIV in order to mitigate the fatigue damage or even failure of structures and maintain structural integrity has been a primary concern for a long time. However, in light of an emerging trend toward sustainability goals for fluid energy generation in recent years, there is an increasing interest in the utilization of FIV phenomena for fluid energy harvesting, especially as it relates to the development of small-scale (portable) wind/water generators—indeed, the energy harnessed from an oscillating body undergoing FIV can be effectively utilized and converted into usable forms of energy, such as electricity, by certain piezoelectric or electromagnetic materials [90, 173, 89]. For example, Bernitsas *et al.* [19] first invented a new VIVACE (Vortex Induced Vibration Aquatic Clean Energy) converter to extract the hydrokinetic energy from water resources and convert it to electricity based on maximizing and exploiting the VIV of single and/or multiple circular cylinders (see Fig. 1.1). This environmentally compatible technology was estimated to produce energy with a density of 0.322 kW/m^3 [19]. Similarly, a Spanish technology start-up [Vortex Bladeless](#) is pioneering the use of bladeless wind turbine as a new and revolutionary alternative to the regular bladed wind power. As shown in Fig. 1.2, this cylindrical turbine is designed to oscillate within the wind range, harnessing wind energy from the structural vibrations and generating electricity by some energy conversion devices.

Furthermore, flow-induced vibration can occur on various bluff bodies, not just on the canonical circular and square cylinders, but on the cylinder with attached or detached passive turbulence control (PTC) devices (e.g., rod, splitter plate, roughness strip, fairing).



Figure 1.2: (a) Bladeless wind turbine and (b) bladeless wind farm [163].

From the perspective of fluid energy harvesting, the PTC–cylinder or cylinder–appendage system could be potentially superior to other plain shapes because it is able to trigger the synergy of multiple forms of FIV, which generally means stronger vibrations.

1.2 Fundamentals of FIV Phenomenon

1.2.1 Classification

Flow-induced vibration can be classified into two general categories based on the generating mechanisms: namely, resonance and instability [104]. The **resonance**-type oscillation is essentially a kind of forced vibration, which is typically driven by external oscillatory forces arising from multiple sources, such as vortex shedding behind the structure (VIV) and vibrations in the incident flow (buffeting). When the fluctuation frequency of external excitation is very close to the natural frequency of the structure, a resonance response may occur resulting in a much larger amplitude in the oscillations. By comparison, if some initial unsteady flow-induced forces are applied to the body to make it move first, the moving system will induce a periodically hydrodynamic force on itself. The motion-induced force and oscillating system mutually reinforce each other until a dynamic equilibrium is reached—a phenomenon that is referred to as an **instability**-type oscillation. In other words, the structure undergoing an instability response requires an initial small disturbance to begin the motion and then this motion is gradually converted to significant periodic oscillations autonomously—this is similar to a self-excited motion. The representative

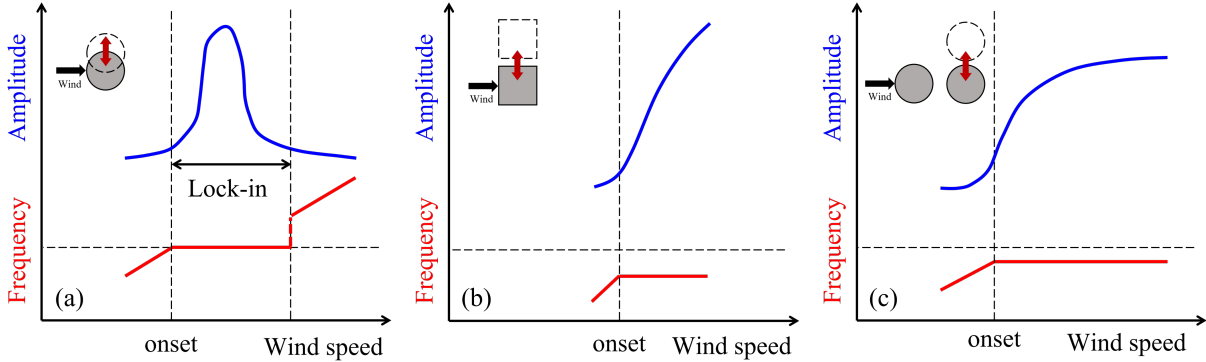


Figure 1.3: Comparison of amplitude-velocity and frequency-velocity of FIV phenomenon: (a) VIV; (b) instability like galloping and flutter; and, (c) wake galloping.

instabilities include galloping and flutter [128].

Figure 1.3 compares the oscillation characteristics of VIV, galloping, flutter, and buffeting (wake galloping) in terms of their amplitude and frequency responses. As shown, all of these oscillatory phenomena have a threshold flow speed for onset. Only VIV exhibits a lock-in of frequency and a limited maximum vibration displacement—the others occur in an unlimited velocity range and are associated with a frequency lower than the structural natural frequency.

1.2.2 Vortex-Induced Vibration

As a resonance-type response, the well-known vortex-induced vibration is generated by unsteady aerodynamic forces exerted by the fluid on an immersed structure. When a viscous flow passes over an elastically-supported rigid body, a boundary layer forms and then separates from near the rear of the body. This action results in vortex shedding from either side of the body producing a von Kármán vortex street in the wake. This alternate vortex shedding from the back of the body causes an asymmetric pressure distribution on body surface giving rise to the fluid forces responsible for VIV of the body [23].

“Lock-in” (or synchronization) occurs when the vortex-shedding frequency f_{vs} is approximately equal to the structural natural frequency f_n . This results in a resonant oscillation that is characterized by a larger but, nevertheless, limited vibration amplitude. The “lock-in” phenomenon occurs for a certain range of incident wind speeds (cf. Fig. 1.3 (a)). From these considerations, VIV is an inherently self-governed, self-regulated, and self-

limiting response which can occur in one- or multi-degree-of-freedom dynamical system. In addition to the “lock-in”, VIV also exhibits various forms of stronger non-linear oscillatory behavior. These include resonance delay (where the vibration amplitude reaches its maximum at a velocity greater than the resonance velocity U_R), hysteresis (producing different amplitude responses with increasing or decreasing flow speed), and a multi-valued response (where a given fixed velocity can result in multiple values of the vibration amplitude) [161].

The dynamical characteristics of “lock-in” makes VIV an ideal choice for fluid energy harvesting. More specifically, a VIV-based energy converter exhibits a better power performance and a higher energy efficiency when the incoming wind speed lies in the synchronization range [173].

1.2.3 Buffeting

Buffeting is also a resonance-type response, but the resonance results from a fluctuating incident flow rather than from a vortex-related instability as in the VIV phenomenon. As an example, the fluctuations in the incident flow can arise from the natural atmospheric turbulence as is commonly observed in long-span bridges [153] or from the oscillating wake generated by structures upstream of a bluff body as in multi-body system—this phenomenon is also referred to as wake galloping [128] (cf. Fig. 1.3 (c)). Investigations undertaken with regard to bridge structures and aeronautics have shown that a buffeting response may occur even at low wind speeds, accompanied by a smaller oscillation amplitude and a wider frequency range than that obtained from VIV [128].

These characteristics suggest that buffeting can be utilized to harness fluid energy in a multi-body design and the power performance from such a design is expected to be strongly dependent on the precise layout (arrangement) of the various oscillating bodies.

1.2.4 Galloping

As a representative instability response, a body subjected to galloping will first undergo a very small oscillatory motion induced by an initial perturbation. These motions result subsequently in significant oscillations once a critical incident flow velocity is exceeded (cf. Fig. 1.3 (b)). Galloping can occur in the transverse direction for an elastically-mounted body or in torsion for a hinged body. Torsional galloping is a much more complex phenomenon due to rotational motion and not as common as transverse galloping in the context of actual engineering applications [88]. In consequence, only transverse galloping (referred to as galloping hereafter) will be discussed in this thesis.

After the onset of galloping, the vibration amplitude will increase monotonically with the flow velocity and will not come to rest again even at very large velocity. This is the most distinct difference between instability and resonance. Moreover, galloping is associated with a much lower vibration frequency than that of vortex shedding. These characteristics are what fundamentally distinguishes a galloping response from a VIV response.

In general, galloping is considered to have a greater energy potential in terms of energy harvesting than VIV owing to its much larger vibration amplitudes and extended range of wind speeds for which galloping occurs. It is noted that galloping occurs only for cylinders with specific cross-sectional shapes (e.g., square, rectangular, triangular, etc.) or for cylinder-appendage system (e.g., cylinder with a splitter-plate)—indeed, galloping does not occur for flow past a circular cylinder. As a consequence, an energy converter utilizing galloping will require a special geometrical design in order to allow the occurrence of galloping or of the interaction of VIV and galloping.

1.2.5 Flutter

Flutter is also a typical unlimited and self-sustained fluid instability usually applicable to dynamical systems involving two or more degrees of freedom. This phenomenon is closely related to the coupling of resonant bending and torsion deformation of a body, and has some common features with galloping.

1.3 Important Parameters to FIV

Flow-induced vibration itself is a multi-parameter problem and closely related to both fluid characteristics and structural properties. Based on three dimensional primary variables, namely, cylinder diameter D (in m), freestream velocity U (in $m\ s^{-1}$) and fluid density ρ (in $kg\ m^{-3}$), some common non-dimensional quantities known to be important in predicting FIV response of a spring-mounted cylinder can be obtained: the Reynolds number Re , the reduced velocity U_r , the mass ratio m^* , the damping ratio ζ and the turbulence intensity I [165]. Some important dimensional and non-dimensional parameters related to the FIV phenomenon are introduced below.

1.3.1 The Reynolds Number (Re)

As a similarity criterion number to reflect the viscosity effect of fluid, the Reynolds number is defined as the ratio of inertial force (for turbulence generation) to viscous force (for turbulence inhibition):

$$Re = \frac{\rho U D}{\mu} = \frac{U D}{\nu}, \quad (1.1)$$

where μ (in $\text{Pa} \cdot \text{s}$) and ν (in $\text{m}^2 \text{s}^{-1}$) are fluid dynamic viscosity and fluid kinematic viscosity, respectively; D is the characteristic length of the structure (equal to the diameter in case of a circular cylinder in cross flow).

In general, for low Reynolds numbers the fluid behavior depends mostly on its viscosity so the flow is steady, smooth or laminar; for high Reynolds numbers the fluid momentum plays more important role to induce an unsteady, roiling and turbulent flow; for intermediate Reynolds numbers the flow can be transitional—partly laminar and partly turbulent.

As shown in Fig. 1.4, the flow around a stationary circular cylinder can be separated into different regimes depending on the Reynolds numbers [127, 130]: (i) $Re < 300$, laminar-dominated regime; (ii) $300 \leq Re \leq 3 \times 10^5$, subcritical regime (with fully turbulent wake flow); (iii) $3 \times 10^5 \leq Re \leq 3.5 \times 10^5$, critical regime (with asymmetrical boundary layer separation); (iv) $3.5 \times 10^5 \leq Re \leq 1.5 \times 10^6$, supercritical regime (with fully turbulent boundary layer separation, narrower wake and disorganized vortex shedding); (v) $Re \geq 4 \times 10^6$, transitional regime (with strong periodicity in the vortex shedding reestablished). It can be seen that the Reynolds number significantly affects the wake topology and vortex shedding process in the flow over a circular cylinder.

1.3.2 The Strouhal Number (St)

A dimensionless number, the Strouhal number St , is commonly used as a measure of the vortex shedding frequency, which can be expressed as:

$$St = \frac{f_{St} D}{U}, \quad (1.2)$$

where f_{St} (in Hz) is the vortex shedding frequency for flow over a stationary body, also called the Strouhal frequency. Moreover, if $f_n = f_{St}$ (viz., lock-in occurs), the resonance velocity can be derived as $U_R \equiv f_n D / St$. Fig. 1.5 indicates that the Strouhal number of a stationary circular cylinder is a function of Reynolds number but less of surface roughness [85]. And the Strouhal number is about 0.2 over a large Reynolds number interval.


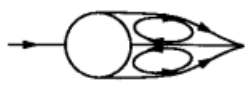



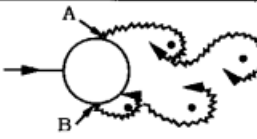
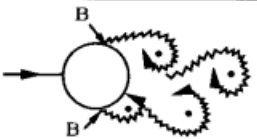
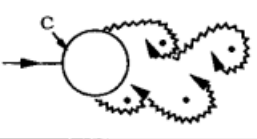
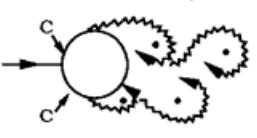
a)		No separation. Creeping flow	$Re < 5$
b)		A fixed pair of symmetric vortices	$5 < Re < 40$
c)		Laminar vortex street	$40 < Re < 200$
d)		Transition to turbulence in the wake	$200 < Re < 300$
e)		Wake completely turbulent. A: Laminar boundary layer separation	$300 < Re < 3 \times 10^5$ Subcritical
f)		A: Laminar boundary layer separation B: Turbulent boundary layer separation; but boundary layer laminar	$3 \times 10^5 < Re < 3.5 \times 10^5$ Critical (Lower transition)
g)		B: Turbulent boundary layer separation; the boundary layer partly laminar partly turbulent	$3.5 \times 10^5 < Re < 1.5 \times 10^6$ Supercritical
h)		C: Boundary layer comple- tely turbulent at one side	$1.5 \times 10^6 < Re < 4 \times 10^6$ Upper transition
i)		C: Boundary layer comple- tely turbulent at two sides	$4 \times 10^6 < Re$ Transcritical

Figure 1.4: Regimes of flow around a smooth, circular cylinder in steady current [127, 130].

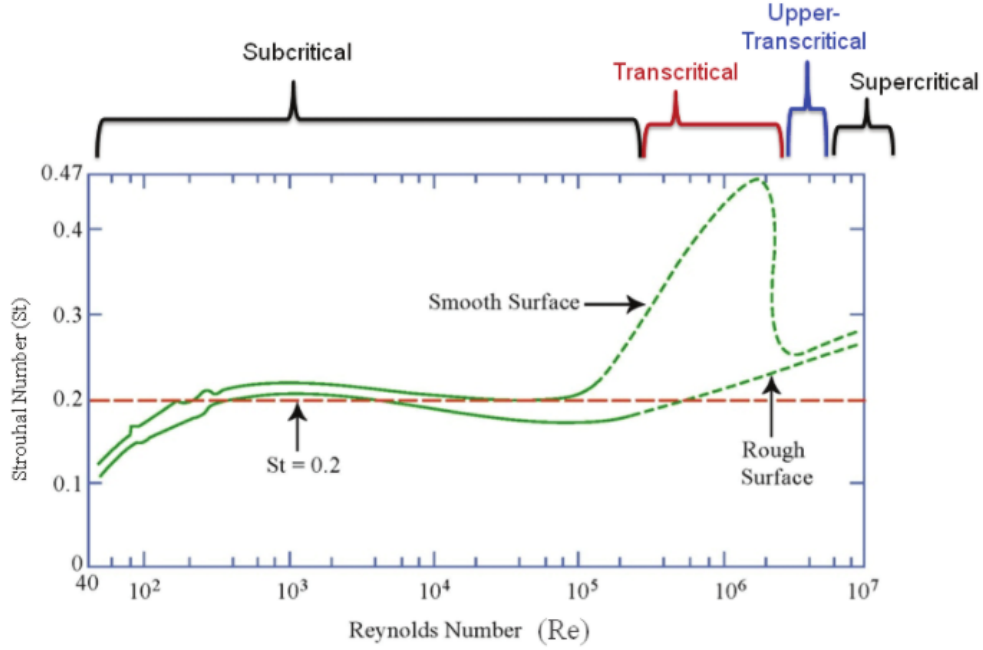


Figure 1.5: Strouhal number versus Reynolds number for circular cylinders [85].

1.3.3 Natural Frequency of Structure

The frequency at which an object tends to naturally vibrate with when disturbed is the natural frequency of the object (represented by f_n), which can be defined by the following formula under ideal conditions (viz., without considering fluid damping):

$$f_n = \frac{1}{2\pi} \sqrt{\frac{k}{m_{osc}}}, \quad (1.3)$$

where k (in N m^{-1}) is the spring stiffness, m_{osc} is the oscillating system mass. It can be seen that f_n only depends on the inherent properties of the object (e.g., shape, size, mass and rigidity of material).

However, the fluid under real conditions is a source of damping, which causes energy loss on the vibrating object and its natural frequency is correspondingly reduced. In this case, an approximate and frequently used analytical solution of f_n is expressed as:

$$f_n = \frac{1}{2\pi} \sqrt{\frac{k}{m_{osc} + m_a}} = \frac{1}{2\pi} \sqrt{\frac{k}{(m^* + C_a)m_d}}. \quad (1.4)$$

As shown, Eq. (1.4) accounts for the added mass of the fluid displaced by the object, viz. $m_a = C_a m_d$ where C_a is added mass coefficient ($C_a = 1$ for circular cylinder).

Above analysis shows that the fluid density has a major effect on the structural natural frequency. For example, the natural frequency of object in vacuum or air ($f_{n,air}$) can be calculated using Eq. (1.3) because the low-density air (e.g., $\rho_{air} = 1.225 \text{ kg/m}^3$ at 15 °C) slightly affects f_n , while that in water ($f_{n,water}$) should be calculated using Eq. (1.4) because the added mass of high-density water (e.g., $\rho_{water} = 999.1 \text{ kg/m}^3$ at 15 °C) can be quite large, which greatly reduces f_n . Moreover, various frequencies in flow-induced vibration phenomenon are often normalized by the structural natural frequency, such as the dimensionless oscillation frequency of structure f_{osc}/f_n .

1.3.4 Mass and Damping of Structure

Mass ratio (m^*)

The structural mass ratio is defined as the ratio of the mass of the oscillating system (m_{osc}) to the mass of the displaced fluid (m_d):

$$m^* = \frac{m_{osc}}{m_d}. \quad (1.5)$$

For a circular cylinder with length L and diameter D , its mass ratio is $m^* = \frac{4m_{osc}}{\rho\pi D^2 L}$. It is obvious that the mass ratio can be very different if the solid body is immersed in different fluids. For instance, the marine structures always have a quite low mass ratio of around 1 to 10 due to the high density of water. While the oscillating body in the air could have a very high mass ratio of around order 100 due to the much lower density of air.

Damping ratio (ζ)

The structural damping ratio is defined as the ratio of the structural damping to the critical damping:

$$\zeta = \frac{c_{sys}}{c_{cri}} = \frac{c_{sys}}{2\sqrt{k(m_{osc} + m_a)}}. \quad (1.6)$$

As shown, the added mass is also taken into account in Eq. (1.6). And c_{sys} (in N s m^{-1}) here refers to the structural damping rather than fluid damping.

Mass-damping parameters

In some FIV-related studies, the mass and damping of structure are also introduced as a combined parameter, such as the Scruton number $Sc = \pi^2 m^* \zeta$ [131], the Skop-Griffin parameter $S_G = 2\pi^3 St^2 m^* \zeta$ [54], and the mass-damping parameter $\alpha = (m^* + C_a)\zeta$ proposed by Khalak and Williamson [73].

1.3.5 The Reduced Velocity (U_r)

The reduced velocity represents the dimensionless freestream velocity in the streamwise direction:

$$U_r = \frac{U}{f_n D}. \quad (1.7)$$

Comparing Eq. (1.2) with Eq. (1.7), it can be found that the reduced velocity is the reciprocal of the Strouhal number if $f_n = f_{St}$ (viz., lock-in). That means U_r is related with vortex shedding and can be applied to predict the occurrence of synchronization.

Chapter 2

Literature Review

2.1 Vibration Response and Flow Analysis of FIV

2.1.1 VIV of a Circular Cylinder

Vortex-induced vibration is a main form of FIV phenomenon, which is a self-limited resonance induced by vortex shedding and frequently occurs in the flow past a circular cylinder. The early representative wind-tunnel experiments carried out by Feng [41] reported important vibration characteristics about the transverse VIV of a circular cylinder by wind tunnel experiments. As shown in Fig. 2.1, the vibration amplitude, frequency and phase angle between lift and displacement are plotted against the reduced velocity, at a high mass ratio 247.7 and a low damping ratio 0.00103. For frequency response, the oscillation frequency always varies around the natural frequency within the tested range of reduced velocity, viz., $f_{osc}/f_n \approx 1$ for $0.6 < U < 1.4$. By contrast, the normalized vortex shedding frequency f_{vs}/f_n is around 1 for $0.8 < U < 1.75$, indicating the occurrence of lock-in in this range, and follows the linear relation of $St = 0.198$ (representing the vortex shedding of flow over a stationary circular cylinder) at other velocities. For amplitude response, the transverse displacement first significantly increases to $0.55D$ within the lock-in range, and then gradually restores to a static condition when out of lock-in. Meanwhile, the oscillation hysteresis loop is observed in the amplitude response (clockwise) and in the phase angle variation (counter-clockwise) at low damping level.

Feng's work [41] indicates that the lock-in of frequency is an important nonlinear characteristic of VIV, which leads to a large-amplitude resonance response. Many follow-up

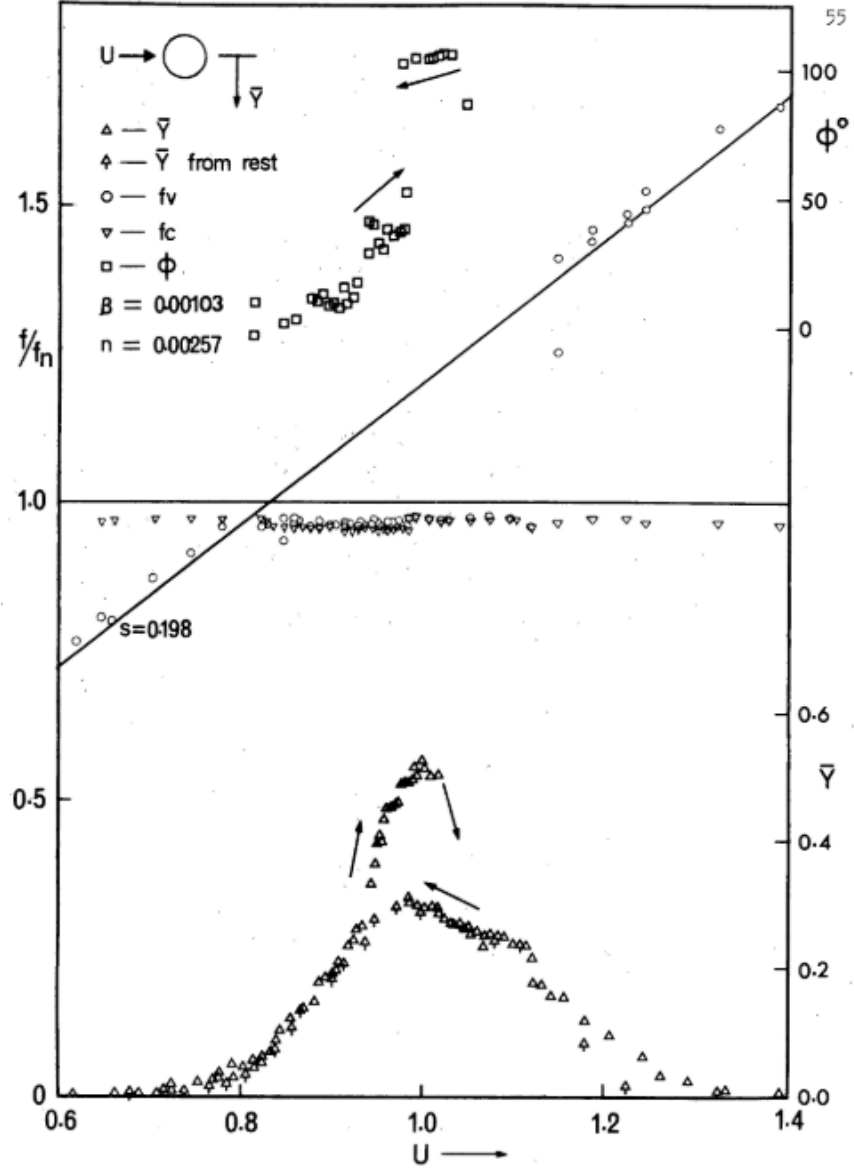


Figure 2.1: Vibration responses for VIV of a circular cylinder in air [41]. The dimensionless mass ratio defined as $n = \rho D^2 L / (2m_{osc}) = 0.00257$ in Feng's experiments is equivalent to $m^* = 4m_{osc} / (\rho \pi D^2 L) = 247.7$ in this thesis. The damping ratio $\beta = 0.00103$ in Feng's experiments has the same definition as Eq. (1.6).

experiments in water channel also observed similar phenomenon at low level mass and damping [71, 72, 73, 52], which will be reviewed in detail in Section 2.2.1.

2.1.2 Influence of Cross-Sectional Shape on FIV

In addition to the external factors (viz., the structure and fluid properties) mentioned above with reference to circular, square and rectangular cylinders, the essence factor like the geometric shape of the structure also has a significant influence on its dynamic response.

Aspect ratio of elliptical cylinder

As a generalization of a circular cylinder, an elliptical cylinder can be geometrically described by a particular quantity called the aspect ratio, which is defined as $AR = b/a$ with a and b being the dimensions of the elliptical cross-section in streamwise and transverse directions, respectively. Therefore, the circular cylinder is simply an elliptical cylinder with $AR = 1$. Compared to the VIV of a circular cylinder, the flow over a freely-vibrating elliptical cylinder has received little attention and, as a result, is relatively unexplored in the literature.

One study conducted by Yogeswaran *et al.* [108] used numerical simulations to investigate the streamwise and cross-flow VIV of a cylinder with various aspect ratios ($0.7 \leq AR \leq 1.43$) in the laminar-flow regime ($60 \leq Re \leq 140$). These investigators reported that the classical initial branch (IB) and lower branch (LB) in the VIV of a circular cylinder can be partitioned into a quasi-periodic (QP) and periodic (P) part for an elliptical cylinder—more precisely, it was found that the aspect ratio determined the branching characteristics of an elliptic cylinder. Yogeswaran *et al.* [108] also suggested that an increasing AR results generally in larger peaks in the vibration amplitude, in a wider lock-in regime, and in a more intense body oscillation.

Zhao *et al.* [192] experimentally investigated the VIV of an elliptical cylinder at moderate values of the Reynolds numbers ($960 \leq Re \leq 8,050$), which reported both similarities and differences of the vibration response of an elliptical cylinder compared to that at low- Re . For one thing, the dynamic response of an elliptical cylinder at low- to moderate-Reynolds numbers was dominated by VIV, with a similar reduced velocity range for the lock-in and a similar response as a function of the aspect ratio. However, increasing the value of Re generally results in a larger vibration amplitude (about 50%), as well as altering the branching behavior. For example, an elliptical cylinder with $AR = 0.67$ displays two separate lock-in regimes.

One common conclusion from above studies is that a “tall” elliptical cylinder (viz., the major axis of the cylinder is oriented perpendicular to the direction of the free-stream velocity) invariably results in a larger amplitude of oscillation, while a “wide” elliptical cylinder (viz., the major axis of the cylinder is oriented parallel to the stream-wise direction) is prone to a weaker dynamic response. Zhao *et al.* [192] interpreted this as the result of a reduced afterbody—structural part of a body downstream of the flow separation points—for a “tall” elliptical cylinder in comparison with that for a “wide” cylinder.

The FIV of an elliptical cylinder includes not only a vortex-induced vibration in either the transverse or streamwise directions (translational motion), but also a vortex-induced rotation (VIR) if the body is free to rotate (rotational motion). Some studies have investigated the dynamic response of an elliptical cylinder undergoing both VIV and VIR. Zhu *et al.* [203] found that a rotatable elliptical cylinder with $AR = 0.5$, possessing a moderate torsional friction, experiences a transition from VIV to galloping. Wang *et al.* [171] used numerical simulations to show that the interaction between VIV and VIR depends on the aspect ratio of an elliptical cylinder, viz., the transverse oscillations were amplified under rotation for $AR = 1$, but weaken for $AR = 2$ and 2.5 . Furthermore, for an elliptical cylinder with $AR = 0.5$, Shahzer *et al.* [137] reported that the rotational degree of freedom amplifies the transverse vibrations, resulting in a 30% greater maximum in the amplitude of vibration. Wan *et al.* [167] investigated the heat transfer and demonstrated the effectiveness of a thermal control on the suppression of the transverse VIV of an elliptical cylinder over a wide range of aspect ratio $AR = 0.25$ – 4 .

The aspect ratio can also affect the flow field and energy transfer of a vibrating elliptical cylinder. Chen *et al.* [27] described and characterized the wake modes behind an elliptical cylinder with various aspect ratios undergoing VIV—this study included an investigation of the energy transfer between the motion of the cylinder and the surrounding flow.

Side ratio of rectangular cylinder

A rectangular prism is a general form of a square cylinder, which has a specifically important geometrical characteristic called the side ratio d/b , where d and b are respectively the in-line and cross-flow side lengths of the prism [92]. The effect of side ratio on the FIV of a rectangular prism has been investigated in a number of experimental and numerical studies [188, 193, 40, 186].

Zhang *et al.* [188] investigated the FIV response of a low-mass-damping rectangular cylinder with $d/b = 1/6$ – 2 in the Reynolds number range from 500–187,500 and reported the negative effect of the side ratio on the vibration amplitude. More specifically, a strong

interference between VIV and galloping occurred for $d/b = 1/6$ – 1.5 , while neither VIV nor galloping was induced at the largest value of $d/b = 2$ investigated. Zhao *et al.* [193] tested an elastically-mounted rectangular cylinder with a larger side ratio of $d/b = 2$ – 5 in a wind tunnel. All the cases studied exhibited a VIV-galloping response, manifesting an unrestricted amplitude for $d/b = 2$ – 4 , but limited amplitude response for $b/d = 5$. The discrepancy in the results for $d/b = 2$ (no oscillation reported by Zhang *et al.* [188] and a combined VIV-galloping reported by Zhao *et al.* [193]) may be due to the different mass-damping and Reynolds number used in these investigations.

Main vertex angle of triangular cylinder

Through a series of systematic static wind-tunnel experiments, Alonso and colleagues [5, 4, 6, 7] demonstrated that the cross-sectional shape (main vertex angle β) and the angle of attack β had a major impact on the transverse galloping instability of a triangular cylinder. These researchers identified potential regions associated with galloping in the (α, β) plane. Focusing on the effect of α , Seyed *et al.* [136] experimentally investigated the cross-flow oscillation of an equilateral triangular cylinder with low mass-damping (viz., $m^* = 9.24$ and $\zeta = 0.0057$) placed in a water channel with $\alpha = 0^\circ$ – 60° in the Reynolds number range of $Re = 490$ – 2700 and observed various response modes of this dynamical system. To be specific, no oscillation was observed for $\alpha < 25^\circ$, VIV-type oscillations with a very small amplitude ($< 0.1D$) were reported for $\alpha = 25^\circ$, a separate regime of VIV and galloping was observed for $\alpha = 30^\circ$ – 35° , and a combined VIV-galloping starting around a reduced velocity associated with the onset of VIV was revealed for $\alpha = 40^\circ$ – 60° . Wang *et al.* [172] also reported similar phenomena in laminar flow simulations at $Re = 100$.

2.1.3 Flow Analysis of FIV

Except for the oscillatory motion of structure, the flow dynamics around the vibrating body such as the shedding of the vortices alternately from one side to the other resulting in a characteristic wake mode is an important part of the study of FIV phenomena.

The characteristic patterns associated with vortex shedding arising from FIV have been studied by a number of researchers. In some seminal work, Williamson and Roshko [175] characterized the pattern of vortex shedding in the wake of an oscillating circular cylinder forced by a sine function. As shown in Fig. 2.2, the wake patterns is related with the ratio of amplitude to diameter (vertical axis) and the ratio of excitation period to vortex shedding period (horizontal axis), with prescribed amplitude and frequency of external

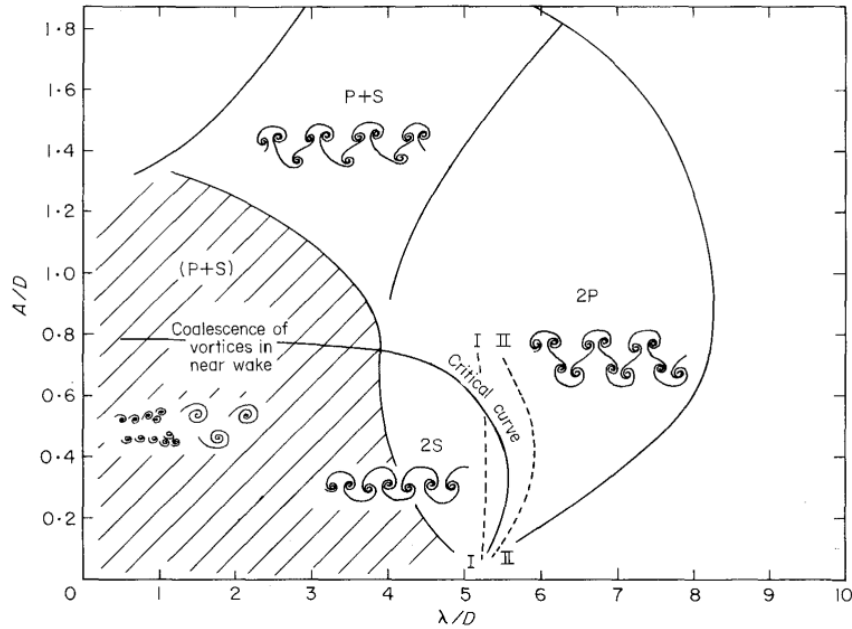


Figure 2.2: Map of vortex modes near the fundamental lock-in region. The critical curve marks the transition from one mode of vortex formation to another [175].

force. More precisely, these researchers studied the topological structure of vortices shed during one oscillation cycle and introduced a taxonomy of vortex-shedding patterns (e.g., designations such as “S”, “P” and “C” for a single vortex, a pair of opposite-signed vortices and an amalgamation of vortices, respectively). In this case, various wake patterns can be defined by the combination of these small vortex structures.

The classical anti-symmetric “2S” wake mode illustrates that two vortices are alternately shed from one side of the cylinder to the other to form the typical Kármán vortex street, which is very common for the flow dynamics associated with the VIV of a circular cylinder, but can be also present in some galloping regimes. For example, Wu *et al.* [179] demonstrated that for a cylinder-plate assembly undergoing galloping the wake mode of a $1:n$ ($n = 3, 5, 7$) synchronization galloping regime between the structural oscillation and the vortex shedding was “ $n \times (2S)$ ”, viz., a “2S” wake mode repeated n times over one oscillation cycle. Similar results have also been reported for the galloping of a square cylinder [198, 162]. In general, a more complex FIV response is associated with more irregular vortex shapes and shedding mode. For example, Sen [132] studied a freely-vibrating square cylinder and reported the presence of a so-called wake mode S_1S_2 , which was related to the beating oscillation.

2.2 Branching Behavior of FIV

In addition to analyzing the vibration properties and flow information of FIV, another essential characteristic that is closely correlated with the physical nature and mechanism of the structural oscillation is the branching behavior of FIV.

2.2.1 Branching of VIV for a Circular Cylinder

As a canonical case, the VIV of a circular cylinder has been systematically investigated, especially in terms of its branching behaviors. Feng [41] identified two branches in the VIV response—the initial branch and lower branch that depend on the reduced velocity. These investigations demonstrated that the transition between the two branches is hysteretic.

Khalak and Williamson [71, 72] studied experimentally the same phenomenon, but at a low mass ratio of 2.4 in a water channel. They reported a new regime between the initial and lower branches of the VIV response: namely, an upper branch (UB) that was characterized by a large-amplitude response—the maximum vibration amplitude here was found to be about D . A subsequent study by Khalak and Williamson [73] demonstrated that these branches of VIV response were closely correlated with various vortex shedding modes—the “2S” (two single counter-rotating vortices) mode in the initial branch and the “2P” (two pairs of counter-rotating vortices) mode in the upper and lower branches. They also reported the presence of a hysteretic transition between the initial and upper branches and an intermittent switching between upper and lower branches.

Jauvtis and Williamson [67] conducted further experimental studies and reported the existence of a new response branch referred to as the super-upper branch (SU) in the two-degree-of-freedom (2DOF) system consisting of the streamwise and transverse VIV of a circular cylinder with a low mass ratio of 2.6. This response corresponded to a large oscillation amplitude of $1.5D$ and was associated with a “2T” (two triplets of vortices) vortex-shedding mode. The super-upper branch assumed the position of upper branch in the one-degree-of-freedom (1DOF) VIV, but its transition to the lower branch was hysteretic in nature rather than intermittent. A comparison of various branches of VIV response identified in above experimental studies is given in Fig. 2.3.

It can be seen that the branching behavior in the VIV of a circular cylinder depends primarily on the mass-damping parameter and the degrees of freedom, which can be accompanied by an unique vortex-shedding mode. We note that the various branches identified in the experimental investigations cited above correspond to a more detailed subdivision of the entire VIV range, and is not simply confined to the more restrictive “lock-in” regime

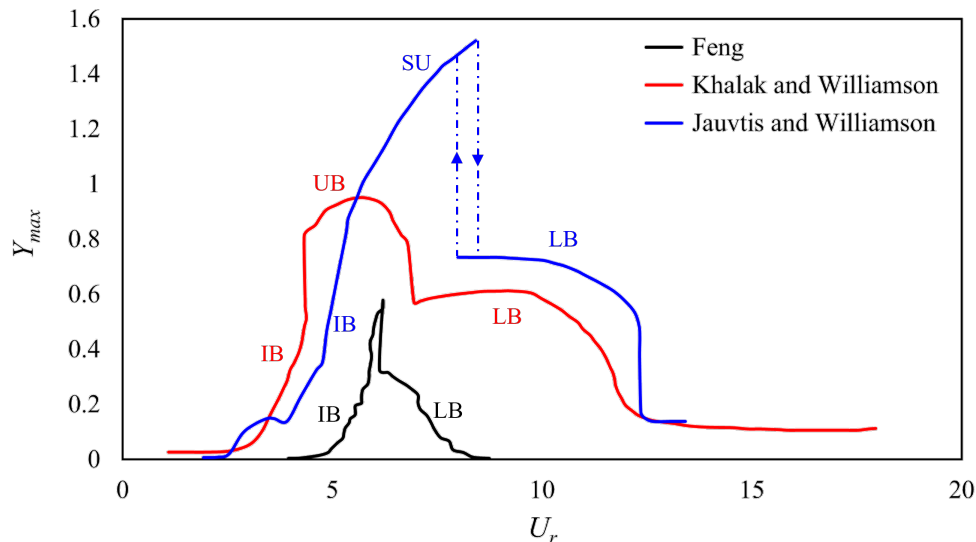


Figure 2.3: Branch identification of VIV responses from different experimental studies: 1DOF VIV at $m^* = 247.7$ by Feng [41], 1DOF VIV at $m^* = 2.4$ by Khalak and Williamson [71, 72], and 2DOF VIV at $m^* = 2.6$ by Jauvtis and Williamson [67].

within this range. According to Zhao *et al.* [195], the oscillations in the initial branch are modulated, the large-amplitude oscillations in the upper branch appear to be unstable and chaotic, and the oscillations in the lower branch (viz., the “lock-in” regime) are periodic and stable. In addition to the experimental studies referenced previously, various numerical studies have been conducted to investigate the VIV of a circular cylinder at different Reynolds numbers, mass-damping parameters, and degrees of freedom. Most of these numerical simulations agree well with the experimental investigations—albeit, these simulations do not perfectly replicate the branching behavior observed in experiments (e.g., the simulations may fail to capture the upper or super-upper branches). Li and Ishihara [81] provided a comprehensive review of the numerical investigations of the branching for VIV of a circular cylinder.

2.2.2 Branching of FIV for a Non-Circular Cylinder

As mentioned in Section 2.1, both VIV and galloping responses can be triggered on prismatic structures with non-circular cross-sections and a sufficient afterbody. Owing to that, the associated branching behavior should be more complex and different than that of VIV on a circular cylinder.

A square cylinder

Zhao *et al.* [195] investigated the transverse FIV of an elastically-mounted square cylinder with low mass ratio of 2.64 at three incidence flow angles ($\alpha = 0^\circ$, 20° , and 45°) in a water channel and analyzed the corresponding branching behavior in the amplitude response. For $\alpha = 0^\circ$, a classical galloping (viz., the maximum transverse displacement increases approximately linearly with the reduced velocity once U_r exceeds a threshold value) was observed and three odd-integer multiple synchronizations between the galloping frequency and the vortex-shedding frequency (namely, 1:1, 1:3 and 1:5) were identified. For $\alpha = 45^\circ$, a VIV-dominated response was triggered, during which the body oscillation transitioned from a periodic to a non-periodic motion—in this transition, the relationship with the vortex shedding was gradually desynchronized. A switch of the wake mode from “2S” to “2P” was thought to be related to this unique branching behavior. For $\alpha = 20^\circ$, a modified VIV response was observed, consisting of three branches: namely, (1) an initial branch, similar to that in the VIV of a circular cylinder; (2) a 1:1 upper branch associated with periodic oscillations; and, (3) a 1:2 higher branch bounded by two transition regimes to the desynchronization regions. The results reported by Zhao *et al.* [195] demonstrate that the branching behavior of a square cylinder experiencing FIV is complex and closely related with the incident flow.

In a subsequent study, Zhao *et al.* [194] investigated the combined effects of the mass ratio ($m^* = 2.64$ –15) and the incidence flow angle ($\alpha = 0^\circ$, 20° and 45°) on the branching behavior of a square cylinder undergoing FIV. For $\alpha = 0^\circ$ (integrated VIV-galloping), the 1:1 synchronization was reduced as the mass ratio increases from 2.64 to 5, and all the synchronizations ceased to exist when $m^* \geq 11.31$. For $\alpha = 45^\circ$ (VIV-dominated), the mass ratio was found to have more of an influence on the desynchronization. For $\alpha = 20^\circ$ (modified VIV), the higher branch was reduced when $m^* > 3.5$.

Sen and Mittal [133, 134, 135] conducted a large number of laminar-flow simulations (with $Re = 50$ –250) to study the effect of mass ratio on the branching behavior of a 2DOF FIV of a square cylinder. These investigators reported a pure VIV response with the initial and lower branches for $m^* = 1$. However, for $m^* \geq 5$, the dynamic response was characterized by three distinct branches: namely, (1) the VIV regime (with a narrower range and a smaller maximum vibration amplitude than that for VIV of a circular cylinder) at low speeds, including the initial and lower branches; (2) desynchronization or pre-galloping; and, (3) secondary lock-in (viz., a galloping branch) at high speeds. It should be noted that the detailed branching in the galloping regime was not explored in the investigations conducted by Sen and Mittal [133, 134, 135].

A rectangular cylinder

A representative study conducted by Zhao *et al.* [193] tested the effect of the side ratio and mass ratios on the branching of FIV of a rectangular cylinder. As d/b ranging from 2 to 4, the vibrating body exhibits an integrated VIV-galloping response, with three branches: namely, (1) an initial branch, similar to that in the VIV of a circular cylinder; (2) a VIV lock-in regime with highly-periodic oscillations; and, (3) a galloping regime with non-periodic oscillations. Moreover, the lock-in regime became wider with increasing d/b . For the highest value of $d/b = 5$, a desynchronization branch was identified, which transitioned to a bounded galloping regime. Zhang *et al.* [188] also identified both VIV and galloping regimes for a rectangular cylinder with $d/b = 1/6$ –2.0. More specifically, a strong interference between VIV and galloping was reported for $d/b = 1/6$ –1.5, while neither VIV nor galloping was induced for $d/b = 2$.

Other shapes

In addition to a rectangular cylinder, the branching behavior of other non-circular cross-sections susceptible to VIV and/or galloping has been investigated (albeit to a lesser extent). Water-channel experiments conducted by Zhang *et al.* [189] identified three response branches (namely, a VIV branch, a transition branch and a galloping branch) in the FIV of an equilateral triangular cylinder. In their numerical investigations of the transverse FIV of a trapezoidal cylinder, Zhu *et al.* [201] reported the presence of VIV branch and desynchronization branch at flow orientations of $\alpha = 0^\circ$ and 90° , while VIV and galloping branches at a flow orientation of $\alpha = 180^\circ$.

2.3 Nonlinear Analysis of FIV

Over the past few decades, there has been an increasing research interest in understanding the fundamental physical phenomena underpinning FIV owing to its importance in engineering and industrial applications. An elastically-mounted body undergoing FIV is essentially a nonlinear dynamical system—indeed, a system which exhibits an extremely rich spectrum of complex nonlinear behavior as it undergoes oscillations. For example, the VIV of a circular cylinder can exhibit strongly nonlinear dynamical characteristics such as frequency lock-in, hysteresis, multi-valued response, and resonance delay [161]. Furthermore, the beating phenomenon in the oscillations, the nature of the limit-cycle revealed in the phase plane portrait, the phase shift between oscillatory motion of the body and the

driving force responsible for this motion, and the vortex dynamics associated with the flow past an elastically-mounted body display strongly nonlinear characteristics of FIV that are important to understand [82].

2.3.1 Beating Phenomenon of FIV

In some cases, the time series of the vibration amplitude of an elastically-mounted body has quasi-periodic waveform. Frequently, these waveforms exhibit a beating phenomenon (also referred to as amplitude modulation) characterized by a time-varying maximum amplitude—this is one of the characteristic nonlinear features of FIV phenomena.

Most of the available experimental and numerical investigations involving beating phenomenon of vibrations concern the VIV of a circular cylinder. Singh and Mittal [143] observed beating in the time series of displacement and fluid force (e.g., lift coefficient) of a circular cylinder near the onset of VIV at a Reynolds number of $Re = 100$. Prasanth and Mittal [124] reported similar beating phenomenon during the transition from the initial branch to the lower branch of a VIV response of a circular cylinder at $Re < 100$. Mittal [102] conducted three-dimensional numerical simulations of the flow past an elastically-supported circular cylinder at $Re = 1,000$ —this researcher observed beating in both the oscillations of the displacement and the lift coefficient in the initial branch. However, beating only occurred in the lift coefficient oscillations in the lower branch owing to the alternating of the vortex shedding from one side of the cylinder to the other in this branch. In the moderate range of Reynolds numbers from 5,300 to 32,000, Xu and Zhu [184] reproduced using numerical simulations the beating observed in experiments of the hysteretic loop between the initial branch and upper branch of a VIV response of a circular cylinder. It can be seen that for VIV of circular cylinder, the beating phenomenon is observed to occur primarily near the two boundaries of the lock-in span (viz., near the onset and end velocity of VIV) for a wide range of Reynolds numbers.

Various researchers have analyzed the characteristics of the beating phenomenon and the factors that are responsible for the beating from a number of different perspectives. It is well-known that beat oscillations occur when two frequencies in the oscillations are close to one another, producing a characteristic alternating constructive and destructive interference pattern in the oscillations—the beat frequency is the absolute value of the difference in these two closely-spaced frequencies. This simple concept has been used by a number of investigators to interpret the beat phenomenon in the vibrations of an elastically-supported body—for example, by Placzek *et al.* [122] for the VIV of a circular cylinder at $Re = 100$ and by Modarres-Sadeghi *et al.* [103] for the VIV of a flexible riser.

The beating phenomenon can exhibit a rich frequency spectrum. Willden and Graham [174] reported a relationship between the amplitude-modulated behavior of VIV at $Re = 50\text{--}400$ and the ratio of the vortex-shedding frequency to the structural natural frequency (f_{St}/f_n). Han *et al.* [59] also investigated the effect of this frequency ratio on beating. Another important characteristic of the flow dynamics during beating is the change in the vortex-shedding mode (through the process of mode competition). Khalak and Williamson [73] experimentally observed the transformation of wake modes from “2S” to “2P” in the transition between the lower and upper branches of the VIV response. In contrast, Placzek *et al.* [122] reported only small modifications of the vortex patterns arising from beating in the VIV response. Leontini *et al.* [80] and Wang *et al.* [170] analyzed the wake dynamics associated with various peaks in the beating and found ordered and disordered wake modes corresponding to the lower and higher peaks in the beating. These investigators concluded that it was the disordering of the wake modes that gave rise to the periodic growth-decay observed in the initial branch of the VIV amplitude response. Furthermore, it is known that the structural mass-damping affects beating. Al-Jamal and Dalton [3] found that the beating was significantly suppressed with increasing structural damping for a flow at $Re = 8,000$.

In addition to the VIV of a circular cylinder, the beating phenomenon is also present in other forms of FIV (e.g., galloping, integrated VIV-galloping) observed in elastically-supported body such as a square cylinder [194], two side-by-side rigid [57] or flexible [185] cylinders, and two tandem or staggered cylinders [55]. Recently, Zhao and Zhao [194] provided a comprehensive discussion of the beating phenomenon as it concerns the effect of rounded corners on a square (or, more generally, a rectangular) cylinder on the FIV response at $Re = 200$. These researchers identified two types of beating in accordance to the variation of the local frequency and related this wake variation to the energy transfer, phase shift and the wake mode.

2.3.2 Nonlinear Dynamical Features of FIV

The FIV of an elastically-mounted cylinder exhibits a number of interesting nonlinear dynamical characteristics in addition to the beating phenomenon. Li *et al.* [82] systematically investigated the limit cycles and bifurcations in the oscillations of the displacement and lift coefficient associated with the VIV of a circular cylinder at $Re = 200$ using phase portraits and Poincaré sections—these geometrical representations were used to study the bifurcations in the periodic solutions (trajectories) of the dynamical system. Feng *et al.* [42] conducted a similar analysis on the VIV of a three-dimensional flexible tube—these researchers found no bifurcations occurred in the dynamical system for a turbulent flow.

The chaotic nature of VIV has also been studied in the context of the dynamic response of a flexible riser [103] and of the vortex-shedding modes of a rigid cylinder [196] using phase-plane portraits. Konstantinidis *et al.* [74] studied the nonlinear phase dynamics in various branches of the VIV amplitude response of a circular cylinder using the information embedded in the instantaneous phase shift between the transverse displacement and the transverse force.

Nonlinearity of FIV phenomena can be manifested in the flow dynamics around the elastically-supported body. Xu *et al.* [182] performed an in-depth analysis of the nonlinear vortex dynamics associated with the FIV of a flexible splitter-plate attached to a square cylinder in laminar flow at $Re = 322.6$ —the results of this analysis were important for the design of structures in the ocean subject to fluid-structure interaction. It should be noted that this analysis involved purely periodic (monochromatic) time variations of the displacement and lift coefficient (which are characterized by a single frequency, so no beating was involved). Sen [132] investigated the beating phenomenon associated with vortex shedding at small values of the reduced velocity U_r (viz., at $U_r = 4.2, 4.6,$ and 4.7) corresponding to the VIV regime in the amplitude response of an oscillating square cylinder and reported new vortex shedding mode S_1S_2 .

2.4 Wake-Oscillator Model of FIV

FIV is a bidirectional FSI problem, in which the structural oscillation is generally modelled in terms of the motion displacement using a mass–spring–damper system, while the fluid dynamics can be formulated in different ways. Depending on the modelling methodology for the fluid, the mathematical models of FIV can be classified unambiguously into two main classes: namely, a coupled wake-oscillator model and a single degree-of-freedom model, as exhibited in Fig. 2.4.

The coupled wake-oscillator model involves the development of a fully non-linear wake model (also referred to as wake oscillator) using either a Rayleigh-type [126] or a Van der Pol-type [164] oscillator, which is then coupled to a structure equation through the motion-related forcing term(s). As a consequence, the coupled wake-oscillator model that describes the complex physics associated with FIV is composed of two ODEs that can be solved numerically with given initial conditions and model parameters, in order to predict important physical quantities of FIV.

In contrast to the more intuitive representation of the structural motion using the readily interpretable concepts of displacement, velocity or acceleration, the wake oscillator

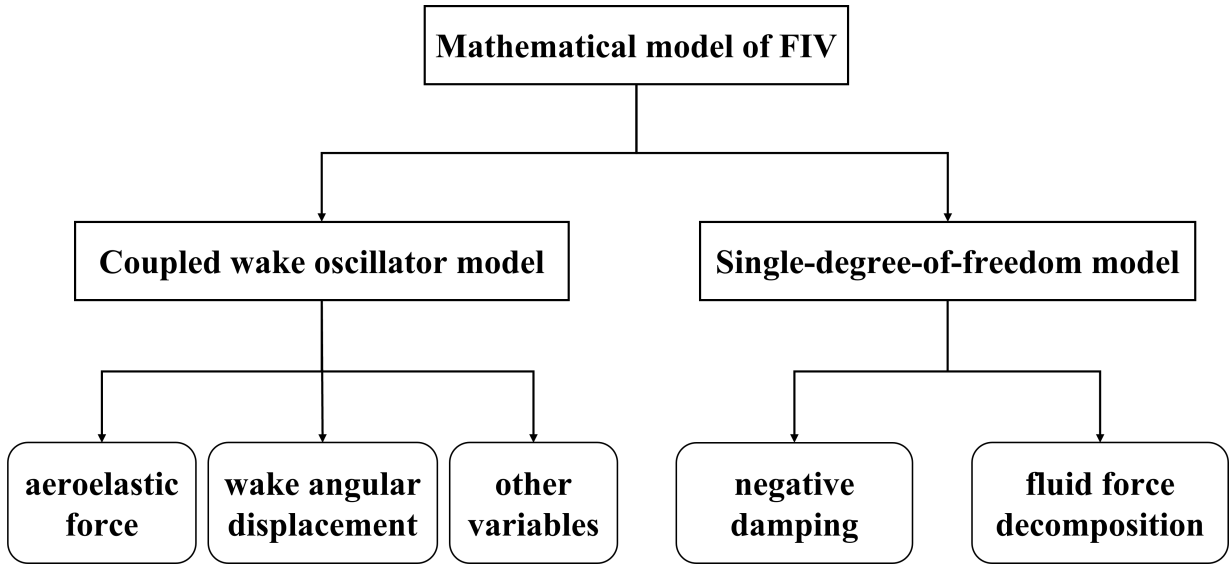


Figure 2.4: Classification of mathematical modelling of FIV.

representing the fluid dynamics is more abstract in the sense that it is characterized by state variable that is more difficult to interpret. The lift coefficient acting on the structure and the angular displacement of the near-wake lamina are two commonly used fluid variables. The corresponding two categories of coupled wake-oscillator model for different FIV responses are reviewed in this section.

2.4.1 C_L -Based Wake Oscillator Model for FIV

All the available coupled wake-oscillator models that use a physical quantity related to the aerodynamic force as the fluid variable is a derivative of the seminal ideas of Bishop and Hassan [22]. These investigators were the first to advocate using a fluctuating lift force acting on a circular cylinder to model the dynamic behavior of the near-wake region. Following on from this effort, Hartlen and Currie [60] formulated a widely used Rayleigh-type wake oscillator in terms of the fluctuating lift coefficient C_L and coupled this model with a damped linear system through the body velocity \dot{y} in order to predict the transverse FIV of an elastically-mounted rigid circular cylinder.

A number of models (both variants and generalizations) have been formulated based on the Hartlen–Currie model [60]. Skop and Griffin [144] and Griffin *et al.* [53] applied a modified Van der Pol wake oscillator with concomitant model parameters describing struc-

tural properties (such as mass and damping ratio) and showed that the model agreed very well with experimental data. Landl [76] reformulated the Hartlen–Currie wake oscillator using a Van der Pol oscillator and introduced a fifth-order non-linear damping term (viz., $\gamma C_L^4 \dot{C}_L$ where γ is a model parameter) in order to account the hysteresis effect of VIV. It is noted that these model variants were developed to predict the VIV of a rigid cylinder.

Skop and Griffin [145] extended their earlier model [144] to predict the VIV arising from a flexible circular cylinder (e.g., a slender cable). This was accomplished by expressing the sectional vibration displacement and lift coefficient using a modal expansion (normal mode) and formulating the governing equations for the various terms in this expansion. Following on from this effort, Skop and Balasubramanian [147] introduced a so-called stall component (viz., $-2\alpha\dot{Y}/\omega_{vs}$ where α is a model parameter) as part of the forcing term in the structure equation. To this purpose, the transverse fluid force consists of two components: namely, one component (modelled using a Van der Pol wake oscillator) used to cause the body to move and another component (proportional to the negative structural velocity) used to reduce the amplitude of the lift coefficient for large structural motion (viz., stall term). This innovative modification of the lift force is significant because it confers on the model the capability to predict the asymptotic VIV response in the vicinity of zero structural damping—this has, up until then, never been realized. Skop and Luo [146] further refined the stall term (viz., $-2\alpha\dot{Y}(\omega_{vs}/\omega_n)^k/\omega_{vs}$) in order to ensure the accuracy of induced asymptotic behavior.

One common characteristic for above models is that the wake variable is explicitly expressed in terms of the instantaneous lift coefficient C_L . Facchinetti *et al.* [39] first introduced a generalized dimensionless wake variable q to characterize the oscillating wake. Although in their case the action of fluid on the structure was still considered as a lift force with q representing the reduced vortex lift coefficient ($q \equiv 2C_L/C_{L0}$), Facchinetti *et al.* [39] demonstrated that q can be chosen to be other physical quantities that were capable of describing the fluctuation characteristics of the near wake. Another contribution arising from the model proposed by Facchinetti *et al.* [39] and inspired by the effort of Skop and Balasubramanian [147] for a flexible body was the inclusion of the stall term (i.e., a fluid-added damping term) in the structure equation using a drag coefficient C_D —as a reminder to the reader, this term was given by $C_D\dot{Y}/(4\pi Stm^*)$. These investigators also examined different forcing terms for the wake oscillator (displacement, velocity, and acceleration) and found that the use of acceleration provided the best conformance with the experimental data.

The model formulated by Facchinetti *et al.* [39] is so popular that many variants of this model have been used in subsequent theoretical studies. For example, Ogink and Metrikine [114] introduced an acceleration–velocity coupling term ($\tilde{A}(\omega)\ddot{Y} + \tilde{B}(\omega)\dot{Y}$)

that was dependent on the oscillation frequency of the cylinder in order to provide good predictions for both forced and free vibrations.

It should be noted that all the models described in this section are designed to predict the transverse (1DOF) VIV of a circular cylinder. To be more realistic, some theoretical studies focus on modelling both the in-line and cross-flow vibrations. A number of 2DOF phenomenological models have been developed based on two motion equations for the x - and y - directions in order to simulate the possible coupling between these oscillations [46, 51, 150, 14, 123].

2.4.2 θ -Based Wake Oscillator Model for VIV

Rather than representing the dynamic wake using the instantaneous lift coefficient, Birkhoff [21] developed a linear wake oscillator based on the concept of wake rotation angle (θ) in order to simulate the oscillation of near wake behind a stationary circular cylinder. As shown in Fig. 2.5 (a), this wake oscillator defined a near-wake lamina of size $2\bar{l}$ in length and h in width, which can be determined from experimental data (e.g., $h = 1.33D$, $\bar{l} = 0.75D$). It is noteworthy that Birkhoff's wake oscillator is derived from physically-based concepts, such as the Kutta–Joukowski lift theory and Newton's second law of rotation. In this case, the θ -based wake oscillator is more of a physical model than that directly incorporates a Van der Pol-type oscillator.

Funakawa [45] slightly modified the Birkhoff's wake oscillator in the following two aspects: (i) the length of near-wake lamina was measured from the rear of cylinder rather than from the cylinder center; (ii) the acting location of the restoring force coincided with the center of gravity. With these modifications, the governing equation was changed accordingly, as shown in Fig. 2.5 (b). Based on their experimental data, the size of near-wake lamina was $h = 1.25D$ and $\bar{l} = 1.1D$.

Tamura [156] basically followed the structure of Funakawa's wake oscillator, but replaced some constant quantities with time-dependent ones, mainly referring to the angular displacement $\theta(t)$ and wake length $l(t)$. Furthermore, Tamura introduced a viscous force into the governing equation by a negative damping term and derived the damping ratio of the near-wake region with the assumption that the work done by the lift force and the viscous force was equal, which was expressed as $\zeta_f = \frac{D}{2\sqrt{2}\pi^2} \frac{f_m}{l}$. With these modifications, the resulting wake oscillator was nonlinear and more complex, as shown in Fig. 2.5 (c). The near-wake size ($h = 1.25D$, $\bar{l} = 1.1D$) and the Magnus parameter $f_m = 1.16$ were determined from the observations in stationary test of a circular cylinder.

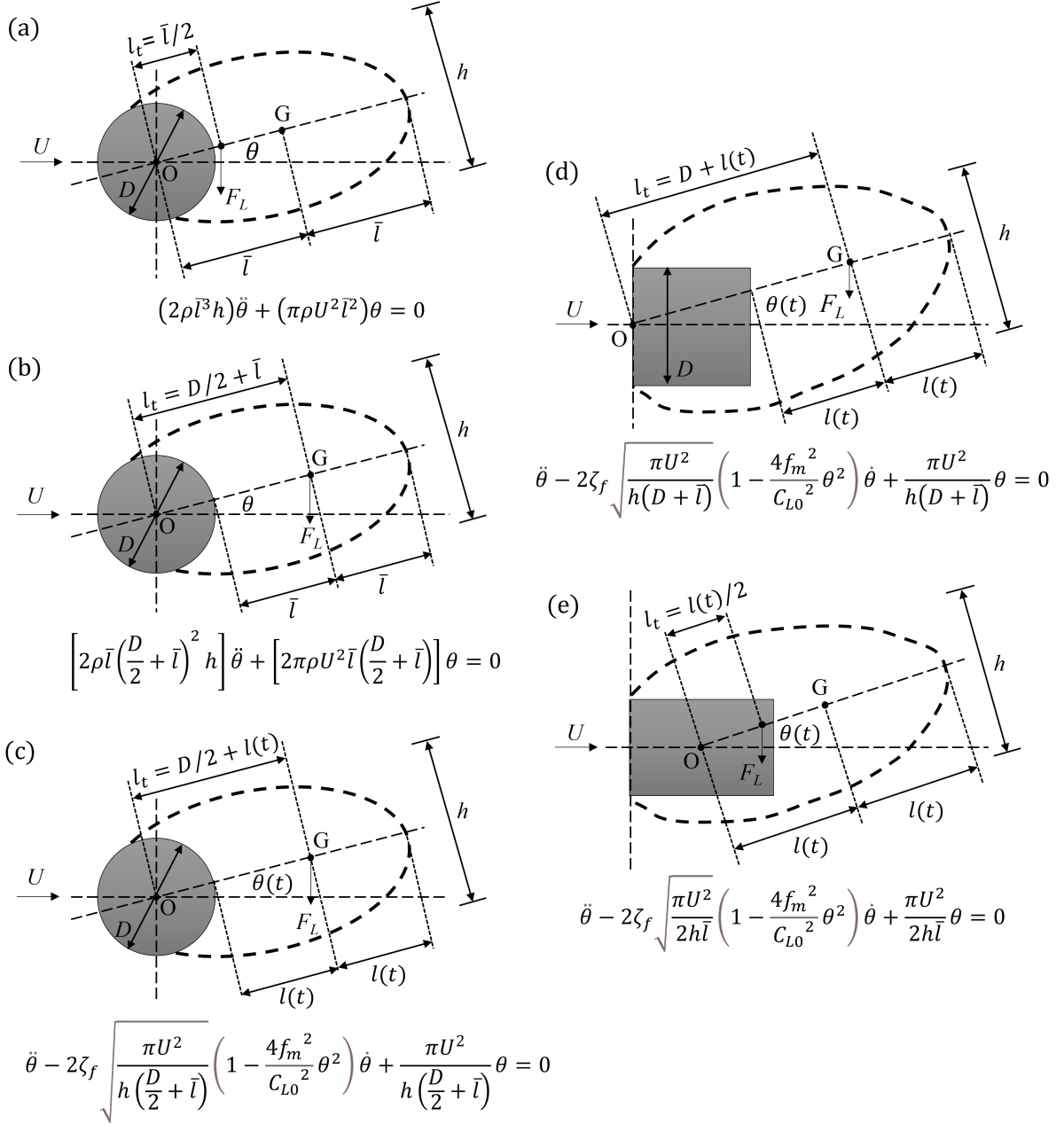


Figure 2.5: Schematic and governing equations of static wake oscillators for (a)–(c) circular cylinder [21, 45, 156], (d) square cylinder [159] and (e) 3:2 rectangular cylinder [97].

Above three wake oscillators are developed for a circular cylinder, while the definition of near-wake region can be different if the cross-sectional shape changes. For example, Tamura and Shimada [159] still applied the framework proposed by Funakawa [45] to develop a wake oscillator for a square cylinder. As shown in Fig. 2.5 (d), the bluff body was contained into the near-wake region, so the center of rotation (point O) was located at the front edge of the square. The governing equation also had some slight changes accordingly. By contrast, Mannini *et al.* [97] developed a wake oscillator for a 3:2 rectangular cylinder based on the definition proposed by Birkhoff [21], for which the center of rotation was in the rectangle center and the lift force acted a quarter wake length ($l(t)/2$) from the point O. The schematic and governing equation were shown in Fig. 2.5 (e).

It should be noted that the wake oscillators reviewed above are used for stationary cylinders. For a freely-oscillating cylinder, the static wake oscillator needs to be modified in two aspects: (i) include external force on the right hand side; (ii) represent the angular displacement (the third term on the left hand side) as a function of moving velocity. Then, the modified wake oscillator can be combined with the structure motion equation to predict the VIV response.

Using this methodology, Tamura and Matsui [157] developed a coupled wake-oscillator model for predicting VIV of a circular cylinder. The driving force in the structure equation was composed of the lift and drag forces. The forcing term of wake oscillator was a linear function of the velocity and acceleration. An obvious advantage of this model is that all the parameters have a clear physical interpretation and can be determined by observations and measurements, while the C_L -based model may include multiple non-physical parameters (e.g., the Van der Pol constant ϵ) that can only be tuned from curve fitting of experimental data. The reason is that the wake oscillator in terms of θ is derived from series of physically-based concepts (as described earlier) instead of assuming, a priori, the applicability of a Van der Pol-type oscillator. Tamura and Amano [158] further extended the two-dimensional (2D) Tamura–Matsui model [157] to a three-dimensional circular cylinder, which was accomplished by utilizing the modal expansion method for the sectional vibration displacement of the cylinder and the angular displacement of the wake.

2.4.3 Quasi-Steady Model for Galloping

Unlike various mathematical models of VIV, the analytical modelling of galloping response is generally based on the so-called quasi-steady hypothesis, which states that the instantaneous aeroelastic force exerted by the fluid on a vibrating structure is the same as that on a stationary body at the same angle of attack. More precisely, the lateral aerodynamic force inducing galloping is calculated using the QS theory.

The well-known Glauert–den Hartog criterion [36] describes the necessary condition for aerodynamically unstable behavior of a 1DOF oscillator based on the QS assumption, which can also be used to evaluate the onset velocity of galloping by setting the mechanical damping to be equal to the fluid dynamic damping, which reads:

$$U_g = -\frac{4m\zeta\omega_n}{\rho D \left(\frac{dC_L(\alpha)}{d\alpha} + C_D(\alpha) \right) \Big|_{\alpha=0}}. \quad (2.1)$$

The rationale underlying this criterion is related to the boundary-layer separation and reattachment phenomenon at a certain angle of attack [99, 6, 142].

Parkinson and Brooks [117] combined the aerodynamic force derived from QS theory with a linear dynamical system to develop a theoretical model for a square cylinder experiencing the 1DOF galloping oscillation. The aerodynamic force coefficient in the transverse direction (C_L^{QS}) was obtained from static test data of the lift and drag coefficients for different angles of attack, which was fitted with a fifth-order polynomial function. This polynomial approximation for $C_L^{QS}(\alpha)$ was then incorporated as a forcing term in a linear mass–spring–damper system. Subsequently, a more accurate seventh-order polynomial fitting of $C_L^{QS}(\alpha)$ was applied in order to reproduce the hysteresis effects observed in wind tunnel experiments [118].

The motion equation in Parkinson–Brooks model [117] resembles the structure equation for VIV, in the sense of the forcing term is related to the aerodynamic force acting on structure—the only difference is that the force coefficient used to model galloping involves a polynomial approximation. This governing equation can be solved analytically using various approximation methods when the mass ratio is small (e.g., in air m^* is typically of order 10^{-3}). As an example, Parkinson and Brooks [117] used Krylov–Bogoliubov asymptotic method to solve this second-order ODE and found that the solution provided a good agreement with some wind-tunnel measurements. Furthermore, the differential equation can be solved numerically (using, for example, the fourth-order Runge–Kutta method).

The result provided by the QS model is highly dependent on the polynomial fitting of $C_L^{QS}(\alpha)$. Luo *et al.* [87] and Ng *et al.* [112] compared different high-order polynomials and found the minimal polynomial order needs to be seven in order to capture the key characteristics of C_L^{QS} as a function of α and to predict certain features of the non-linear dynamics of galloping, such as hysteresis. Using a ninth- or eleventh-order polynomial may provide a better fit to the variation of C_L^{QS} , but this does not change the characteristics of governing equation, such as the number of positive real roots representing the stationary oscillation amplitude of a bluff body, implying that the predicted galloping hysteresis would be the same as that obtained from a seventh-order polynomial approximation. Barrero-Gil

et al. [16] and Joly *et al.* [68] also incorporated the Reynolds number into the classical QS galloping model by expressing the fitting coefficients as a function of Re in order to investigate the occurrence of galloping and the hysteresis effect of a square cylinder in the laminar flow regime.

From a physical and mathematical viewpoint, the underlying QS assumption is that the transverse galloping force depends on the instantaneous position of the body, as well as on the instantaneous relative velocity between the body and the fluid [121]—this is true in certain circumstances, such as when the vortex shedding frequency is much larger than the structural oscillation frequency (viz., $f_{osc} \ll f_{vs}$), implying that the wake dynamics is essentially uncoupled from the body motion so that the influence of vortex force on the motion driving force is negligible. In addition, the applicable velocity range of the QS model is determined by the condition $U^{QS} = U/(f_{osc}D) \gg (U/D)(D/(StU)) = 1/St$ where St often has an order of magnitude of 0.1, suggesting that the QS assumption can be satisfied at large values of velocity [18, 113, 16, 121]. Even with these limitations, the easy-to-use QS model still plays a fundamental role in the mathematical modelling of galloping, especially when few experimental or numerical data is available.

The Glauert–den Hartog criterion and QS galloping models are limited to the 1DOF translational galloping. There also exists some QS-based theoretical models for 2DOF (vertical and torsional) galloping [37, 69, 88] or for 3DOF (vertical, lateral, and torsional) galloping [62, 121].

2.4.4 Wake-Oscillator Model for FIV

Instead of undergoing only VIV or galloping, some engineering structures with aerodynamically unstable cross-sectional shapes can experience both FIV phenomena. Parkinson and Sullivan [119] and Parkinson and Wawzonek [120] conducted some wind tunnel experiments involving square and rectangular towers, which demonstrated that the synergy between VIV and galloping can provoke large-amplitude transverse vibrations that cannot be predicted by VIV or galloping models reviewed above. As a consequence, it is of practical importance to construct a simple and efficient mathematical model for both VIV and galloping responses. Based on above discussions, the essential problem reduces to the correct simulation of the unsteady aerodynamic force responsible for the specific dynamic response—the most straightforward way to accomplish this is to simply superimpose the aerodynamic VIV force and quasi-steady galloping force components.

For one thing, the QS galloping force can be incorporated into the C_L -based wake oscillator model. An early theoretical work following this methodology was proposed by

Parkinson and Bouclin [116] who used the Hartlen–Currie lift oscillator [60] to calculate the fluctuating lift force due to vortex shedding that induces VIV (C_L) and the Parkinson–Smith QS model [118] to represent the perturbational transverse force that triggers galloping (C_L^{QS}). In this approach, the sum of both forces was incorporated as the forcing term in the structure equation. Corless and Parkinson [32] basically applied the identical model structure, but added an acceleration coupling term in the right hand side of wake equation. Following the same strategy, Han *et al.* [58] incorporated the QS galloping force with a seventh-order polynomial approximation into another lift-type wake oscillator model—Fachinetti *et al.*’s model [39]—to give a coupled mathematical model for VIV and galloping of a square prism.

For another, the QS galloping force is possible to combine with the θ -based wake oscillator model. Tamura and Shimada [159] proposed a mathematical model for both VIV and galloping for 2D and 3D rigid square cylinders, in which the unsteady vortex shedding and galloping forces were simulated using the Tamura–Matsui VIV model [157] and the Parkinson’s QS model [117, 118], respectively. Based on this basic model, Mannini *et al.* [97] replaced Funakawa’s wake oscillator (see Fig. 2.5 (b)) with Birkhoff’s wake oscillator (see Fig. 2.5 (a)) and used an improved tuning process of model parameters. A later work [93] further incorporated the effect of turbulence into the modified model. Finally, Chen *et al.* [26] proposed a more reasonable definition of the near-wake lamina for a rectangular cylinder—the modified wake oscillator was shown to provide better predictions of the combined VIV-galloping instability.

The two types of models described above have been important mathematical tools for the prediction of FIV phenomenon. In particular, Mannini *et al.* [96] compared the C_L -based model by Corless and Parkinson [32] and the θ -based model by Tamura and Shimada [159] for the prediction of FIV of a rectangular cylinder and evaluated the model performance using their wind-tunnel test data. A key conclusion of this investigation was that the Tamura–Shimada model [159] is more accurate than the Corless–Parkinson model [32] in terms of their predictions of the correlation between the oscillation amplitude and the wind speed over the range where galloping occurs.

2.5 FIV of Cylinder-Plate Assembly

In addition to a free-standing cylindrical structure (e.g., circular and square cylinders), a cylinder with passive turbulence control device (e.g., rod, splitter-plate) can also experience FIV response. The former has been widely investigated in many experimental and

numerical studies as reviewed above, while in contrast the research effort on the latter is relatively few.

Recently, the investigations of FIV-based energy harvesting have shown that the configuration of a rigid splitter-plate attached to a circular cylinder seems to be comparable or even potentially superior to other shapes in terms of energy harvesting owing to the synergy of VIV and galloping [63, 148, 64]. In fact, the dynamic response of a cylinder-plate assembly depends on a number of factors—how the assembly is constrained (fixed or movable), the assembly material (rigid or flexible), and the location of the plate relative to that of the cylinder (attached or detached). Furthermore, various geometric characteristics will influence the structural vibrations and flow dynamics of this structure [44, 43]. To fully understand the complex dynamics of cylinder-plate assembly, it is necessary to briefly review this special dynamical system for various configurations.

2.5.1 Configuration of Cylinder-Plate Assembly

A stationary cylinder and splitter-plate

The most basic configuration is a rigid splitter-plate attached to a stationary cylinder, in which the former functions as a wake stabilizer to divide the shear flow and eliminate the vortex shedding—as a result, the system oscillations are inhibited at the source. Some earlier studies demonstrated that introducing a splitter-plate can significantly result in a narrower width of the near-wake flow, increase the base pressure, reduce the drag force up to about 30–36% and alter the Strouhal number St of the stationary cylinder [9, 8, 75]. Moreover, the critical plate length above which the vortex shedding can be completely suppressed to give a minimum drag force on the cylinder is dependent on the Reynolds number [75].

If placing a splitter-plate in the near wake (completely detached from the cylinder), the system vibration is also significantly suppressed owing to the weakening of the vortex strength and the reduction of the fluid force [66, 2, 101]. The drag reduction and oscillations suppression in the cylinder-plate assembly are essentially unchanged, regardless of the number and the location of the splitter plate(s) in the assembly (e.g., asymmetric arrangement of the plates [115, 35], two downstream plates [35, 12], two plates with one placed upstream and the other downstream [65]).

Another common configuration is that of a freely rotating cylinder-plate assembly which mimics a practical real-world scenario involving a multi-directional free stream. More specifically, rather than being aligned with the incident free stream, the splitter-plate in

this case can rotate to an off-axis equilibrium position (symmetry-breaking bifurcation) in order to give a drag force reduction and a suppression of the vortex shedding, as observed in experimental studies [30, 12, 56] and numerical investigations [183, 86, 191, 200].

A freely-vibrating cylinder and splitter-plate

In practice, many engineering structures are free to oscillate (e.g., bridges, high-rise buildings, power lines, marine risers). An elastically-supported cylindrical structure can be used to model this scenario with either a flexible (free to continuously deform along its length) or a rigid splitter-plate attached to it.

Shukla *et al.* [141] experimentally showed that the periodic travelling-wave type deformations can be induced on a flexible plate with a specific length, Reynolds number and flexural rigidity. Lee *et al.* [78] numerically showed that the flexibility of a splitter-plate can reduce the drag and lift forces acting on the cylinder, as well as promote oscillations in the plate. Wu *et al.* [176] reported increased drag reduction and vortex suppression for both a fixed and an elastically-mounted cylinder with a long flexible splitter-plate compared to that of a rigid splitter-plate.

A number of researchers investigated the dynamic response of a rigid splitter-plate attached to an elastically mounted cylinder and noted an interesting phenomenon: namely, the occurrence of a galloping-type instability. Consequently, this configuration has the potential to be one of the most promising candidates for a high-performance fluid energy harvester. Some earlier studies demonstrated that a circular cylinder with a long splitter-plate (viz., with a length of about $10D$ where D is the cylinder diameter) is susceptible to galloping at a large flow velocity [106, 70], which might arise from a negative aerodynamic damping associated with the rolling up of the shear layer and its subsequent reattachment on the splitter plate.

2.5.2 Effect of Splitter-Plate Length

A few experimental and numerical studies [151, 154, 181] have demonstrated that an elastically-mounted rigid assembly composed of a circular cylinder and a splitter-plate attachment is prone to both VIV and galloping. And the splitter plate length is a key factor in the determination of the response mode—VIV, galloping, and integrated or separated VIV-galloping.

Nakamura *et al.* [105] replaced a circular cylinder with a rectangular prism of various side ratios and demonstrated that any short bluff cylinder, whether sharp-edged or

smooth, can exhibit galloping in the presence of a long splitter-plate. Stappenbelt [151] systematically studied the influence of plate length L_{SP}/D (from 0–4) on the nature of the response of a freely-oscillating cylinder, by undertaking a number of still-water experiments at high Reynolds numbers in the range from $Re = 12,600$ – $84,000$. The author classified the dynamic instabilities into three categories: namely, (1) vibrations dominated by VIV (for $L_{SP}/D = 0.34$ – 0.5); (2) vibrations dominated by galloping (for $L_{SP}/D = 1$ – 2.4); and, (3) no vibrations (for $L_{SP}/D = 2.8$ – 4). Recently, Sun *et al.* [154] performed laminar flow simulations to investigate the dynamic behavior of a cylinder-plate assembly with plate lengths ranging from 0 to $1.5D$. With increasing plate length, these investigators observed three distinct response modes: namely, (1) pure VIV for $L_{SP}/D = 0$ – 0.5 ; (ii) coupled VIV-galloping for $L_{SP}/D = 0.75$; and, (3) separate VIV and galloping for $L_{SP}/D = 1$ – $1.5D$. Sun *et al.* [154] further explained the transition from VIV to galloping as arising from the competition between the lift forces on the plate (which promotes galloping) and cylinder (which suppresses galloping).

In addition to plate length, Sahu *et al.* [129] numerically investigated the effect of the mass ratio m^* (2–1000) and the Reynolds number (92–150) on the dynamic response of cylinder-plate assembly. Some variants of the rigidly-connected splitter plate can also induce a galloping-type instability on an elastically mounted cylinder such as a detached plate [84, 199] and a porous plate (solid and slotted) [11], but some appendages cannot, such as a fairing or a C -shaped attachment [77].

Rather than focusing on the translational vibration of a cylinder-plate assembly, Zhang *et al.* [191] investigated numerically the torsional vibration of an elastically mounted circular-plate assembly in a laminar flow. These researchers reported the presence of an amplified torsional VIV and a symmetry-breaking bifurcation at small and large values of the reduced velocities, respectively. In a subsequent study, Zhang *et al.* [190] investigated a three-degree-of-freedom (in-line, cross-flow, and torsional) coupled FIV of a cylinder-plate assembly in which the vibration dynamics was found to be strongly dependent on the torsional-to-vertical frequency ratios.

2.6 Motivations and Novelties

The key takeaway from above literature review is that the cylinder-plate assembly’s FIV response has more theoretical and practical relevance due to three reasons: (i) the presence of a splitter-plate can induce a richer spectrum of dynamic oscillation on the assembly than that of a simple cylinder; (ii) the intricate interaction and synergy between VIV and galloping make this geometry an excellent option for the innovative design of new

generations of unique energy harvesters with the goal of harnessing fluid energy (wind, tidal, water) through structural oscillation and converting this oscillatory motion into electricity; (iii) the transition between various vibration modes can be readily accomplished by simply changing the splitter-plate length, which can be used effectively as a passive control strategy for the utilization of cylinder-plate assembly as an energy harvester. However, it is evident that there is currently a dearth of research concerning the FIV response of this special dynamical system.

The drawbacks of predecessor’s research in this field can be summarized as follows.

1. Several (limited) previous studies about the FIV of cylinder-plate assembly have focused on the influence of splitter-plate length on the assembly’s FIV. But there has been no investigation on the combined effect of the aspect ratio of cylinder, the splitter-plate length and the reduced velocity (over a large range of these factors) on the assembly’s FIV.
2. The investigation of branching behavior for the galloping-dominated response is still limited. To this contention, most of previous studies involving the branching analysis only identify the various response modes (e.g., VIV, galloping, or integrated VIV-galloping), and do not conduct further analysis and identification on the branching behavior within the galloping regime. However, Zhao *et al.* [195, 194, 193] demonstrated that the galloping regime is invariably associated with a wide reduced velocity range and, as a result, can include complex branching characteristics. In addition, there exists currently no research on the branching behavior of a cylinder-plate assembly experiencing VIV and/or galloping. Also, the research concerning the flow dynamics and vortex-shedding patterns associated with various branches of this structure is extremely limited at present.
3. Many of previous investigations concerning the nonlinear dynamics of the FIV response only involved the canonical case of VIV for a circular cylinder [82, 42, 74, 182]. However, the generality of these results to other FIV forms of non-circular cylinder or cylinder-appendage system is unknown—for example the beating phenomenon has been reported for both circular and square cylinders, but there are important differences in the nonlinear behaviors of the two dynamical systems (e.g., changes in the vibration characteristics and wake modes). Moreover, there is a paucity of analysis concerning the nonlinear dynamical characteristics of a cylinder-plate assembly, despite the fact that this assembly exhibits a much richer dynamical features with respect to the FIV than that provided by the canonical cases.

4. The existing wake-oscillator model for FIV phenomenon is limited to the VIV of circular cylinder or the VIV-galloping of rectangular (square) cylinder. In addition, these semi-empirical models can only be used in combination with the static test data in order to determine the values of model parameters. No theoretical model is available for the prediction of FIV response for a cylinder-plate assembly.

In consequence, there is certainly more that can be done in the investigation of the intrinsic dynamical characteristics of the cylinder-plate assembly to address the deficiencies (knowledge gaps) identified above. With this in mind, this thesis is constructed with the following motivations.

1. Comprehensive numerical simulations of a cylinder-plate assembly's FIV response covering a large range of three important factors: aspect ratio of cylinder, splitter-plate length and reduced velocity.
2. Detailed investigation of the full spectrum FIV phenomena associated with the cylinder-plate assembly in terms of the structural vibration, branching behavior, flow analysis and the nonlinear dynamical characteristics.
3. Prediction of the FIV for a cylinder-plate assembly using the mathematical wake-oscillator model.

From the perspective of engineering application, the assembly is subjected to a three-dimensional turbulent flow at high Reynolds numbers of around 10^3 – 10^4 . However, the 3D numerical simulation at high- Re , especially in conjunction with a bidirectional FSI problem such as FIV, is prohibitively computationally expensive. In consequence, all the computations in the current work are conducted for a two-dimensional laminar flow with a low Reynolds number of 100, in order to effectively acquire large number of numerical results needed to conduct a systematic study.

The novelty of this thesis arises in the following aspects.

1. Identify the branching behavior of the FIV response of a circular cylinder-plate assembly with plate length of $L_{SP}/D = 0$ – 4 , reveal the underlying physical mechanisms by means of the flow analysis, and analyze the associated nonlinear dynamical characteristics from multiple points of view.
2. Investigate the synergistic effect of two geometrical factors, viz., the aspect ratio of cylinder and the splitter-plate length, on the cylinder-plate assembly's FIV response using numerical simulation.

3. Propose a genetic algorithm optimized nonlinear grey-box estimation framework to determine the free parameters of wake-oscillator models and apply to predict various FIV responses.

2.7 Outline of Thesis

This thesis is organized as follows.

Chapter 3 describes the numerical simulations of the transverse FIV for an elastically mounted circular cylinder-plate assembly, over a board range of splitter-plate length $L_{SP}/D = 0-4$ and reduced velocity $U_r = 2-30$, at a low Reynolds number of $Re = 100$, a fixed mass ratio of 10 and zero structural damping ratio. First, the establishment, independence study and validation of the numerical model are introduced in Section 3.2. Then, the simulation results are analyzed in terms of the vibration response (Section 3.3), the branching behavior (Section 3.4) and the nonlinear dynamical characteristics (Section 3.5).

Chapter 4 describes the synergy effect of the aspect ratio of cylinder ($AR = 0.5-2$) and the splitter-plate length ($L_{SP}/D = 0.5, 0.75$ and 2.5) on the transverse FIV of an elliptical cylinder-plate assembly under the same conditions. The assembly's FIV responses can occur either in a limited (Section 4.2) or an unlimited (Section 4.3) range of reduced velocity, which are analyzed in terms of the vibration responses, the branching behaviors, the dynamical characteristics in the synchronization and non-synchronization branches. Moreover, the physical mechanisms underpinning some interesting response characteristics of the assembly are interpreted in Section 4.4.

Chapter 5 describes the mathematical prediction of FIV response using the wake-oscillator models. First, the existing wake-oscillator models are improved from multiple aspects in Section 5.2. Based on that, a generic algorithm optimized grey-box estimation framework is proposed to determine the free model parameters (see Section 5.3), which is then verified with respect to the VIV of circular cylinder and galloping of cylinder-plate assembly (see Section 5.4).

Chapter 6 gives important conclusions of this thesis.

Chapter 3

FIV of Circular Cylinder-Plate Assembly with Various Plate Lengths

3.1 Problem Description

The problem investigated in this chapter is the one-degree-of-freedom vibration of an elastically-mounted cylinder-plate assembly that is free to move only in the cross-flow direction (viz., along the y -axis). As shown in Fig. 3.1, a rigid splitter plate with a length of L_{SP} and a width of $W_{SP} = 0.06D$ is attached to the afterbody midpoint of a circular cylinder with a diameter D and oriented in the streamwise direction (viz., along the x -axis). The elastic spring supporting the cylinder is characterized by the spring stiffness k and a mechanical damping coefficient c . The uniform velocity of free stream is U . In our simulations, both U and D are assumed to be unity.

The flow past the cylinder-plate assembly is usually laminar at a low-Reynolds number, consequently, the flow dynamics is governed by the two-dimensional unsteady incompressible Navier-Stokes (NS) equations:

$$\frac{\partial u_i}{\partial x_i} = 0 , \quad (3.1)$$

$$\frac{\partial u_i}{\partial t} + u_j \frac{\partial u_i}{\partial x_j} = -\frac{1}{\rho} \frac{\partial p}{\partial x_i} + \nu \frac{\partial^2 u_i}{\partial x_j \partial x_j} , \quad (3.2)$$

where the subscript i refers to the Cartesian component of a vector in the i -th direction with $i = 1, 2$ for a two-dimensional problem; $x_1 \equiv x$ and $x_2 \equiv y$ are the Cartesian components of the position vector in the streamwise and transverse directions, respectively; $u_1 \equiv u$ and

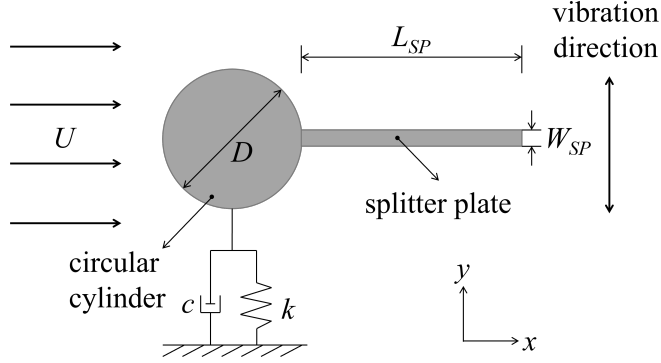


Figure 3.1: Sketch of a splitter plate attached to an elastically-mounted circular cylinder constrained to oscillate in the transverse (y -) direction.

$u_2 \equiv v$ are the components of the velocity vector in x - and y -directions, respectively; p , ρ and ν are the pressure, fluid density, and fluid kinematic viscosity; and, t is time. In the numerical simulations conducted herein, $\rho = 1.225 \text{ kg m}^{-3}$ and $\nu = 0.01 \text{ m}^2 \text{ s}^{-1}$.

The transverse vibration of cylinder-plate assembly, driven by the unsteady hydrodynamic fluid forces acting on it, can be modelled by a mass-spring-damper system, which assumes the following form:

$$m\ddot{y} + c\dot{y} + ky = F_y(t) , \quad (3.3)$$

where y , \dot{y} and \ddot{y} represent the displacement (in m), velocity (in m s^{-1}) and acceleration (in m s^{-2}) of the moving body in the cross-flow direction, respectively; m is the total oscillating mass per unit length (in kg m^{-1}); c and k are structural damping coefficient per unit length (in N s m^{-2}) and spring stiffness per unit length (in N m^{-2}), respectively; $F_y(t)$ denotes the fluctuating transverse force per unit length acting on the vibrating system (in N m^{-1}). Other non-dimensional quantities used here include: the dimensionless transverse displacement $Y \equiv y/D$; the reduced velocity $U_r \equiv U/(f_n D)$; the damping ratio $\zeta \equiv c/(2\sqrt{km})$; and, the mass ratio m^* . The instantaneous lift and drag coefficients are defined as $C_L(t) \equiv 2F_y(t)/(\rho U^2 D)$ (i.e. transverse force coefficient) and $C_D(t) \equiv 2F_x(t)/(\rho U^2 D)$ (i.e. streamwise force coefficient), respectively. Here, F_y and F_x are force components in the cross-flow and in-line directions, respectively. The dimensionless time τ is defined as $\tau \equiv tU/D$ —since $D = 1 \text{ m}$ and $U = 1 \text{ m s}^{-1}$, the dimensional time t has the same numerical value as τ so, for simplicity, we will henceforth use t to refer to both the dimensional and dimensionless time. Finally, the mass ratio is fixed at $m^* = 10$ and the damping ratio is $\zeta = 0$ in the numerical simulations conducted herein, in order to gain the strongest system dynamics.

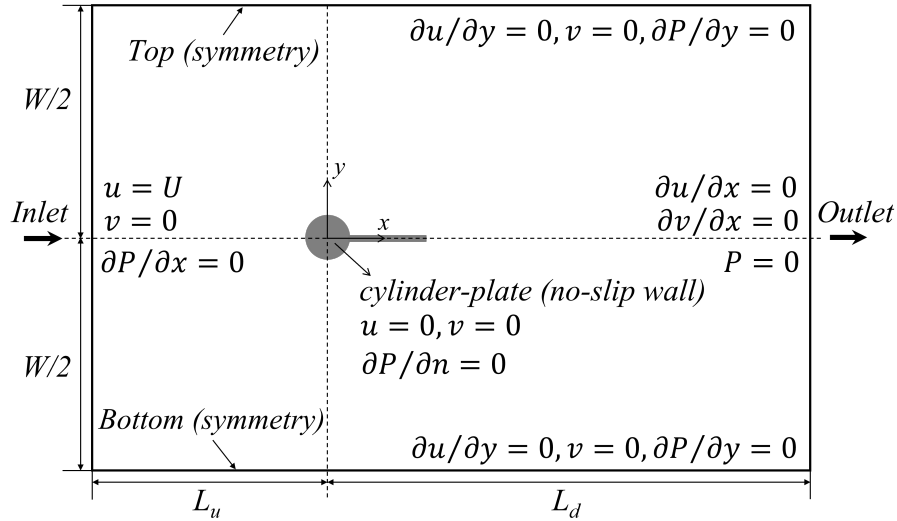


Figure 3.2: Sketch definition of computational domain and boundary conditions used in the numerical simulations.

3.2 Numerical Methodology

3.2.1 Simulation Set-Up

As shown in Fig. 3.2, the elastically-mounted cylinder-plate assembly is located at the origin of a rectangular Cartesian computational domain, the dimensions of which are $L_u + L_d$ (where L_u and L_d are the distance from cylinder center to inlet and outlet planes, respectively) in the x -direction and W in the y -direction. The center of the cylinder (in the equilibrium position) is equidistant ($W/2$) from the top and bottom boundaries of the domain. Considering that large-amplitude transverse oscillations may occur, the size of computational domain is chosen carefully to ensure that the four (artificial) boundaries of the domain do not have an effect on the motion of structure. The choice of an optimal computational domain size to satisfy this condition is described in Section 3.2.3.

Figure 3.2 also summarizes the boundary conditions used in our numerical simulations. A Dirichlet boundary condition is applied for the two velocity components (u and v) at the inlet plane and along the assembly surface as well as for fluid pressure (P) at the outlet plane. A Neumann boundary condition [77, 129, 154] is imposed for the fluid pressure at the inlet plane and along the assembly surface and for velocity components at the outlet plane. The specified boundary conditions and the corresponding mathematical expressions

Table 3.1: Boundary conditions and their corresponding mathematical expressions.

Boundary	Velocity	Pressure
Inlet	Uniform velocity ($u = 1, v = 0$)	Zero pressure gradient normal to boundary ($\partial P/\partial x = 0$)
Outlet	Zero velocity gradients normal to boundary ($\partial u/\partial x = 0, \partial v/\partial x = 0$)	Zero average reference pressure ($P = 0$)
Top/Bottom (symmetry plane)	Zero velocity and zero velocity gradient normal to boundary ($\partial u/\partial y = 0, v = 0$)	Zero pressure gradient normal to boundary ($\partial P/\partial y = 0$)
Cylinder/splitter-plate walls	No-slip wall condition ($u = 0, v = 0$)	Zero pressure gradient normal to walls ($\partial P/\partial n = 0$)

of these boundary conditions are summarized in Table 3.1. Moreover, the initial velocity and pressure fields in the computational domain are set to be zero.

In this study, the proprietary software package Ansys ICEM CFD is used to generate a two-dimensional structured hexahedral grid to cover the entire computational domain—this structured grid design is used to reduce the computational time and to obtain more accurate results. As depicted in Fig. 3.3, the grid cells surrounding the cylinder and the splitter plate are refined and the entire mesh covering the computational domain is of high quality—more specifically, the quality of the mesh used in our numerical simulations is between 0.95 to 1 as confirmed using the mesh check tool in the Ansys ICEM CFD package.

3.2.2 Numerical Techniques

The numerical schemes used to discretize the various terms in the NS equations are as follows: (1) temporal derivative term is discretized using a second-order accurate implicit backward scheme; (2) spatial discretization of the convective term uses a second-order accurate Gaussian linear upwind scheme; and, (3) the diffusion term is discretized using a second-order accurate Gauss linear corrected scheme. After the discretization of the NS equations, an iterative method is used to solve the linear algebraic equation system. To this purpose, the smoothSolver with symGaussSeidel smoother and the geometric-algebraic multi-grid (GAMG) with GaussSeidel smoother in OpenFOAM are used to solve the discretized systems of equations for velocity and pressure, respectively. The fluid dynamics

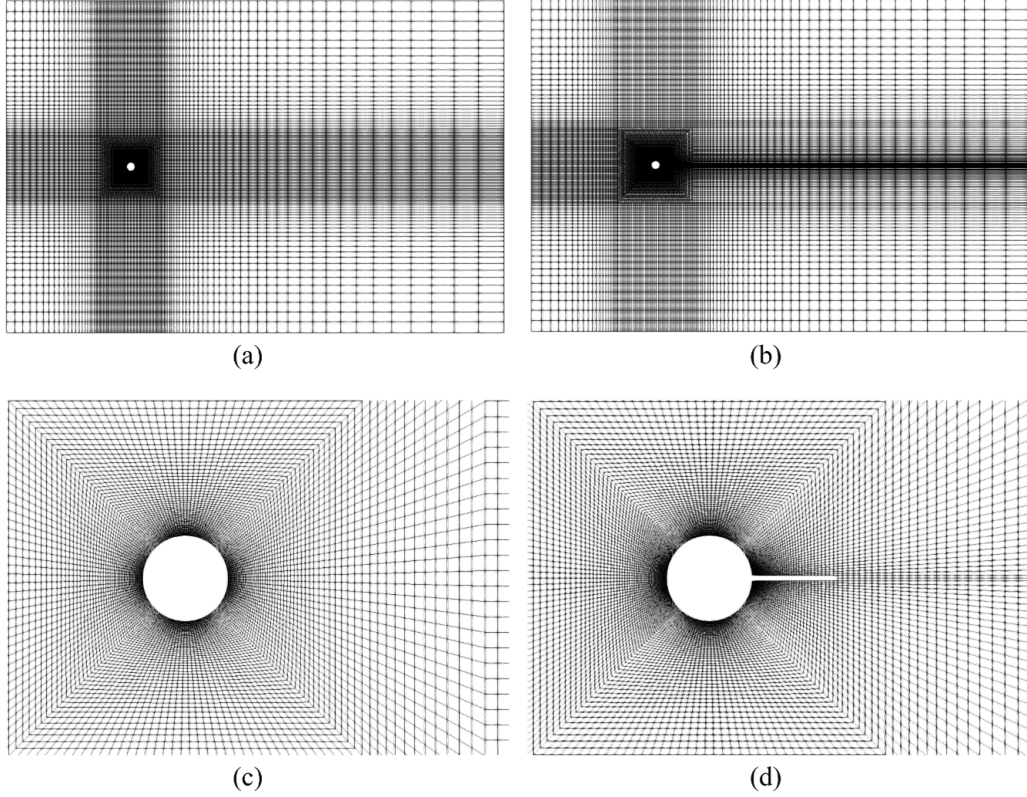


Figure 3.3: Computational mesh used to discretize the computational domain. Mesh partitioning of whole domain and local mesh refinement close to the surface of the bare circular cylinder ((a), (c)) and the cylinder-plate assembly ((b), (d)).

is addressed using the transient `pimpleFOAM` solver which the PIMPLE algorithm—a hybrid between the steady SIMPLE (Semi-Implicit Method for Pressure-Linked Equations) and transient PISO (Pressure Implicit with Splitting Operators)—is used to deal with the pressure-velocity coupling of the continuity and momentum equations. The `pimpleFOAM` solver allows a larger time step size to be used in the numerical simulations. In order to ensure a stable and convergent calculation at every time step, the time step is adjusted to control the maximum Courant-Friedrichs-Lewy (CFL) number which, for our numerical simulations, is specified to have a value of 0.8 at each time step.

With respect to the structural motion, the implicit Newmark- β scheme ($\gamma = 0.5$, $\beta = 0.25$) is utilized to numerically solve the mass-spring-damper equation of motion (Eq. (3.3))

to give the displacement, velocity and acceleration of the cylinder-plate assembly at each time step.

Owing to the oscillatory motion of the cylinder-plate assembly, a dynamic meshing methodology which can accommodate a changing geometry due to this motion is utilized in our numerical simulations. To this purpose, the whole computational domain is divided into three distinct regions through the definition of two parameters—`innerDistance` and `outerDistance`—which (1) allows the moving mesh zone between the body surface and `innerDistance` to move with the cylinder-plate assembly without any deformation; (2) defines a mesh morphing zone between `innerDistance` and `outerDistance`, allowing the mesh in this zone to be deformed and updated at each time step using a spherical linear interpolation scheme (SLERP); and, (3) specifies the static mesh zone beyond `outerDistance`. The partitioning of computational domain into three regions through the specification of `innerDistance` and `outerDistance` is displayed in Fig. 3.4. The existence of a directly-moving mesh zone can effectively improve the simulation accuracy in the mesh region surrounding the cylinder-plate assembly, and guarantee the computational stability of the numerical solution, particularly when the structure undergoes a significant displacement [177].

In order to achieve a two-way FSI during the simulation, the original NS equations are reformulated in the framework of the arbitrary Lagrangian Eulerian (ALE) methodology—this involves the inclusion of the relative velocity between the fluid and mesh in the convective term of momentum transport equation (Eq. (3.2)) to give

$$\frac{\partial u_i}{\partial t} + (u_j - u_{j,\text{mesh}}) \frac{\partial u_i}{\partial x_j} = -\frac{1}{\rho} \frac{\partial p}{\partial x_i} + \nu \frac{\partial^2 u_i}{\partial x_j \partial x_j}. \quad (3.4)$$

Here, $u_{j,\text{mesh}}$ is j -th component of the grid velocity vector characterizing the moving mesh.

An explicit FSI algorithm is applied in our numerical simulations, for which the governing equations for the fluid and structure are solved successively at each time step. More precisely, the numerical solution of the FSI problem uses the following three-step procedure: namely, (1) solve the ALE-based NS equations (Eqs. (3.1) and (3.4)) to obtain the flow field information, so that the fluid force acting on the structure can be calculated by integrating the pressure and viscous friction on its surface; (2) substitute the computed fluid force into the right-hand side of Eq. (3.3) as the forcing term and numerically solve the resulting equation to obtain the displacement, velocity and acceleration of the vibrating structure; and, (3) update the mesh (both the directly-moving and morphing regions) based on the state of motion determined in step (2).

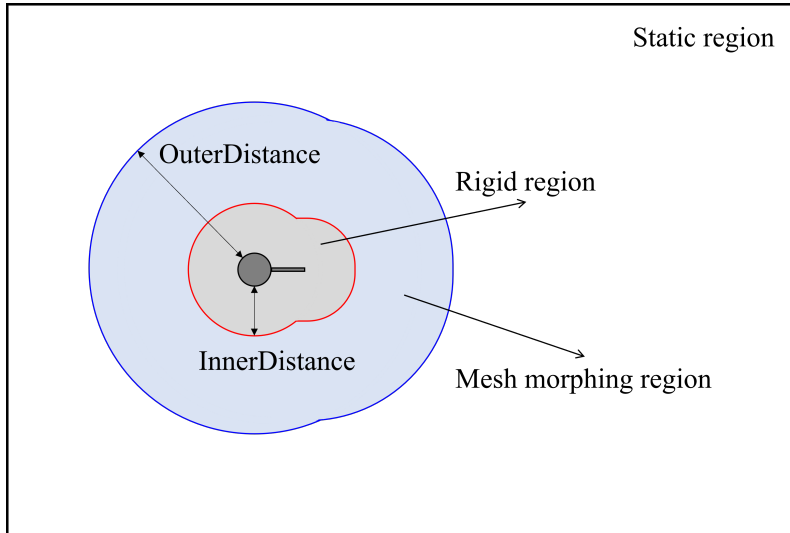


Figure 3.4: Partitioning of the computational domain into three regions by the specification of two parameters (innerDistance and outerDistance) in the dynamic meshing methodology.

3.2.3 Independence Study

Domain independence study

The sensitivity of the numerical solution to the size of the computational domain is investigated by varying the distance from the cylinder center to the outlet plane ($L_d/D = 25, 45,$ and 65) and the width of the domain ($W/D = 30, 40, 50,$ and 60) for a fixed distance from the cylinder center to the inlet plane ($L_u/D = 15$)— L_u is fixed owing to the fact that the flow information “propagates” in the downstream direction so the impact of this dimension is negligible on the numerical solution. To investigate the influence of the computational domain size, we fixed the grid stretching ratio around the cylinder to a value of 1.06, the number of mesh elements (cells) around the circumference of the cylinder to a value of $N_c = 160$ and the total number N_E of cell elements used to discretize the computational domain to a value of about 20,000. Moreover, the time step used in domain tests is fixed at $\Delta t = 0.01$ s.

Table 3.2 summarizes the results of a sensitivity study on the computational domain size. All the numerical simulations were conducted for a reduced velocity of $U_r = 6$. Domains 1–3 embody the effect of the downstream domain dimension L_d on the numerical solution and show the relative differences in the three quantities of interest as L_d/D increases from 25 to 45 to 65 with the width W/D fixed at a value of 40. It can be seen

Table 3.2: Dependence of numerical results on the size of the computational domain. All the numerical simulations were conducted at fixed values of $L_u/D = 15$, $Re = 150$, $m^* = 2.5465$, $\zeta = 0$, and $U_r = 6$.

Domain	$(L_x \times L_y)/D^2$	Y_{max}	$C_{L,rms}$	$C_{D,mean}$
1	$(15 + 25) \times 40$	0.50	0.03	1.73
2	$(15 + 45) \times 40$	0.46 (8.08%)	0.02 (24.38%)	1.66 (4.16%)
3	$(15 + 65) \times 40$	0.46 (0.15%)	0.02 (0.62%)	1.66 (0.05%)
4	$(15 + 45) \times 30$	0.50	0.03	1.73
2	$(15 + 45) \times 40$	0.46 (8.26%)	0.02 (22.24%)	1.66 (4.33%)
5	$(15 + 45) \times 50$	0.46 (0.32%)	0.02 (1.25%)	1.66 (0%)
6	$(15 + 45) \times 60$	0.47 (1.39%)	0.02 (0.52%)	1.66 (0.33%)

that the percent relative differences in the predicted values of the three quantities between domains 1 and 2 are significant. Moreover, the percent relative differences in the predicted values of Y_{max} , $C_{L,rms}$ and $C_{D,mean}$ are only 0.15%, 0.62% and 0.05%, respectively, between domains 2 and 3. In view of these results, $L_d/D = 45$ (or, equivalently, $L_x/D = 60$ where $L_x \equiv L_u + L_d$) is chosen as the downstream dimension for the computational domain. Domains 4, 2, 5, and 6 embody the influence of the domain width W on the numerical solution for a fixed value of the domain length $L_x/D = 60$. It is seen that $C_{L,rms}$ shows the largest percent relative difference of 22.24% between $W/D = 30$ and 40, while Y_{max} and $C_{D,mean}$ exhibit smaller percent relative differences of 8.26% and 4.33%, respectively. Moreover, the relative percent differences in the quantities of interest are small for $W/D = 40$ compared to those for $W/D = 50$ —a percent relative difference of 1.25% is observed for $C_{L,rms}$ and generally negligible percent relative differences for Y_{max} and $C_{D,mean}$. Similarly, the percent relative differences are very small for $W/D = 50$ when compared to those for $W/D = 60$. As a consequence, an appropriate domain width for the numerical simulations is $W/D = 40$. In summary, a computational domain with a length of $L_x = 60D$ (viz., $L_u = 15D$ and $L_d = 45D$) and a width $L_y \equiv W = 40D$ provides the best balance between computational effort and accuracy for the numerical simulations. The corresponding blockage (ratio of cylinder diameter D to domain width W) is 0.025.

Grid independence study

A grid sensitivity study has been conducted to ensure the numerical results are independent of the grid resolution. To simulate the VIV of a circular cylinder, a non-uniform stretched

Table 3.3: Dependence of numerical results on the grid resolution. All the numerical simulations were conducted at fixed values of $Re = 150$, $m^* = 2.5465$, $\zeta = 0$, and $U_r = 6$.

Grid	N_c	N_r	N_E	Y_{max}	$C_{L,rms}$	$C_{D,mean}$
1	80	48	7,815	0.52	0.03	1.77
2	120	56	12,217	0.50 (3.52%)	0.02 (9.20%)	1.73 (2.32%)
3	160	67	18,513	0.49 (1.97%)	0.02 (6.55%)	1.71 (1.14%)
4	200	76	25,201	0.49 (0.40%)	0.02 (0.86%)	1.71 (0.08%)

mesh composed of quadrilateral elements is used to tessellate in the entire computational domain (see Figs. 3.3 (a) and (c)). The mesh is characterized by the number of nodal points (N_c) along the circumference of the cylinder, the height of first grid layer away from the cylinder surface (δ), and the number of nodes along the radial direction within the dense mesh area surrounding cylinder (N_r). More specifically, N_r grid cells are distributed along the length of the splitter plate and three grid cells are distributed evenly along the width of the plate. Four different meshes ranging from coarse to dense are used in the sensitivity study—for each mesh, δ is fixed at $0.01D$ in order to satisfy the criterion of $y^+ \equiv yu_\tau/\nu \approx 1$ (where y^+ is the normal wall coordinate, y is the distance from the wall, and u_τ is the friction velocity). The grid resolution is varied by changing the values of N_c in the range from 80 to 200 and of N_r in the range from 48 to 76—these variations change the total number of cell elements (N_E) in the mesh. In these numerical simulations, a computational domain size of $L_x/D \times L_y/D = 60 \times 40$ and a time step of $\Delta t = 0.01$ s are used.

Four different meshes (grids) and their influence on the numerical solution are exhibited in Table 3.3. It can be seen that the percent relative differences in the predicted quantities between grid 1 (coarse) and grid 2 (intermediate) are significant as are those between grid 2 (intermediate) and grid 3 (fine). Moreover, the percent relative differences in the three quantities between grid 3 (fine) and grid 4 (very fine) is small, with the largest percent relative difference of 0.86% occurring for $C_{L,rms}$. In order to balance computational effort with accuracy, we will use grid 3 for the numerical simulations conducted in this paper.

Temporal convergence study

The sensitivity of numerical results on the dimensionless time step size has been investigated. These sensitivity tests were conducted on a fixed computational domain size (domain 2) and grid resolution (grid 3) with the numerical solutions obtained using three

Table 3.4: Dependence of numerical results on the time step size. All the numerical simulations were conducted at fixed values of $Re = 150$, $m^* = 2.5465$, $\zeta = 0$, and $U_r = 6$.

Time step size (s)	Y_{max}	$C_{L,rms}$	$C_{D,mean}$
0.02	0.51	0.03	1.76
0.01	0.49 (3.60%)	0.02 (19.39%)	1.71 (2.77%)
0.005	0.49 (0.27%)	0.02 (5.45%)	1.71 (0.16%)

different time step sizes: namely, $\Delta t = 0.02$ s, 0.01 s, and 0.005 s. The results are summarized in Table 3.4. A perusal of this table shows that significant percent relative differences in the three quantities are observed between the results obtained for $\Delta t = 0.02$ s and those for $\Delta t = 0.01$ s. More specifically, the percent relative difference for the predicted value of $C_{L,rms}$ using $\Delta t = 0.02$ s compared to that using $\Delta t = 0.01$ s is 19.393%. In contrast, the percent relative differences between results obtained for $\Delta t = 0.01$ s and 0.005 s is much smaller—again, the largest percent relative difference occurs for $C_{L,rms}$ but this difference is only 5.45%. From these considerations, a time step of $\Delta t = 0.01$ s is used in our numerical simulations as this choice represents the best compromise between computational efficiency and solution accuracy.

3.2.4 Model Validation

To validate the predictive accuracy of the numerical model used in this study, we will simulate the transverse VIV of a circular cylinder and the transverse FIV of the cylinder-plate assembly, and compare our predictions with some previous numerical results. Three different simulation cases are used for this purpose, involving different Reynolds numbers, and structural mass and damping ratios.

The numerical properties of first simulation case are the same as that in sensitivity studies: namely, $Re = 150$, $m^* = 2.5465$, and $\zeta = 0$ for a range of reduced velocity $U_r = 2 - 9.5$. The predictions of the dependence of three (dimensionless) quantities of interest Y_{max} , $C_{L,rms}$ and $C_{D,mean}$ on the reduced velocity U_r is exhibited in Fig. 3.5. These results are compared with the predictions obtained from some previous numerical investigations [1, 24, 15, 197, 169]. A careful examination of the figure shows that the normalized maximum transverse displacement and the lift and drag force coefficients are in excellent conformance with previous numerical simulations. This implies that the numerical model used in this study can accurately predict the VIV response of a circular cylinder in terms of the onset of VIV, the lock-in range and the maximum amplitude of oscillation.

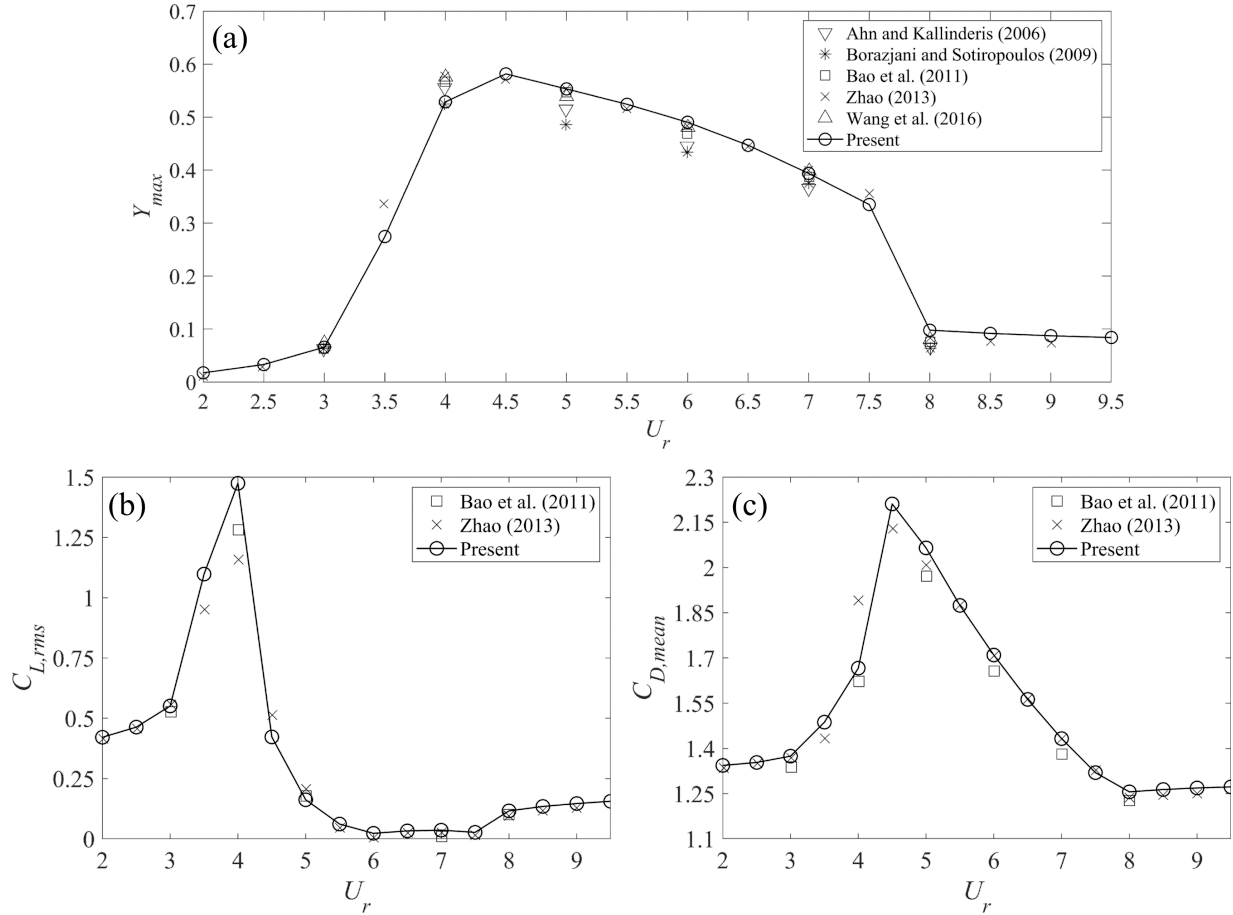


Figure 3.5: Comparison of numerical results between this thesis and previous numerical investigations (Ahn and Kallinderis [1], Borazjani and Sotiropoulos [24], Bao *et al.* [15], Zhao [197], and Wang *et al.* [169]): (a) normalized maximum transverse displacement Y_{max} as a function of U_r ; (b) root-mean-square lift coefficient $C_{L,rms}$ as a function of U_r ; and, (c) mean drag coefficient $C_{D,mean}$ as a function of U_r . The current numerical simulations are of the VIV response of a circular cylinder for $Re = 150$, $m^* = 2.5465$, and $\zeta = 0$. The resolution of U_r used in the present simulations is 0.5.

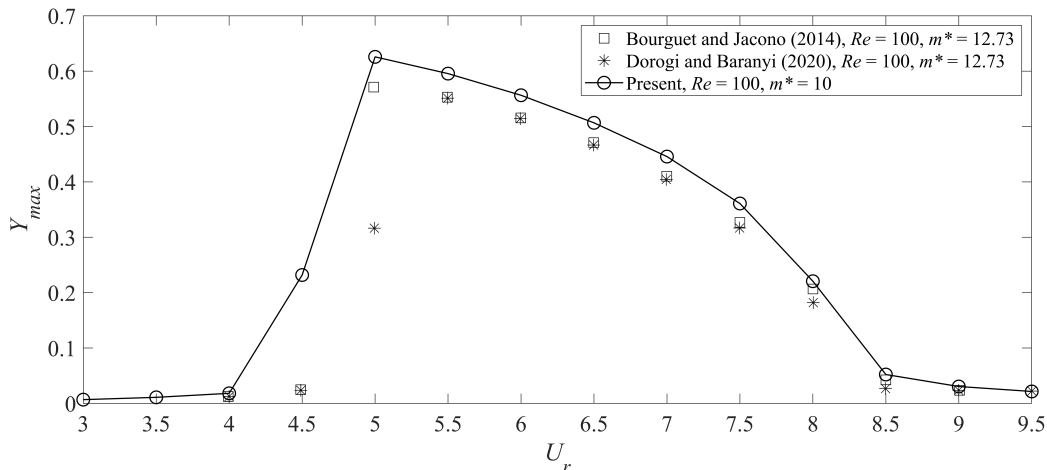


Figure 3.6: Comparison of numerical results between this thesis and previous numerical investigations (Bourguet and Jacono [25], Dorogi and Baranyi [38]) for the normalized maximum transverse displacement Y_{max} as a function of U_r . The current numerical simulations are of the VIV response of a circular cylinder for $Re = 100$, $m^* = 10$, and $\zeta = 0$. The resolution of U_r used in present simulations is 0.5.

The second case involves the numerical simulation of the VIV response of a circular cylinder for $Re = 100$, $m^* = 10$, and $\zeta = 0$ for $U_r = 3 - 9.5$. The numerical parameters in this example correspond exactly to those used for the numerical simulations of the cylinder-plate assembly conducted herein. Fig. 3.6 compares our predictions of the normalized maximum transverse displacement as a function of U_r with results obtained from some previous numerical studies [25, 38]. A good agreement is obtained between the present simulations and these previous numerical results—albeit, our predictions of Y_{max} are slightly larger than those obtained from previous numerical studies in the range of reduced velocities U_r from about 4.5 to 8. The reason for this small difference is that the mass ratio used in these previous numerical studies was $m^* = 12.73$ —this value of the mass ratio is larger than that used in the current simulations where $m^* = 10$.

Figure 3.7 compares the maximum transverse displacement of elastically-mounted cylinder-plate assemblies with plate lengths of $L_{SP}/D = 0.25, 0.5, 0.75$ and 1 with the corresponding numerical results of Sun *et al.* [154] and Zhang *et al.* [190]. All the numerical simulations shown here were conducted at $Re = 100$, $m^* = 10$ and $\zeta = 0$. A careful perusal of Fig. 3.7 shows that the present simulations are in excellent conformance with previous numerical results for both short plate lengths associated with self-limiting oscillations at small values of the reduced velocity (see Figs. 3.7 (a)–(b)) and for the longer plates associated with

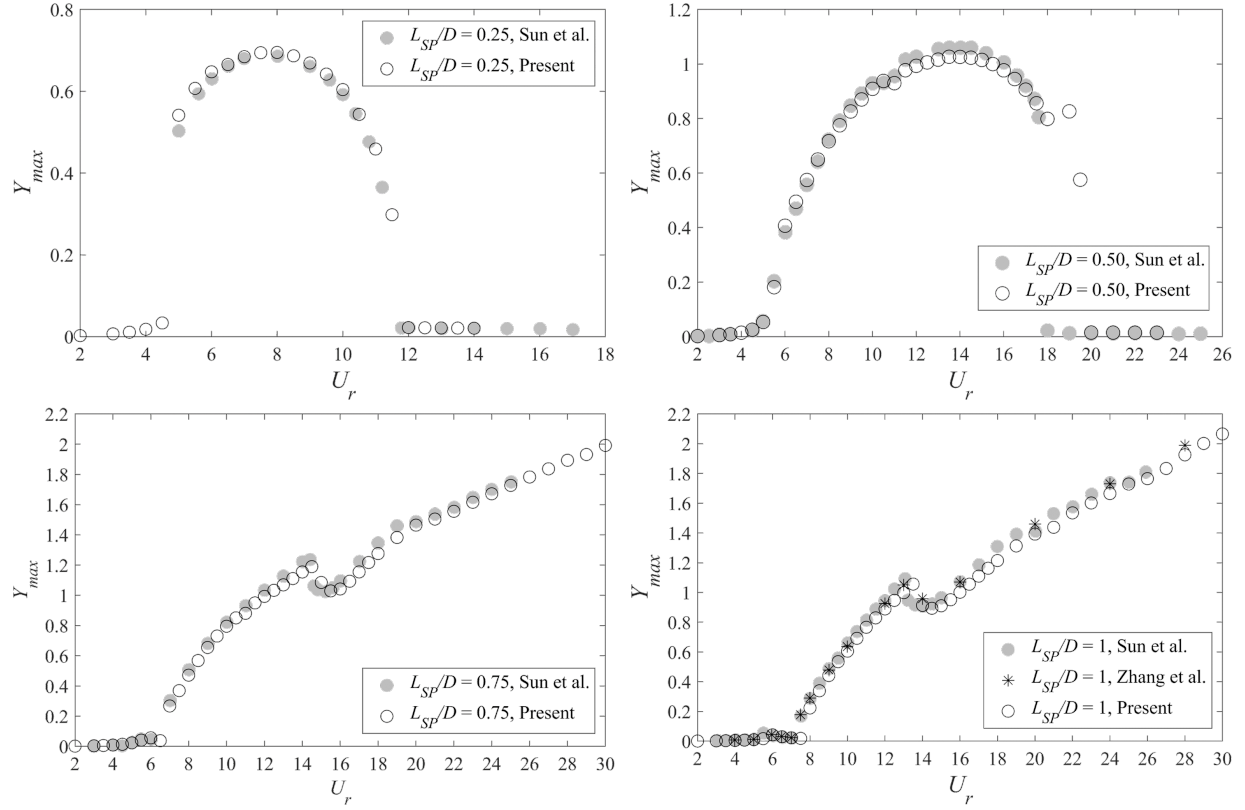


Figure 3.7: Comparison of numerical results between this thesis and previous numerical investigations (Sun *et al.* [154], Zhang *et al.* [190]) for the normalized maximum transverse displacement Y_{max} as a function of U_r . The current numerical simulations are of the FIV response of a cylinder-plate assembly with various plate lengths L_{SP}/D for $Re = 100$, $m^* = 10$, and $\zeta = 0$.

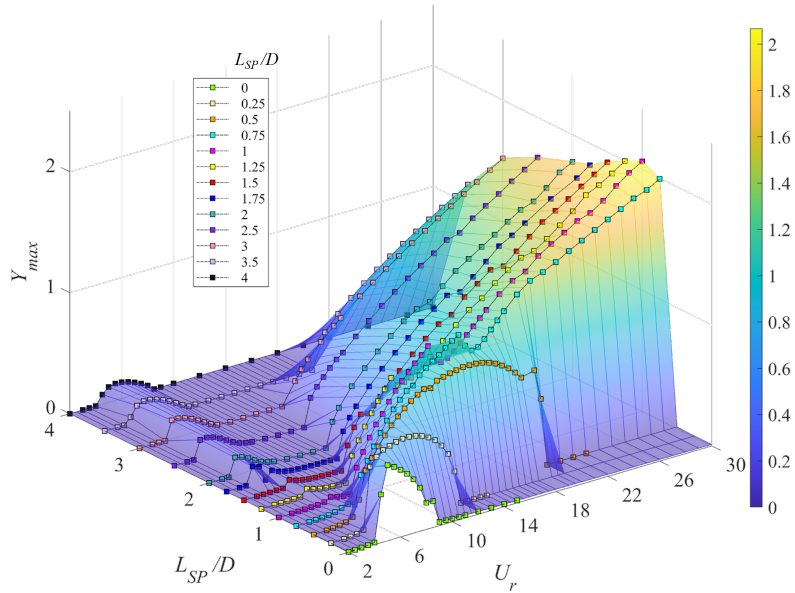


Figure 3.8: The normalized vibration amplitude plotted as a function of L_{SP} and U_r .

non-limiting oscillations at the larger values of the reduced velocity (see Figs. 3.7 (c)–(d)).

3.3 Vibration Response

In this section, the combined effect of splitter-plate length L_{SP} and reduced velocity U_r on the FIV of cylinder-plate assembly is analyzed in terms of the vibration amplitude, the oscillation frequency and the fluid forces acting on the moving system.

3.3.1 Vibration Characteristics

Figures 3.8–3.9 display the three-dimensional plots of the maximum transverse displacement Y_{max} and the non-dimensional dominant transverse displacement oscillation frequency f_Y^*/f_n , respectively, as a function of L_{SP} and U_r . A careful examination of these plots reveals the dynamical characteristics of the nonlinear system that can be divided into three regimes: namely, (1) in the regime where $L_{SP}/D = 0$ – 0.5 , the cylinder-plate assembly undergoes a self-limiting vibration that occurs over a limited U_r range with the oscillation

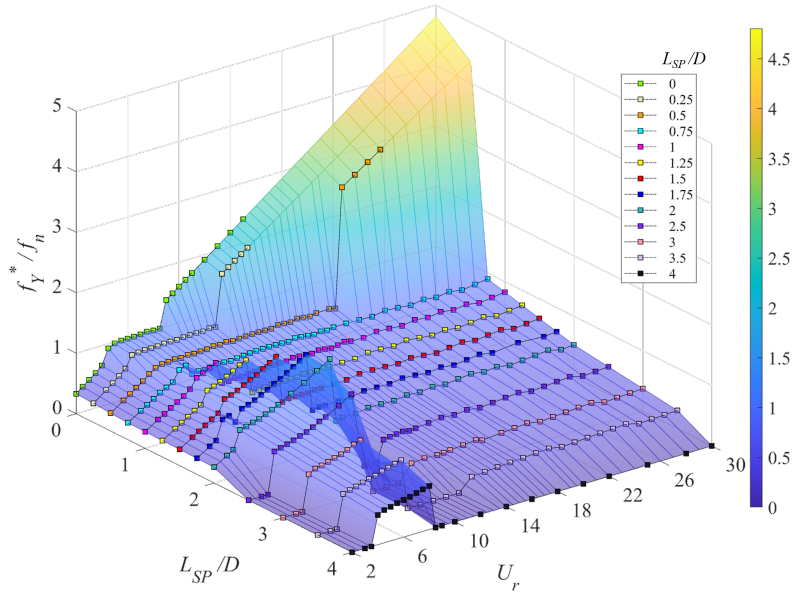


Figure 3.9: The dominant vibration frequency normalized by structural natural frequency (f_Y^*/f_n) plotted as a function of L_{SP} and U_r .

frequency locked near the structural natural frequency (which can be identified as a VIV-type response); (2) in the regime where $L_{SP}/D = 0.75\text{--}3.5$, the cylinder-plate assembly undergoes a non-limited vibration with a monotonically increasing oscillation amplitude with increasing U_r —this regime exhibits complex frequency characteristics and can be identified as a galloping-type response; and, (3) in the regime where $L_{SP}/D = 4$, there is no obvious oscillation induced on cylinder-plate assembly, at least for values of U_r up to 30. Figs. 3.8–3.9 show clearly that the dynamical response of a cylinder-plate assembly has a strong dependence on the splitter-plate length and the reduced velocity.

Although the three-dimensional plots exhibit qualitatively the relationship between the plate length, reduced velocity, and maximum transverse displacement, a detailed and more quantitative elucidation of the various controlling factors that influence the oscillatory response of a cylinder-plate assembly requires two-dimensional plots. Consequently, in order to obtain more details on the nature of the amplitude and frequency response for a cylinder-plate assembly, Fig. 3.10 exhibits two-dimensional plots of Y_{max} and f_Y^*/f_n as a function of U_r stratified by the value of L_{SP} . The bare circular cylinder (without the splitter plate, so $L_{SP} = 0$) undergoes VIV with a lock-in range of $U_r = 5\text{--}8.5$ and a maximum vibration amplitude of about $Y_{max}/D \approx 0.6$ at $U_r = 5$. The non-dimensional

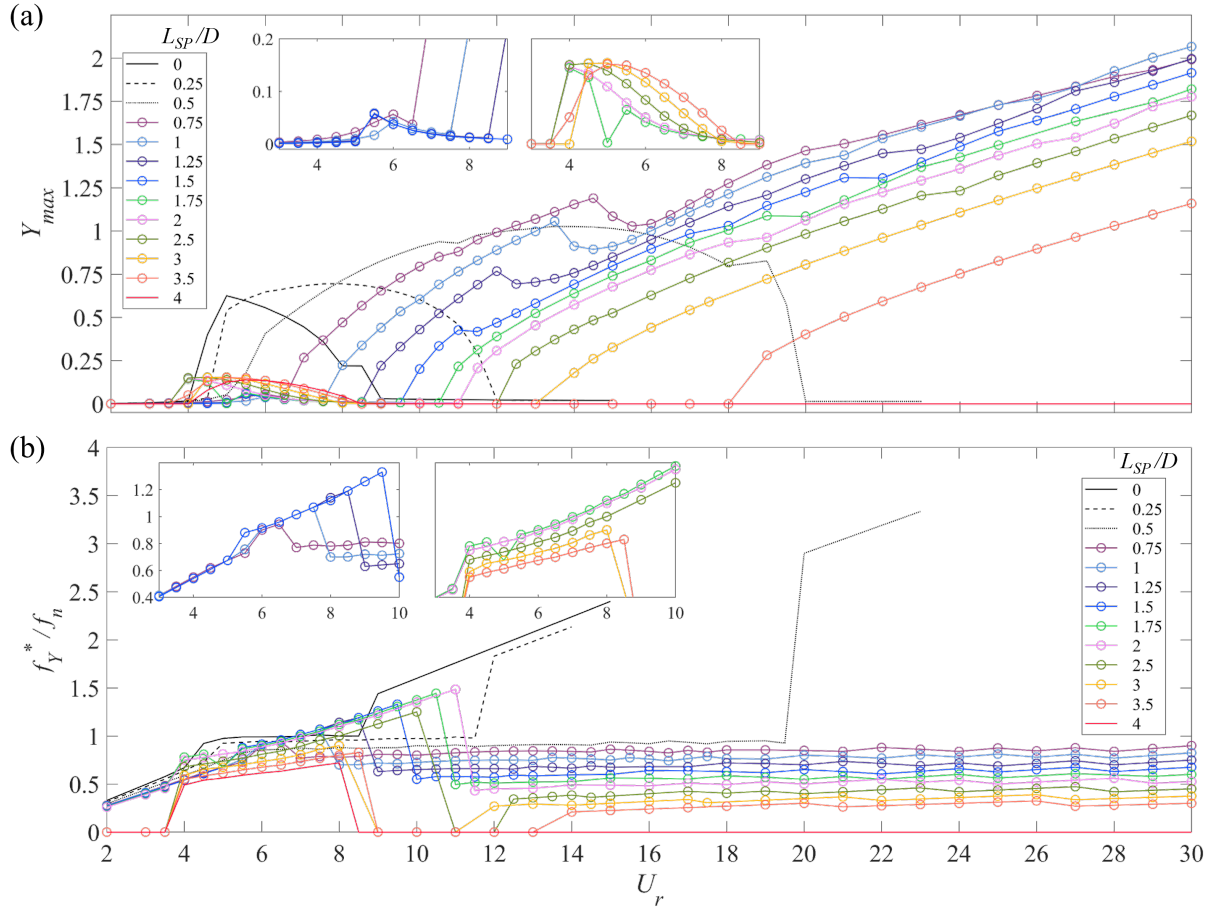


Figure 3.10: Plots of (a) the normalized vibration amplitude (Y_{max}) and (b) the normalized dominant vibration frequency (f_Y^*/f_n) as a function of the reduced velocity U_r stratified in terms of the splitter-plate length L_{SP} .

dominant frequency of displacement oscillations f_Y^*/f_n increases with U_r before the onset of VIV, attaining a value of unity when lock-in is achieved (implying that f_Y^* is exactly locked to f_n). The non-dimensional dominant frequency increases linearly again when the system transitions out of lock-in. The dynamic response of the bare circular cylinder is significantly different than that of a splitter plate attached to the cylinder.

With the inclusion of a relatively short splitter-plate of length $L_{SP}/D = 0.25$, the pure VIV response is enhanced in the sense that it has a wider lock-in range (namely, $U_r = 4.5\text{--}12$). The magnitude of the transverse displacement has a maximum value of about $0.7D$ over an extended range of U_r , in contrast to the case of a bare cylinder where Y_{max} decreases rapidly in magnitude with increasing U_r after achieving a peak value at lock-in. Furthermore, with the inclusion of the short splitter-plate, f_Y^* is approximately equal to f_n over the wider range of reduced velocities where lock-in occurs.

A cylinder-plate assembly with $L_{SP}/D = 0.5$ undergoes a further reinforced vibration over a much wider lock-in range of $U_r = 5.5\text{--}20$ (almost four times the VIV lock-in range of a bare cylinder) with a larger amplitude of vibration. The frequency response exhibits a similar pattern, but the dominant oscillation frequency f_Y^* is locked on to a value that is smaller than the natural frequency (more specifically, to $0.93f_n$). Consequently, a reasonable guess is that the cylinder-plate assembly with $L_{SP}/D = 0.5$ undergoes an integrated VIV-galloping response.

For an even longer plate length of $L_{SP}/D = 0.75$, the cylinder-plate assembly first undergoes a weak oscillation with $Y_{max}/D = 0.06$ at $U_r = 6$ where f_Y^* also exhibits a small increase. The system manifests an onset of galloping at $U_r = 7$ with a nearly linear increase in amplitude with increasing U_r —attaining an amplitude of $2D$ at $U_r = 30$. The associated dominant frequency f_Y^*/f_n maintains a constant value of 0.84 over the range of U_r where galloping occurs. Cylinder-plate assemblies with $L_{SP}/D = 1, 1.25$ and 1.5 exhibit very similar dynamical response characteristics as that with $L_{SP}/D = 0.75$. However, the onset of galloping occurs at larger values of U_r and the dominant frequency f_Y^*/f_n over the range of U_r where galloping occurs is smaller for the longer plate lengths. For example, the onset of galloping for $L_{SP}/D = 1, 1.25$, and 1.5 occurs at $U_r = 8, 9$, and 10 , respectively. Furthermore, $f_Y^*/f_n = 0.76, 0.7$, and 0.65 in the range of U_r associated with galloping for plate lengths of $L_{SP}/D = 1, 1.25$, and 1.5 , respectively. Therefore, with increasing L_{SP} the amplitude decreases (albeit slowly)—the only exception to this rule occurs at the larger U_r (e.g., the amplitude for $L_{SP}/D = 1$ crosses that for $L_{SP}/D = 0.75$ at about $U_r = 23\text{--}27$). Another interesting phenomenon is that the amplitude plots of $L_{SP}/D = 0.75, 1$ and 1.25 exhibits a “kink” in the amplitude response (where the amplitude decreases abruptly) at $U_r = 15, 14$ and 12.5 respectively. However, for $L_{SP}/D = 1.5$, the expected “kink” morphs instead into an interval where the amplitude is constant at $U_r = 11\text{--}11.5$.

When the plate length is increased to $L_{SP}/D = 1.75$, the small vibrations occurring at small U_r become stronger with increasing U_r , attaining a maximum amplitude of $0.15D$ at $U_r = 4$. The onset of galloping in this case does not occur until $U_r = 10.5$ and the dominant vibration frequency in the galloping regime is reduced (to $0.57f_n$) as is the transverse displacement Y_{max} compared to that for the shorter plate lengths. The cylinder-plate assemblies for $L_{SP}/D = 2, 2.5, 3$ and 3.5 exhibit similar dynamical response characteristics as those for $L_{SP}/D = 1.75$ —however, the onset of galloping occurs at progressively larger U_r (e.g., at $U_r = 11, 12, 13$ and 18 , respectively) and the dominant oscillation frequency in the galloping regime is progressively smaller (e.g., $f_Y^*/f_n = 0.5, 0.43, 0.35$ and 0.3 , respectively). In addition, the frequency response exhibits some noteworthy attributes: namely, (1) for $L_{SP}/D = 3$ – 3.5 , the dominant oscillation frequency in the lower range of U_r gradually increases to f_n (but does not exceed this value), in contrast to the behavior for shorter plate lengths (e.g., for $L_{SP}/D = 1$ – 2.5) where the dominant oscillation frequency can exceed f_n (and, indeed can attain values up to about $1.5f_n$); and, (2) for $L_{SP}/D = 2.5$ – 3.5 , there exist ranges of the reduced velocity where vibration ceases (e.g., $U_r = 11$ – $12, 9$ – 11 and 9 – 13).

For the longest plate length $L_{SP}/D = 4$ considered in this study, a small oscillation occurs in the range $U_r = 4$ – 8 . Moreover, no galloping is triggered, at least over the range of U_r investigated in this study—although, it cannot be ruled out that galloping might not occur at still larger values of U_r .

3.3.2 Fluid Force Characteristics

Figures 3.11–3.12 exhibit three-dimensional plots of $C_{L,rms}$ and of $C_{D,mean}$, respectively, as a function of L_{SP} and U_r for a cylinder-plate assembly. A perusal of this figure suggests that the lift force is strongly correlated with the onset of VIV and galloping—the lift force is seen to increase significantly in the range of reduced velocities associated with VIV or galloping. In contrast, the mean drag force embodied in $C_{D,mean}$ exhibits appreciable variations only when the self-limiting VIV response occurs (e.g., for $L_{SP}/D = 0$ – 0.25).

Figures 3.13 (a) and (b) display the fluid force coefficients $C_{L,rms}$ and $C_{D,mean}$ of the cylinder-plate assembly, respectively, as a function of U_r stratified by the different values of L_{SP} . For the bare circular cylinder, the lift and drag coefficients first increase sharply at the onset of VIV, reaching peak values of $C_{L,rms} = 1.38$ and $C_{D,mean} = 2.3$ at $U_r = 5$. After VIV onset, $C_{L,rms}$ decreases rapidly to near zero during lock-in and thereafter increases slightly again to a value of 0.2 and remains constant at this value when the system has transitioned out of lock-in. Furthermore, $C_{D,mean}$ also undergoes a sudden decrease from

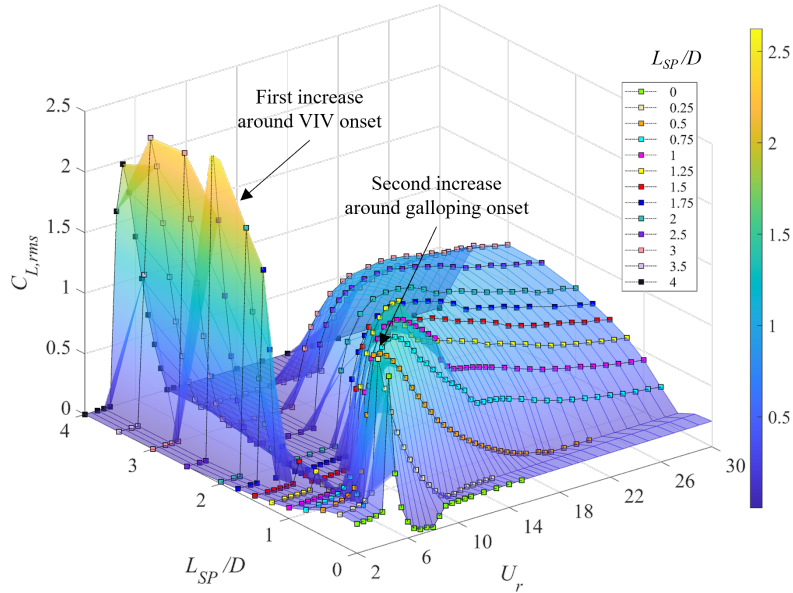


Figure 3.11: Three-dimensional plot of (a) the root-mean-square lift coefficient $C_{L,rms}$ and (b) the time-averaged (mean) drag coefficient $C_{D,mean}$ as a function of L_{SP} and U_r .

a peak value of 2.35 to a value of 1.35 where it remains constant with increasing U_r —the latter value for $C_{D,mean}$ is the same as that before lock-in.

If cylinder-plate assembly undergoes a galloping-type response, the lift coefficient exhibits a completely different behavior. For $L_{SP}/D = 0.75$ – 1.5 , $C_{L,rms}$ first increases to a small peak value (first peak) at $U_r = 5.5$ (which is associated with a very small oscillation) and then decreases towards zero until the onset of galloping, at which point $C_{L,rms}$ increases again to attain a large peak value (second peak) of about 1.2–1.4. This is followed by a gradual decrease in the value of $C_{L,rms}$ within the galloping regime. On the other hand, $C_{D,mean}$ only exhibits a very small increase in value at the onset of oscillatory motion and remains at a constant value within the galloping regime. There are also variations in the values of $C_{L,rms}$ and $C_{D,mean}$ at the location of “kinks” in the amplitude response.

For $L_{SP}/D = 1.75$ – 3.5 , the first peak of the lift coefficient attains a much higher value of between 1.75–2.7. This is comparable to the fluid force responsible for the VIV of a bare circular cylinder. However, the corresponding vibration at small values of U_r has a maximum amplitude of $0.2D$ which is only one-third of the value associated with the VIV response (cf. Fig. 3.13). Moreover, attaching a longer plate to the cylinder results in a smaller second increase in the lift coefficient before the onset of galloping followed by a

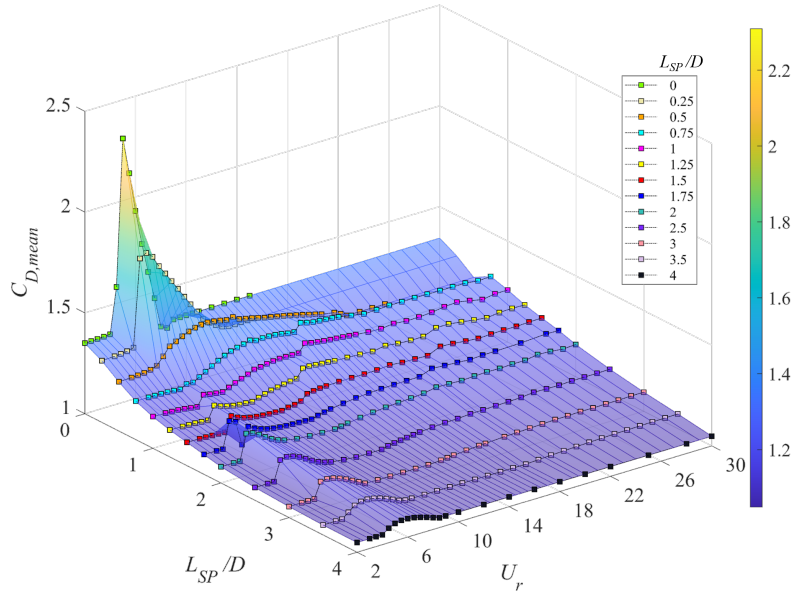


Figure 3.12: Three-dimensional plot of (a) the root-mean-square lift coefficient $C_{L,rms}$ and (b) the time-averaged (mean) drag coefficient $C_{D,mean}$ as a function of L_{SP} and U_r .

slow decrease of $C_{L,rms}$ within the galloping regime. In contrast, the variation $C_{D,mean}$ as a function of U_r is much simpler—there is a rapid increase at the onset of the small oscillatory motion and a gradual increase at the onset of galloping. Moreover, the drag coefficient is constant within the galloping regime. Finally, this constant value of $C_{D,mean}$ in the galloping regime is smaller for longer plate lengths.

A cylinder-plate assembly with $L_{SP}/D = 4$ only exhibits very small vibrations at small values of U_r . In this case, it is seen that both $C_{L,rms}$ and $C_{D,mean}$ first increase at $U_r = 4$ – 8 and then decrease again to zero at larger values of U_r .

3.3.3 Components of Transverse Force

For a cylinder-plate assembly moving together as a rigid body, the aerodynamic force will act on both the circular cylinder and the splitter-plate—the latter cannot be ignored, especially for a long plate. To determine the contribution of various force components to the system oscillations, Fig. 3.14 displays the oscillation amplitude superimposed on the fluid forces exerted on the cylinder and the plate. It should be noted that the drag force is included only for the self-limiting VIV-type oscillations (which are present when

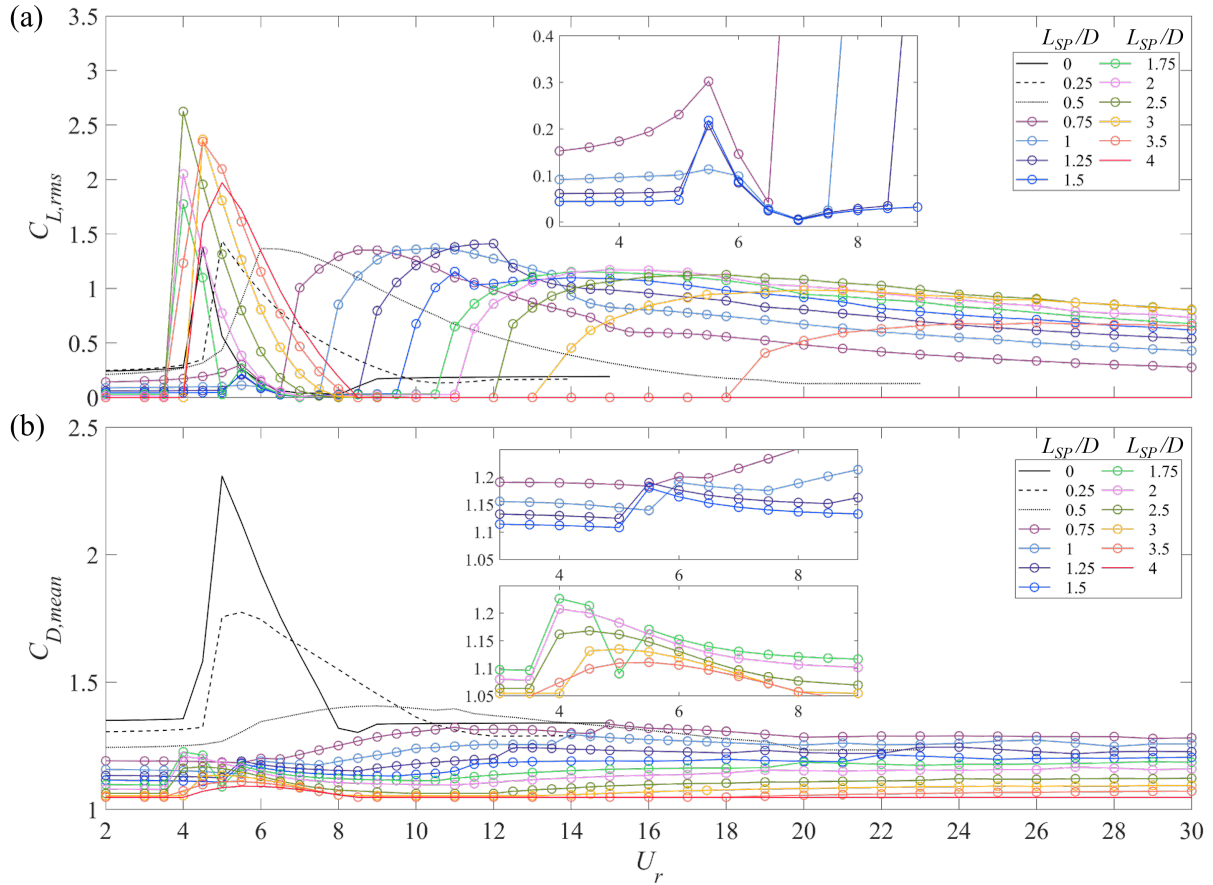


Figure 3.13: Variation of aerodynamic fluid forces acting on a cylinder-plate assembly: (a) the root-mean-square lift coefficient $C_{L,rms}$ and (b) the time-averaged (mean) drag coefficient $C_{D,mean}$ as a function of the reduced velocity U_r and stratified with respect to the plate length L_{SP} .

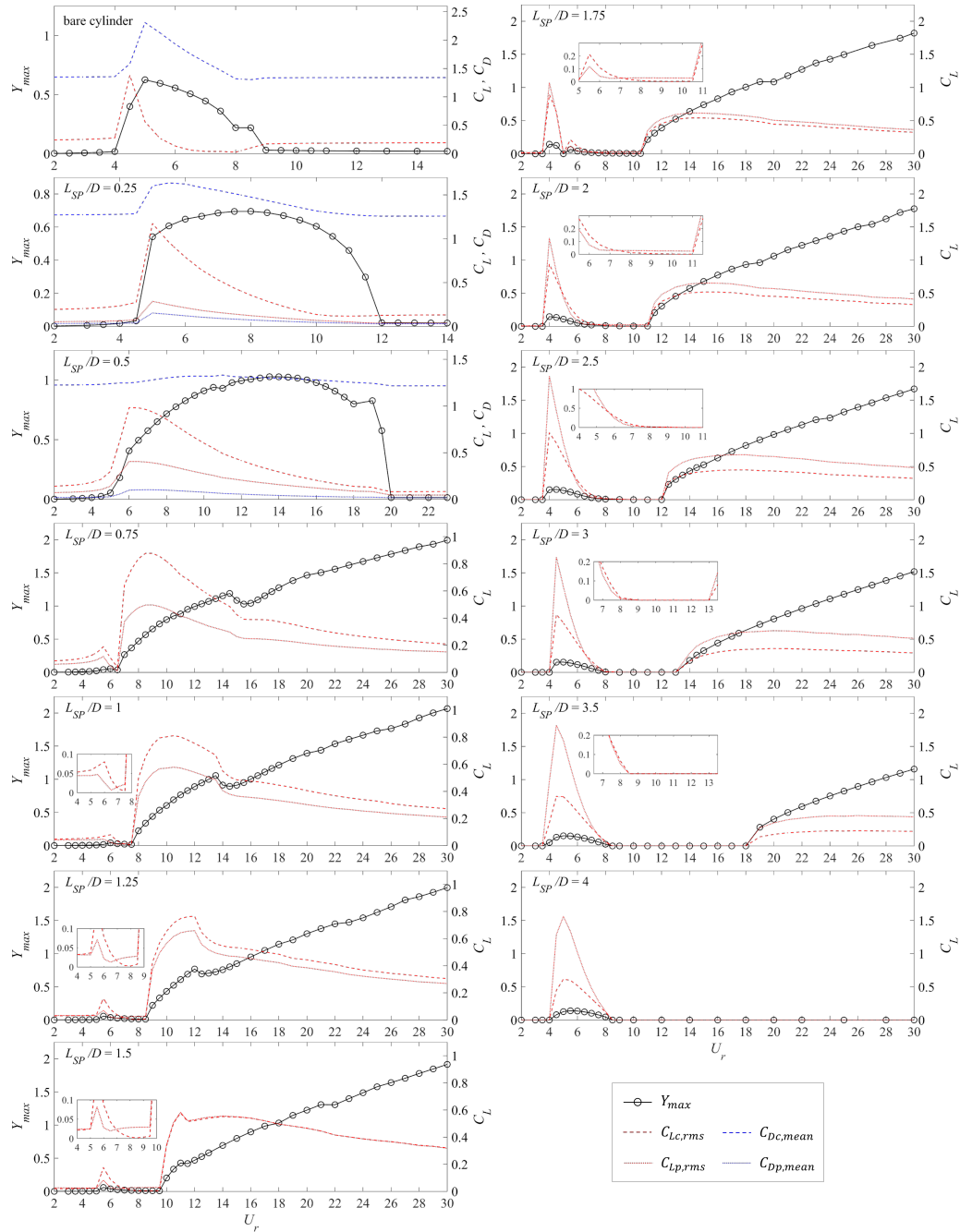


Figure 3.14: The maximum vibration amplitude Y_{max} , the root-mean-square lift force coefficient and the mean drag force coefficient acting on the cylinder ($C_{L,rms}$, $C_{Dc,mean}$) and splitter-plate ($C_{Lp,rms}$, $C_{Dp,mean}$) as a function of U_r for six plate lengths.

$L_{SP}/D = 0\text{--}0.5$)—the drag force has a negligible effect in the galloping regime.

For the cylinder-plate assembly undergoing a self-limiting oscillation ($L_{SP}/D = 0.25\text{--}0.5$), the transverse force acting on the cylinder is much larger than that acting on the splitter-plate, although the former decreases while the latter increases with an increasing L_{SP} . As a consequence, the additional plate-force might play a leading role in inducing stronger oscillations in the system over a wider range of U_r and in producing a larger vibration amplitude over this range.

For $L_{SP}/D = 0.75\text{--}1.5$, the cylinder-plate assembly undergoes a galloping-dominated response. The lift force on the cylinder in the galloping regime is larger than that on the splitter plate in general. The difference in the lift force between the cylinder and the plate decreases with increasing plate length until $L_{SP}/D = 1.5$ at which point the lift force on the cylinder and plate are nearly equal in value. Before the onset of galloping, the lift force on the cylinder is twice as large as that on the plate for small oscillations, but after that the former decreases towards zero, eventually becoming smaller than the latter (e.g., this occurs at $U_r = 7\text{--}7.5$, $7\text{--}8.5$, and $7\text{--}9.5$ for $L_{SP}/D = 1$, 1.25 , and 1.5 , respectively).

For $L_{SP}/D \geq 1.75$, the situation is reversed: namely, the lift force on the plate is generally larger than that on the cylinder for small oscillations and for galloping—this response may be associated with some special flow patterns. The difference between these two forces increases with increasing L_{SP} . As discussed above, the magnitude of transverse (lift) force with small oscillations is greatly increased relative to that for shorter plate lengths. In the quasi-stationary regime before the onset of galloping, the variation of the transverse force with U_r exhibits some interesting behavior. More specifically, for $L_{SP}/D = 1.75$, the lift force on the cylinder gradually decreases to zero, while the lift force on the plate remains small (but, non-zero)—this occurs at $U_r = 7\text{--}10.5$ and $7.5\text{--}11$ for plate lengths of $L_{SP}/D = 1.75$ and 2 , respectively. In contrast, the lift force on the cylinder and plate both are zero over this range of reduced velocities for longer plate lengths with $L_{SP}/D = 2.5\text{--}4$.

It appears that the lift force on the cylinder (C_{Lc}) has a greater effect on the resulting dynamic response of the vibrating system, even though the value of this lift force is less than that on the plate (C_{Lp}). This is supported by the fact that C_{Lp} increases sharply at small values of U_r for $L_{SP}/D \geq 1.75$. However, this sharp increase does not appear to induce a stronger secondary vibration—indeed, the lift force on the cylinder and the oscillation amplitude remain unchanged. The effect of C_{Lp} appears to be closely related to the wake flow dynamics behind a vibrating cylinder-plate assembly in the form of the interaction between the splitter plate and the near-wake flow. Finally, when C_{Lp} is larger than C_{Lc} for the longer plates, the amplitude response appears to increase linearly with U_r .

with less tendency for the existence of a “kink” (discontinuity in the slope) in this response.

3.4 Branching Behavior

3.4.1 Branching Identification

This section identifies various response branches for a cylinder-plate assembly undergoing VIV and/or galloping. Thirteen plate lengths are simulated to facilitate the comparison and discussion, which are categorized into five distinct groups according to their branching characteristics: namely, Group I for $L_{SP}/D = 0\text{--}0.5$, Group II for $L_{SP}/D = 0.75$, Group III for $L_{SP}/D = 1\text{--}1.5$, Group IV for $L_{SP}/D = 1.75\text{--}2$, and Group V for $L_{SP}/D = 2.5\text{--}4$.

Group I: $L_{SP}/D = 0\text{--}0.5$

It is widely known that a circular cylinder exhibits a VIV response only. The dynamics of a cylinder-plate assembly with a very short splitter-plate of $L_{SP}/D = 0.25$ is similar to that of a circular cylinder. The only difference is that the VIV for this cylinder-plate assembly occurs over a wider range of the reduced velocity. In marked contrast, the cylinder-plate assembly with $L_{SP}/D = 0.5$ exhibits a number of interesting and novel dynamical characteristics involving an integrated VIV-galloping response.

Figure 3.15 displays the normalized displacement amplitude Y_{max} , the root-mean-square lift coefficient $C_{L,rms}$, the power spectral density (PSD) of the oscillation and the instantaneous lift force, as well as the branching behavior for the case of $L_{SP}/D = 0.5$. The PSD isopleths shown here are constructed using the methodology described by Zhao *et al.* [195]. More precisely, we obtain the fast Fourier transform of the time series of Y (displacement) and C_L (lift force) at each value of U_r , normalize the resulting power spectrum (squared modulus of the Fourier transform) by the maximum power, and stack (composite) the normalized power spectra together for all values of U_r .

As shown in Fig. 3.15 (a), three synchronization branches are identified within the vibration range of $U_r = 5\text{--}20$. These include a wider resonance at $U_r = 5.5\text{--}10$, as well as two narrower branches at $U_r = 11\text{--}11.5$ and $U_r = 19\text{--}19.5$ —the onset of the latter two branches is signalled by the presence of a “kink” in the amplitude response. Here, “kink” refers to the bending or inflection (discontinuity in the slope) of the amplitude curve, following the nomenclature introduced by Zhao *et al.* [195]. A more detailed discussion of the “kink” in the amplitude response is given in Section 3.4.3. Within the first resonance,

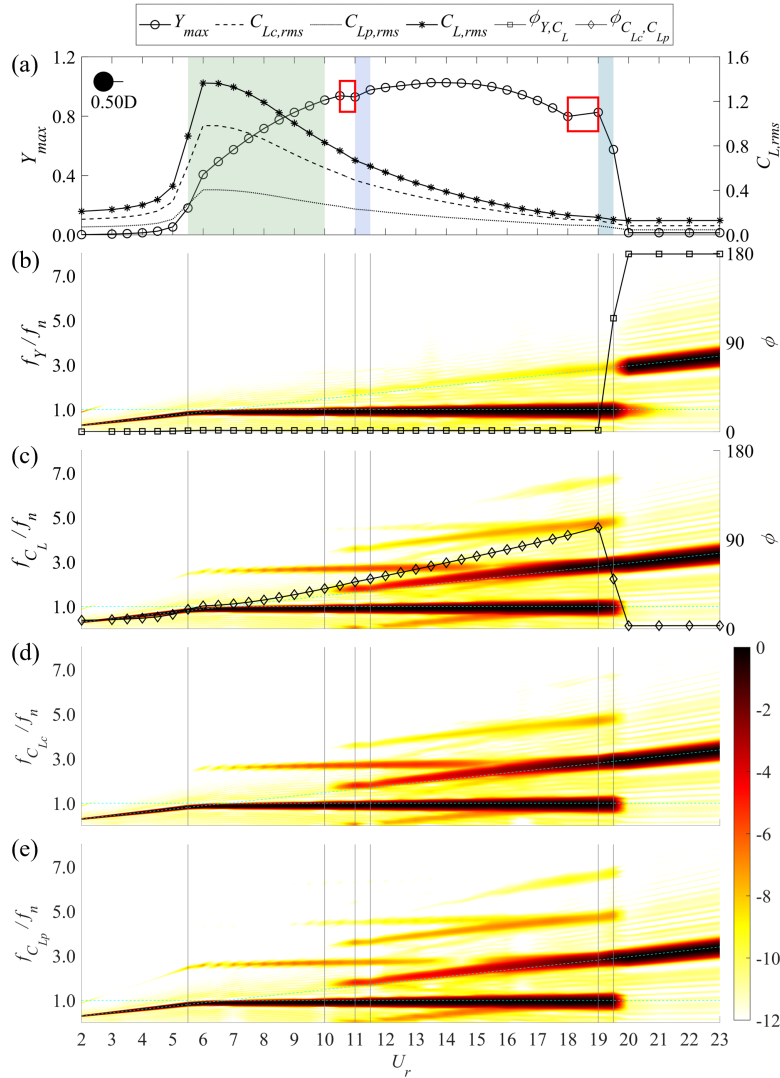


Figure 3.15: The branch identification of cylinder-plate assembly with $L_{SP}/D = 0.5$. (a) Dependence on U_r of Y_{max} and of the RMS lift coefficients ($C_{L,rms}$, $C_{Lc,rms}$, $C_{Lp,rms}$). Power spectral density isopleths of (b) Y , (c) C_L , (d) C_{Lc} and (e) C_{Lp} plotted against the associated normalized frequency and U_r . In (b)–(e), the diagonal and horizontal dashed lines represent the Strouhal frequency ($St = 0.148$) and the unit normalized frequency, respectively. The solid lines in (b) and (c) represent the phase differences between Y and C_L (square) and between C_{Lc} and C_{Lp} (diamond), respectively. The assembly undergoes an integrated VIV-galloping, with three synchronizations identified: namely, 1:1 at $U_r = 5.5$ –10, 1:2 at $U_r = 11$ –11.5, and 1:3 at $U_r = 19$ –19.5. “Kinks” (identified by red boxes) in the amplitude response signal the onset of synchronizations.

the PSD isopleths of the displacement and transverse force are seen to have a dominant frequency close to f_n (see Figs. 3.15 (b) and (c)). This suggests that VIV is induced in the assembly, so the range of reduced velocity $U_r = 5.5\text{--}10$ can be identified as the “lock-in” regime. However, in contrast to the VIV of a bare circular cylinder, this particular VIV branch exhibits an increasing amplitude response and the emergence of a third-harmonic in the C_L -spectrum.

A more complex fluid force with a spectrum consisting of various harmonics up to seventh-order that criss-cross one another is observed in Fig. 3.15 (c) for the range of $U_r = 10.5\text{--}20$. In contrast, the displacement spectrum still has a single frequency, suggesting the occurrence of galloping. It should be noted that the system oscillation and transverse force (viz., vortex shedding) over the latter two narrow branches are synchronized at $f_Y^* : f_{C_L}^* = 1 : n$ (where f_Y^* and $f_{C_L}^*$ are the dominant frequencies in the PSD of Y and C_L respectively; n is an integer greater than 1). More specifically, $f_Y^* : f_{C_L}^* = 1:2$ and $1:3$ for $U_r = 11\text{--}11.5$ and $U_r = 19\text{--}19.5$, respectively. Note that this synchronization phenomenon can be seen only in the colored regimes in Fig. 3.15 (a). The high-order synchronizations observed here are in stark contrast to the lock-in regime where a 1:1 synchronization (viz., the dominant oscillation frequency is equal to the dominant transverse force frequency) occurs because the VIV is directly induced by the vortex shedding. Above branching analysis implies that an integrated VIV-galloping response is triggered on the cylinder-plate assembly with $L_{SP}/D = 0.5$. More specifically, a special VIV response (or, lock-in) with a larger amplitude is triggered first at lower reduced velocity and then smoothly transitions to a self-limiting galloping response at $U_r \approx 10.5$.

To study the properties of synchronization, Fig. 3.16 exhibits various aspects of the dynamical response of the cylinder-plate assembly with $L_{SP}/D = 0.5$, including time series, phase portraits, Lissajous figures and power spectra of the displacement and fluid force at three different reduced velocities (viz., $U_r = 6, 11.5,$ and 19) for the 1:1, 1:2, and 1:3 synchronizations. A careful examination of the figure shows the oscillations of $Y(t)$ and $C_L(t)$ in all three synchronizations are periodic, as evidenced by the time series and phase portrait (which corresponds to a stable limit cycle associated with the closed trajectory of a perfectly periodic system involving self-sustained oscillations). Nevertheless, it is evident that the dynamics becomes more complex with increasing U_r —this is so can be seen by comparing the sinusoidal time series and the elliptical shape of phase portraits (viz., Y' – Y and C'_L – C_L where the primed superscript denotes a time derivative) at $U_r = 6$ (see Figs. 3.16 (ai) and (aii)) with the severely distorted time series and more complex phase portraits of transverse force at $U_r = 19$ (see Figs. 3.16 (ci) and (cii)). The Lissajous figures of the instantaneous transverse force coefficient C_L versus the transverse displacement Y (see third column of panels in Fig. 3.16) are inclined towards the first and third quadrants

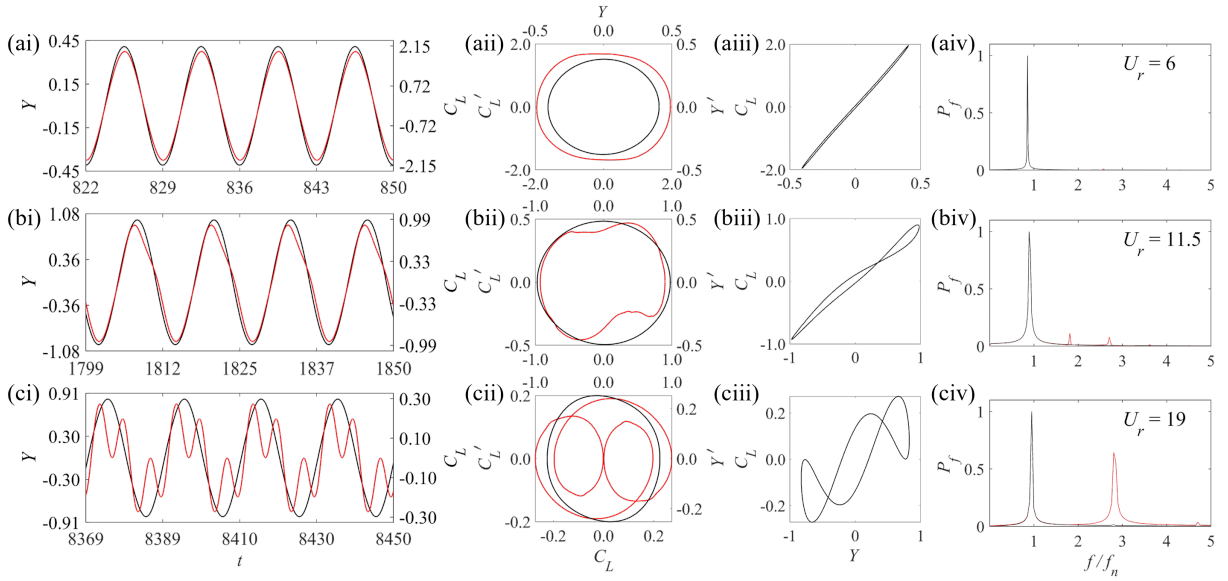


Figure 3.16: Dynamical characteristics of the cylinder-plate assembly with $L_{SP}/D = 0.5$ at three reduced velocities $U_r = 6, 11.5$ and 19 in (a)–(c), corresponding to the three synchronizations identified in Fig. 3.15. The dynamical characteristics are displayed in terms of the time series of Y and C_L (first column of panels), the phase portraits C'_L – C_L (second column of panels), the Lissajous figures C'_L – Y (third column of panels), and the power spectra of Y and C_L (fourth column of panels). In all these plots, the results for Y and C_L are shown as the black and red curves, respectively.

of the plane, suggesting that C_L and Y are in-phase in the synchronization branches—this is supported also from a perusal of the time series of C_L and Y .

It should be noted that the relationship between f_Y^* and $f_{C_L}^*$ in the synchronization branch can be determined using various methods. These include ascertaining the number of closed loops in the (C_L – Y) Lissajous figure (e.g., two at $U_r = 11.5$ and three at $U_r = 19$) or confirming the presence of higher harmonic components in the power spectrum of C_L (e.g., smaller red peaks in the C_L -spectrum at $U_r = 11.5$ and 19). At $U_r = 6$, the dominant frequency of C_L is identical to that of Y . However, perhaps the most intuitive and accurate approach is to simply observe the vortex-shedding mode in the wake field as in Fig. 3.17. At $U_r = 6$, a clockwise (negative) vortex labelled “ $-S_I$ ” and a counter-clockwise (positive) vortex labelled “ S_I ” are alternately shed from the shear layers on the structure during one oscillation cycle—these form the so-called “ $2S$ ” wake mode and the classical Kármán vortex street. At $U_r = 11.5$, four vortices (two clockwise ($-S_{I,-}S_{II}$) and two counter-clockwise (S_I

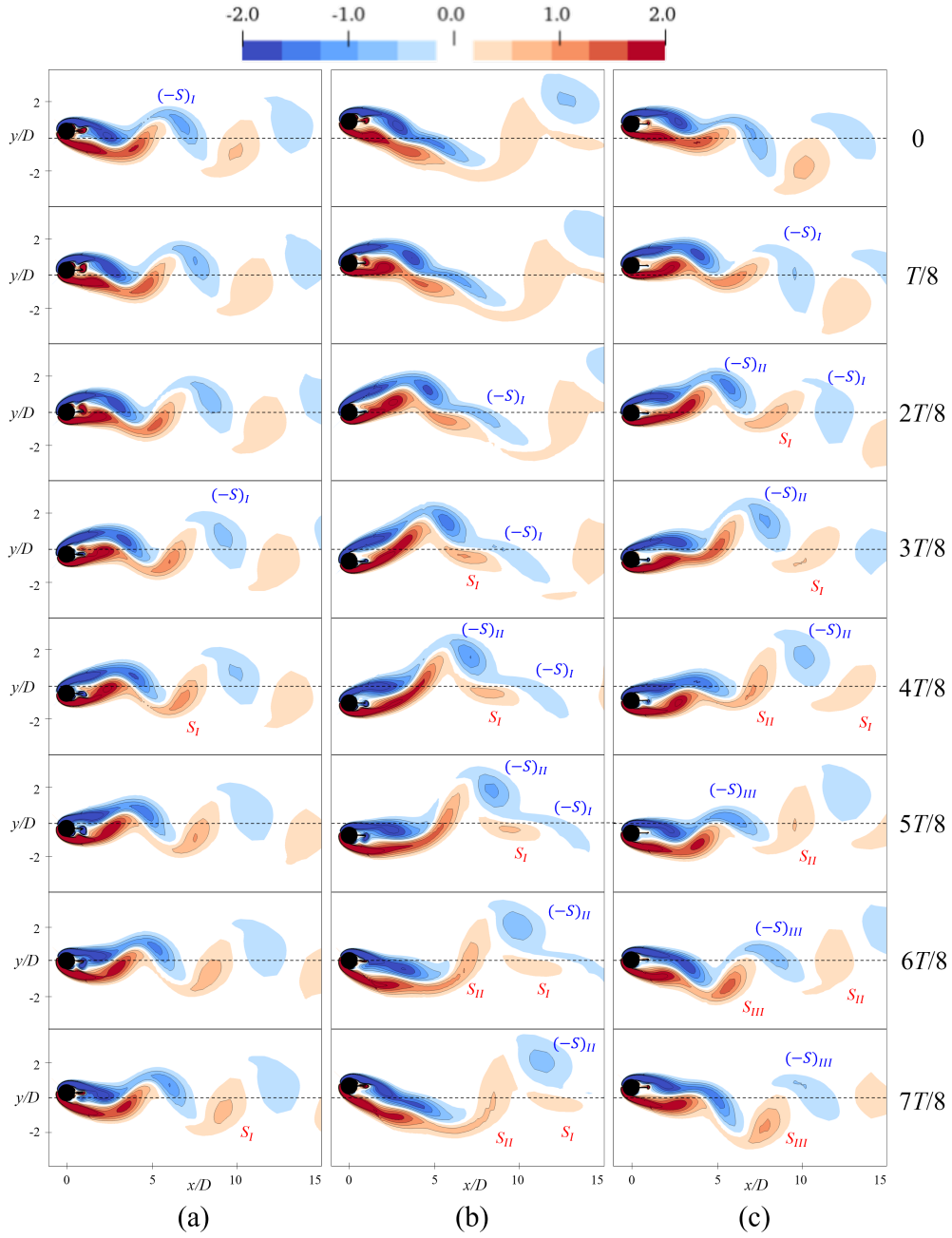


Figure 3.17: Instantaneous vorticity fields in one oscillation cycle T of a cylinder-plate assembly with $L_{SP}/D = 0.5$ at three $U_r =$ for three synchronizations: (a) $U_r = 6$ for 1:1; (b) $U_r = 11.5$ for 1:2; and, (c) $U_r = 19$ for 1:3. The corresponding wake modes are “2S”, “T+S” and “ $3 \times (2S)$ ”, respectively.

and S_{II}) are shed during one oscillation cycle, corresponding to the frequency ratio of 1:2. However, the vortex shedding pattern here is obviously asymmetric as shown in Fig. 3.17 (b). In particular, vortices $-S_I$ and $-S_{II}$ are connected and shed together with S_I , whereas S_{II} is shed separately. This pattern seems to be consistent with “T+S” (triplet and singlet) mode. Finally, at $U_r = 19$, the alternating vortex shedding manifests itself again, with the difference that the “2S” mode is repeated three times (viz., “ $3 \times (2S)$ ” to give six vortices in total)—which corresponds to the frequency ratio of 1:3 for this synchronization. Taken together, the flow information provides further support for the assertion that the cylinder-plate assembly with $L_{SP}/D = 0.5$ undergoes an integrated VIV-galloping response.

Group II: $L_{SP}/D = 0.75$

A freely-oscillating cylinder-plate assembly with $L_{SP}/D = 0.75$ is a *special* dynamical system, which corresponds to a boundary case—a assembly with a plate length less than or greater than the critical value of $0.75D$ exhibits self-limited or unlimited oscillations, respectively. As a result, the case of $L_{SP}/D = 0.75$ is in a group by itself as it is associated with the transition from two different oscillation modes.

The branching of the amplitude response and the PSD of the displacement and various transverse force coefficients are shown in Fig. 3.18. For this assembly, three distinct synchronization branches are identified in the galloping regime ($U_r \geq 6.5$), each of whose onset is signalled by the presence of a “kink” in the amplitude response—this is similar to the case of $L_{SP}/D = 0.5$. The first synchronization occurs in the narrow range $U_r = 11$ – 11.5 , which is associated with a dominant oscillation frequency $f_Y^*/f_n \approx 1$ (more precisely, slightly smaller than the structural natural frequency). The corresponding PSD of transverse force exhibits both odd and even high-order harmonics. The second synchronization occurs over the more extended range $U_r = 15$ – 20 , during which a weaker third-harmonic at $f_Y/f_n \approx 3$ is present in the PSD of Y (see Fig. 3.18 (b)). While the PSD of C_L is regular and structured—clearly containing only the odd-harmonics of the fundamental frequency at $f_{C_L}/f_n = 3, 5,$ and 7 . Of these odd harmonics, the third harmonic is the strongest while other higher components progressively diminish in strength. The third synchronization occurs around $U_r \approx 29$, and its dynamical characteristics are similar to that of the second branch—the main difference is that the fifth harmonic in the PSD of transverse force becomes stronger and is comparable to the third harmonic.

Another interesting feature that is easily overlooked is the presence of a secondary (weaker) oscillation in the amplitude response at around $U_r \approx 6$ with a maximum amplitude of only $0.05D$ —occurring just before the onset of galloping. The flow field analysis below will show that this small vibration is induced by the vortex shedding (viz., a VIV

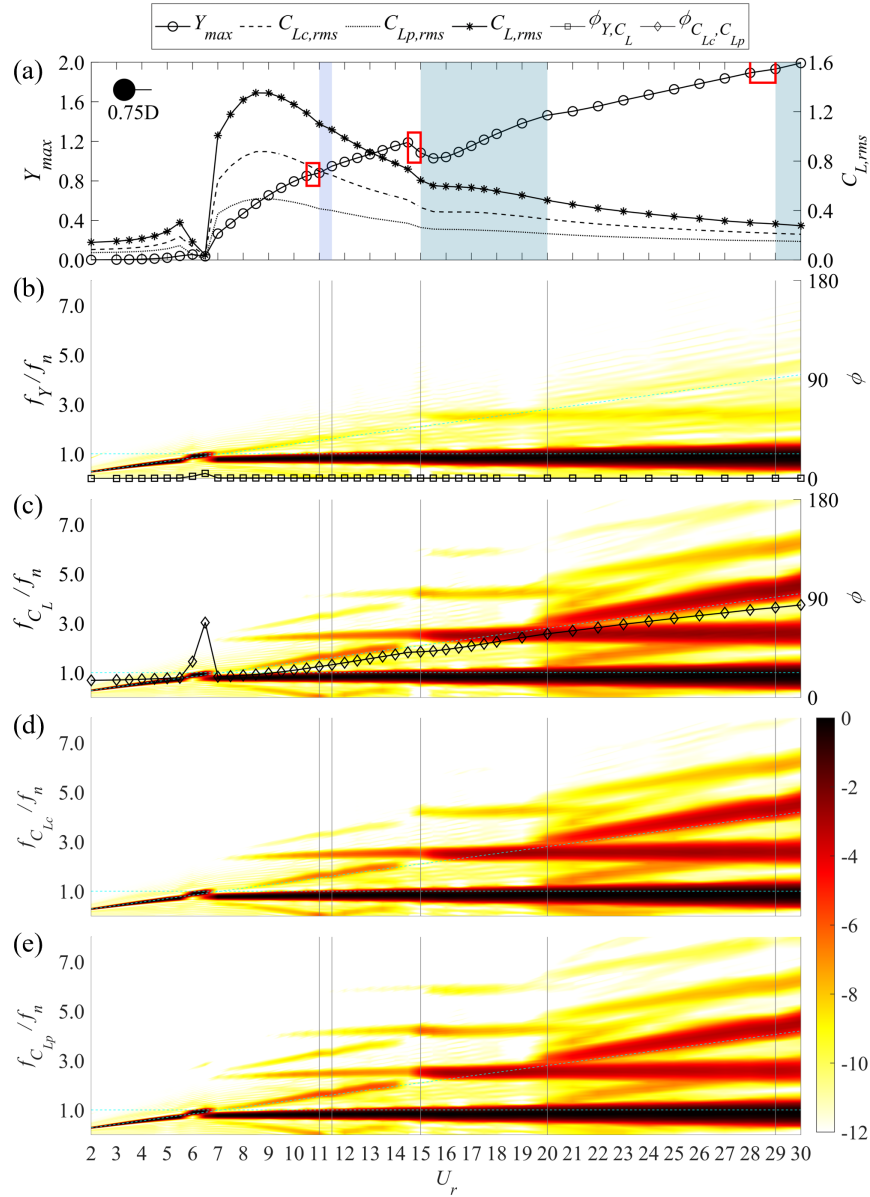


Figure 3.18: The branch identification of cylinder-plate assembly with $L_{SP}/D = 0.75$. The notations used here have been described in Fig. 3.15. The assembly undergoes an unlimited galloping response, with three synchronizations identified: namely, 1:2 at $U_r = 11-11.5$, 1:3 at $U_r = 15-20$ and 1:5 at $U_r = 29-30$. The onset of synchronization is signalled by a “kink” in the amplitude response.

response) that has not attained lock-in—more precisely, the oscillation frequency here is “synchronized” to the Strouhal frequency, rather than the natural frequency. In view of this, it is reasonable to treat this secondary oscillation as merely the initial stage of a VIV.

The dynamical features in the synchronization branch of the cylinder-plate assembly with $L_{SP}/D = 0.75$ are similar to those for $L_{SP}/D = 0.5$. The vortex shedding in the 1:2, 1:3 and 1:5 synchronization branches involve vortices shed alternately from one side of the assembly to the other—the pattern of this shedding has been identified as “ $2 \times (2S)$ ”, “ $3 \times (2S)$ ” and “ $5 \times (2S)$ ”, respectively. However, the wake pattern associated with 1:2 synchronization branch is asymmetric—this pattern is associated with the presence of an elongated and bent vortex.

Group III: $L_{SP}/D = 1-1.5$

The third group involves cylinder-plate assemblies with $L_{SP}/D = 1, 1.25$ and 1.5 . The most striking feature of this group is that the assemblies experience first a VIV lock-in regime (albeit with a very small amplitude over a narrow range of U_r) before the galloping onset, then an unlimited galloping regime (with vibration amplitude always increasing with U_r without apparent self-limiting mechanism). The cylinder-plate assembly with $L_{SP}/D = 1.5$ will be used as an exemplar for the analysis of the branching characteristics and synchronization properties for assemblies in this group.

As shown in Fig. 3.19 (a), the amplitude in the galloping regime increases smoothly and monotonically with U_r , except for the existence of several “kinks” in the amplitude curve (where the slope is discontinuous). The branch identification here suggests that the even- and odd-multiple synchronizations appear successively with increasing U_r with frequency ratios of 1:2, 1:3, 1:4, 1:5, 1:6, 1:7, and so forth. Moreover, the reduced velocity ranges associated with the even-multiple synchronizations are generally narrower than those associated with the odd-multiple synchronizations. Finally, we note that a “kink” in the amplitude response always signals the onset of a synchronization branch in the galloping regime.

In contrast to the case for $L_{SP}/D = 0.75$, a distinct lock-in regime is present before the galloping for the cases of $L_{SP}/D = 1, 1.25$, and 1.5 . Although the amplitude response here is only a small bump with a magnitude less than about $0.06D$, the response nevertheless embodies the major characteristics of VIV such as lock-in ($f_Y^* \approx f_n$) as well as a sudden phase shift between Y and C_L when out of lock-in (see panel (b) in Fig. 3.19). It is remarkable that in this lock-in branch, the oscillation frequency is not strictly locked on the natural frequency—rather, on a value that is slightly smaller (more precisely, $0.9f_n$).

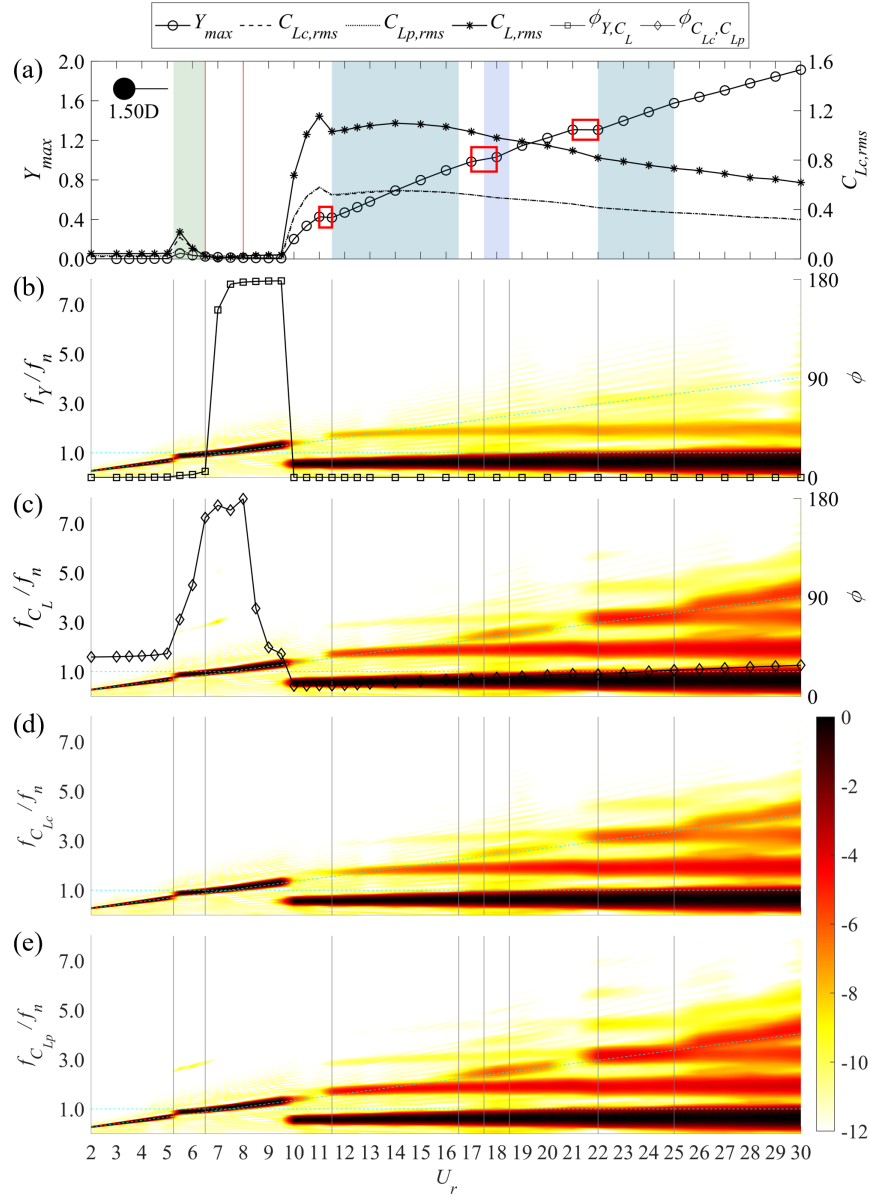


Figure 3.19: The branch identification of cylinder-plate assembly with $L_{SP}/D = 1.5$. The notations used here have been described in Fig. 3.15. Four synchronizations have been identified: namely, one lock-in branch (1:1 at $U_r = 5.25-6.5$) and three galloping synchronizations (beginning with a “kink”)—1:3 at $U_r = 11.5-16.5$, 1:4 at $U_r = 18$, and 1:5 at $U_r = 22-25$. The lift components C_{Lc} and C_{Lp} are out-of-phase at $U_r = 6.5-8$.

This is a so-called “soft lock-in” in the terminology of Darbhamulla and Bhardwaj [34]. For simplicity, hereinafter, we will still use “lock-in” to refer to this case.

The wake modes in the 1:1, 1:3, 1:4 and 1:5 synchronization branches are “2S”, “3×(2S)”, “4×(2S)” and “5×(2S)”, respectively. These wake modes are associated with regular elliptically-shaped vortices shed alternately from one side to the other of the assembly.

Group IV: $L_{SP}/D = 1.75-2$

The fourth group is for $L_{SP}/D=1.75$ and 2, in which the transverse force responsible for VIV at small reduced velocity increases dramatically, which leads to an earlier onset of VIV at around $U_r = 3-4$ and a wider lock-in range. A comprehensive analysis of the branching behavior and the wake modes in the synchronizations for this group of assemblies is provided for the cylinder-plate assembly with $L_{SP}/D = 2$.

As shown in Fig. 3.20, five synchronizations are identified for assembly with $L_{SP}/D = 2$, namely, 1:1 at $U_r = 3.5-7$, 1:3 at $U_r = 12-18$, 1:5 at $U_r = 19-20$, 1:6 at $U_r = 24$, and 1:7 at $U_r = 27-29$.

Figure 3.21 further exhibits the temporal evolution of the instantaneous vorticity over one oscillation cycle at time intervals of $T/12$ for the assembly with $L_{SP}/D = 2$. It is evident that the wake mode and vortex shape in the lock-in regime are different from those in the galloping synchronizations. The former is characterized by a “2S” mode and elliptical vortices. While the latter exhibits “ $n \times (2S)$ ” wake mode where n is determined by the frequency ratio $f_{C_L}^*/f_Y^*$, namely, $n = 3, 5, 6,$ and 7 at $U_r = 17, 19, 24,$ and 28 , respectively. Furthermore, it is seen that the shear layers around the oscillating assembly are significantly extended in the streamwise direction and the vortices shed downstream of the obstacle have markedly irregular shapes—this is particularly evident at $U_r = 17$ where the crescent-shaped vortices S_{III} and $-S_I$ and vortices S_{II} and $-S_{III}$ in the shape of a quasi-parallelogram (due to the drag with the front and back vortices) are clearly seen. All the wake modes in Fig. 3.21 are anti-symmetric.

Some new dynamical features emerge for the cylinder-plate assemblies in Group IV. Firstly, the VIV onset occurs at a smaller value of $U_r \approx 3.5$ and the lock-in range is widened to $U_r \approx 3.5-7$ —the vibration amplitudes in this range increase to about $0.2D$. These features are related to the sudden increase of the transverse force C_L on the assemblies up to 2.0 (significantly larger than the value of 0.2 observed for previous cases) in the VIV regime. Secondly, the range of U_r where the phase between C_{Lc} and C_{Lp} is significantly out-of-phase becomes wider. Moreover, the quasi-steady regime associated with very small (practically zero) oscillations in the amplitude response is narrower than the U_r range corresponding

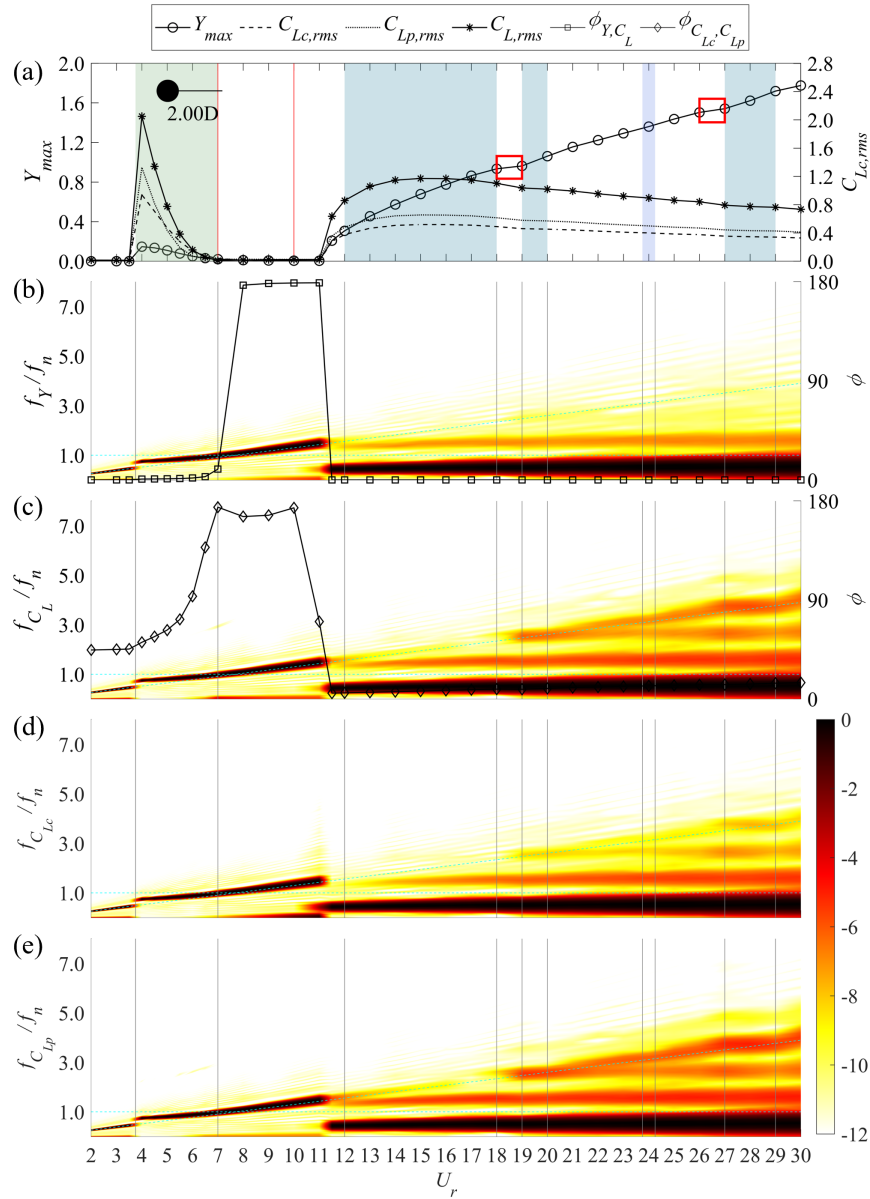


Figure 3.20: The branch identification of cylinder-plate assembly with $L_{SP}/D = 2$. The notations used here have been described in Fig. 3.15. Five synchronizations are identified: namely, one lock-in (1:1 at $U_r = 3.5-7$) and four galloping synchronizations—1:3 at $U_r = 12-18$, 1:5 at $U_r = 19-20$, 1:6 at $U_r = 24$, and 1:7 at $U_r = 27-29$. Only 1:5 and 1:7 synchronizations are signalled by a “kink” in the amplitude response. The lift components C_{Lc} and C_{Lp} are out-of-phase at $U_r = 7-10$.

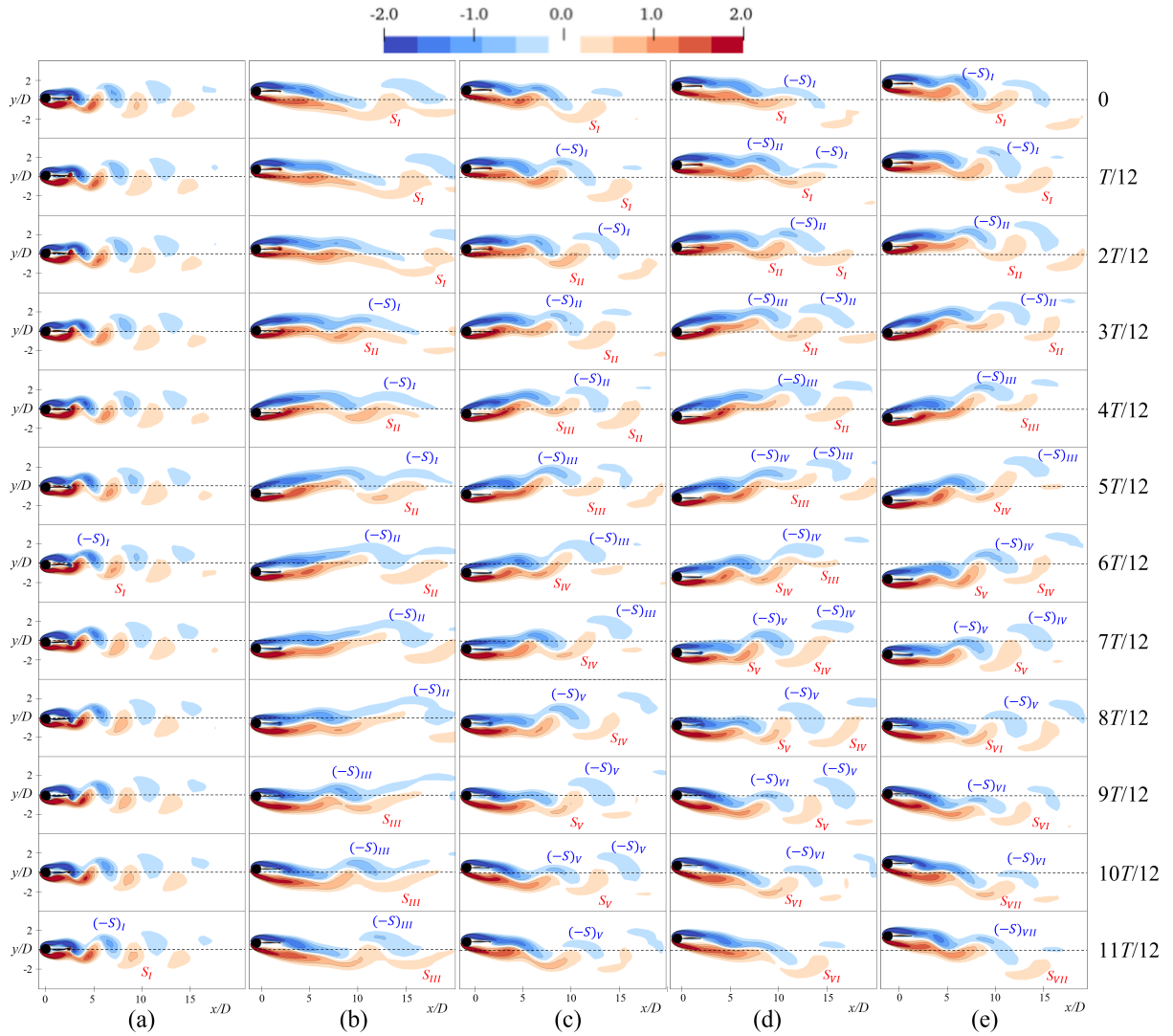


Figure 3.21: Instantaneous vorticity fields in one oscillation cycle T of a freely-vibrating cylinder-plate assembly with $L_{SP}/D = 2$ at five reduced velocities for five synchronizations: (a) $U_r = 4$ for 1:1; (b) $U_r = 17$ for 1:3; (c) $U_r = 19$ for 1:5; (d) $U_r = 24$ for 1:6; and, (e) $U_r = 28$ for 1:7. The corresponding wake modes are “2S”, “ $3 \times (2S)$ ”, “ $5 \times (2S)$ ”, “ $6 \times (2S)$ ” and “ $7 \times (2S)$ ”, respectively.

to the region where the phase ϕ between C_{Lc} and C_{Lp} is significantly out-of-phase for the Group IV assemblies. This is different from the Group III where the width of the quasi-steady regime is equal to the width in the U_r range where ϕ is significantly different than zero (out-of-phase condition). Thirdly, a 1:3 synchronization that occurs immediately after the galloping onset and the unsynchronized regime where the characteristic frequency for the transverse displacement and transverse force are equal (present in the Groups II and III) is absent in the Group IV. Finally, the number of “kinks” in the amplitude response is decreased for the Group IV because these “kinks” do not necessarily signal the onset of each synchronization in the galloping regime, which is not the case for the Groups II and III. The reasons for this will be explored in Section 3.4.3.

Group V: $L_{SP}/D = 2.5\text{--}4$

The last group (Group V) concerns cylinder-plate assemblies with $L_{SP}/D = 2.5\text{--}4$. In this group, two new branches in the amplitude response emerge that have not been seen (or reported) previously—namely, the still (quiescent) branch and the initial galloping branch. The former emerges at either very small reduced velocity before the VIV onset or at larger U_r in the region corresponding to VIV lock-out but before the galloping onset, during which both the structure and flow are perfectly “still” (quiescent)—a term that we use to describe the situation where the cylinder-plate assembly is not moving (so, $Y = 0$) and the flow field does not exhibit any wake dynamics (e.g., vortex shedding). In contrast, the flow dynamics in the initial galloping branch is enhanced immediately after the onset of galloping—here the structure oscillation is associated with a new fluid phenomenon known as *wake meandering*.

Figure 3.22 shows that the cylinder-plate assembly with $L_{SP}/D = 2.5$ has various synchronizations, including a VIV branch, an initial galloping branch and three odd-multiple synchronizations. In comparison, the assemblies with longer plate lengths only have an initial galloping branch ($L_{SP}/D = 3\text{--}3.5$) or a VIV branch ($L_{SP}/D = 4$) at least for $U_r \leq 30$. Owing to its rich response characteristics, the case of $L_{SP}/D = 2.5$ is taken as the example for the analysis of assemblies in Group V.

Figure 3.23 displays the temporal variations of flow field associated with the cylinder-plate assembly with $L_{SP}/D = 2.5$ at four representative values of the reduced velocity: namely, at $U_r = 4, 19, 23$ and 25 selected from the VIV branch and three galloping synchronizations (1:3, 1:5 and 1:7). The vorticity fields display obvious differences in the dynamics of the assembly with $L_{SP}/D = 2.5$ compared to those with shorter plate lengths. For example, for the 1:3 and 1:5 synchronizations, the closely-connected vortices downstream of the assembly have a more elongated shape in the streamwise direction and

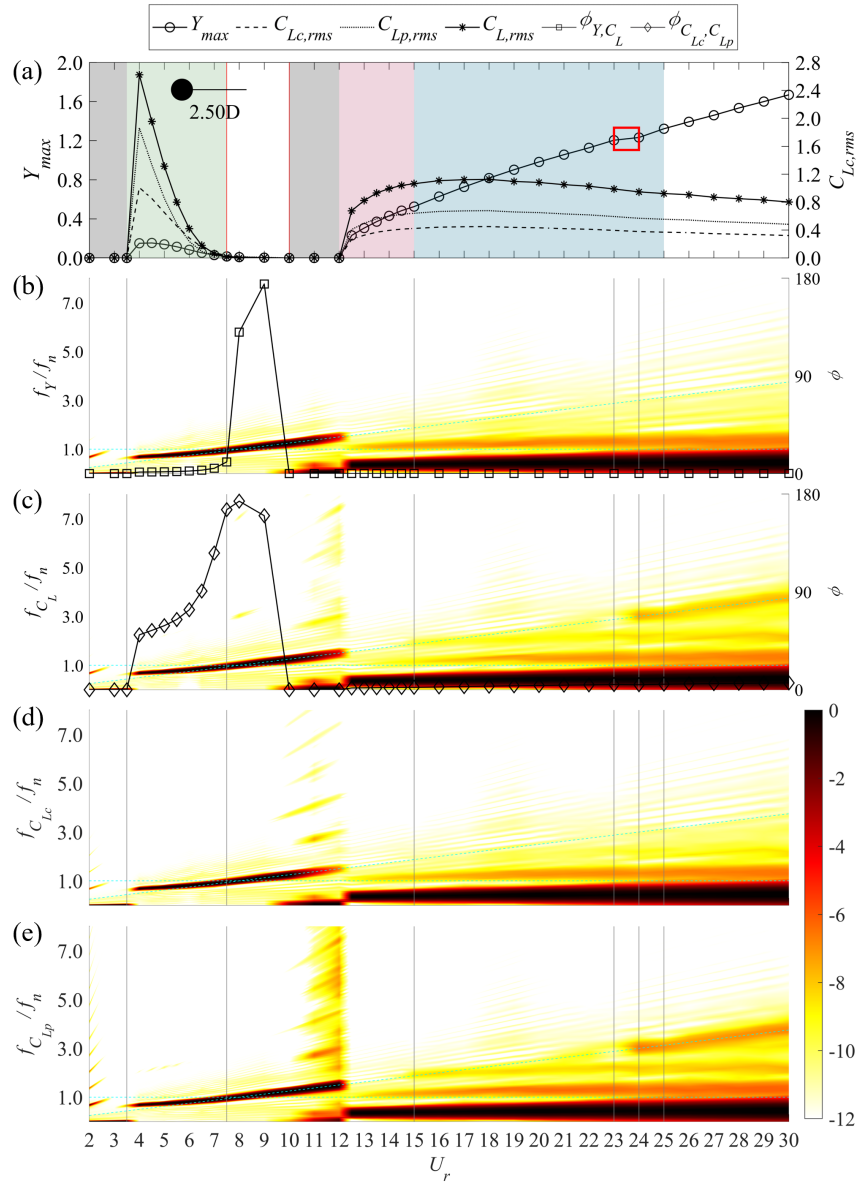


Figure 3.22: The branch identification of cylinder-plate assembly with $L_{SP}/D = 2.5$. The notations used here have been described in Fig. 3.15. An initial galloping branch (pink vertical strip) is identified at $U_r = 12$ – 15 . A still branch (gray vertical strip) is identified at $U_r = 2$ – 3.5 and 10 – 12 . Four synchronizations are identified: namely, one lock-in (1:1) at $U_r = 3.5$ – 7.5 and three galloping synchronizations—1:3 at $U_r = 15$ – 23 , 1:5 at $U_r = 23$ – 24 , and 1:7 at $U_r = 24$ – 25 . Only the 1:5 synchronization is signalled by a “kink” in the amplitude response. The lift components C_{Lc} and C_{Lp} are out-of-phase at $U_r = 7.5$ – 10 .

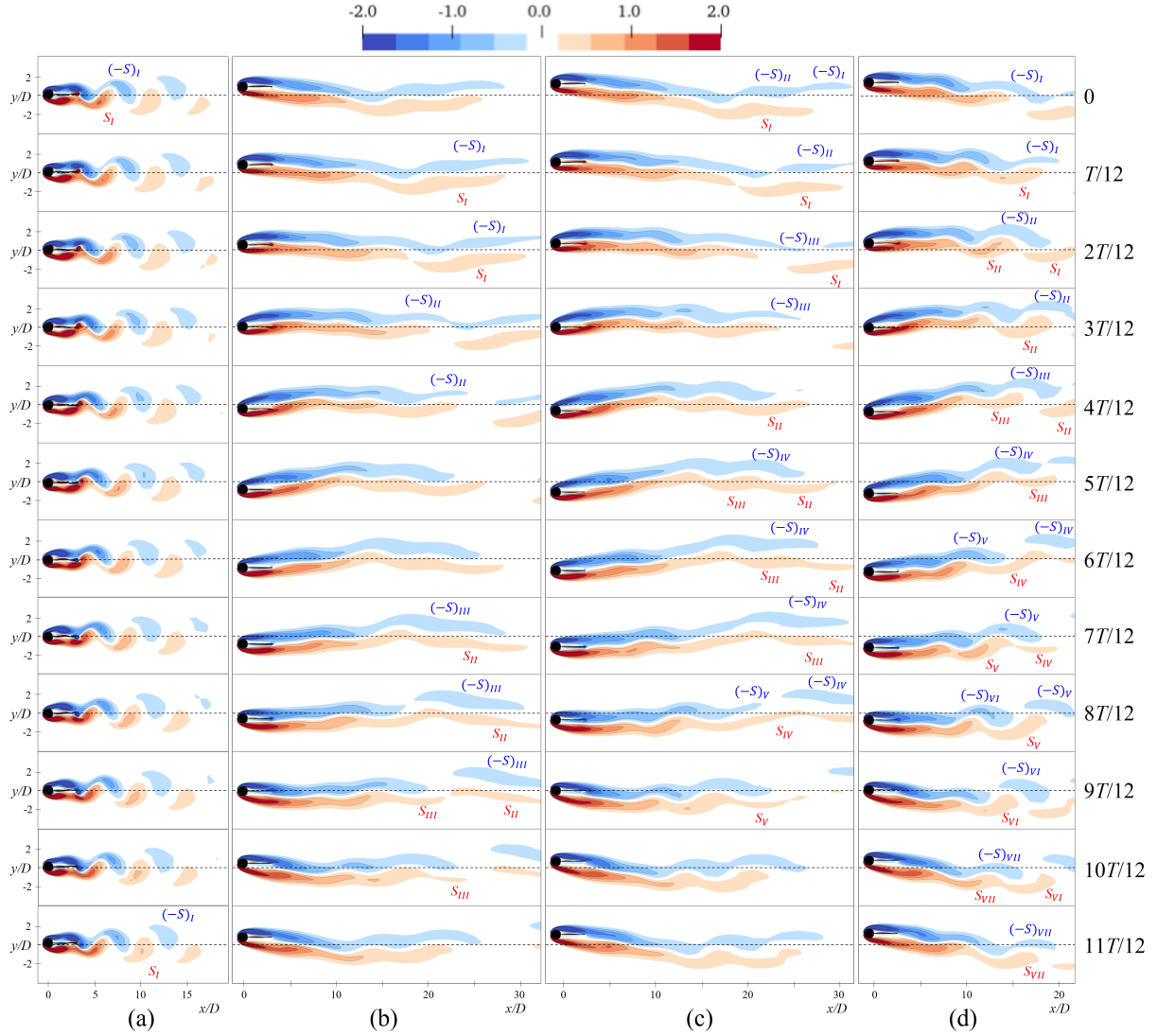


Figure 3.23: Instantaneous vorticity fields in one oscillation cycle T of cylinder-plate assembly with $L_{SP}/D = 2.5$ at four reduced velocities for four synchronizations: (a) $U_r = 4$ for 1:1; (b) $U_r = 19$ for 1:3; (c) $U_r = 23$ for 1:5; and, (d) $U_r = 25$ for 1:7. The wake modes for the first two cases are “2S” and “ $2 \times (P+S)$ ”, respectively. There is no identifiable wake pattern for the third case. For the fourth case, the associated wake pattern is “ $7 \times (2S)$ ”.

these vortices are shed in the far-wake region. Moreover, there are six and ten vortices shed in total at $U_r = 19$ and $U_r = 23$, respectively, although sometimes this fact is not easy to discern owing to the large number of oscillating shear layers that are detached from the structure in an unbroken succession. With this caveat, a careful perusal of Fig. 3.23 yields the following identification of the vortex shedding modes. The wake mode at $U_r = 19$ is “ $2 \times (\text{P}+\text{S})$ ”, rather than “ $3 \times (2\text{S})$ ”, with $(-\text{S}_I, \text{S}_I)$ being one pair (P) of vortices that are shed together followed by a single (S) vortex $-\text{S}_{II}$, whereas $(-\text{S}_{III}, \text{S}_{II})$ and S_{III} are shed as the second (P+S) pair. For $U_r = 23$ in Fig. 3.23 (c), the wake mode appears to be rather complicated with no clear-cut pattern. More specifically, it is suggested here that two continuous vortices $-\text{S}_I$ and $-\text{S}_{II}$ appear to lead to a triplet (T) vortex shedding with S_I , and a similar pattern applies to $(-\text{S}_{IV}, \text{S}_{II}, \text{S}_{III})$. The other smaller vortices (e.g., $-\text{S}_{III}$ and S_{IV}) have no clear-cut (unambiguously identifiable) vortex shedding pattern. At $U_r = 25$ in Fig. 3.23 (d), the wake pattern is easily identifiable again as a “ $7 \times (2\text{S})$ ” mode.

Précis

Table 3.5 summarizes the key takeaways of this section in terms of the various synchronizations and their corresponding reduced velocity ranges for cylinder-plate assembly with $L_{SP}/D = 0$ to 4 at $2 \leq U_r \leq 30$.

3.4.2 Mechanism Analysis

Although the effect of the splitter-plate length on the branching behavior of the cylinder-plate assembly, as well as on the dynamic characteristics in the synchronization branches of the amplitude response, have been analyzed in detail in Section 3.4.1, a number of aspects related to the physical mechanisms responsible for these characteristics have not been resolved. These unresolved issues are the focus of this section.

Group I: $L_{SP}/D = 0-0.5$

A careful perusal of the branching behavior for the cylinder-plate assemblies in Group I ($L_{SP}/D = 0-0.5$) raises a number of questions. To address these questions, we analyze the flow field in greater detail.

Firstly, *why is the VIV regime of a circular cylinder significantly widened when we attach even a short splitter-plate of length $L_{SP}/D = 0.25$ to the cylinder?* To answer this question, Fig. 3.24 zooms in on the vorticity field in the immediate region around the

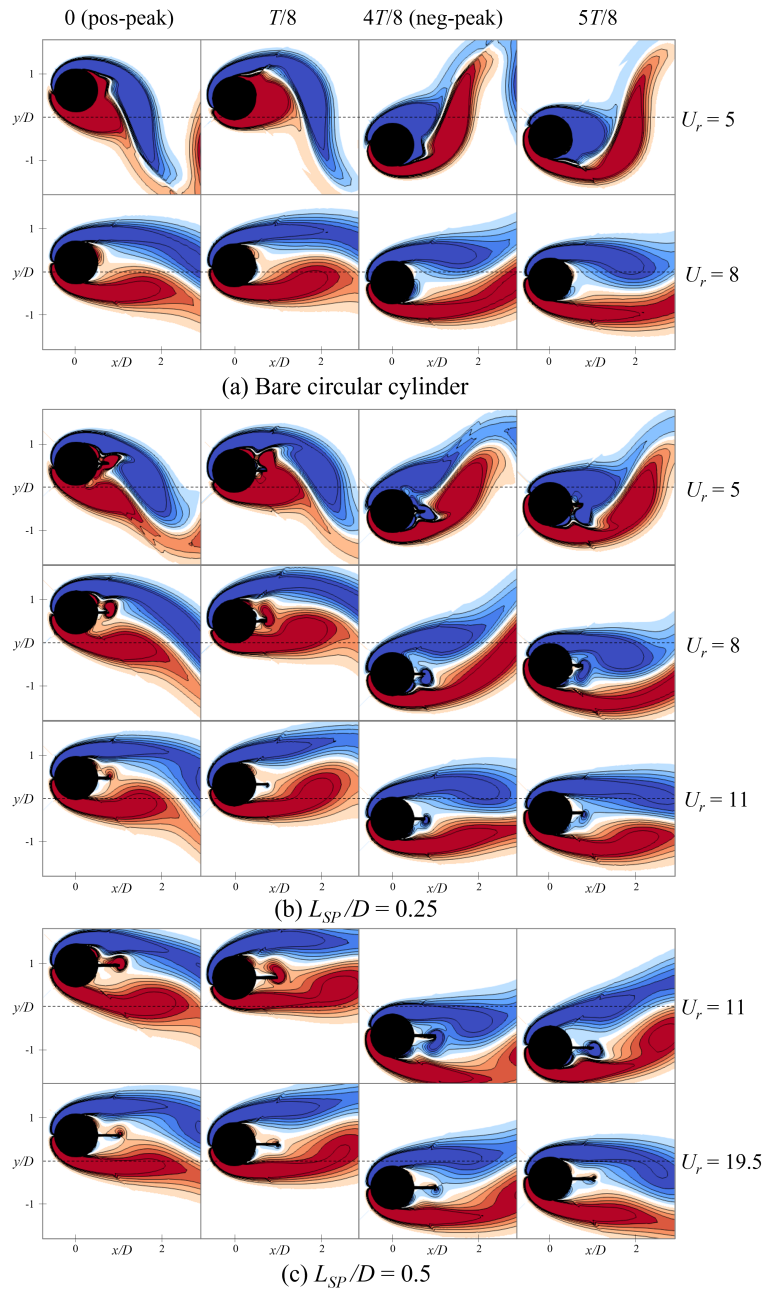


Figure 3.24: Instantaneous interaction between the shear layers and the vortex behind moving body: (a) circular cylinder at $U_r = 5$ and 8; (b) assembly with $L_{SP}/D = 0.25$ at $U_r = 5, 8, 11$; and, (c) assembly with $L_{SP}/D = 0.5$ at $U_r = 11, 19.5$. Snapshots are obtained at oscillation maxima ($t = 0$ and $T/8$) and minima ($t = 4T/8$ and $5T/8$).

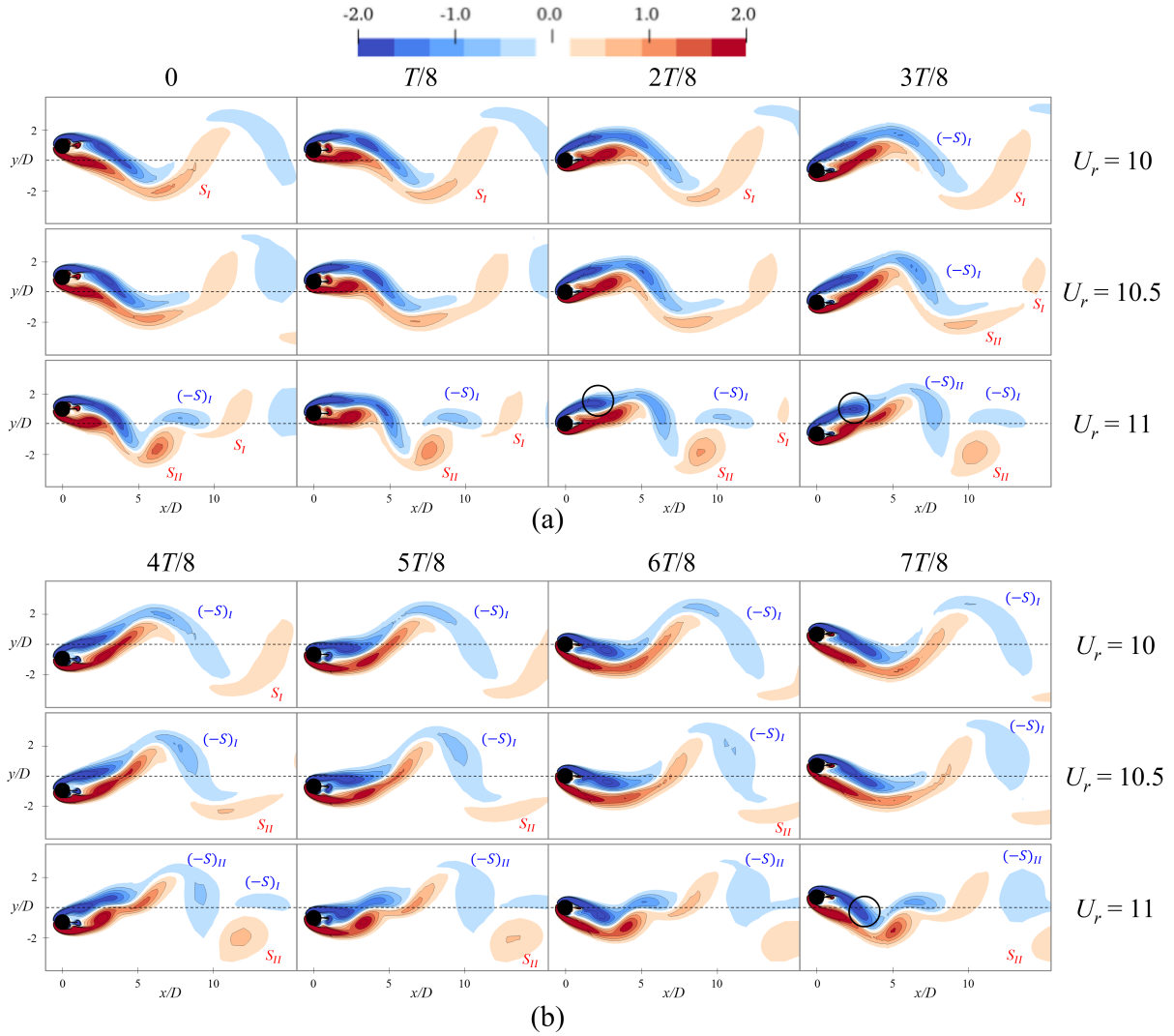


Figure 3.25: Vortex shedding mode in the range of reduced velocities that are close to the transition from VIV to galloping for cylinder-plate assembly with $L_{SP}/D = 0.5$. An oscillation cycle is divided into the (a) first and (b) second halves of the cycle. At $U_r = 10$, VIV response corresponds to a “2S” wake mode. At $U_r = 10.5$, three vortices are shed in total, whereas at $U_r = 11$, a galloping response is triggered with “ $2 \times (2S)$ ” wake mode.

Table 3.5: Summary of branching (synchronization) behaviors for cylinder-plate assemblies for $L_{SP}/D = 0-4$.

L_{SP}/D	1:1	1:2	1:3	1:4	1:5	1:6	1:7	SB ¹	IGB ²
bare	4.5–8.5	/	/	/	/	/	/	/	/
0.25	5–10.5	/	/	/	/	/	/	/	/
0.50	5.5–10	11–11.5	19–19.5	/	/	/	/	/	/
0.75	/	11–11.5	15–20	/	29–30	/	/	/	/
1.00	5.75–6.5	10–10.5	14–19	~21	26–28	/	/	/	/
1.25	5.25–6.5	/	12.5–18	19–20	23–26	/	/	/	/
1.50	5.25–6.5	/	11.5–16.5	~18	22–25	/	/	/	/
1.75	3.5–6.5	/	11–14	~17	20–22	/	29–30	/	/
2.00	3.5–7	/	12–18	/	19–20	~24	27–29	/	/
2.50	3.5–7.5	/	15–23	/	23–24	/	24–25	2–3.5, 10–12	12–15
3.00	4–9	/	/	/	/	/	/	2–4, 9–13	13–30
3.50	3.5–8.5	/	/	/	/	/	/	2–3.5, 8.5–18	18–30
4.00	4–8.5	/	/	/	/	/	/	2–4, 8.5–30	/

1. SB represents the still branch.
2. IGB represents the initial galloping branch.

free-vibrating bare circular cylinder and the cylinder-plate assembly with the objective of understanding how the flow is modified by the presence of the splitter-plate and on how the shear layer evolves as a function of the reduced velocity. The exhibited results are for those time instants close to the oscillation maxima and minima (viz., $t = 0$ and $T/8$ around $+Y_{max}$, $t = 4T/8$ and $5T/8$ around $-Y_{max}$). A perusal of Fig. 3.24 (a) shows that the vortex behind the bare circular cylinder at $U_r = 5$ has completely merged with the shear layer of the same sign (viz., positive vortex (red) around $+Y_{max}$ and negative vortex (blue) around $-Y_{max}$). However, at $U_r = 8$, the system oscillations are small—in this case, the slender shear layers generated by the high velocity have little or no contact with the vortices shed by the cylinder. In contrast, for the assembly with $L_{SP}/D = 0.25$ shown in Fig. 3.24 (b), it is seen that at $U_r = 8$, a vortex is formed at the tip of splitter plate and interacts strongly with the shear layers—this interaction sustains the oscillation of the assembly at U_r value at which the bare cylinder is nearly stationary. As U_r increases

further to 11, the shear layers become so elongated that the $0.25D$ splitter plate cannot interact with them any longer and the size of the tip vortex becomes much smaller, yielding a small-amplitude oscillation and a transition out of lock-in. Therefore, the attachment of a splitter plate of length $0.25D$ to the cylinder ensures a stronger interaction between the tip vortex and the shear layers at larger values of U_r , and for this reason the VIV regime is extended significantly to the range $U_r = 4.5\text{--}12$. Similarly, the reduced velocity range for the body oscillation is extended to $U_r = 5\text{--}20$ for the assembly with $L_{SP}/D = 0.5$ (albeit the oscillation amplitude is still limited) as shown in Fig. 3.24 (c).

Secondly, *why does a galloping regime emerge when we attach a splitter-plate of length $L_{SP}/D = 0.5$ and why does the observed galloping here occur only over a limited reduced velocity range?* In view of the fact that a large vortex-shedding frequency is a characteristic feature of the galloping regime, Fig. 3.25 displays the vortex mode over one oscillation cycle for three values of U_r (viz., $U_r = 10, 10.5$ and 11). These values of U_r are close to the transition from VIV to galloping. For $U_r = 10$, the VIV regime is associated with a “2S” mode—however, the vortices shed here are more slender in shape compared to the more elliptically-shaped vortices shed from this assembly at lower $U_r = 6$ (cf. Fig. 3.17 (a)). Furthermore, for $U_r = 10.5$, the one large vortex system generated near the body splits into two smaller vortices as it evolves downstream. Consequently, three vortices are shed in total during one oscillation cycle. Finally, for $U_r = 11$, the wake mode is “ $2 \times (2S)$ ”, which is associated with galloping.

Thirdly, *why does the number of vortices shed during one oscillation cycle increase with U_r ?* To address this question, let us focus on the first half of the cycle shown in Fig. 3.25 (a). A counter-clockwise slender vortex S_I is shed in the wake at $U_r = 10$ —this shape of vortex is more likely to break up into multiple smaller vortices compared to an elliptically-shaped vortex. At $U_r = 10.5$, this vortex (which has a distinct bent shape) is composed of two parts—namely, a horizontal and vertical part evident at $t = 0$ to $2T/8$ and these two parts break apart into two smaller vortices (S_I and S_{II}) at $t = 3T/8$. At $U_r = 11$, the highly-bent (deformed) shape of the upper shear layer breaks apart into the two vortices S_I and S_{II} —as a result, these vortices are more separated than those at $U_r = 10.5$. The second half of the oscillation cycle is exhibited in Fig. 3.25 (b)—the corresponding vortical structures are the mirror reflection (about a horizontal axis) of those in Fig. 3.25 (a). Given this, it appears that a higher inflow velocity tends to accelerate the growth of shear layers in the streamwise direction which facilitates the “piling” up of the vorticity at the downstream terminus of the shear layers (delineated by the black circles in Fig. 3.25). This “piling up” of the vorticity causes the shear layers to bend. When two bent shear layers interact and develop downstream, vortices are generated and shed from the layers more readily.

Groups II and III: $L_{SP}/D = 0.75-1.5$

Although the cylinder-plate assembly with $L_{SP}/D = 0.75$ (Group II) undergoes only an initial VIV (without lock-in) at a small U_r , it nevertheless undergoes unlimited galloping at higher U_r and, as a result, has similar branching behavior as those with $L_{SP}/D = 1-1.5$ (Group III). Here, we provide an in-depth discussion concerning several fundamental aspects of the dynamics observed in Groups II and III.

One intriguing aspect of the dynamics of assemblies in Groups II and III is the following puzzle: *why is the VIV occurring at low U_r suppressed before the eventual onset of galloping, rather than there being a smooth transition from VIV to galloping as for the assembly with $L_{SP}/D = 0.5$?* From a more careful analysis of the dynamics of assemblies belonging to Groups II and III, it is suggested that this behavior is the result of a rapid increase in the phase difference ϕ between the two transverse force components acting on the cylinder (C_{Lc}) and on the splitter plate (C_{Lp}). From a careful examination of the solid lines marked by diamonds in Fig. 3.19 (c), it is seen that ϕ increases rapidly once VIV occurs—which, in turn, results in a decreasing total transverse force on the vibrating assembly, thus suppressing the occurrence of strong VIV. More precisely, when $\phi \approx 180^\circ$ (out-of-phase), the total force acting on the assembly is near zero. As a consequence, VIV is almost completely suppressed—indeed, the assembly exhibits only very small oscillations (with an amplitude of only about $0.02D$). This phase reversal from 0° (in-phase) to 180° (out-of-phase) occurs over a small range of U_r (delineated using the two vertical red lines in Fig. 3.19 (a)). At the end of this U_r range, ϕ sharply decreases back to 0° with increasing U_r , at which point the galloping occurs. At this point, the total transverse force acting on the assembly increases rapidly, provoking galloping. Within the galloping regime, ϕ increases slowly with U_r , but never exceeds 90° .

Another question is *why does the galloping onset become larger when attaching longer splitter-plate?* The quasi-steady regime in the amplitude response that occurs after the suppression of VIV and before the galloping onset is of $\phi \approx 180^\circ$ or of ϕ decreasing towards 0° . It is worth noting that the quasi-steady region (e.g., $U_r = 8-9.5$ for $L_{SP}/D = 1.5$ in Fig. 3.19) correlates exactly with the region where C_{Lc} and C_{Lp} are increasingly out-of-phase. Furthermore, the U_r range corresponding to the quasi-steady regime increases with plate length—hence, the galloping onset is delayed to larger values of U_r with increasing plate length following the cessation of VIV.

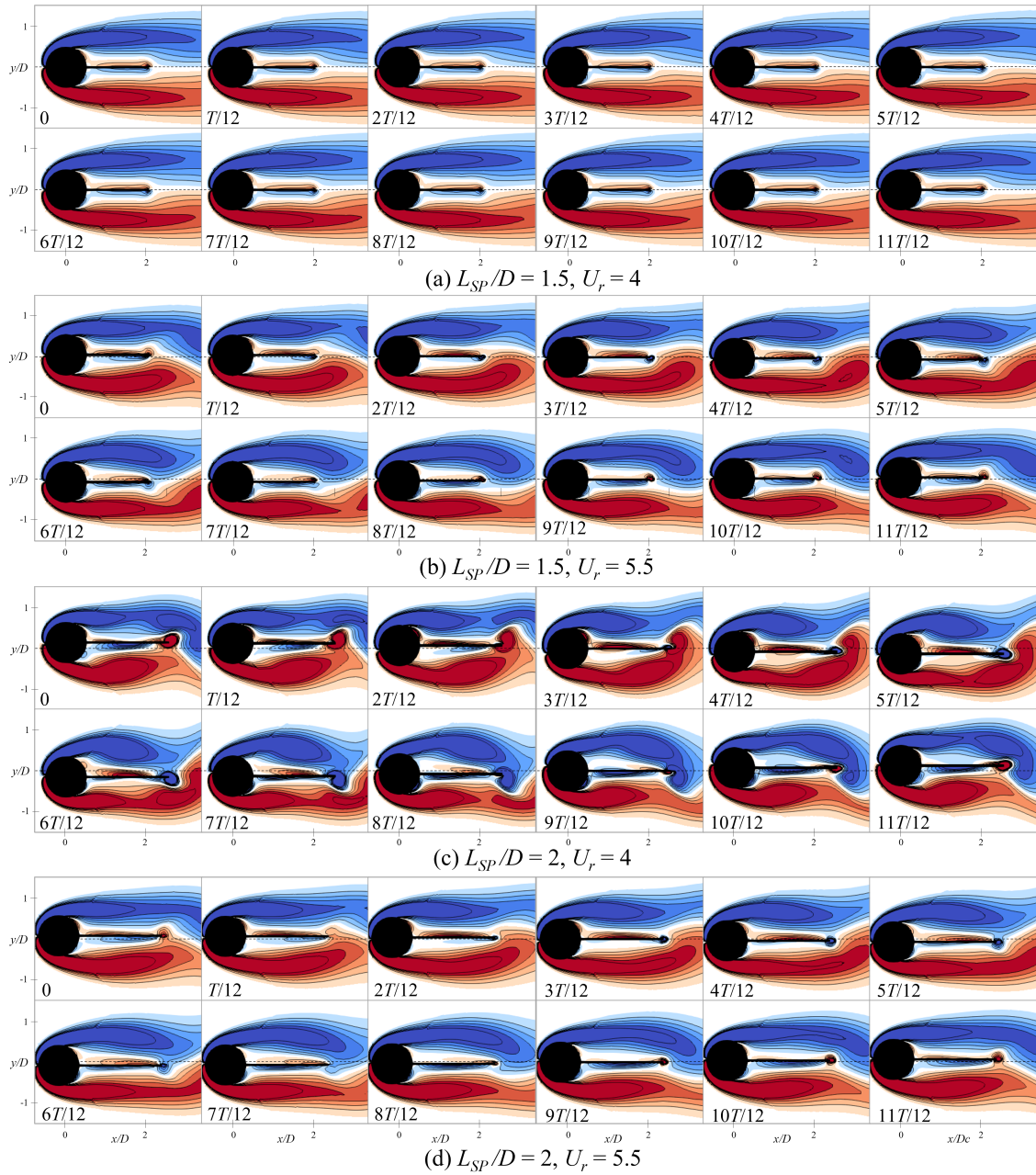


Figure 3.26: Temporal evolution of instantaneous shear layers around a cylinder-plate assembly over one oscillation cycle at a time interval of $T/12$: (a) $L_{SP}/D = 1.5$ at $U_r = 4$; (b) $L_{SP}/D = 1.5$ at $U_r = 5.5$; (c) $L_{SP}/D = 2$ at $U_r = 4$; and, (d) $L_{SP}/D = 2$ at $U_r = 5.5$. Both values of U_r correspond to the VIV branch. The positive and negative peaks in the cycle occur at time $t = 0$ and $t = 6T/12$, respectively.

Groups IV: $L_{SP}/D = 1.75\text{-}2$

As mentioned in Section 3.4.1, the most striking feature of the cylinder-plate assembly in Group IV is the presence of a strong transverse force which induces the secondary VIV responses. To examine this phenomenon in greater detail, it is useful to study the formation and evolution of the shear layers that are generated around the assembly. To this purpose, Fig. 3.26 displays the comparison of the dynamical evolution of the shear layers formed around a bare circular cylinder and two cylinder-plate assemblies (with $L_{SP}/D = 1.5$ and 2) undergoing small VIV at low reduced velocity. More precisely, the assembly with $L_{SP}/D = 1.5$ is quasi-stationary at $U_r = 4$ and exhibits only a very small oscillation amplitude of $Y_{max} = 0.06D$ with a small lift coefficient of $C_{L,rms} = 0.2$ at $U_r = 5.5$ (see Fig. 3.19). In stark contrast, for the assembly with $L_{SP}/D = 2$, the oscillation amplitude $Y_{max} = 0.15D$ is about three times as large and the lift coefficient of $C_{L,rms} = 2$ is ten times as large at $U_r = 4$ (see Fig. 3.20).

A perusal of Figs. 3.26 (a) and (c) shows that at $U_r = 4$, increasing the plate length from $1.5D$ to $2D$ results in a stronger flow in the near wake involving the generation of a tip vortex (at the free end of the plate)—this vortex merges with the shear layers and with vortices shed from these shear layers owing to the fact that the longer plate is more likely to interact with the to-and-fro motion of the shear layers that “lift off” (partial detach) from the cylinder surface downstream of the obstacle. By contrast, the plate length of $L_{SP}/D = 1.5$ is too short to interact significantly with these shear layers, so the wake field is almost steady. At an increased value of $U_r = 5.5$, both splitter plates only interact weakly with the shear layers—a similar vorticity field is generated here but for a different reason. A larger value of the incident flow facilitates the bending of the shear layers and the vortices shed from these layers, so a shorter plate length $L_{SP}/D = 1.5$ can interact with these aspects of the flow to induce a small oscillation on the assembly (see Fig. 3.26 (b)). On the other hand, for an assembly with $L_{SP}/D = 2$, the total transverse force decreases rapidly after the VIV onset because of the increasing phase difference between C_{Lc} and C_{Lp} (e.g., $\phi \approx 90^\circ$ at $U_r = 5.5$) which, in turn, results in smaller system oscillations (cf. Fig. 3.26 (d)). The key takeaway of this analysis is that the inclusion of a splitter plate with a length greater than or equal to $1.75D$ can induce strong interactions between the plate tip vortex and the shear layers formed around the structure at the lower values of U_r . This physical mechanism generates large transverse force on the cylinder-plate assembly which is responsible for the stronger secondary oscillations with a wider VIV branch and an earlier onset.

Finally, it is noted that the larger transverse force on the cylinder-plate assembly with $L_{SP}/D \geq 1.75$ induces a relatively small VIV motion with an amplitude of only one-third

($Y_{max} = 0.2D$) that for the assemblies with $L_{SP}/D = 0-0.5$ ($Y_{max} = 0.6D$). The reason for this may stem from the fact that a cylinder with a much longer splitter-plate requires a much larger driving force in order to sustain the oscillation.

Group V: $L_{SP}/D = 2.5-4$

For assemblies in Group V, we focus on the emergence of the still branch and initial galloping branch.

To begin, it is important to state the differences between the still branch and the quasi-steady regime. These differences can be seen from an examination of the time series of Y and C_L and of the instantaneous vorticity field as shown in Fig. 3.27. With reference to Figs. 3.19 and 3.20, the reduced velocity ranges before VIV onset and after VIV lock-out, but before the galloping onset, are referred to as the quasi-steady regime. As shown in Fig. 3.27 (a), the amplitudes of $Y(t)$ and $C_L(t)$ gradually increase with time and reach (attain) a stable periodic motion (albeit with approximately—but not exactly—zero transverse displacement and a transverse force of $\approx 10^{-4}-10^{-2}$) after a certain interval of time. Moreover, the meandering of the shear layers promotes vortex shedding, especially at larger reduced velocity (e.g., $U_r = 10$). Here, the vortices are expected to be generated and shed earlier, resulting in larger magnitudes of $Y(t)$ and $C_L(t)$, compared to those at lower reduced velocity (e.g., $U_r = 3$). By contrast, the still branch is associated with very different time series variations and wake patterns. Indeed, a careful perusal of Fig. 3.27 (b) shows that $Y(t)$ and $C_L(t)$ consist of a rapidly varying impulse with a small amplitude at the earlier times which subsequently decay to a near zero and constant value. Moreover, the flow over the assembly is completely steady in the sense that there are no interactions between the shear layers and the vortex shedding. Therefore, it should be stressed that the quasi-steady regime and the still branch correspond to distinct branches in terms of the physical mechanisms responsible for these two regimes and the manifestation of the dynamical characteristics arising from these mechanisms. This is the case even though plots of Y_{max} and $C_{L,rms}$ as a function of U_r are very similar.

A natural question follows from these considerations: *why does the still branch appear when the plate length increases from $2D$ to $2.5D$ at same reduced velocity?* From a comparison of the near-wake regions in Figs. 3.27 (aiii)–(aiv) and (biii)–(biv), it is seen that the shear layers on both sides of the stationary assembly have a fixed length of about $2.5D$ (marked using vertical black lines in the figure), regardless of the plate length and the reduced velocity. As a result, the two shear layers interact with one another for a given incident flow if the plate length is shorter than $2.5D$, while no longer interact once the plate exceeds $2.5D$ and the vortex shedding occurs only in the far wake. In the latter

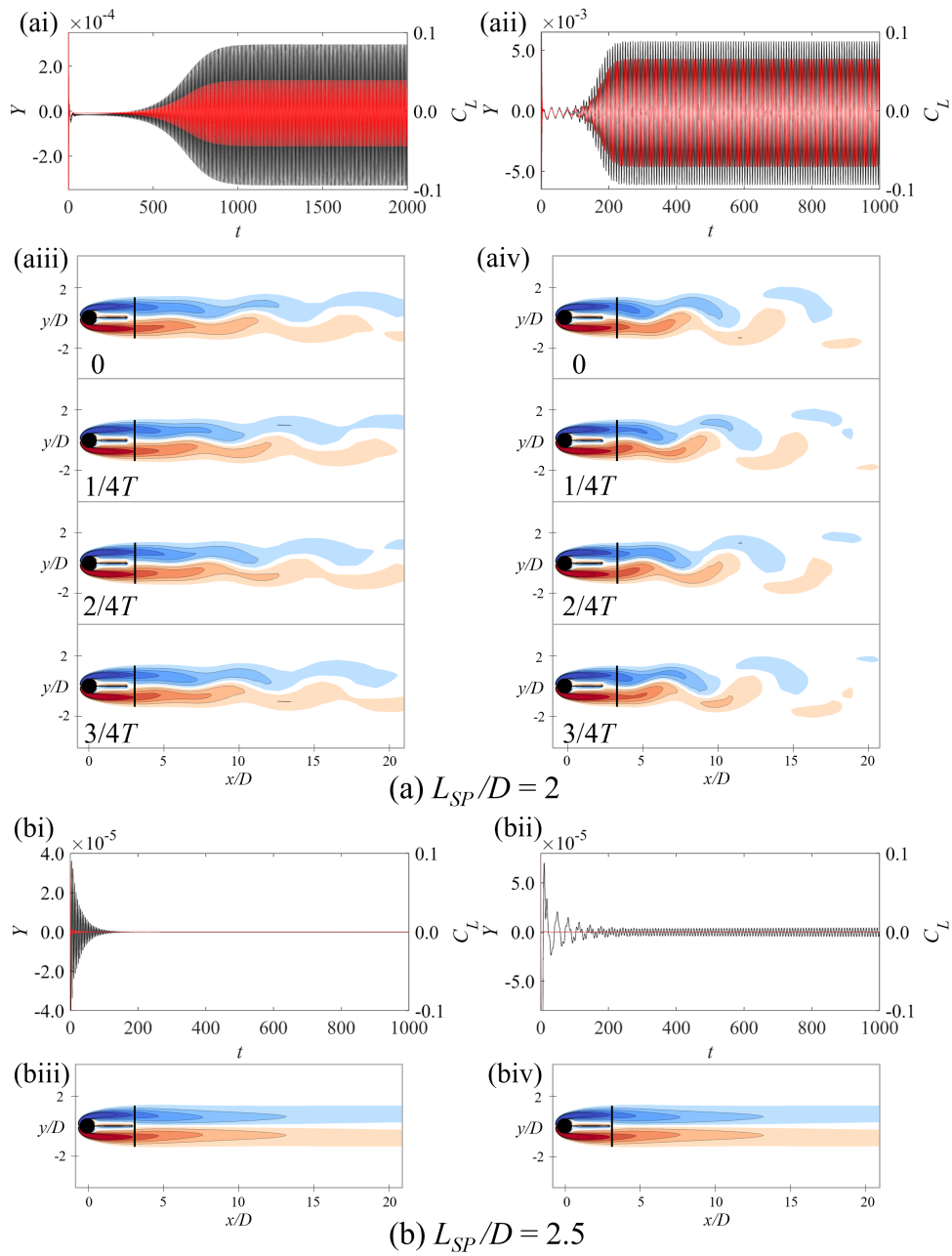


Figure 3.27: Time series of the instantaneous displacement (black curve) and lift coefficient (red curve) and the wake patterns within (a) quasi-steady regime for $L_{SP}/D = 2$ and (b) still branch for $L_{SP}/D = 2.5$ at two reduced velocities: namely, $U_r = 3$ (parts (i) and (iii)) and $U_r = 10$ (parts (ii) and (iv)).

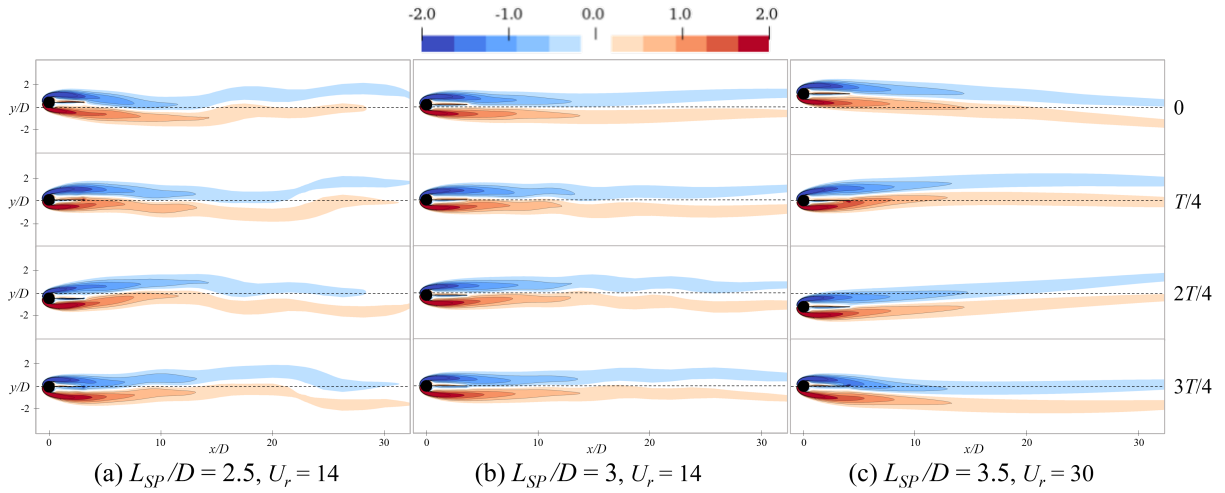


Figure 3.28: Snapshots of the instantaneous vorticity fields in one oscillation period T for the initial galloping branch: (a) $L_{SP}/D = 2.5$ at $U_r = 14$; (b) $L_{SP}/D = 3$ at $U_r = 14$; and, (c) $L_{SP}/D = 3.5$ at $U_r = 30$.

case, the upper and lower shear layers are completely isolated by a plate whose length is equal to or greater than $2.5D$ —consequently, the flow remains parallel and straight as it moves downstream (viz., the flow is purely steady in the sense that it appears not to evolve downstream). Note that the still branch is present even for $L_{SP}/D \geq 2.5$.

Another interesting thing is that a quasi-steady regime exists between the VIV and still branches for a plate length $L_{SP}/D = 2.5$ at $U_r = 7.5$ – 10 . However, for $L_{SP}/D = 3$, the end of VIV regime at $U_r = 9$, determined by the phase shift between Y and C_L , is coincident with the start (onset) of the still branch. Furthermore, for plate lengths $L_{SP}/D = 3.5$ – 4 , the VIV branch overlaps the still branch—the system transitions to the still branch before VIV lock-out. Indeed, for $L_{SP}/D = 2.5$ – 4 , the still branch between the VIV lock-out and the onset of galloping widens with plate lengths. More precisely, for plate lengths $L_{SP}/D = 2.5, 3, 3.5$ and 4 , the VIV regimes start at $U_r = 10, 9, 8.5$, and 8.5 and stops at $U_r = 12, 13, 18$, and a value > 30 , respectively. The upshot of this analysis is that a longer splitter plate attached to a circular cylinder is prone to become stationary (so, no motion) even for a reduced velocity as large as 30 . This is because the longer plate fully separates the upper and lower shear layers from each other and, as a result, it is more difficult for these shear layers to interact with each other, except perhaps under a very large incident flow velocity.

We examine in detail the initial galloping branch. From a perusal of the PSD of Y and

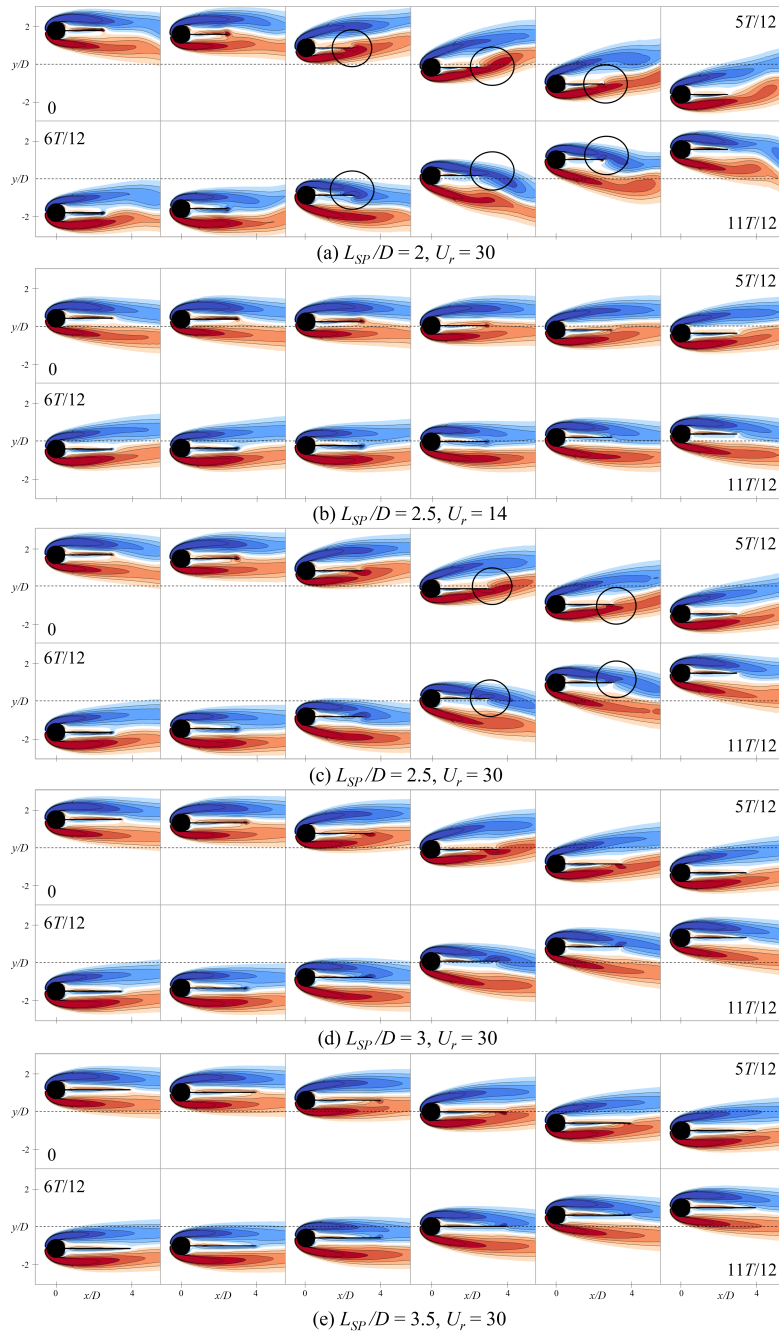


Figure 3.29: Temporal evolution of the instantaneous shear layer around cylinder-plate assembly over one oscillation cycle: (a) $L_{SP}/D = 2$ at $U_r = 30$; (b) $L_{SP}/D = 2.5$ at $U_r = 14$; (c) $L_{SP}/D = 2.5$ at $U_r = 30$; (d) $L_{SP}/D = 3$ at $U_r = 30$; and, (e) $L_{SP}/D = 3.5$ at $U_r = 30$.

C_L for assembly with $L_{SP}/D = 2.5$, we see that in the initial galloping branch, C_L has a simpler power spectrum (consisting only of the fundamental frequency) compared to that of Y (consisting of the fundamental frequency and a third harmonic). For $L_{SP}/D = 3.5$, the spectra of Y and C_L consist of only one oscillation frequency. This is an interesting dynamic characteristic of a cylinder-plate assembly that does not seem to have been reported previously, which raises the following questions: *is the oscillation observed in the initial galloping regime induced by flow (viz., is the oscillation here is FIV)? If yes, what type of response does this regime belong to—viz., VIV or galloping or some other mechanism? Does vortex shedding from the body occur in this regime?* To address these questions, it is necessary to focus our attention on the instantaneous wake dynamics.

Figure 3.28 shows a number of snapshots of the instantaneous vorticity field over one oscillation cycle for the initial galloping branch associated with assembly of $L_{SP}/D = 2.5$ –3.5. A perusal of this figure shows that there is no vortex shedding as the system oscillates—this fact explains the much simpler power spectrum of C_L . Furthermore, the two sinuous thread-like shear layers that form on the upper and lower surfaces of the cylinder have the appearance of two meandering plumes—more precisely, the two shear layers meander to-and-fro in concert with one another as they develop (“disperse”) in the streamwise direction. Indeed, for a larger incident flow velocity associated with $U_r = 30$ (see Fig. 3.28 (c)), the two shear layer “plumes” are almost parallel to one another and they move to-and-fro in the transverse direction in concert with one another and with the cylinder-plate assembly—albeit, the meandering of the two shear layers are in the opposite (counter) direction to that of the assembly.

From these considerations, the system oscillations in the initial galloping branch are still related to the flow—however, it is not accompanied by the vortex shedding but, rather, is associated with the meandering of shear layers. From this perspective, this phenomenon should be interpreted as a special galloping regime that is distinct from the classical forms of galloping where a rapid vortex shedding from a body (e.g., square cylinder) is expected to occur. The special regime of galloping observed here for certain assembly signals the onset of galloping for these cases which is why we refer to it as the initial galloping branch.

To ascertain the reason for the emergence of the initial galloping branch for cylinder-plate assembly with longer plate length, Fig. 3.29 exhibits in detail the influence of plate length and reduced velocity on the temporal evolution of the two shear layers. At $U_r = 30$, the galloping associated with a rapid vortex shedding occurs for $L_{SP}/D = 2$ –2.5—this is directly related to the interaction and merger of the plate tip vortex with one or the other of the two shear layers (highlighted by the circled regions in Figs. 3.29 (a) and (c)). In contrast, for longer plate lengths $L_{SP}/D = 3$ –3.5 at the same U_r , the plate can move closer to one or the other of the shear layers (owing to its greater length) but the plate tip

vortex does not interact or merge with them (see Figs. 3.29 (d) and (e)). Consequently, the shear layers are less affected in this case, which, in turn, result in a “gentler” form of wake dynamics (meandering rather than vortex shedding).

A longer splitter plate can effectively separate the upper and lower shear layers so there can be no interaction between them. This occurs for $L_{SP}/D = 2.5$ and, as a result, the initial galloping branch is first observed for this case and becomes wider with increasing plate lengths thereafter. The effect of reduced velocity can be seen by comparing Figs. 3.29 (b) and (c). For $U_r = 14$, an initial galloping branch associated with wake meandering is observed, in contrast to that at $U_r = 30$ where galloping is associated with vortex shedding. Consequently, increasing U_r can strengthen the mutual interaction between the splitter plate and the shear layers formed on the cylinder—as a result, the flow dynamics associated with galloping is transferred from wake meandering to vortex shedding. It is expected that the assembly with $L_{SP}/D = 3\text{--}4$ might display various branch patterns that include synchronizations similar to those with shorter plates.

3.4.3 A Further Discussion

“Kinks” in the amplitude response

The presence of “kinks” in the amplitude response has been noted previously in the context of the simpler galloping instability of a square cylinder [195, 194]. In these investigations, the “kink” was also referred to as a “step” or a “plateau” representing the near constant or slow growth of the amplitude with U_r . The vibration amplitude in classical galloping increases linearly with U_r once a critical reduced velocity is exceeded [195]. However, the presence of one or more “kinks” in the amplitude response “destroys” the linear growth of Y_{max} with increasing U_r —the amplitude response can be partitioned by the “kinks” into various sections. After a “kink”, Y_{max} increases linearly again but at a smaller rate (as measured by the slope of amplitude curve) until the next “kink”. Therefore, a “kink” in the amplitude response can be interpreted as a deceleration or buffering zone that limits the rapid increase of the vibration amplitude in the galloping regime.

From the detailed analysis of the branching behavior of a cylinder-plate assembly with various plate lengths conducted previously, the presence of a “kink” in the amplitude response (if one exists) is often observed at the onset of a galloping synchronization. In order to understand the connection between “kink” and synchronization, we compile the information on those assemblies with “kinks” in their amplitude responses (viz., $L_{SP}/D = 0.5\text{--}2.5$) in Table 3.6, which includes the details of the characteristic frequencies in the spectra of

Table 3.6: Frequency content of the displacement (Y) and the transverse force coefficient (C_L) in the various galloping synchronization (GS) branches for cylinder-plate assemblies with $L_{SP}/D = 0.5-2.5$. The Arabic numbers in spectra column refer to the fundamental frequency (1) as well as the order of harmonics present in the frequency spectra.

L_{SP}/D	No.(GS)	Spectra (Y)	Spectra (C_L)	“kink”
0.5	1	1	1,2,3,4	✓
	2	1	1,3,5,7	✓
0.75	1	1	1,2,3,4	✓
	2	1,3	1,3,5,7	✓
	3	1,3,5	1,3,5,7,9	✓
1	1	1	1,2,3,4	✓
	2	1,3	1,3,5,7	✓
	3	1,3	1,2,3,4,5,6	✓
	4	1,3	1,3,5,7	✓
1.25	1	1,3	1,3,5	✓
	2	1,3	1,2,3,4,5,6	✓
	3	1,3	1,3,5,7,9	✓
1.5	1	1,3	1,3,5	✓
	2	1,3	1,3,4,5	✓
	3	1,3	1,3,5,7	✓
1.75	1	1,3	1,3	×
	2	1,3	1,3,4	×
	3	1,3	1,3,5,7	✓
	4	1,3	1,3,5,7,9	×
2	1	1,3	1,3	×
	2	1,3	1,3,5	✓
	3	1,3	1,3,5,6	×
	4	1,3	1,3,5,7,9	✓
2.5	1	1,3	1,3	×
	2	1,3	1,3,5,7	✓

Y and C_L associated with the galloping synchronizations and whether a “kink” signals the onset of each of these branches. The results in Table 3.6 are compiled from information obtained from the figures exhibiting the branching behavior and power spectral density information presented earlier in this paper (viz., Figs. 3.15, 3.18, 3.19, 3.20 and 3.22) and from similar figures provided in the supplementary material. A careful examination of Table 3.6 suggests that if the C_L -spectrum exhibits a more complex form with more harmonic frequencies than that of Y , then a “kink” is present at the onset of synchronization in the amplitude response. Alternatively, there is no “kink” if the spectra of C_L and Y have the same frequency content. This also explains why no “kink” appears before lock-in branch where the spectra of C_L and Y are identical. It should be noted that the absence of a “kink” before the third synchronization for $L_{SP}/D = 2$ is probably due to limited resolution of the amplitude response here—a higher resolution of U_r might enable the “kink” to be adequately resolved and identified. It can be concluded that the more complex and irregular vortex shedding patterns as revealed in the transverse force spectrum (in the synchronization branch) result in a moderation of the growth of the oscillation amplitude in the galloping regime.

In summary, if a high-order harmonic emerges in the transverse force spectrum, a “kink” will be present in the amplitude response, followed by an integral-multiple synchronization between the system oscillation and the associated vortex shedding, during which Y_{max} linearly increases with U_r (with a smaller growth rate) until the appearance of next (still) higher-order harmonic in the C_L -spectrum. The synchronizations in the galloping regime emerge in same order as the emergence of the high-order harmonics in the C_L -spectrum. For longer plate lengths ($L_{SP}/D \geq 2.5$), the initial galloping branch associated with wake meandering may appear before this sequence of synchronizations in the galloping regime.

Comparison of galloping for square cylinder and cylinder-plate assembly

In this section, we compare the classical galloping response of a square cylinder with that of a cylinder-plate assembly based on the branching behaviors reported in the present study and those from a representative experimental study conducted by Zhao *et al.* [195].

For a square cylinder undergoing galloping with a steadily increasing amplitude, Zhao *et al.* [195] experimentally identified three odd-multiple synchronizations (1:1, 1:3, and 1:5). These investigators explained the absence of even-multiple synchronizations for a square cylinder as follows. They noted that the mean fluid force acting on the body during one complete oscillation cycle is zero, which must be true necessarily if a clear-cut alternating pattern of the vortex shedding is manifest (e.g., such as a “2S” mode that is representative of the classical Kármán vortex). If so, this “2S” mode must be repeated an integral number

of times in a half-oscillation cycle for the even-multiple synchronizations (viz., the wake mode must necessarily be “ $(n/2) \times (2S)$ ” for a 1: n synchronization where $n = 2, 4, 6, \dots$ is even). This form of wake mode will generate a zero fluid force on the moving body and, as a result, cannot have any continuous influence on the system oscillations. This is the reason why even-multiple synchronizations cannot appear in the galloping of a square cylinder.

In contrast, both even- and odd-multiple synchronizations are identified in the galloping regime of a cylinder-plate assembly in this study, although the U_r range for the former is always narrower than that for the latter. The presence of even-multiple synchronizations in galloping of an assembly is due to the disruption of the alternating vortex shedding. The detailed flow information presented in Sections 3.4.2 has shown that for an even-multiple synchronization, the vortices are always not shed alternately from both sides of the body—rather, the vortex shedding here may display more complicated patterns like the “T+S” mode in the 1:2 synchronization for $L_{SP}/D = 0.5$, so the mean transverse force during a half-oscillation cycle is not zero. In consequence of the asymmetry in the vortex shedding over each half-oscillation cycle, even-multiple synchronizations can be supported in the galloping regime of a cylinder-plate assembly. In some cases, the even-multiple synchronizations might be absent (e.g., the absence of 1:4 and 1:6 synchronizations for $L_{SP}/D = 0.75$ and 1.75). The upshot of this analysis is that the wake flow behind an assembly undergoing galloping exhibits more complicated dynamics compared to that of a square cylinder and, as a result, can support both even- and odd-multiple synchronizations unlike that of a square cylinder.

3.5 Nonlinear Characteristics Analysis

The objective of this section is to elucidate the nonlinear dynamical characteristics of the FIV of cylinder-plate assembly, in terms of the beating phenomenon, the limit-cycles and the vortex-shedding modes.

A comprehensive overview of FIV dynamics of a cylinder-plate assembly is displayed in Fig. 3.30. This figure exhibits the branching behavior of the cylinder-plate assembly in the $(L_{SP}/D, U_r)$ plane. In this diagram, the lock-in branch (region shaded in green) occurs for a wide swath of plate lengths from $L_{SP}/D = 0$ –4 at small reduced velocity $U_r = 4$ –12. In contrast, the galloping regime (region enclosed by the purple solid line) is present only for splitter-plates of greater lengths at larger reduced velocity. A strong interaction between VIV and galloping occurs for $L_{SP}/D = 0.5$ –0.75, but this interaction is reduced significantly with increasing plate length.

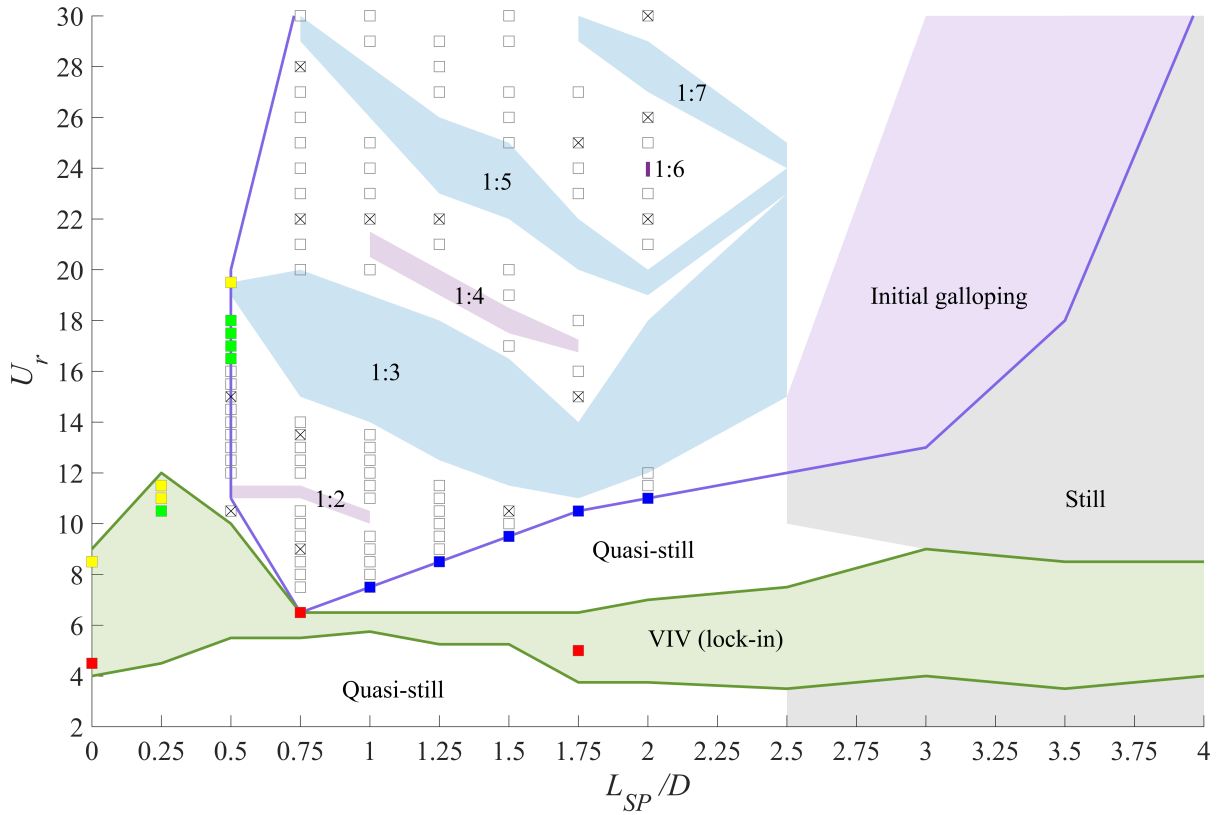


Figure 3.30: The identification and characterization of the branching behavior of a cylinder-plate assembly in the $(L_{SP}/D, U_r)$ plane. The assembly is undergoing a flow-induced vibration in a low-Reynolds number of $Re = 100$ with a mass ratio of $m^* = 10$ and a zero structural damping ($\zeta = 0$). The galloping regime is enclosed within the solid purple line. The synchronization branches are shaded in green (VIV regime), blue (odd-multiple synchronization in the galloping regime), and dark purple (even-multiple synchronization in the galloping regime). The initial galloping and the still (quiescent) branches are shaded in light purple and grey, respectively. The square symbols in the plane delineate various types of beating phenomena of the lift coefficient—Type 1 (red squares), Type 2 (green squares), Type 3 (yellow squares), Type 4 (blue squares) and Type 5 (unfilled squares).

The regions in the $(L_{SP}/D, U_r)$ plane associated with various synchronizations in the galloping regime with various frequency ratios $f_Y^*/f_{C_L}^*$ are indicated by different colors. Here, f_Y^* and $f_{C_L}^*$ are the fundamental frequencies associated with the transverse displacement $Y(t)$ and the transverse force coefficient $C_L(t)$, respectively—the integral modes of synchronization are characterized by $f_Y^*/f_{C_L}^* = 1:n$ where $n = 2, 3, 4, 5, 6$, and 7 . The even-multiple synchronizations (region shaded in dark purple) occur over a more restricted region of the $(L_{SP}/D, U_r)$ plane than the odd-multiple synchronizations (region shaded in blue), especially the 1:6 synchronization. Moreover, the initial galloping branch (region in light purple) associated with wake meandering occurs immediately after the onset of galloping for the longer splitter-plates with $L_{SP}/D \geq 2.5$.

In addition to the colored regions, the remainder of the $(L_{SP}/D, U_r)$ plane (white region within purple solid line) represents the non-synchronization of the system oscillations and vortex shedding. Typically, non-synchronizations display very complicated and irregular dynamical characteristics. The various square symbols scattered across the various branches correspond to the occurrence of beating in the time series of the transverse displacement and lift coefficient which will be explained in greater detail later in Section 3.5.1. In addition to the VIV and galloping regimes, the dynamics of the cylinder-plate assembly can exhibit a quasi-still status (associated with very small structural oscillations and weak wake dynamics) for the case of shorter splitter-plate or a so-called still (quiescent) branch (associated with no structural motion and wake dynamics) for the case of a longer splitter-plate (region shaded in grey).

3.5.1 Beating Phenomenon

Beating in the VIV regime

For a cylinder-plate assembly undergoing FIV, the temporal variations of the transverse displacement and the transverse force coefficient are generally periodic (viz., the time series repeat its values at regular intervals with a single amplitude and a single frequency). However, in some cases, the lift coefficient C_L can exhibit prominent aperiodicity with a time-varying amplitude—resulting in beating (amplitude modulation). Moreover, the transverse displacement Y can also exhibit quasi-periodic oscillations, but the nature of these oscillations can be subtle. This section characterizes the properties of beating in the time variations of C_L . The square symbols in Fig. 3.30 mark the locations in the $(L_{SP}/D, U_r)$ plane corresponding to the different types of beating in $C_L(t)$. A careful examination of this figure shows that the beating of $C_L(t)$ occurs with higher probability for cylinder-plate assemblies with short and moderate splitter-plate lengths ($L_{SP}/D < 2$),

at values of the reduced velocity close to either the boundaries of VIV regime or in the non-synchronization branch of the galloping regime.

The beating in the time series of C_L has different characteristics depending on the splitter-plate length and the reduced velocity. To examine these dynamics in greater detail, Fig. 3.31 displays the time series of transverse displacement $Y(t)$ (grey lines) and lift coefficient $C_L(t)$ (black lines) and the local frequency associated with lift coefficient f_{C_L} (red lines) for selected combinations of L_{SP}/D and U_r . Following the lead of Zhao and Zhao [194], the local frequency is defined as the reciprocal of the local period, which refers to the duration between two consecutive zero-crossing points (from negative to positive) in the time series of a signal. Using the local frequency associated with the transverse displacement f_Y , Zhao and Zhao [194] identified two types of beating associated with the FIV of a rectangular cylinder with rounded corners: namely, Type A where f_Y varies around the structural natural frequency f_n for a square cylinder and Type-B where f_Y varies between the Strouhal frequency f_{St} and f_n for a circular cylinder. By contrast, the beating of $C_L(t)$, corresponding to the FIV of a cylinder-plate assembly, exhibits much more complex characteristics. Consequently, we identify five distinctive types of beating in the temporal variations of f_{C_L} in the present work.

Figure 3.31 (a) shows a Type 1 beating for which f_{St} is less than f_n and the local frequency f_{C_L} fluctuates between these two frequency (lower and upper) limits. For the first two cases, the temporal variations of f_{C_L} are significant—fluctuating strongly between the lower and upper limits. In contrast, the beating in $C_L(t)$ for the third case is very weak— $f_{C_L}(t)$ exhibits very small fluctuations near the lower frequency limit of f_{St} . These results in conjunction with those exhibited in Fig. 3.30 suggest that a Type 1 beating occurs either near the onset of VIV for a bare circular cylinder (e.g., $U_r = 4.5$ is within the initial branch of VIV for a bare circular cylinder) or near the onset of pure galloping for a cylinder-plate assembly (e.g., $U_r = 6.5$ corresponds to the onset of pure galloping for a cylinder-plate assembly with $L_{SP}/D = 0.75$). The third case in Fig. 3.31 (a) corresponding to $L_{SP}/D = 1.75$ at $U_r = 5$ is a special case where beating in $C_L(t)$ occurs in the middle of VIV regime. In accordance to the analysis conducted in Sections 3.3–3.4, the transverse displacement of the assembly with $L_{SP}/D = 1.75$ exhibited a sudden decrease to near zero at $U_r = 5$ during VIV and then increased again before the transition to lock-out—this behavior was different from the other assemblies where a more gradual and smooth decrease of the transverse displacement in the VIV was observed as lock-out was approached. A perusal of the third panel in Fig. 3.31 (a) provides a possible reason—in this case, the local frequency $f_{C_L}(t)$ is nearly constant and equal to the vortex-shedding frequency of the *stationary* cylinder-plate assembly (viz., f_{St}) with the consequence that a structure subjected to such a transverse force will correspondingly exhibit a near stationary behavior

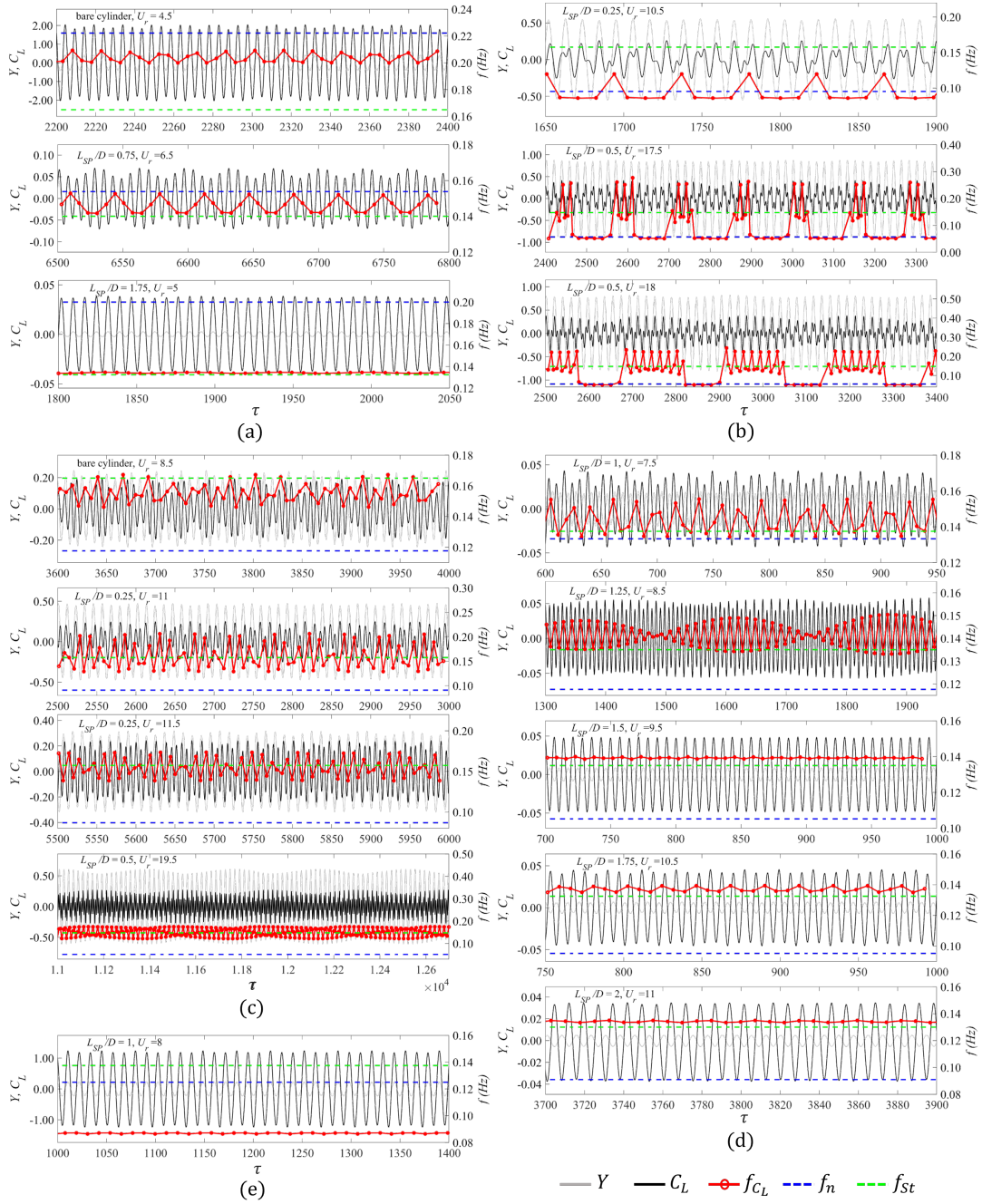


Figure 3.31: Time series of Y (grey) and C_L (black) for various combinations of L_{SP}/D and U_r . These time series are superimposed on the time variations of the local frequency of lift coefficient f_{CL} (red), the structural natural frequency f_n (blue) and the Strouhal frequency f_{St} (green). Five distinctive types of beating are classified: (a)–(e) Type 1–5.

(with little or no transverse displacement).

Figure 3.31 (b) shows a Type 2 beating where f_n is less than f_{St} (opposite of Type 1 beating). In a Type 2 beating, the local frequency $f_{CL}(t)$ fluctuates around either f_n or f_{St} with reference to the weaker or stronger oscillations of lift coefficient, respectively. A Type 3 beating exhibited in Fig. 3.31 (c) is very similar to a Type 2 beating—the only difference is f_{CL} is invariably larger than f_n (in contrast to a Type 2 beating where f_{CL} can be approximately equal to f_n in certain cases) and fluctuates only around f_{St} . A careful examination of Fig. 3.30 indicates that Type 2 and Type 3 beatings are present near the boundaries either of VIV for a bare circular cylinder or of galloping for a cylinder-plate assembly undergoing self-limited oscillation (e.g., $L_{SP}/D = 0.25$ and 0.5). Furthermore, the value of f_{CL} can approach the value of f_{St} a certain times which, in turn, implies a state corresponding to the suppression of the system vibration. A Type 3 beating corresponds typically to the circumstance where f_{CL} is not locked on to f_n and is either larger or smaller than f_{St} .

Figure 3.31 (d) displays a Type 4 beating which is characterized by a periodic variation of f_{CL} around a value that is slightly larger than f_{St} . It is well known that the vortex-shedding frequency is generally larger than the vibration frequency in the galloping regime. Consequently, a larger value of f_{CL} implies a more rapid vortex shedding from the structure which, in turn, makes the dynamical system more prone to galloping. For this reason, a Type 4 beating occurs at the onset of galloping for cylinder-plate assemblies with longer splitter-plates (e.g., $L_{SP}/D = 1-2$). From Section 3.4, it is known that splitter-plates with lengths $L_{SP}/D \geq 2.5$ induces an initial galloping branch associated with wake meandering once a critical value of the reduced velocity is exceeded. A natural question is why does the onset of galloping for a cylinder-plate assembly with $L_{SP}/D = 0.75$ trigger a Type 1 beating rather than a Type 4 beating as is the case for assemblies with $L_{SP}/D = 1-2$? This arises from the inherent differences in geometry. For assembly with $L_{SP}/D = 0.75$, f_n is larger than f_{St} , while the opposite is true for assemblies with $L_{SP}/D = 1-2$.

Figure 3.31 (e) displays a Type 5 beating—here, f_{CL} is invariably smaller in value than both f_n and f_{St} . Furthermore, f_{CL} approach f_n with increasing U_r for each plate length. Both the amplitude and the local frequency associated with a Type 5 beating are characterized by small fluctuations—these occur in the unsynchronized branch of the galloping regime for cylinder-plate assemblies with $L_{SP}/D \geq 0.5$.

The taxonomy of different types of beating identified for a cylinder-plate assembly can be compared to those of a rectangular cylinder with rounded corners [194]. We note that Zhao and Zhao [194] conducted an analysis of the beating characteristics associated with the transverse displacement Y of a rectangular cylinder in the low reduced-velocity range

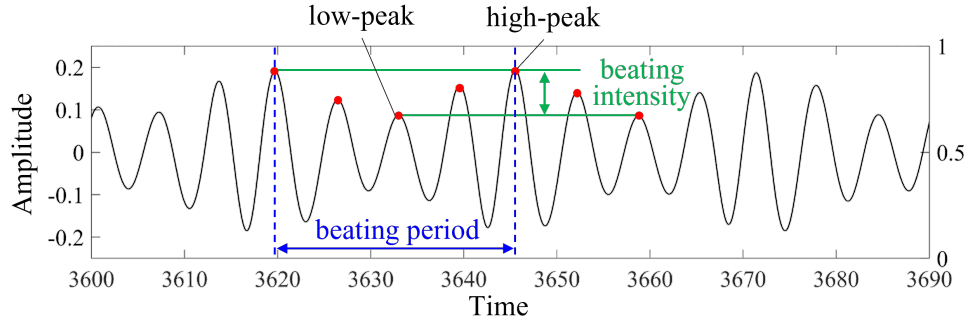


Figure 3.32: The periodic beating behavior in the amplitude envelope of time history of a signal. The beating intensity is defined as the difference between largest peak value (high-peak) and lowest peak value (low-peak) over one beating period.

only and identified two types of beating in this range. The reduced-velocity range here is associated with the VIV regime—naturally, a rectangular cylinder with rounded corners can also exhibit galloping at larger values of the reduced velocity. In marked contrast, the present work focuses on the beating characteristics of the lift coefficient C_L for both the VIV and galloping regimes, and identifies five types of beating for the cylinder-plate assembly using the same classification schema—based on the local frequency—as used by Zhao and Zhao [194]. It is stressed that a cylinder-plate assembly exhibits a more complex and subtle amplitude modulation than that of a rectangular cylinder with rounded corners, exhibiting a broader and richer spectrum of nonlinear beating characteristics. The differences in the flow and structural dynamics associated with a cylinder-plate assembly and a rectangular cylinder—two significantly different geometrical structures—are responsible for the important differences in the types of beating supported by these two structures.

Beating in the galloping regime

The local frequency was used to classify the different types of beating for a cylinder-plate assembly at the smaller values of the reduced velocity U_r , corresponding to the VIV regime. In addition to the local frequency, the beating phenomenon can be characterized using a number of global properties. One attribute is the symmetry of amplitude modulation over one beating period [194]. Most of the examples displayed in Fig. 3.31 involve time series whose amplitude modulations are symmetric (or, quasi-symmetric). However, some examples such as those corresponding to the second and third panels of Fig. 3.31 (c) exhibit randomly-changing amplitudes with no clear-cut increasing or decreasing trends—

the time series of C_L assumes the shape of a comb or pitchfork tines. Periodicity is another important attribute that can be used to characterize the beating. Most of the examples of symmetric beating displayed in Fig. 3.31 are also periodic, whereas the more random beatings associated with comb-shaped patterns in the $C_L(t)$ have more complex variations that do not exhibit any clear-cut repetitions in the amplitude modulation over one beating period. A schematic depicting a periodic beating is given in Fig. 3.32.

In addition to beating that occurs in the VIV regime, it should be stressed that the beating phenomenon also occurs at the larger values of U_r corresponding to the galloping regime—open squares in Fig. 3.30 are examples of this. From the perspective of local attributes, the beating in the galloping regime is similar to that exhibited in Fig. 3.30 (e) with reference to a Type 5 beating. In light of this, we proceed to analyze beating from a global perspective.

Figure 3.33 shows some selected examples of beating in the galloping regime (marked by the squares with crosses in Fig. 3.30), with respect to L_{SP}/D and U_r . These beatings are characterized in terms of the time series of lift coefficient (black curves) and the amplitude envelope of time series (red curves) which encapsulates the changes in the amplitude of C_L over time. As shown, the plate length and reduced velocity affect the characteristics of beating primarily by two geometrical properties: namely, symmetry and periodicity. For example, the beatings displayed in Fig. 3.33 are periodic, except for the case shown in Fig. 3.33 (b) where the amplitude modulation increases and decreases rapidly resulting in a comb-like (pitchfork-tines-like) amplitude envelope. Moreover, most of beatings in Fig. 3.33 are associated with symmetric or quasi-symmetric amplitude modulations, except for the case displayed in Fig. 3.33 (f)—the pattern of beating here is asymmetric with an amplitude modulation consisting of a slow rate of increase followed by a rapid rate of decrease in the amplitude resulting in a skewed triangular-shaped envelope over one beating period. The periodic and symmetric beatings shown in Fig. 3.33 are characterized by different beating periods and intensities (viz., the difference in value between the high peak (maximum) and the low peak (minimum) in the amplitude envelope during one beating period—see Fig. 3.32). Furthermore, it is noted that as the splitter-plate length increases, the beating intensity decreases and tends to zero for a splitter-plate of sufficient length (see Figs. 3.33 (h)–(n)). Finally, a careful perusal of Fig. 3.33 suggests that there is no obvious (simple) relationship between the beating in the galloping regime and the reduced velocity.

Energy transfer during beating

The FIV of a bluff body involves a bidirectional fluid-structure interaction—the vibrations are initialized and sustained by the energy extracted from the fluid flow by the elastically-

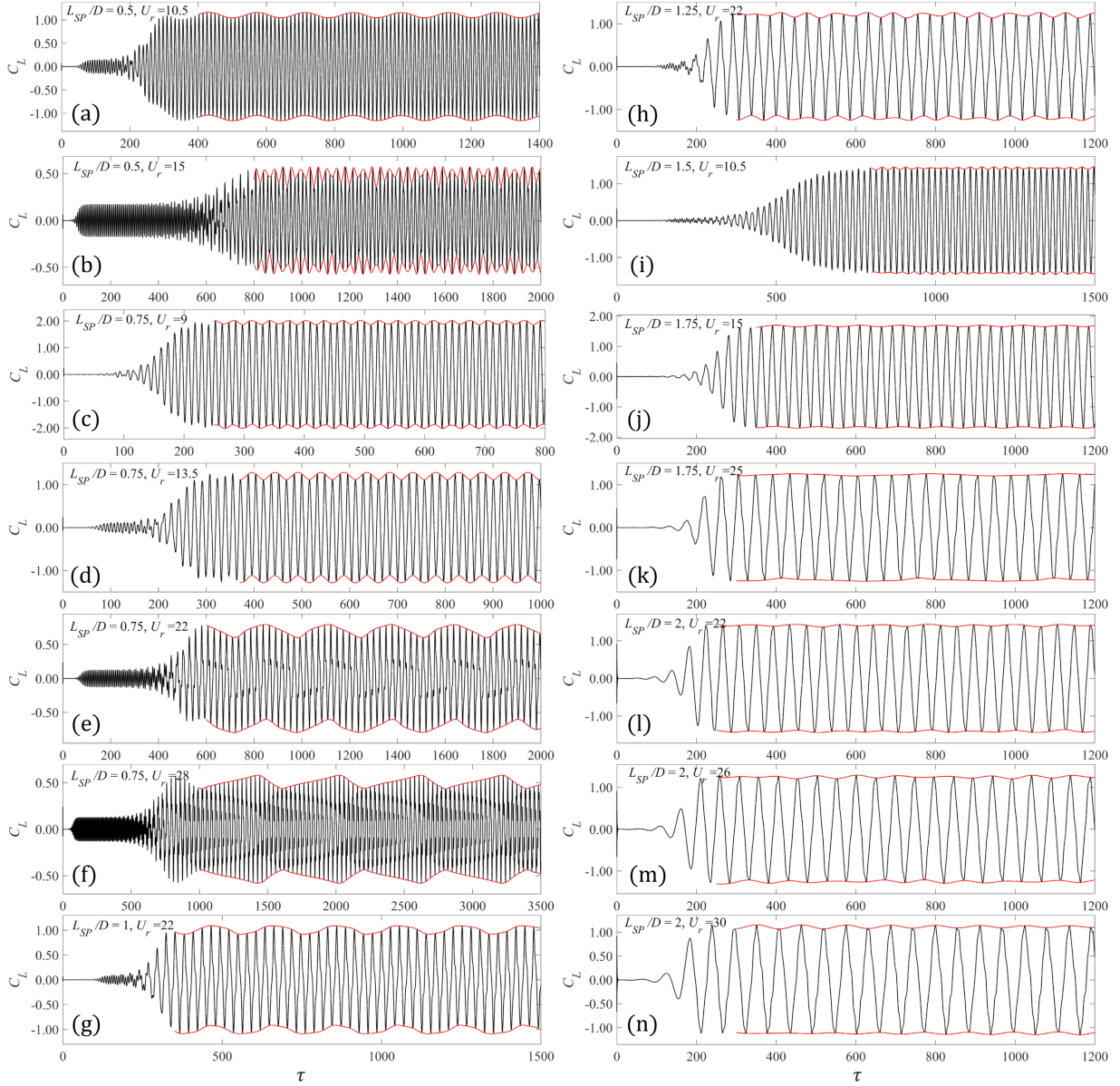


Figure 3.33: Time series of the transverse force coefficient C_L (black curves) and the corresponding amplitude envelopes (red curves) for a number of selected examples of beating in the galloping regime. The examples are characterized by the plate length L_{SP}/D of the cylinder-plate assembly and the reduced velocity U_r .

supported body. In view of this, a careful analysis of the energy transfer between the fluid and the body is useful for providing deeper insights into the physical mechanisms underpinning FIV and the concomitant characteristics of the nonlinear beating. The energy transferred to the cylinder-plate assembly per unit length (of cylinder) in each cycle of the oscillation is given by:

$$P = \int_t^{t+T} F_y(t)y'(t) dt , \quad (3.5)$$

where T is the oscillation cycle, $F_y(t)$ is the transverse force per unit length, $y'(t)$ is the transverse velocity of the body (recall that $y(t)$ is the dimensional transverse displacement). An energy-based analysis of various dynamical systems subjected to FIV has shown that P is either positive or negative—depending on the kinematics of the oscillation. The positivity or negativity of the energy transfer P increases or decreases the amplitude of oscillations, respectively [98]. Moreover, if the structural damping is zero, the oscillation of the dynamical system reaches a stable state when $P = 0$ —the phase difference between the transverse displacement and the transverse fluid force acting on the body is either 0° or 180° [73, 194].

The energy per cycle transferred to or from the surrounding flow by the cylinder-plate assembly at a low-Reynolds number ($Re = 100$) is shown in Fig. 3.34 (a) as a function of the splitter-plate length L_{SP}/D and the amplitude of the non-dimensional transverse displacement Y_{max} for $U_r = 6$ in the VIV regime. Furthermore, the time series of the non-dimensional transverse displacement $Y(t)$ for three selected plate lengths are displayed in Figs. 3.34 (b), (c), and (d) for $L_{SP}/D = 0$ (bare circular cylinder), 0.75 and 4, respectively. At $U_r = 6$, all the oscillations in $Y(t)$ are purely periodic without any amplitude modulation. More precisely, $Y(t)$ gradually increases with time at first and eventually reaches a stationary state of vibration—in this state, the vibrations have a constant amplitude and are characterized by a single frequency (“pure tone”). However, the transients in the initial stage of temporal development are different (sometimes irregular) for various splitter-plate lengths. The stationary state of vibration (that is eventually attained) implies that a dynamic equilibrium has been established in the dynamical system with no net (zero) energy transfer (per oscillation cycle) between the vibrating body and the surrounding fluid—this observation is consistent with previous studies.

Next, it is of interest to investigate the energy transfer between the cylinder-plate assembly and the surrounding fluid during the presence of beating. To this objective, Fig. 3.35 displays the time series of transverse displacement $Y(t)$ together with the total energy transfer $P(t)$ (first column of panels) and the net energy transferred over one oscillation cycle $P_{net}(t)$ (second column of panels) for six selected examples of beating involving various plate length L_{SP}/D and reduced velocity U_r . We focus on the role of the two lift

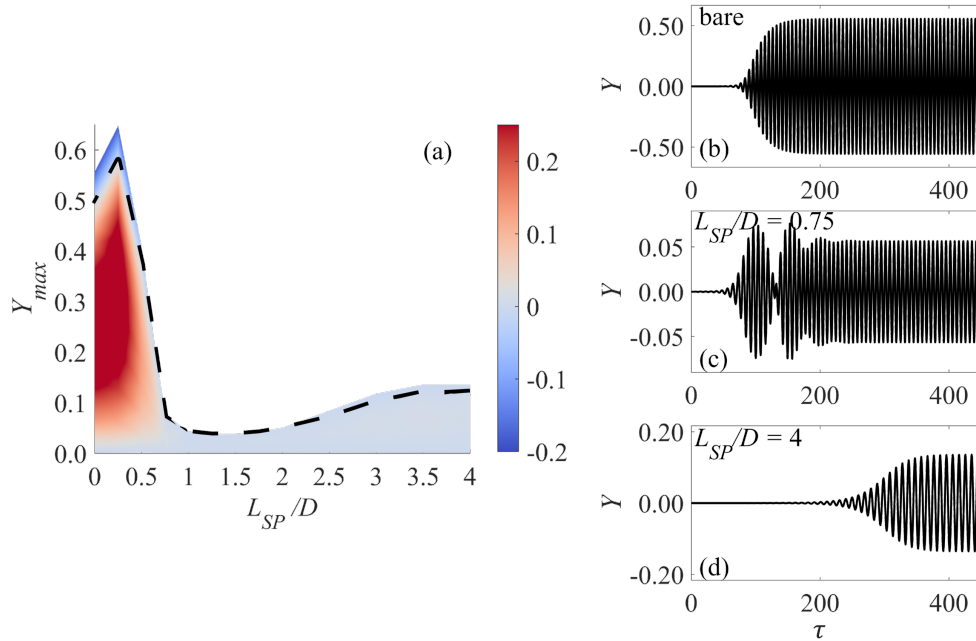


Figure 3.34: (a) Isoleths of the energy transfer per unit length (in J/m) between the elastically-supported cylinder-plate assembly and surrounding flow shown as a function of the non-dimensional amplitude of the transverse displacement (Y_{max}) and the splitter-plate length (L_{SP}/D) at a fixed value of the reduced velocity $U_r = 6$ within the VIV regime. The black dashed line represents the condition of zero energy transfer. Time series of the transverse displacement $Y(t)$ at $U_r = 6$ for (b) a bare circular cylinder, (c) a cylinder-plate assembly with $L_{SP}/D = 0.75$, and (d) a cylinder-plate assembly with $L_{SP}/D = 4$.

components on the generated power: namely, the energy transferred to the cylinder $P_{net,C}$ and to the splitter-plate $P_{net,SP}$, as well as the energy transferred by the total lift ($P_{net,T}$) on the entire assembly. Even though the beating of $Y(t)$ is less obvious than that of the $C_L(t)$, fluctuations in the amplitude peaks can, nevertheless, provide useful and physically insightful information regarding the relationship between the dynamics of the energy transfer and that of the local oscillations. As an example, for the bare circular cylinder (see Fig. 3.35 (a)), the energy transfer is positive for the second oscillation cycle ($\tau = 3200$ – 3208) yielding to a positive net energy transfer of 0.1 J/m—the corresponding amplitude of Y exhibits a subtle increase from a second peak of 0.2 to a third peak of 0.25. In contrast, the energy transfer is mostly negative over the third oscillation cycle ($\tau = 3208$ – 3217) giving a negative energy transfer of -0.7 J/m with a decrease in the corresponding amplitude of Y during this cycle to a fourth peak of 0.2. For the cylinder-plate assembly (see Figs. 3.35

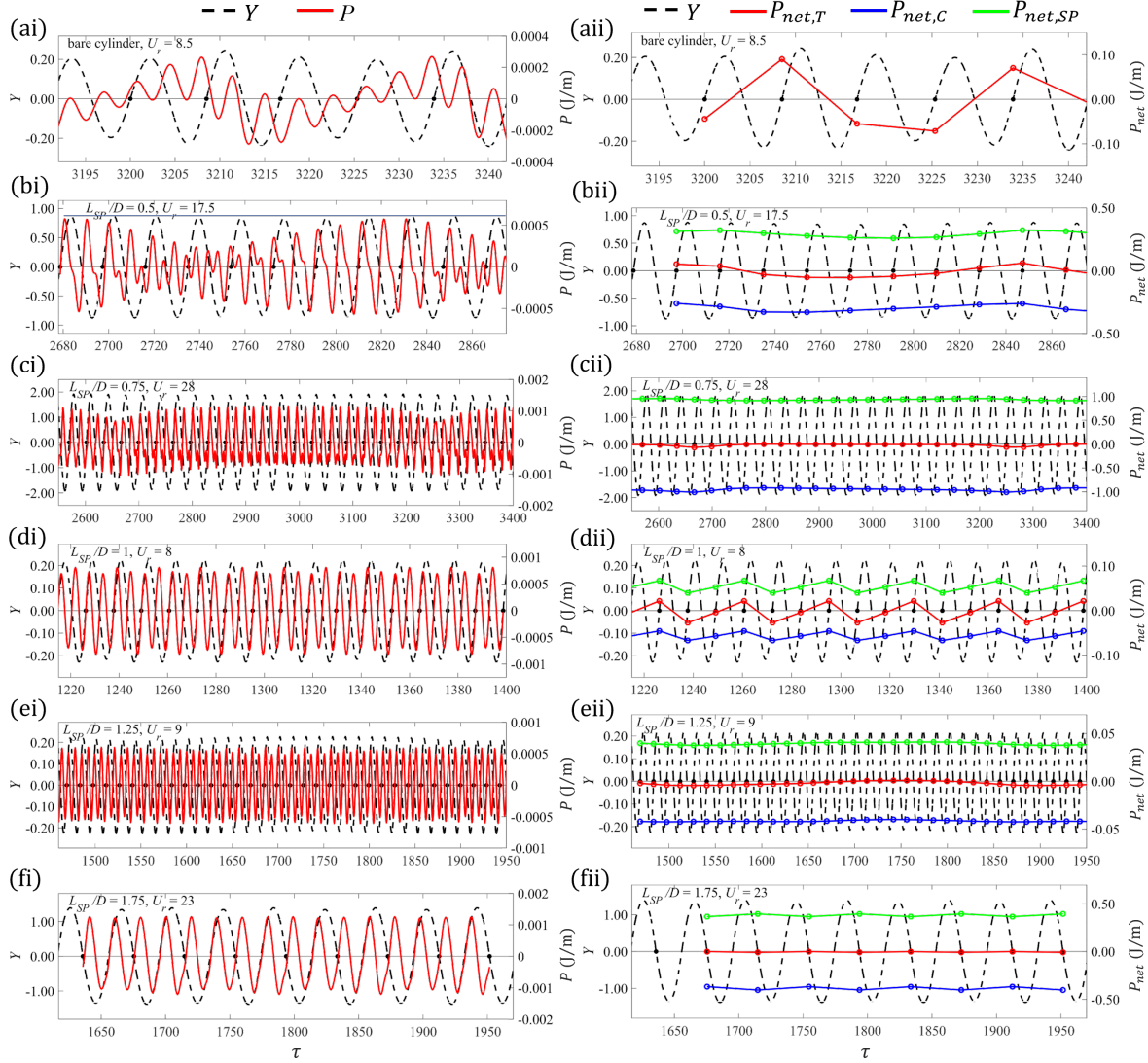


Figure 3.35: (a) Time series of $Y(t)$ (dashed black lines) and the energy transferred per unit length over one oscillation cycle between the structure (cylinder-plate assembly) and the surrounding fluid (solid red lines). (b) Time series of the total net energy per unit length $P_{net,T}$ transferred to the cylinder-plate assembly, the energy per unit length transferred to the cylinder $P_{net,C}$ only, and the energy per unit length transferred to the splitter-plate $P_{net,SP}$ only. The examples shown here are selected values of the splitter-plate length L_{SP}/D and the reduced velocity U_r .

(b)–(f)), the temporal variations in the amplitude during beating are also consistent with these observations—viz., a net positive energy transfer P (the oscillating system receives energy from the surrounding flow) increases the amplitude of Y , whereas a net negative P (the oscillating system loses energy to the surrounding flow) decreases the amplitude of Y . This is consistent with results for a rectangular cylinder with rounded corners reported by Zhao and Zhao [194]. Furthermore, a careful examination of Figs. 3.35 (bii)–(fii) shows that the net energy extracted by the splitter-plate from the surrounding fluid is always greater than zero (viz., positive), while that extracted by the circular cylinder is invariably less than zero (viz., negative), with the total net energy transfer fluctuating around the zero level. This implies that for an oscillating cylinder-plate assembly, the splitter-plate absorbs the energy from fluid, whereas the circular cylinder dissipates the energy into the surrounding flow. The sum of these two energies determines the local oscillations of the amplitude. In Fig. 3.35 (f), the *net* energy transfer per oscillation cycle is zero, so the periodic oscillations of the dynamical systems attain a stationary state—the amplitude of the oscillations is constant in time.

The beating phenomenon associated with the oscillations of the transverse displacement and lift coefficient (and, especially the latter) is an essential nonlinear characteristic of the cylinder-plate assembly undergoing FIV. The amplitude modulation is a quasi-periodic phenomenon and dominated by two different characteristic frequencies—one is associated with the oscillation frequency of the dynamical system and the other is the beating frequency [103]. Moreover, beating is closely related to the flow patterns and vortex dynamics in the wake. In light of this, a more in-depth analysis is required in order to explore the underlying physics of the beating phenomenon for the cylinder-plate assembly (see Section 3.5.3).

3.5.2 Nonlinear Dynamical Characteristics

In this section, a number of important nonlinear dynamical features (e.g., limit cycle, bifurcations, and presence of chaos) in the non-synchronization branches of a cylinder-plate assembly are examined in detail using a number of different methodologies: time series analysis, power spectral density (PSD) analysis, phase-plane portrait analysis, and Poincaré maps. The focus here is still the lift force (C_L) acting on a cylinder-plate assembly owing to its much stronger nonlinearity in comparison to that of the transverse displacement (Y).

We provide a brief description of the methodologies used to characterize the various aspects of the nonlinear dynamics of a cylinder-plate assembly. A phase-plane portrait is a geometric visualization of the temporal evolution of a dynamical system—in its simplest

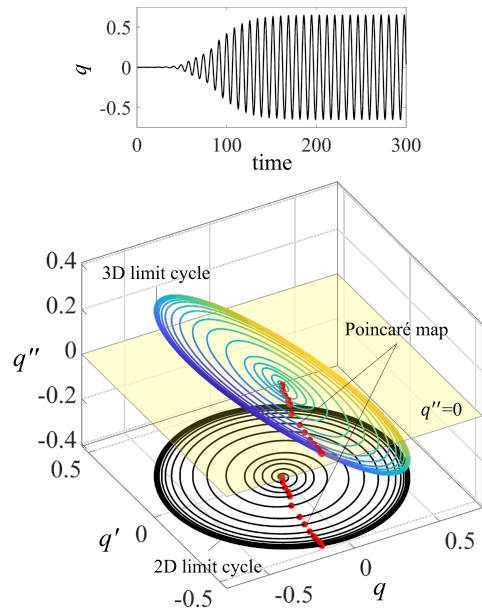


Figure 3.36: Schematic depiction of the geometric visualization tools used to analyze the nonlinear dynamics of a dynamical system. A dynamical quantity of interest is q . The time series $q(t)$ is a periodic oscillation with a quasi-sinusoidal waveform, corresponding to the closed orbits in the three-dimensional phase space (q, q', q'') which start from the origin of the space, gradually spiral outward and finally converge to the stable limit cycle when a stationary state of the oscillatory motion is reached. The red points correspond to the intersections between closed orbits and the Poincaré section ($q'' = 0$).

manifestation, the time development of a dynamical quantity (e.g., $Y(t)$) is plotted against its time derivative, or generalized velocity (e.g., $Y'(t)$). In other words, the axes of a phase-plane portrait are the state variables of the dynamical system. The topology of a phase-plane portrait is inextricably associated with the states of the dynamical system—for example, a fixed point and a closed orbit correspond to a static equilibrium and a periodic motion of the dynamical system, respectively. Moreover, the shape of the closed orbits is reflective of the period, amplitude, waveform, and energy of the temporal variations. The common single elliptical orbit in the phase plane is representative of a simple harmonic oscillation with a sinusoidal waveform. For highly complex systems, the closed orbits can be rather irregular—interpretations for these types of orbits will be provided below with reference to the dynamics of a cylinder-plate assembly. A limit cycle is a unique closed trajectory in the phase plane for which all neighboring trajectories can approach it as time t

goes to (1) infinity (stable or attractive limit cycle) and (2) negative infinity (unstable limit cycle). A particular type of limit cycle can be indicative of the presence of a self-sustained vibration in a dynamical system such as a circular cylinder undergoing VIV. A Poincaré map is another common geometric visualization tool that can be used, especially when the topological characteristics of the trajectories in the phase plane are too complex to extract any useful information—Poincaré maps may be especially relevant for dynamical systems that involve bifurcations and chaos. A Poincaré map can be constructed as follows: (1) define a Poincaré section transverse to the flow; (2) record the intersections of the closed orbits with this section; and, (3) map from Poincaré section to itself. More information concerning these various methodologies for the analysis of nonlinear dynamical systems can be found in Strogatz [152].

Figure 3.36 is a schematic depiction of the geometric visualization tools used in this study for the nonlinear analysis of an elastically-supported cylinder-plate assembly. The oscillation of a dynamical quantity of interest $q(t)$ leads to multiple closed orbits in the three-dimensional phase space (q, q', q'') and to an elliptically-shaped limit cycle when a stationary state of the oscillatory motion is achieved. There are multiple intersections (red points) of the closed orbits and the $q'' = 0$ plane in Poincaré map. Note that only those instances when the trajectory transitions from a positive to a negative value are considered in the analysis. Finally, it is stressed that all results reported in this section are obtained after the stationary state of the oscillatory motion of the dynamical system has been reached.

Figures 3.37–3.40 display the amplitude response (maximum transverse displacement Y_{max} as a function of U_r) with branching and various statistical characteristics of lift coefficient (power spectral density normalized by the maximum power, phase-plane portrait, and Poincaré section) of cylinder-plate assemblies for four plate lengths ($L_{SP}/D = 0.5, 0.75, 1.5$ and 2). Three values of the reduced velocity are considered for each plate length.

For $L_{SP}/D = 0.5$, the analysis is conducted at $U_r = 13.5, 18$ and 19.5 —these three values of U_r are within the unsynchronized branch of the galloping regime (marked with the red dots in Fig. 3.37 (a)). A perusal of Fig. 3.37 (bi) shows that the time variations in $C_L(t)$ at $U_r = 13.5$ repeat every three oscillation cycles (viz., three period-doubling oscillation). This suggestion is also supported by a closed trajectory consisting of three distinct circulations in the phase-plane portrait (see Fig. 3.37 (di)). Each of these three circulations involve a band of trajectories (rather than three clear-cut limit cycles), implying that the beatings in $C_L(t)$ at $U_r = 13.5$ are not identical to each other—these correspond to a quasi-periodic beating. Moreover, the time variations of $C_L(t)$ exhibit a small deviation from a pure sinusoidal waveform—this is also supported by the presence of multiple harmonic frequencies in the associated power spectrum shown in Fig. 3.37 (ci). Taken together, these

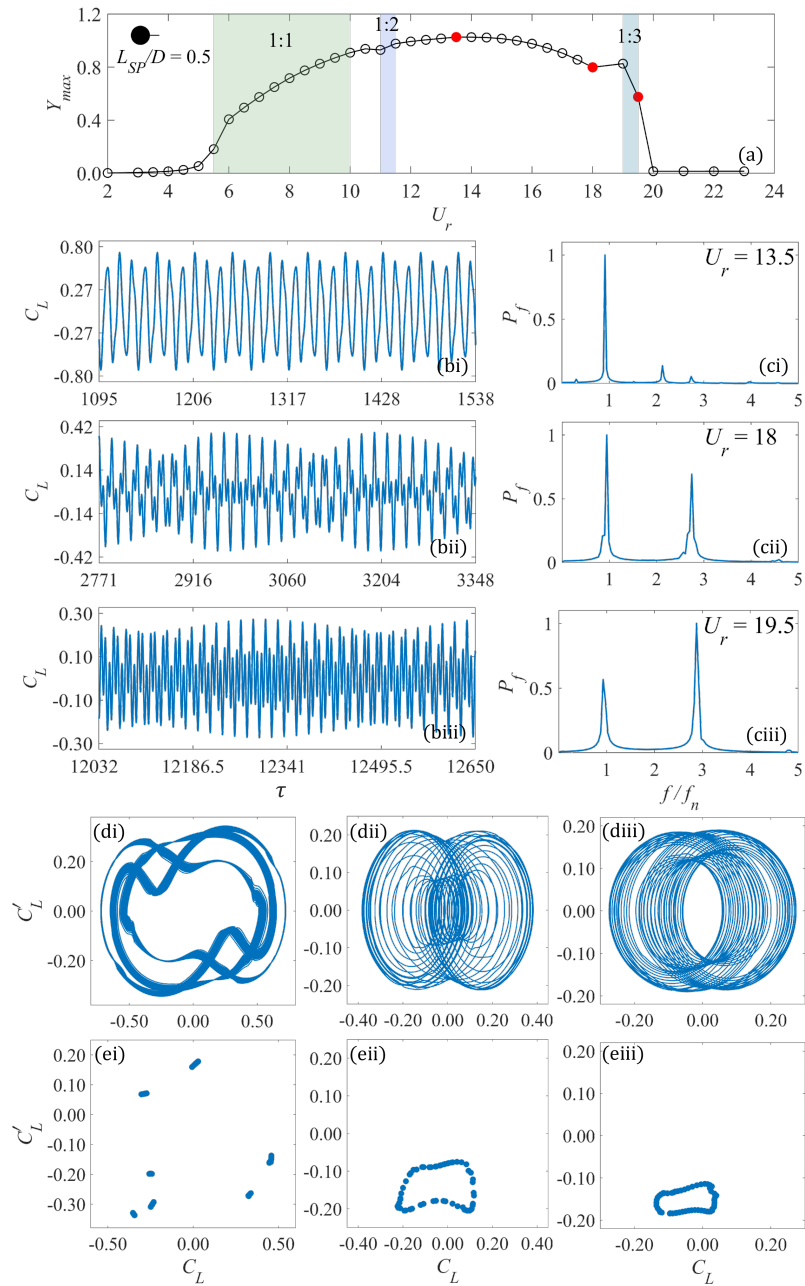


Figure 3.37: (a) Amplitude response of the cylinder-plate assembly with $L_{SP}/D = 0.5$. Dynamical characteristics of lift coefficient with respect to (b) time series $C_L(t)$, (c) power spectral density, (d) phase-plane portrait (C_L, C'_L) , and (e) Poincaré section, at three representative reduced velocities: (i) $U_r = 13.5$, (ii) $U_r = 18$, (iii) $U_r = 19.5$.

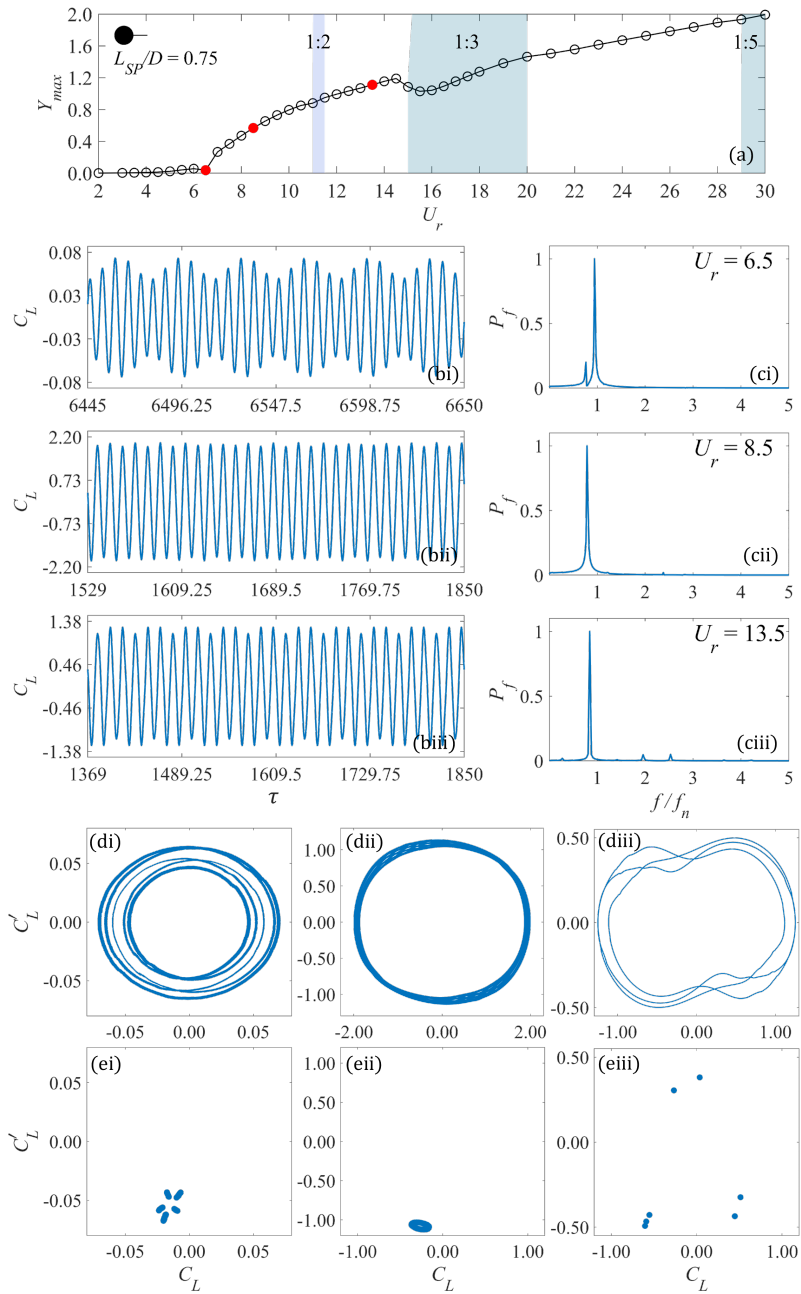


Figure 3.38: (a) Amplitude response of the cylinder-plate assembly with $L_{SP}/D = 0.75$. Dynamical characteristics of lift coefficient with respect to (b) time series $C_L(t)$, (c) power spectral density, (d) phase-plane portrait (C_L, C'_L), and (e) Poincaré section, at three representative reduced velocities: (i) $U_r = 6.5$, (ii) $U_r = 8.5$, (iii) $U_r = 13.5$.

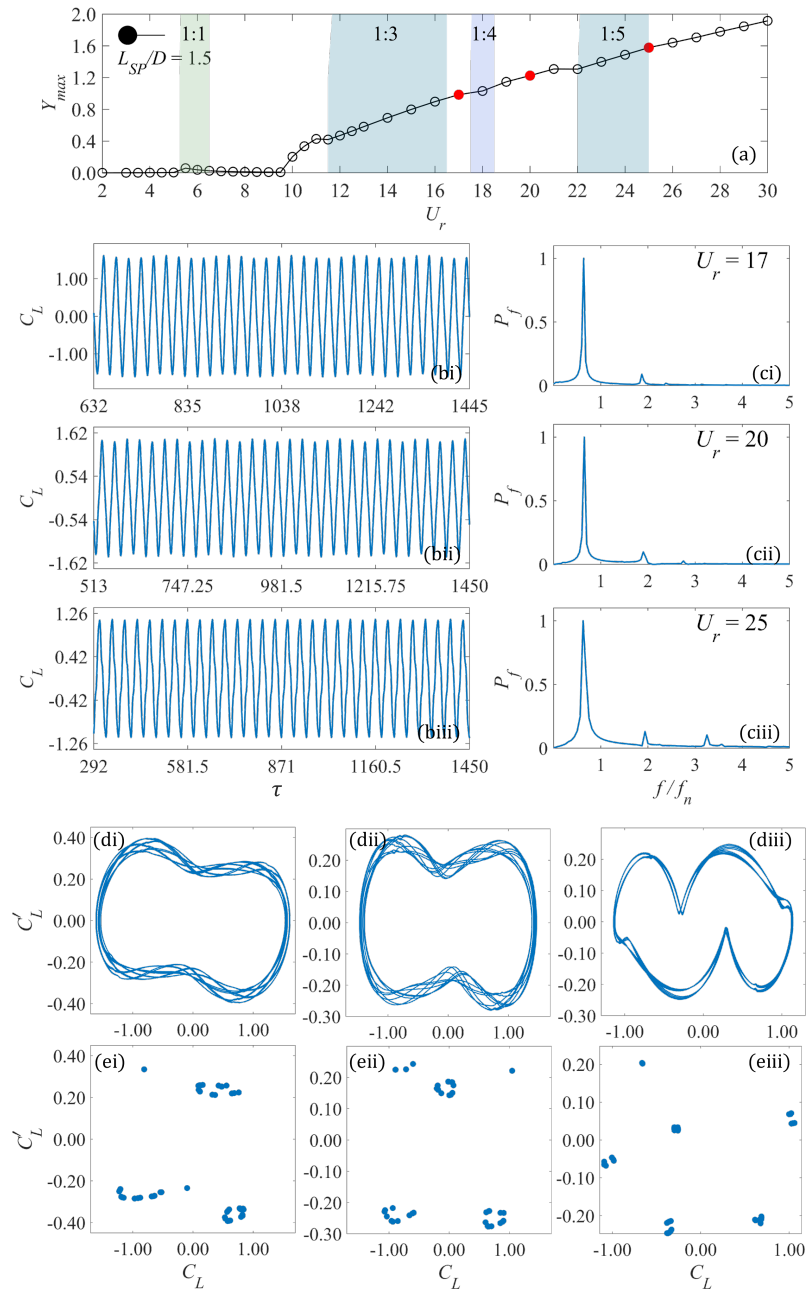


Figure 3.39: (a) Amplitude response of the cylinder-plate assembly with $L_{SP}/D = 1.5$. Dynamical characteristics of lift coefficient with respect to (b) time series $C_L(t)$, (c) power spectral density, (d) phase-plane portrait (C_L, C'_L), and (e) Poincaré section, at three representative reduced velocities: (i) $U_r = 17$, (ii) $U_r = 20$, (iii) $U_r = 25$.

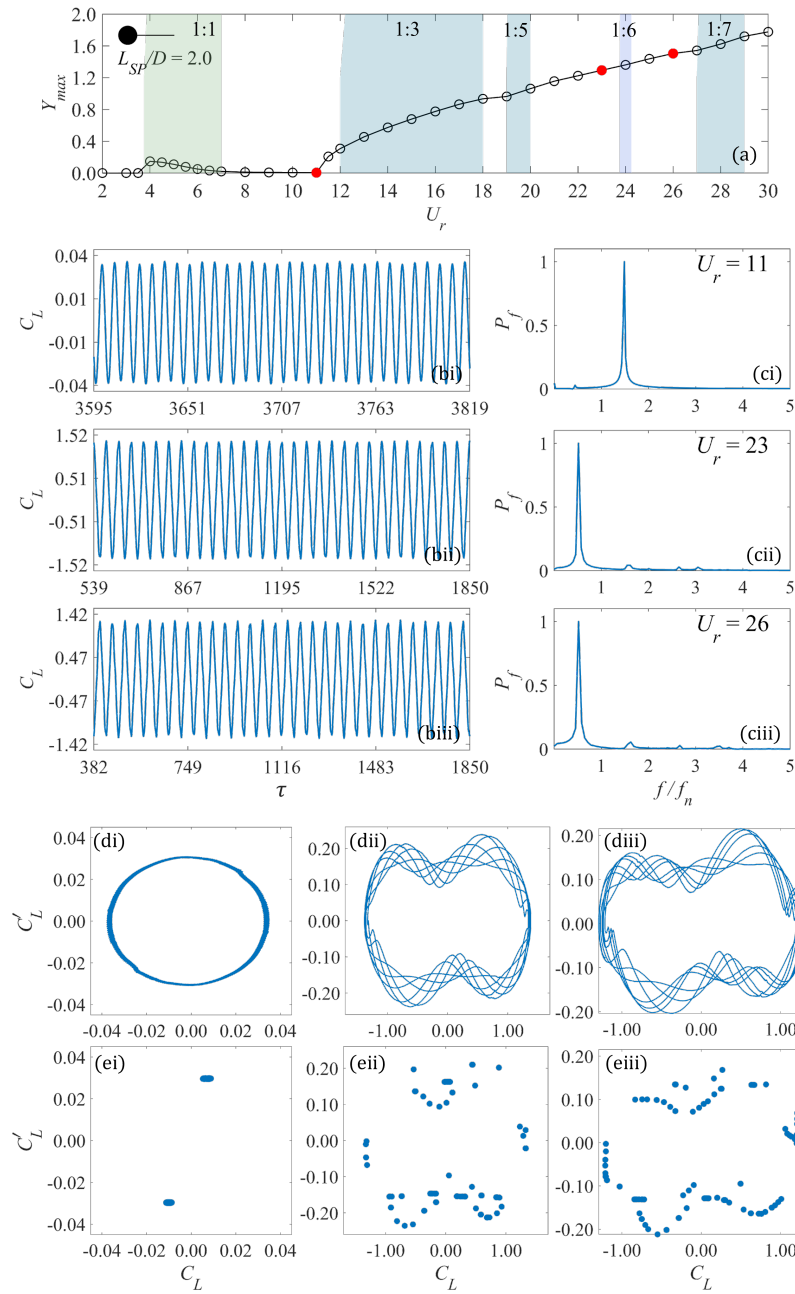


Figure 3.40: (a) Amplitude response of the cylinder-plate assembly with $L_{SP}/D = 2.0$. Dynamical characteristics of lift coefficient with respect to (b) time series $C_L(t)$, (c) power spectral density, (d) phase-plane portrait (C_L, C'_L) , and (e) Poincaré section, at three representative reduced velocities: (i) $U_r = 11$, (ii) $U_r = 23$, (iii) $U_r = 26$.

characteristics are responsible for the fact that the corresponding Poincaré map consists of more than three clusters of points (see Fig. 3.37 (ei)). At $U_r = 18$ and 19.5 , the beatings in $C_L(t)$ over a short time window appear to exhibit a periodic behavior (albeit, of a more complex and subtle) nature. However, this periodicity disappears when examined over a longer time window. The complex trajectories and point sets in the phase portraits and Poincaré sections, respectively, also imply that for $U_r = 18$ and 19.5 there is no discernible deterministic pattern in the time variations of C_L —these variations appear chaotic and may be associated with the much stronger harmonic content in the C_L power spectrum.

For a cylinder-plate assembly with $L_{SP}/D = 0.75$ at $U_r = 6.5$ corresponding to the onset of galloping, the quasi-periodic and symmetric beating in $C_L(t)$ is congruous with a five period-doubling oscillation. This assertion is supported by the donut-shaped trajectory in the phase-plane portrait of Fig. 3.38 (di) and by the presence of five clusters of points in the Poincaré section of Fig. 3.38 (ei). Moreover, the power spectrum of C_L consists of two closely-spaced frequencies—the primary frequency peak at $f/f_n = 0.95$ corresponds to characteristic oscillation in $C_L(t)$, whereas the secondary peak at $f/f_n = 0.76$ is associated with the time-varying beating (amplitude modulation) in $C_L(t)$ which becomes more obvious when examined over a longer time window. Previous studies [122, 170] showed that the local beating phenomenon is due to the presence of these two closely-spaced frequencies, resulting in a frequency shift in $C_L(t)$ from the Strouhal frequency to the structural natural frequency. At $U_r = 8.5$, the amplitude modulation of $C_L(t)$ is very small—as a result, the phase-plane consists of a series of tightly-bunched elliptically-shaped orbits that constitute the limit cycles (cf. Fig. 3.38 (dii)) and the Poincaré section consists of one (extended) cluster of points (cf. Fig. 3.38 (eii)). The three period-doubling oscillation of $C_L(t)$ at $U_r = 13.5$ is similar to that at the same value of the reduced velocity shown in Fig. 3.37.

For the cylinder-plate assembly with $L_{SP}/D = 1.5$, we focus on the beating in the region of the amplitude response near the 1:3, 1:4, and 1:5 synchronization branches. Inspection of the time series of C_L in Fig. 3.39 suggests that the beating phenomenon in these regions is less obvious—more precisely, there is little or no discernible amplitude modulation in the C_L time series. Moreover, the limit cycles in the phase-plane portraits are not circular (or, elliptical) in shape but, rather, consist of multiple “bulges” in their closed-looped orbits. In summary, the oscillations in $C_L(t)$ for a cylinder-plate assembly with $L_{SP}/D = 1.5$ are effectively periodic or quasi-periodic, without any evidence for chaotic behavior.

For the cylinder-plate assembly with $L_{SP}/D = 2$, the beating in the time series of C_L is less obvious. However, at larger reduced velocities $U_r = 23$ and 26 , the limit cycles in the phase-plane portrait become more complex (viz., they consist of a tangle of closed-loop orbits) and the point set structure of the Poincaré section consists of a multiplex of points with no discernible pattern.

Although the time sequences of the lift coefficient can be very similar for the cylinder-plate assembly with various L_{SP} and U_r , this similarity is deceptive as these highly nonlinear oscillations can have significantly different signatures with respect to their phase-plane portraits and Poincaré sections. To distinguish their nonlinear dynamical characteristics, a conjoint analysis of the limit cycles in the phase-plane and the point sets in the Poincaré sections is conducted with reference to Figs. 3.37–3.40. As a result, we identify three types of distinctive nonlinearities associated with the FIV of a cylinder-plate assembly.

A Type-I nonlinear oscillation is characterized by wider loops (multiple closed orbits) in the limit cycles and a small (limited) number of point clusters in the Poincaré section. These characteristics are representative of a quasi-periodic amplitude modulation (beating) and a period-doubling oscillation. The corresponding phase-plane portrait consists of either loops of similar size that intersect one another before closing to form a closed orbit (Figs. 3.37 (di), 3.38 (diii), and 3.39 (d)) or loops that appear to be stacked on top of one another to give the appearance of a donut-shaped orbit (Figs. 3.38 (di), 3.38 (dii), and 3.40 (di)). A Type-I nonlinear oscillation occurs in a cylinder-plate assembly with moderate splitter-plate lengths (e.g., $L_{SP}/D = 0.75$ and 1.5) or in a cylinder-plate assembly with either a short or a long splitter-plate at small values of the reduced velocity (e.g., $L_{SP}/D = 0.5$ at $U_r = 12.5$ and $L_{SP}/D = 2$ at $U_r = 11$).

A Type-II nonlinear oscillation is evident in Figs. 3.37 (ii) and 3.37 (iii)—the limit cycles in the phase-plane portrait have a “slinky” appearance consisting of numerous helical loops and the point set of the Poincaré section consists of clusters of points arranged in a closed loop (deformed ring). These characteristics are representative of a long-period beating where the maxima and minima of the amplitude envelope vary slowly in time. This type of nonlinear oscillation occurs only in a cylinder-plate assembly with a short splitter-plate length near the termination of the VIV regime in the amplitude response.

A Type-III nonlinear oscillation (see Figs. 3.40 (ii) and 3.40 (iii)) has the following distinctive signature: namely, the limit cycles appear to be disordered in the sense that the loops have different shapes and combine to give the appearance of a tangled web of “string” and the point set of the associated Poincaré section consists of point clusters that are arranged in a loop that has a similar shape to that of the phase-plane portrait. This type of nonlinear oscillation occurs in a cylinder-plate assembly with a long splitter-plate length at large values of the reduced velocity.

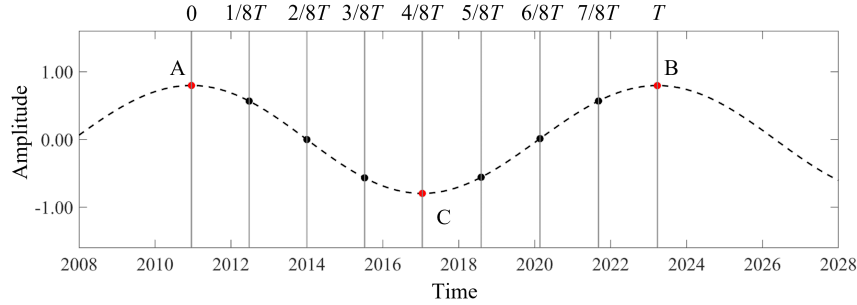


Figure 3.41: Division of consecutive oscillation cycles during beating.

3.5.3 Wake Modes During Beating

In this section, the wake modes associated with the various types of beating are studied. Based on the beating observed in Section 3.5.1, two representative scenarios are analyzed: namely, (1) a periodic beating in the cylinder-plate assembly with $L_{SP}/D = 0.75$ at $U_r = 10$; and, (2) an aperiodic beating in the cylinder-plate assembly with $L_{SP}/D = 0.5$ at $U_r = 14$.

Before we begin the analysis, it is necessary to clarify how to split a consecutive sequence of oscillation cycles into representative constituent parts during beating. One strategy is to use the division method proposed by Sen [132]. This method consists of three steps: (1) calculate the uniform oscillation cycle based either on the vibration frequency or the vortex-shedding frequency; (2) choose a starting time and identify several successive oscillation cycles; and, (3) divide each of these cycles into a number of equal segments. Unfortunately, this division method seems not very appropriate for the analysis of dynamical system oscillations on a cycle-by-cycle basis because the local frequency of beating can change as explained earlier in Section 3.5.1, implying that the temporal period of each cycle during beating is different. To circumvent this difficulty, we use an alternative method to identify the period of a sequence of consecutive cycles based on the positions of the positive and negative peaks in each cycle. In Fig. 3.41, two positive peaks (located at A and B) and one negative peak (located at C) are determined for a given time sequence of the transverse displacement. With this determination, the time period from A to B is taken to correspond to an oscillation cycle. Next, the time intervals AC and BC are divided into four equal parts. An oscillation cycle, of course, can also be determined as the time period between two negative peaks. The division method used here minimizes the influence of the local frequency of beating and, as a result, we obtain a more accurate identification of the wake mode.

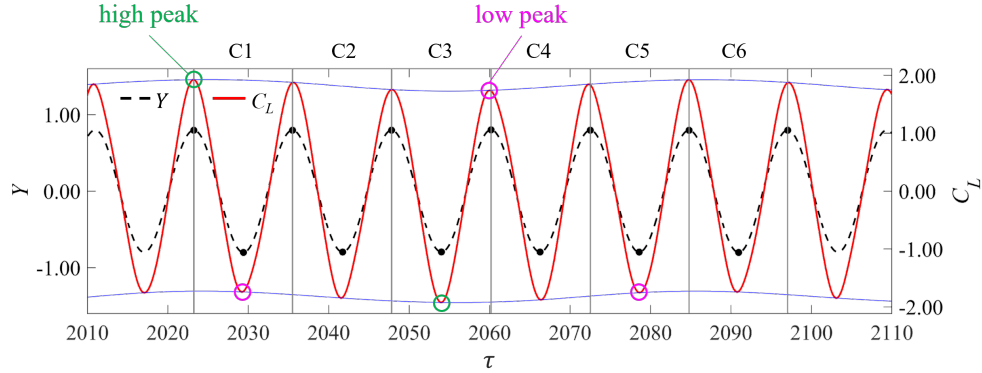


Figure 3.42: Six consecutive oscillation cycles (C1–C6) for analyzing the wake modes of quasi-periodic beating, in terms of the time series of Y (black curve) and C_L (red curve). Blue curves connect multiple positive and negative peaks during beating of $C_L(t)$ and determine the amplitude envelope.

Wake modes during periodic beating

Figure 3.42 exhibits the time sequence of the transverse displacement Y and lift coefficient C_L over six consecutive oscillation cycles (C1–C6) for a cylinder-plate assembly with $L_{SP}/D = 0.75$ at $U_r = 10$ —this reduced velocity corresponds to the non-synchronization branch before the 1:2 synchronization (see Fig. 3.38 (a)). An examination of the amplitude envelopes (blue lines) shows that the beating here is periodic (viz., the beating pattern repeats for every five oscillation cycles) and symmetric (viz., the positive peak is the mirror image of the succeeding negative peak about the horizontal line $C_L = 0$). To study the flow structures that trigger this periodic beating, Fig. 3.43 exhibits the instantaneous vorticity field of the cylinder-plate assembly at various temporal snapshots in C1–C6 (more precisely, there are eight snapshots shown for each cycle). In this figure, the clockwise (negative) and counter-clockwise (positive) vortices are shown in blue and red, respectively.

In the first cycle, two counter-rotating vortices (S and -S) are shed alternately from the lower and upper shear layers of the cylinder at $t = 2T/8$ and $t = 4T/8$ (T is the period of one oscillation cycle) to form a typical anti-symmetric 2S mode. This pattern is repeated again at $t = 6T/8$ to $t = 7T/8$. Therefore, the vortex-shedding mode in C1 is unambiguously identified as “ $2 \times (2S)$ ” (viz., a 2S wake mode shed twice over one oscillation cycle).

In the second cycle, the wake dynamics of the cylinder-plate assembly is more complex. More specifically, a positive vortex is first shed from the lower shear layer at $t = T$, followed

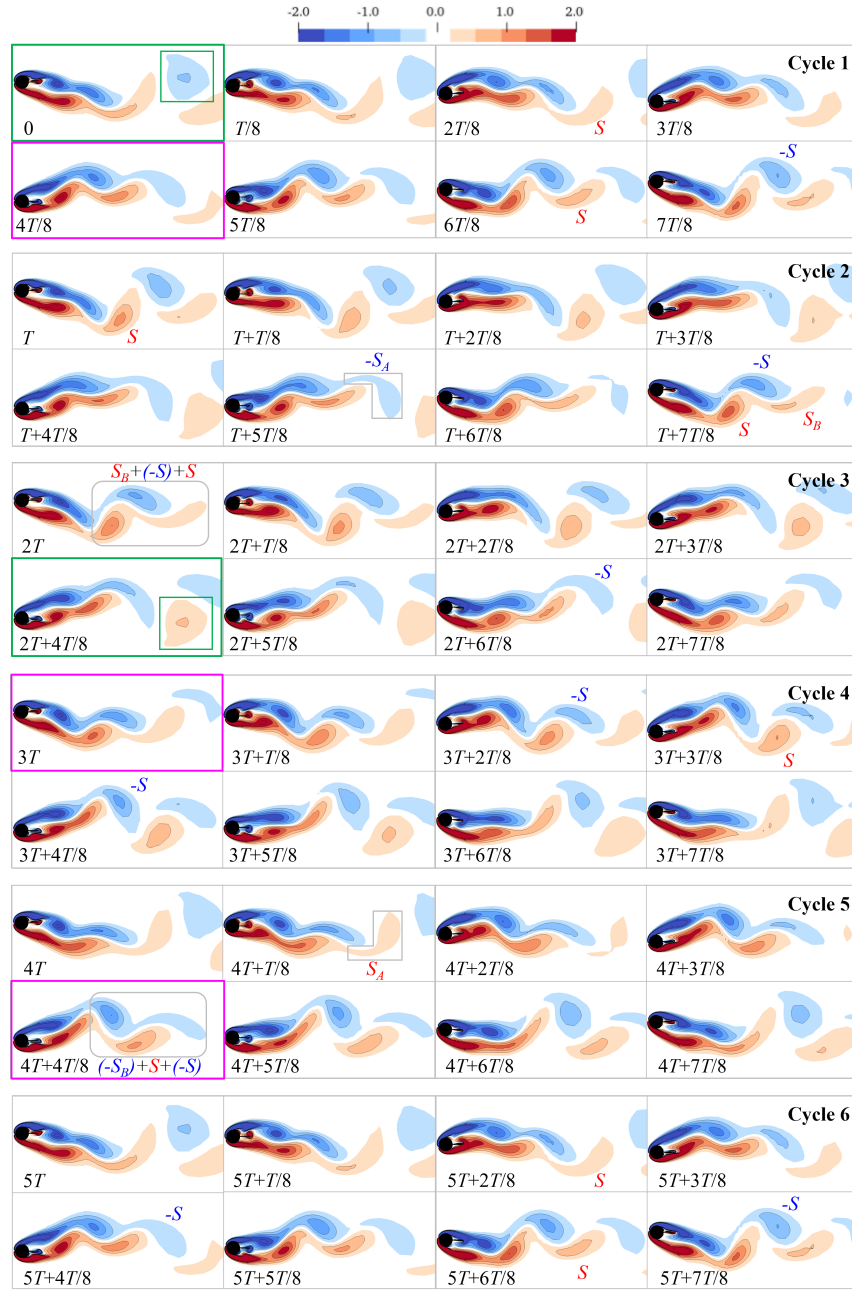


Figure 3.43: Snapshots of the instantaneous vorticity field over six consecutive oscillation cycles (each cycle with period T) for a cylinder-plate assembly with $L_{SP}/D = 0.75$ at $U_r = 10$. Each cycle includes eight vorticity snapshots equally spaced in time. The corresponding wake modes are “ $2 \times (2S)$ ”, “ $S+S_A$ ”, “ $G(S_B+2S)+S$ ”, “ $2 \times (2S)$ ”, “ $S_A+G(S_B+2S)$ ”, and “ $2 \times (2S)$ ”, respectively.

by a downstream extension of the upper shear layer over the first half of C2 which then coalesces to form a specially-shaped vortex (denoted by $-S_A$) at $t = T + 5T/8$. We note that the vortex $-S_A$ identified here has the shape of a right-angle bend consisting of an elongated streamwise portion and an elliptical form in the cross-flow direction, which is similar to the composite vortex designated as S_1S_2 by Sen [132]. The major difference in these two vortical forms is as follows: $-S_A$ always occurs as a whole entity in our analysis, whereas the S_1S_2 mode can appear individually either as an S_1 or an S_2 vortex—this is due to the particular division method used in the analysis conducted by Sen [132]. In consequence, the wake mode in C2 is identified as $S+S_A$.

At the beginning of the third cycle, a group of vortices is shed together from the cylinder-plate assembly—these include an elongated and slightly curved vortex in the streamwise direction (S_B) and a pair of counter-rotating elliptically-shaped vortices (S and $-S$). We note that the crescent-shaped vortex S_B observed here appears to be unique to the cylinder-plate assembly. At $t = 2T + 6T/8$, another vortex $-S$ is shed from the upper shear layer of the cylinder. In view of this, the vortex-shedding mode for C3 is identified as $G(S_B+2S)+S$, where G is used to designate a group of vortices.

The fourth cycle is seen to have simpler wake dynamics, with “ $2 \times (2S)$ ” mode identified. In the fifth cycle, a counter-clockwise right-angled-shaped vortex S_A is generated initially and shed at $t = 4T + T/8$ —following this event, three additional vortices ($-S_B$ and $(2S)$) are shed as one group at $t = 4T + 4T/8$. In consequence, the wake mode in C5 is identified as “ $S_A+G(S_B+2S)$ ”. Finally, the wake pattern in C6 is identical to that in C1—the vortex-shedding pattern corresponds to a “ $2 \times (2S)$ ” wake mode. The upshot of this analysis is that the vortex-shedding pattern of an elastically-mounted cylinder-plate assembly with $L_{SP}/D = 0.75$ repeats over an interval of time spanning five consecutive oscillation cycles.

Except for the periodicity, the beating in Fig. 3.42 also exhibits symmetry. Not coincidentally, a global view of the vorticity field reveals that the wake patterns in C1, C2 and the first half of C3 (encompassing a time span of $2.5T$ in total) are anti-symmetric to that in second half of C3, C4 and C5 (again encompassing a total time span of $2.5T$). This anti-symmetric vortex-shedding pattern is consistent with the five period-doubling oscillation of the symmetrical beating exhibited in Fig. 3.42.

Wake modes during aperiodic beating

The amplitude envelope of some oscillatory motions of a cylinder-plate assembly can be irregular—indeed, complex enough that the time variations of the amplitude modulation

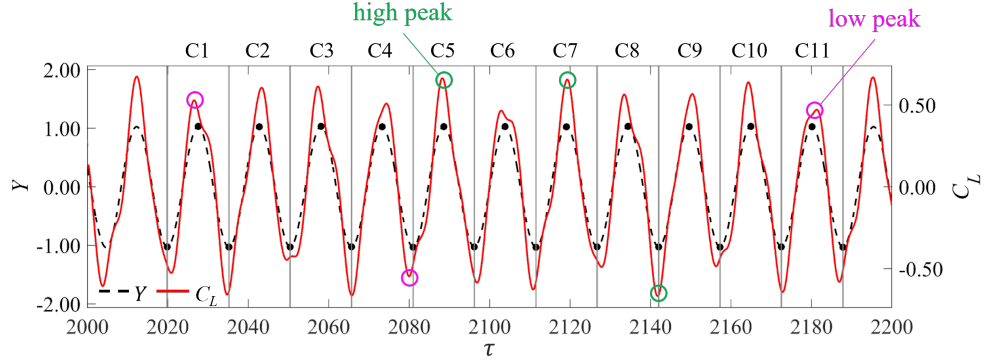


Figure 3.44: Eleven consecutive oscillation cycles (C1–C11) for analyzing the wake modes of aperiodic beating of the lift coefficient. Time series of the transverse displacement Y and lift coefficient C_L are shown as the black and red curves, respectively.

appear to be random. In this section, we focus on the wake dynamics associated with an aperiodic beating.

To this purpose, Fig. 3.44 displays the time series of the transverse displacement Y and lift coefficient C_L over a temporal duration encompassing eleven consecutive oscillation cycles (C1 to C11) of the cylinder-plate assembly with $L_{SP}/D = 0.5$ at $U_r = 14$. This reduced velocity corresponds to the unsynchronized regime between the 1:2 and 1:3 synchronization branches (see Fig. 3.37 (a)). We note that each cycle starts from the negative peak (minimum transverse displacement) rather than from the positive peak (maximum transverse displacement) in Fig. 3.42. Fig. 3.44 shows that the maximum amplitude of $C_L(t)$ exhibits time-varying peaks and valleys without discernible pattern—there is no regularity or periodicity in the amplitude modulation.

Figure 3.45 displays snapshots of the instantaneous vorticity field for five selected cycles: namely, C1, C5, C7, C9, and C11. In the first cycle, a group of three vortices $G(S_B+2S)$ is shed at $t = 2T/8$ and this is followed by the shedding of three additional elliptically-shaped vortices (two $-S$ and one S) in succession at $t = 5T/8$, $6T/8$, and $7T/8$. From these considerations, the wake mode of C1 is identified as “ $G(S_B+2S)+1.5\times(2S)$ ”. In the fifth cycle, “one and a half” $2S$ vortices (two S and one $-S$ vortices) are shed initially, followed by the generation of a right-angled counter-clockwise rotating vortex ($-S_A$)—hence, the wake mode of C5 is “ $1.5\times(2S)+S_A$ ”. In the seventh cycle, a positive right-angled vortex S_A is shed at $t = 6T + 2T/8$ and this is immediately followed by the generation of a $2S$ vortex. At the end of the seventh cycle, another negative right-angled vortex $-S_A$ is shed. This multiplet of vortices shed in C7 is identified as a “ $2\times S_A+2S$ ” wake mode. The ninth

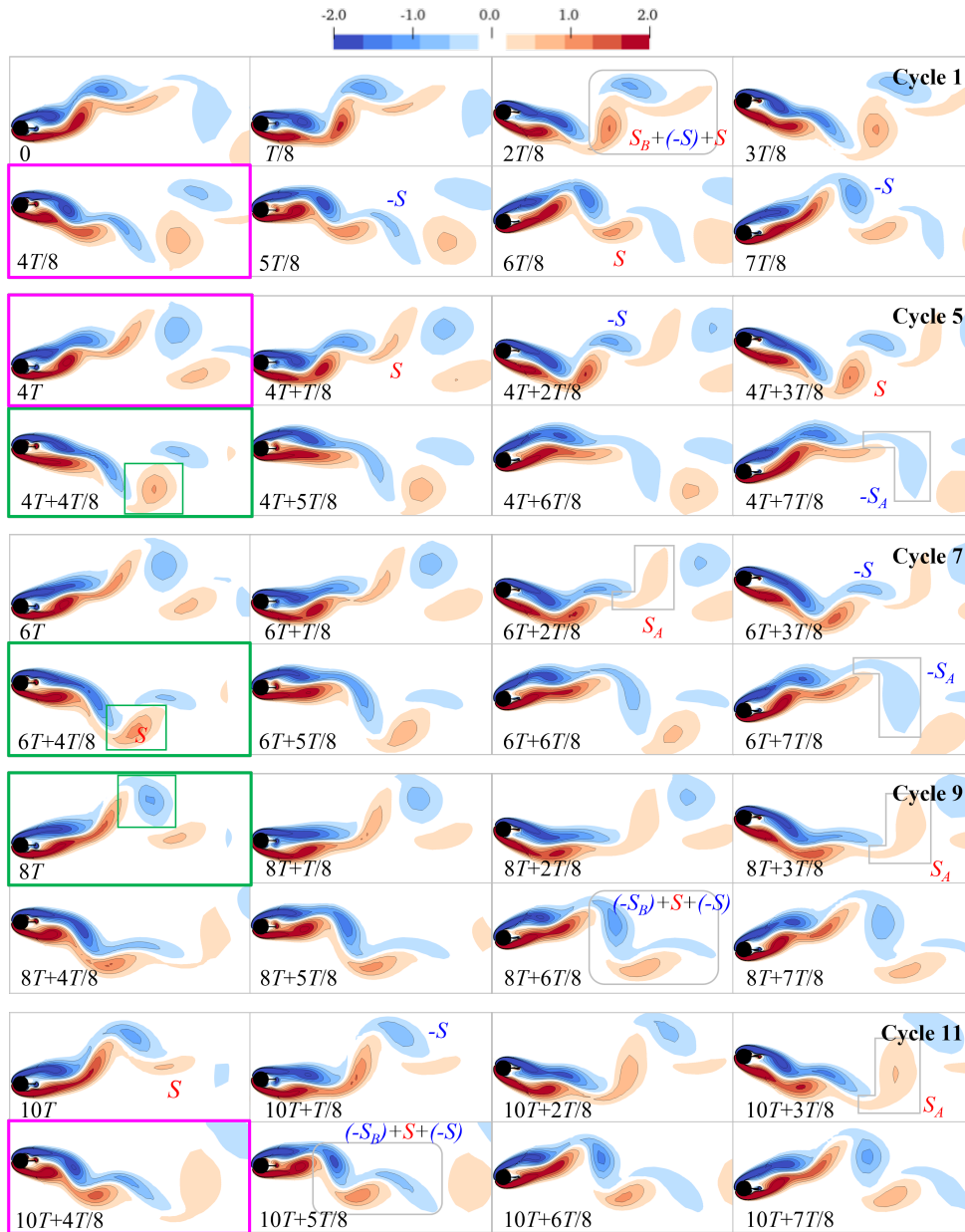


Figure 3.45: Snapshots of the instantaneous vorticity field over five selected oscillation cycles (C1, C5, C7, C9, and C11) for a cylinder-plate assembly with $L_{SP}/D = 0.5$ at $U_r = 14$. Each cycle includes eight snapshots of the vorticity equally spaced in time.

cycle is associated with a “ $S_A+G(S_B+2S)$ ” wake mode. Furthermore, the eleventh cycle involves a more complex wake pattern—a “ $2S$ ” wake mode is shed initially, followed by a right-angled vortex S_A and a three-vortex group “ $G(-S_B+2S)$ ”. Finally, the vortex-shedding patterns associated with the other cycles are summarized as follows: “ $S_A+G(S_B+2S)$ ” for C2, “ $1.5 \times (2S)+S_A$ ” for C3, “ $(2S)+S_A+G(S_B+2S)$ ” for C4, “ $G(S_B+2S)+1.5 \times (2S)$ ” for C6 and C8, and “ $1.5 \times (2S)+S_A$ ” for C10.

The vortex-shedding mode associated with the quasi-periodic beating adheres also to a cyclic pattern with a period that encompasses a number of oscillation cycles (viz., the wake mode is repetitive with a period occupying n consecutive oscillation cycles for an n -period beating). Consequently, there is a close relationship between the wake dynamics and the transverse force. In contrast, the highly irregular and asymmetric wake modes lead to an aperiodic beating with no discernible pattern.

Relationship between beating intensity and flow structures

A careful examination of Figs. 3.42 and 3.44 suggests that the multiple amplitude peaks during one beating cycle of $C_L(t)$ can exhibit different intensities (i.e., higher peaks (marked by the green circle) and lower peaks (marked by the pink circle) in the amplitude envelope). A natural question arises here: *Is there any underlying relationship between the different-intensity amplitude peaks and specific flow patterns?*

To address this question, we examine the instantaneous vorticity field in Figs. 3.43 and 3.45, where the temporal snapshots corresponding to the higher and lower peaks of the amplitude envelope are highlighted in the panels with the green and pink borders, respectively. The higher peak of the amplitude envelope is associated with the shedding of a big circular- or elliptically-shaped vortex (demarcated using the green box in panels with the green borders) from the shear layer of the cylinder. In contrast, the lower peak of the amplitude envelope appears to arise from the steady growth of a group of three vortices that are present downstream of the assembly—this process is not accompanied by any vortex shedding.

The instantaneous vorticity fields at $t = 8T/12$ for the 1:5, 1:6 and 1:7 synchronization branches of a cylinder-plate assembly with $L_{SP}/D = 2$ are displayed Fig. 3.46. The oscillations of both the transverse displacement and lift coefficient within the synchronization branches are highly periodic, consisting of a single amplitude and frequency—no beating occurs, so the beating intensity is zero. This is most likely due to the presence of elliptically-shaped vortices associated with an anti-symmetric “ $n \times (2S)$ ” vortex-shedding pattern, as shown in Fig. 3.46.

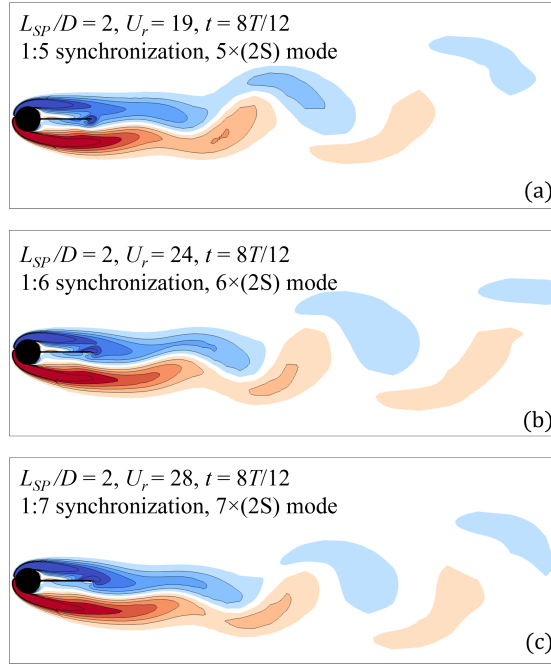


Figure 3.46: Temporal snapshots of the instantaneous vorticity field for the 1:5, 1:6 and 1:7 synchronization branches of a cylinder-plate assembly with $L_{SP}/D = 2$. In this example, C_L undergoes a periodic oscillation without beating.

The wake modes associated with beating are invariably asymmetric—these modes can have a multitude of forms and frequently consist of multiplets that are composed of a number of basic (atomic) vortices. In addition to the conventional elliptically-shaped vortex, two new vortical shapes have been identified for a cylinder-plate assembly: namely, a right-angled vortex (designated S_A) and the crescent-shaped vortex (designated S_B) that are associated with the occurrence of beating. Moreover, the vortex S_B often occurs as a basic component, together with two additional elliptically-shaped vortices, to form a three-vortex group (multiplet). As a consequence, the wake dynamics observed for a cylinder-plate assembly is more complex than that for a square cylinder reported in Sen [132].

3.6 Chapter Summary

In this chapter, the transverse FIV of an elastically-mounted circular cylinder-plate assembly with various plate lengths in the range of $0 \leq L_{SP}/D \leq 4$ is investigated using

numerical simulation at a low Reynolds number $Re = 100$, with a mass ratio of 10 and a zero structural damping ratio.

For $L_{SP}/D \leq 0.5$, a self-limiting oscillation is induced on the cylinder-plate assembly—this consists of either a VIV-only response ($L_{SP}/D = 0.25$) or an integrated VIV-galloping response ($L_{SP}/D = 0.5$). In comparison to the pure VIV of a bare circular cylinder, the former case has a significantly extended lock-in range, whereas the latter case has a larger U_r range for structural motion with a smaller oscillation frequency. For cylinder-plate assemblies with $0.75 \leq L_{SP}/D < 4$, an unlimited oscillation is triggered consisting of a steadily increasing vibration amplitude that is preceded by a VIV regime before the onset of galloping. The two regimes here become increasingly separated from one another as L_{SP} increases (viz., from a significant to no overlap between VIV and galloping). The lift force acting on the circular cylinder has an important contribution on the structural oscillation. In contrast, the lift component acting on the splitter-plate affects more on the dynamics of surrounding flow.

The influence of the splitter-plate length on the branching behavior of the assembly’s FIV is particularly emphasized, as well as the associated flow dynamics and physical mechanisms underpinning these behaviors. Based on branching behavior, five groups of the assembly are categorized: Group I ($L_{SP}/D \leq 0.5$) with a self-limited oscillation; Group II ($L_{SP}/D = 0.75$) with a pure galloping oscillation; Groups III–V ($0.75 < L_{SP}/D < 4$) with a gradually separated VIV (secondary) and galloping (dominated).

Both even- and odd-multiple synchronization branches between the structural oscillation and the vortex shedding are identified for the FIV of cylinder-plate assembly, which appear successively in increasing order, viz., $f_Y^* : f_{C_L}^* = 1:n$ where $n = 1, 2, 3$, and so forth. More precisely, one observes synchronizations with frequency ratios of 1:2, 1:3, and 1:5 for $L_{SP}/D = 0.75$, of 1:1, 1:2, 1:3, 1:4, and 1:5 for $L_{SP}/D = 1$, of 1:1, 1:3, 1:4, and 1:5 for $L_{SP}/D = 1.25$ –1.5, of 1:1, 1:3, 1:4, 1:5, and 1:7 for $L_{SP}/D = 1.75$, of 1:1, 1:3, 1:5, 1:6, and 1:7 for $L_{SP}/D = 2$, of 1:1, 1:3, 1:5 and 1:7 for $L_{SP}/D = 2.5$, and of 1:1 for $L_{SP}/D = 3$ –4. It should be noted that the interesting “Kinks” in the amplitude response of a cylinder-plate assembly within the galloping regime occur at the onset of the synchronization if the highest harmonic frequency in the power spectrum of C_L is larger than that in the power spectrum of Y . The presence of “kinks” results in a slower linear growth of the maximum vibration displacement with reduced velocity. In contrast to the “step” and slow-growth “kink” observed in the galloping of a square cylinder, the “kink” in the amplitude response of a cylinder-plate assembly can exhibit a decrease with U_r for certain plate lengths ($L_{SP}/D = 0.75$ –1.25).

The rich spectrum of branching behavior is associated with the more complex wake dynamics and concomitant vortex-shedding patterns observed for cylinder-plate assembly. To be specific, the classical alternating vortex shedding with a “2S” wake mode occurs in the lock-in branch. In the galloping regime, the odd-multiple synchronization is featured by “ $n \times (2S)$ ” mode (viz., repeat “2S” mode for n times in an oscillation cycle), while the wake patterns associated with the even-multiple synchronizations tend to be more complicated and irregular (e.g., “T+S”, “P+S”).

Two new branches are identified (for the first time) for a cylinder-plate assembly with longer plate length $L_{SP}/D \geq 2.5$. One is the so-called initial galloping branch immediately after the onset of galloping, in which the system oscillation is accompanied by wake meandering, rather than vortex shedding. The other is still branch where the structure is stationary (viz., no vibration) and the flow field is steady (viz., no vortex shedding or meandering of the shear layers). The still branch is essentially due to the complete separation of the shear layers generated on the upper and lower surfaces of the cylinder through the presence of the longer splitter plate.

The nonlinear dynamical characteristics of the cylinder-plate assembly undergoing FIV are also significantly affected by the plate length and reduced velocity. The beating phenomenon (or amplitude modulation) of the oscillation in the lift coefficient usually occurs near the boundary of VIV or in the non-synchronization branch of galloping. In the former, five types of beating are identified based on the relationship between the local frequency of the beating, the structural natural frequency f_n and the Strouhal frequency f_{St} . For the latter case, the beating is characterized qualitatively in terms of global characteristics (periodicity and symmetry). The (net) power transfer between the vibrating assembly and surrounding fluid during beating can be either positive or negative—the former is associated with an increase and the latter with a decrease in the oscillation amplitudes of both Y and C_L .

Three types of nonlinear oscillations are identified for a cylinder-plate assembly. A Type-I nonlinearity is characterized by either a donut-shaped orbit or a limit-cycle consisting of a small number of closed orbits that intersect one another—these correspond to a quasi-periodic beating with a period-doubling oscillation. This situation occurs for an assembly with a moderate splitter-plate length (e.g., $L_{SP}/D = 0.75\text{--}1.5$) over a wide range of U_r , or for an assembly with either a long (e.g., $L_{SP}/D = 2$) or short (e.g., $L_{SP}/D = 0.5$) splitter-plate at small U_r . A Type-II nonlinearity exhibits wide limit cycles composed of numerous loops and corresponds to a long-period beating, which occurs for an assembly with a short splitter-plate near the termination of VIV. A Type-III nonlinearity is associated with disordered phase-plane portraits and corresponds to a chaotic form of oscillation, which occurs for an assembly with a long splitter-plate length at large U_r .

Two new vortex shapes that are specific to the oscillation of a cylinder-plate assembly have been identified: namely, a right-angled vortex S_A and a crescent-shaped vortex S_B . Each of these vortices frequently occur in a multiplet of three vortices that includes two additional elliptically-shaped vortices. Moreover, a wake mode that repeats every n consecutive oscillation cycles leads to a quasi-periodic beating with an n period-doubling oscillation, while an irregular and disordered wake mode is associated with an aperiodic beating having a random amplitude envelope.

Chapter 4

FIV of Elliptical Cylinder-Plate Assembly with Various Aspect Ratios

4.1 Problem Description

This chapter investigates the transverse FIV of an elliptical cylinder with a splitter-plate attachment immersed in a laminar flow ($Re = 100$). As shown in Fig. 4.1, the (elliptical) cylinder-plate assembly is elastically supported by a spring-mass-damper in the transverse (y) direction and subjected to a uniform free-stream velocity U in the streamwise (x) direction. The aspect ratio of the cross-section of the elliptical cylinder is defined as $AR = b/a$ where a and b are respectively the lengths of the ellipse in x and y directions, so the area of the ellipse is $A = \pi ab$. An important quantity—the equivalent length D of the elliptical cylinder—is defined as the diameter of the “equivalent” circular cylinder whose cross-section has the same area as that of the elliptical cylinder, so $D = 2(ab)^{1/2}$. The rigid splitter-plate has a non-dimensional length L_{SP}/D and width $W_{SP}/D = 0.06$. The incident velocity U is aligned with either the major or minor axes of the elliptical cylinder depending on the orientation of the cylinder—for example, when $AR > 1$, the minor axis is aligned in the streamwise direction.

In this chapter, six aspect ratios of the elliptical cylinder are studied: namely, $AR = 0.5$, 0.67 , 0.75 , 1 , 1.5 and 2 . The case $AR = 1$ corresponds to a circular cylinder. The ellipses with $AR = 0.5$ and 2 are geometrically identical, but have a different orientation with respect to the flow incident angle—more precisely, for the cases $AR = 0.5$ and 2 , the major and minor axes of the ellipse are oriented in streamwise direction, respectively. The same is true for the cases $AR = 0.67$ and 1.5 . The range of aspect ratios ($0.5 \leq AR \leq 2$)

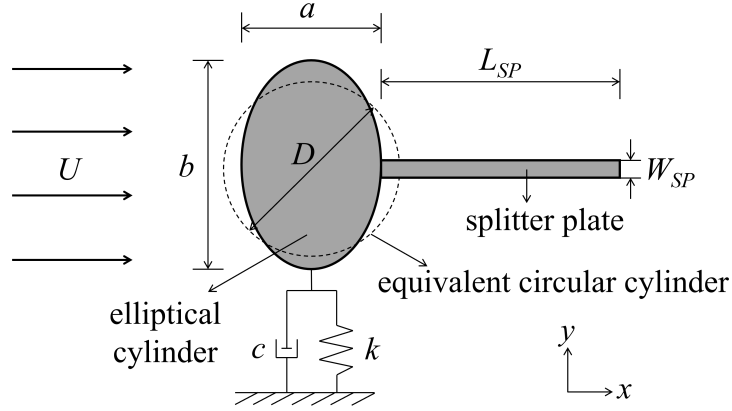


Figure 4.1: A sketch of an elastically-mounted elliptical cylinder-plate assembly constrained to oscillate in the transverse direction. An equivalent circle (with diameter D) whose cross-sectional area is equal to that of an ellipse (with length a and width b) is plotted as the dashed curve.

studied here is determined from some previous works related to the FIV of an elliptical cylinder—these values correspond to a moderate (but not large) geometric deviation from a circular cylinder [192] and this AR range is large enough to explore the influence of the aspect ratio on the dynamic response of an elliptical cylinder-plate assembly. Finally, with the splitter-plate length fixed at a value of $L_{SP}/D = 0.5$, the cases investigated herein correspond to the FIV response occurred in a limited range of reduced velocity.

In order to make a comparison of the cases involving various aspect ratios, the dimensionless quantities used in this chapter are normalized with respect to the equivalent diameter D , rather than the ellipse dimension in the y direction (viz., b) [61, 79, 192] or the length of the major axis (viz., a for $AR < 1$ and b for $AR > 1$) [108]. All the computations are conducted at $Re = 100$, with a low mass ratio of $m^* = 10$ and zero structural damping ratio $\zeta = 0$ in order to facilitate high-amplitude oscillations in the system. Other non-dimensional parameters have similar definitions with that in Chapter 3.

The numerical methodology used in this chapter has been described and validated in detail in Chapter 3. Fig. 4.2 displays the structured grid topology in whole domain and around an elliptical cylinder-plate system.

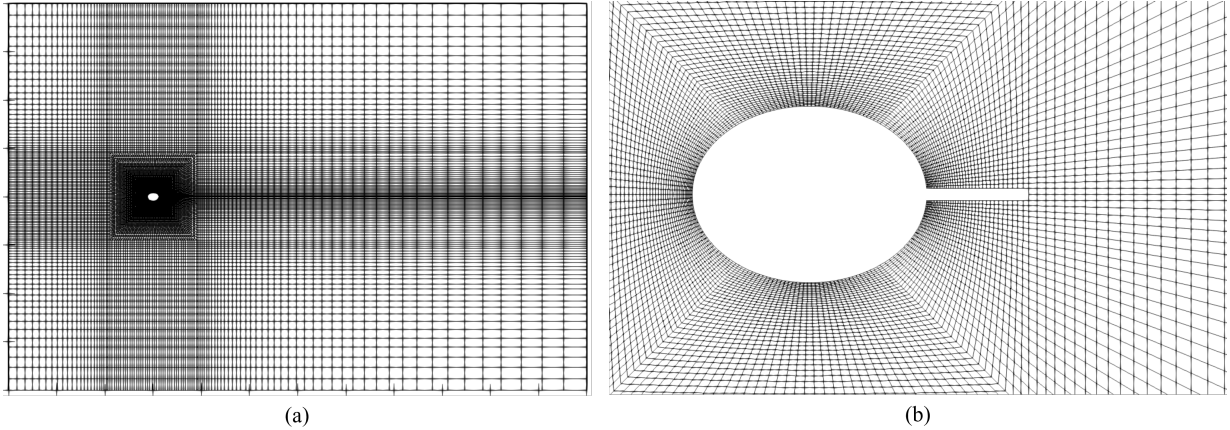


Figure 4.2: The computational mesh used for the numerical simulation of the FIV of an elliptical cylinder-plate assembly: (a) entire domain; (b) in the vicinity of the elliptical cylinder and the splitter-plate.

4.2 FIV Occurred in a Limited Range of U_r

This section discusses in detail the free vibration of an elliptical cylinder with aspect ratio in the range $AR = 0.5\text{--}2$ to which a splitter-plate of length $L_{SP}/D = 0.5$ is attached. As a consequence, all the FIV cases investigated herein are self-limited, viz., the range of reduced velocity over which the assembly undergoes oscillations is limited. The attributes that will be explored include the vibration (oscillatory) characteristics (Section 4.2.1), the branching behavior in conjunction with the power spectral density (PSD) of the transverse vibration displacement Y and the lift coefficient C_L (Section 4.2.2) as well as the dynamical characteristics in the synchronization and non-synchronization branches of the amplitude response (Sections 4.2.3–4.2.4).

4.2.1 Vibration Characteristics

The effects of the elliptical ratio AR and reduced velocity U_r on the self-limited FIV response of an elliptical cylinder-plate assembly are examined with respect to the maximum vibration amplitude Y_{max} , the non-dimensional dominant frequency of the transverse oscillation f_Y^*/f_n , and the aerodynamic forces responsible for these oscillations—the latter includes the root-mean-square lift coefficient $C_{L,rms}$ and the time-averaged (mean) drag coefficient $C_{D,mean}$. These quantities of interest are exhibited as a function of U_r ranging

from 2 to 30 for six values of the elliptical ratio (viz., $AR = 0.5, 0.67, 0.75, 1, 1.5$ and 2) in Fig. 4.3.

An examination of Fig. 4.3 (a) shows that the elliptical cylinder-plate assemblies with $AR = 0.5$ and 0.67 are stationary (viz., these assemblies do not vibrate). The plots of Y_{max} as a function of U_r for these two cases remain at a near-zero value over the entire reduced velocity range—this is associated with a near-zero value of the lift coefficient as seen in Fig. 4.3 (c) and with a constant value of the drag coefficient (viz., $C_{D,mean} = 0.83$ and 0.93 for $AR = 0.5$ and 0.67 , respectively) as seen in Fig. 4.3 (d). However, there are essential differences between these two cases, which are particularly evident on a comparison of their frequency responses as seen in Fig. 4.3 (b). A vibration frequency of zero implies that the structural motion is completely suppressed in the elliptical cylinder-plate assembly with $AR = 0.5$. However, for $AR = 0.67$, f_Y^*/f_n is no longer zero—rather, it is equal to the vortex-shedding frequency of the stationary assembly (with a Strouhal frequency $f_{St} = 0.158$). This suggests that the elliptical cylinder-plate assembly with $AR = 0.67$ actually undergoes oscillations, albeit with a very small amplitude (viz., $Y_{max} \approx 0.001D$). These two stationary cases will be analyzed and explored in greater detail in Section 4.4.2.

In marked contrast, the elliptical cylinder-plate assemblies with $AR \geq 0.75$ undergo a self-limited FIV. Furthermore, changing AR has a significant impact on the resulting dynamic response—more precisely, the maximum vibration amplitude and the effective range of U_r (over which the assembly oscillates) are altered. For example, the onset velocity in an elliptical cylinder-plate assembly with $AR = 0.75$ is $U_r = 6$ —the oscillation in this structure occurs over a limited range $U_r = 6$ –14, resulting in a maximum transverse displacement of $Y_{max} = 0.36D$. As AR increases to unity (circular cylinder), the FIV response occurs over a much wider range $U_r = 6$ –20, associated with a smaller onset $U_r = 5$ and a larger maximum vibration amplitude $Y_{max} = 1D$. For the case of $AR = 1.5$, the structural oscillation in the assembly is further enhanced—the vibration occurs over a wider range $U_r = 6$ –24, showing a larger Y_{max} of around $2D$, although the onset velocity is roughly the same as that of the circular cylinder-plate assembly. From these considerations, it is seen that increasing AR from 0.75 to 1.5 leads gradually to the promotion of a self-limited FIV in the assembly through both an enlargement of the effective reduced-velocity range and an increase in the value of Y_{max} . In contradistinction, when the aspect ratio is $AR = 2$, this trend is reversed in certain respects—more precisely, the U_r range with FIV is reduced significantly (viz., $U_r = 6$ –16), although Y_{max} and the onset velocity remain essentially the same.

Unlike the amplitude response, the frequency response exhibited in Fig. 4.3 (b) does not depend strongly on the aspect ratio. Indeed, all the dominant frequencies of the transverse displacement for all cases of the aspect ratio are essentially the same, which

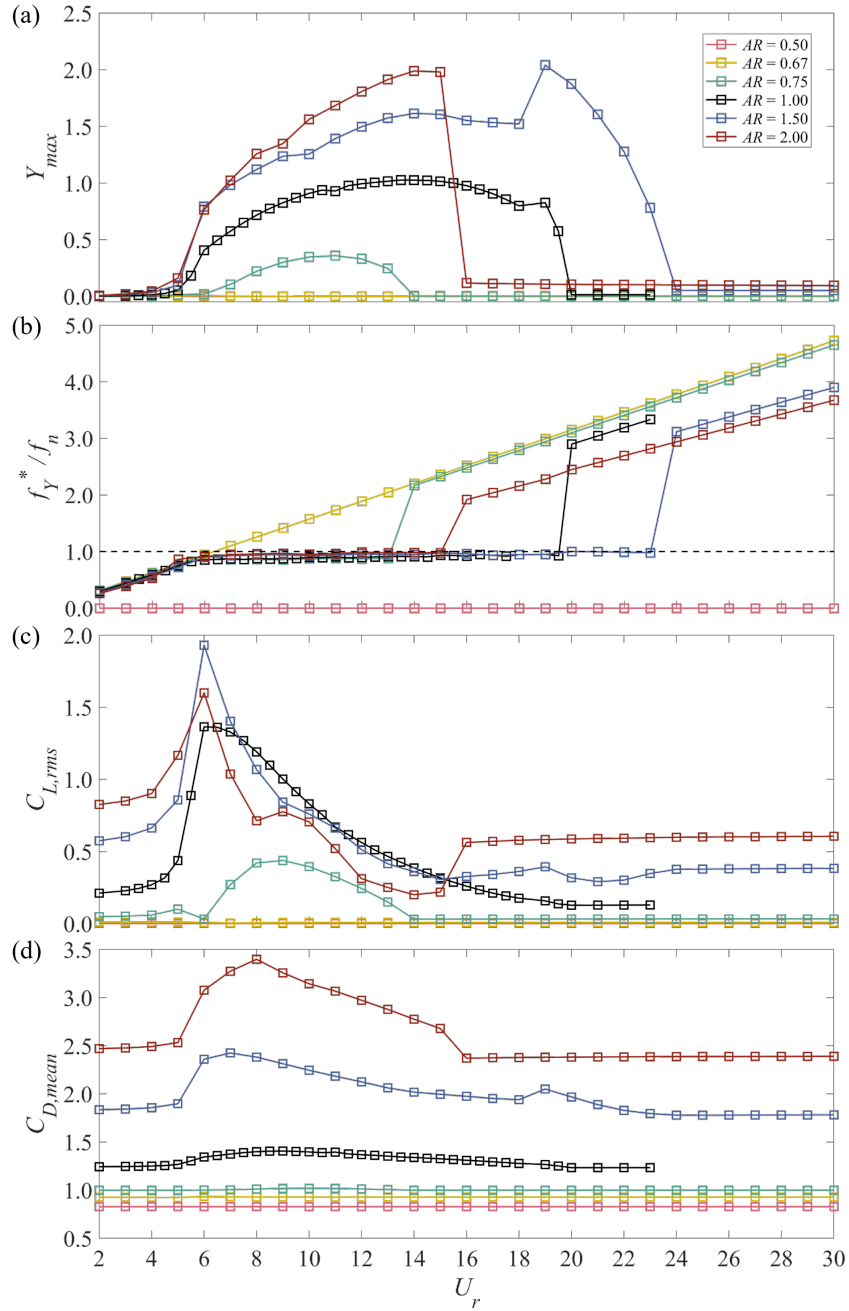


Figure 4.3: (a) The non-dimensional maximum transverse displacement Y_{max} ; (b) the dominant frequency of oscillation f_Y^*/f_n ; (c) the root-mean-square lift coefficient $C_{L,rms}$; and, (d) the mean drag coefficient $C_{D,mean}$. All these quantities are plotted as a function of U_r for six values of elliptical ratio: $AR = 0.5, 0.67, 0.75, 1, 1.5$ and 2 .

are approximately equal to the structural natural frequency (viz., f_Y^*/f_n is in the range 0.9–1.0) within the FIV regime and are equal to the associated Strouhal frequencies out of the FIV regime. Moreover, both the lift and drag coefficients exhibit a rapid increase near the onset velocity of FIV—larger peak values of the lift are associated with larger maximum transverse displacements (cf. Figs. 4.3 (a) and (c)) and the maximum drag increases monotonically with an increasing elliptical ratio (see Fig. 4.3 (d)).

4.2.2 Branching Behavior

Figure 4.4 displays the branch identification in the vibration amplitude responses of various elliptical cylinders ($AR = 0.75, 1, 1.5$ and 2) with a splitter-plate attachment of length $L_{SP}/D = 0.5$. Figs. 4.5–4.6 show the corresponding power spectral density (PSD) isopleths of the frequency in the system vibration f_Y and in the transverse force acting on the assembly f_{C_L} . The construction of PSD contours in this section is the same as that in Section 3.4.1.

As can be seen in Fig. 4.4 (a), no synchronization branch between the system oscillation and the vortex shedding is identified for $AR = 0.75$, although its amplitude response exhibits a broad maximum. This is further supported by the fact that the dominant frequency of the transverse displacement is a constant with a value around f_n (see Fig. 4.5 (b)) over $U_r = 6$ –14. Furthermore, the power spectrum of lift coefficient over this reduced-velocity range consists of a constant dominant frequency (dark-colored horizontal band) of about f_n and harmonic frequencies (light-colored diagonal band) as seen in Fig. 4.6 (b). This analysis suggests that the self-limited FIV of an elliptical cylinder-plate assembly with $AR = 0.75$ is still associated with the vortex shedding from the assembly. However, the vortices are not shed at an integral multiple of the system oscillation frequency—that’s why no synchronization branch is observed. Moreover, the absence of synchronization may explain why the $Y_{max} = 0.4D$ here is smaller than other cases.

In marked contrast, three synchronization branches corresponding to $f_Y^*/f_{C_L}^* = 1:1, 1:2$ and $1:3$ are evident for the elliptical cylinder-plate assemblies with $AR = 1, 1.5$ and 2 , as seen in Figs. 4.4 (b)–(d). In these cases, the assemblies enter the lock-in regime (or, 1:1 synchronization) at a reduced velocity slightly larger than the onset of VIV—the VIV response occurs over a certain reduced-velocity range (viz., $U_r = 5.5$ –10 for $AR = 1$, $U_r = 6$ –9.5 for $AR = 1.5$, $U_r = 6$ –8 for $AR = 2$). The corresponding PSD isopleths of the transverse displacement only exhibit a single (dominant) frequency (see Figs. 4.5 (c)–(e)), while that of the lift coefficient display multiple weaker odd harmonics with $f_{C_L}/f_n = 3, 5$, and 7 as is evident on examination of Figs. 4.6 (c)–(e).

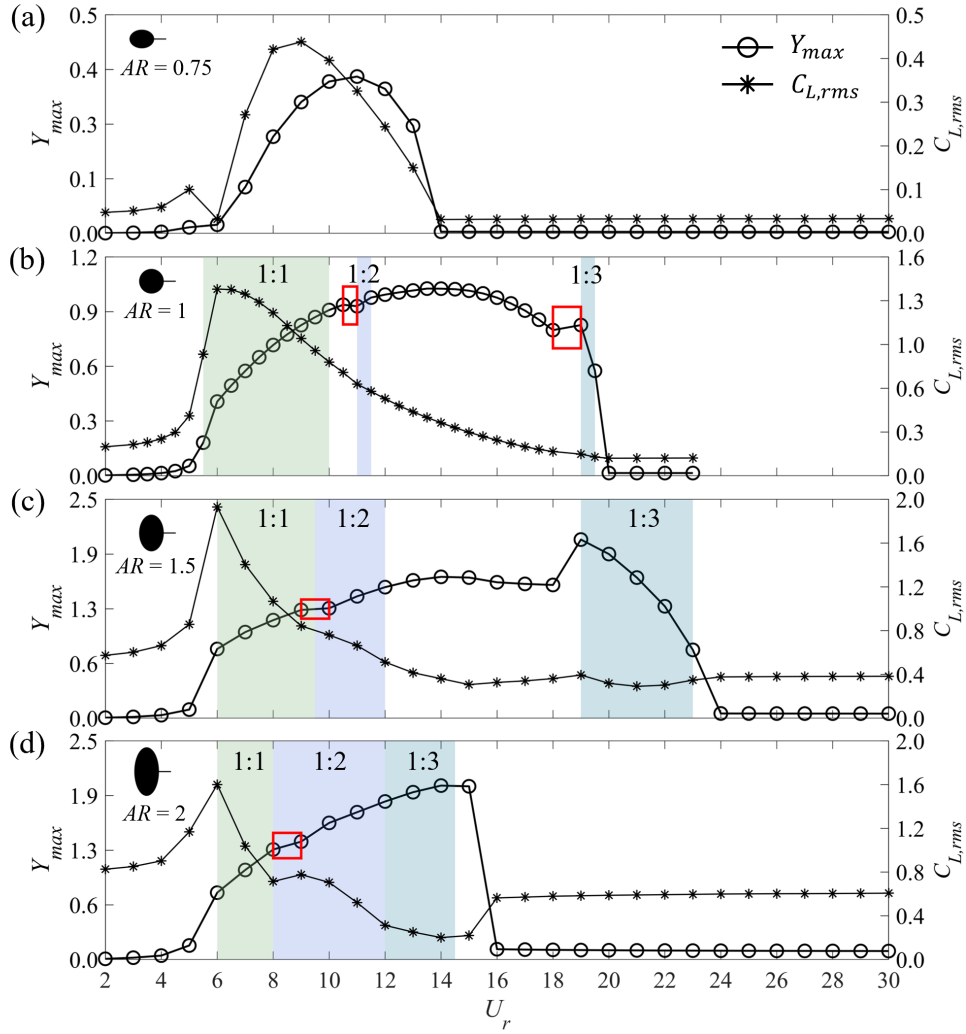


Figure 4.4: The branch identification of the FIV for an elliptical cylinder-plate assembly with a fixed plate length $L_{SP}/D = 0.5$ and various aspect ratios: (a)–(d) $AR = 0.75, 1, 1.5$ and 2 . In each case, the maximum transverse displacement Y_{max} and the root-mean-square lift coefficient $C_{L,rms}$ are shown as function of U_r . The synchronization branches in the amplitude response are identified as the shaded regions with different colours. “Kinks” in the amplitude responses are marked by the red boxes.

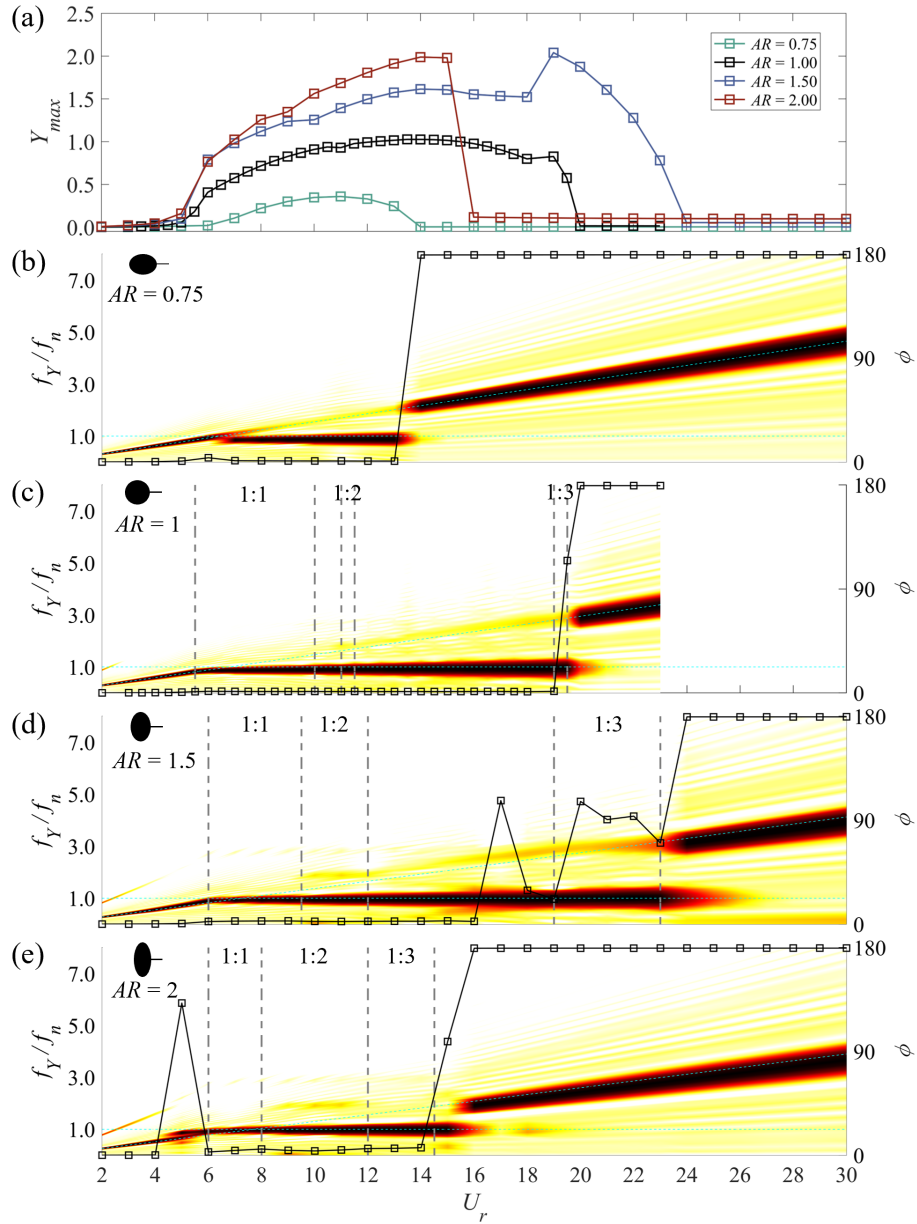


Figure 4.5: (a) The maximum transverse displacement Y_{max} as a function of U_r for an elliptical cylinder-plate assembly with various aspect ratios. PSD of Y plotted against f_Y/f_n and U_r for (b)–(e) $AR = 0.75, 1, 1.5$ and 2 . In (b)–(e), the vertical, horizontal and diagonal dashed lines represent the boundaries of synchronization branches, the unit normalized frequency $f_Y/f_n = 1$ and the Strouhal frequency f_{St} , respectively. The solid line with squares represents the phase difference ϕ between the oscillations in Y and C_L .

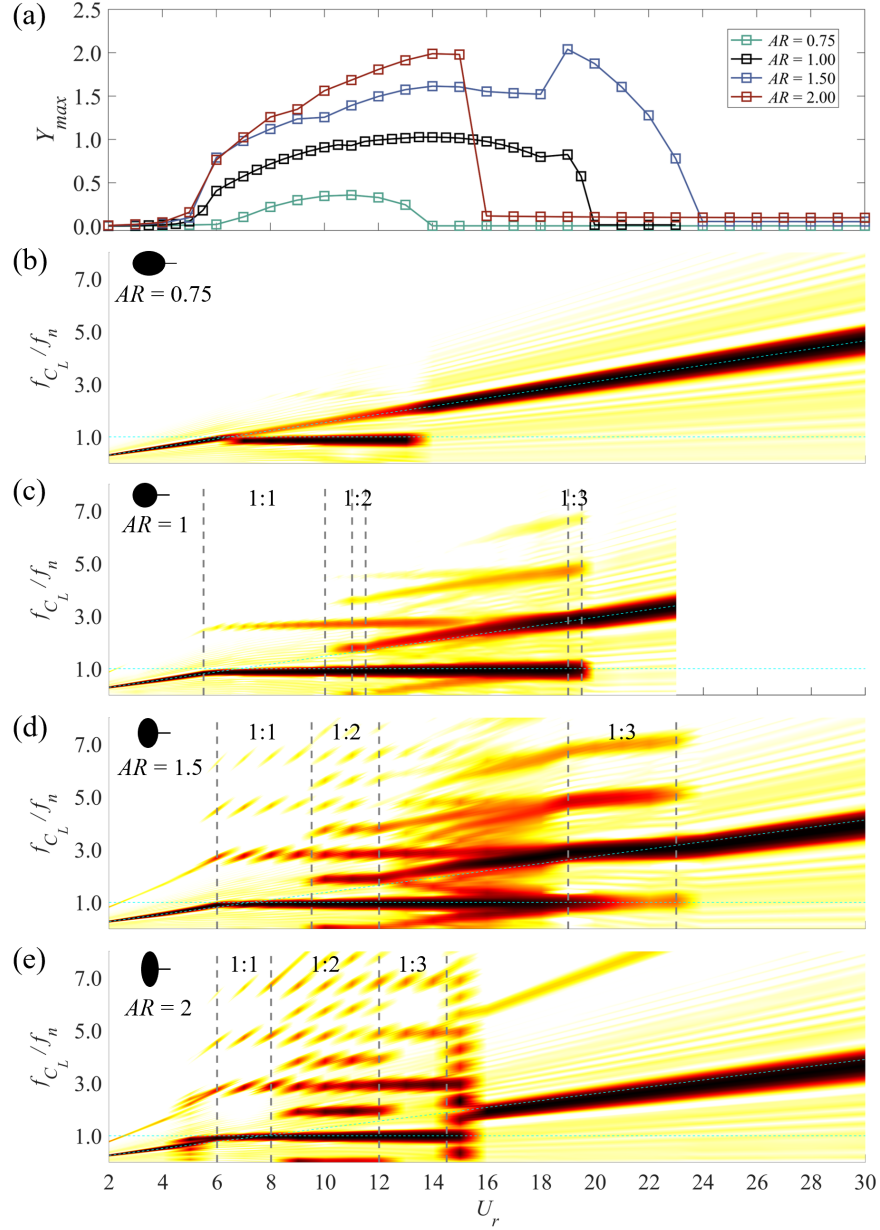


Figure 4.6: (a) The maximum transverse displacement Y_{max} as a function of U_r for an elliptical cylinder-plate assembly with various aspect ratios. PSD (logarithmic scale) of C_L plotted against f_Y/f_n and U_r for (b)–(e) $AR = 0.75, 1, 1.5$ and 2 . Other notations used here are the same as those in Fig. 4.5.

In Figs. 4.4 (b)–(d), it is seen that the beginning of the 1:2 synchronization is associated with the presence of a “kink” in the amplitude response (marked by the red box). The 1:2 synchronization is either separated from (for $AR = 1$) or contiguous with (for $AR = 1.5$ and 2) the lock-in regime. The corresponding U_r ranges are $U_r = 11$ –11.5 for $AR = 1$, $U_r = 9.5$ –12 for $AR = 1.5$, and $U_r = 8$ –12 for $AR = 2$. In the 1:2 synchronization, the transverse displacement PSD consists of a single dominant frequency around f_n , but the power spectrum of the transverse force has a more complicated frequency structure consisting of both odd- and even-harmonics.

Near the upper bound for the existence of self-limited oscillations in the elliptical cylinder-plate assembly, a 1:3 synchronization branch is identified. This branch is either separate from (for $AR = 1$ and 1.5) or contiguous with (for $AR = 2$) the 1:2 synchronization. The corresponding reduced-velocity ranges are $U_r = 19$ –19.5 for $AR = 1$, $U_r = 19$ –23 for $AR = 1.5$, and $U_r = 12$ –14.5 for $AR = 2$. Moreover, the assembly oscillates primarily at f_n , although the third-harmonic is evident within the 1:3 synchronization for the case $AR = 1.5$ (cf. Fig. 4.5 (d)). However, in the transverse force PSD, the even harmonics ($f_{C_L}/f_n = 2, 4, 6$) disappear and the odd harmonics ($f_{C_L}/f_n = 3, 5, 7$) become more prominent—this is especially true for the third-harmonic whose power level is comparable to (for $AR = 1$ and 2) or even larger than (for $AR = 1.5$) that of the fundamental frequency.

In summary, increasing AR of an elliptical cylinder-plate assembly from $AR = 1$ to 2 reduces the lock-in regime, widens the U_r range over which the higher-order (e.g., 1:2 and 1:3) synchronization branches occur, and results in a more complicated frequency structure in the transverse force power spectra. However, the aspect ratio has no significant effect either on the frequency content of the transverse displacement power spectra or on the dominant frequency of Y and C_L .

4.2.3 Periodic Oscillation in Synchronization Branch

This section focuses on various aspects of the dynamical response in the synchronization branches identified above (viz., 1:1, 1:2 and 1:3), including time series, phase portraits, Lissajous figures, power spectra of the transverse displacement Y and lift coefficient C_L , as well as the associated vortex-shedding patterns. Owing to the fact that no synchronization branch is observed in an elliptical cylinder-plate assembly with $AR = 0.75$, we focus only on the elliptical cylinder-plate assemblies with $AR = 1, 1.5$ and 2.

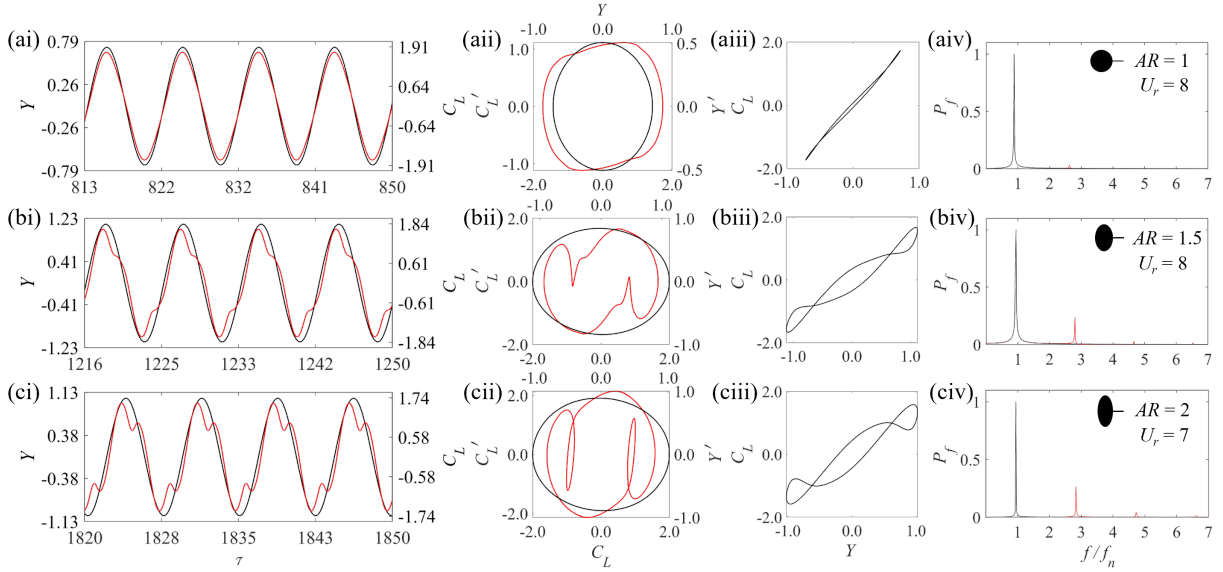


Figure 4.7: Dynamical characteristics in the 1:1 synchronization branch (viz., lock-in) for an elliptical cylinder-plate assembly with (a) $AR = 1$ and $U_r = 8$; (b) $AR = 1.5$ and $U_r = 8$; and, (c) $AR = 2$ and $U_r = 7$. The dynamical characteristics are displayed in terms of the time series of Y and C_L (first column of panels), the phase portraits C_L-C_L' and $Y-Y'$ (second column of panels), the Lissajous figures $Y-C_L$ (third column of panels), and the normalized power spectra of Y and C_L (fourth column of panels). In all plots, the results for Y and C_L are presented as black and red curves, respectively.

The 1:1 synchronization

The effect of the aspect ratio of an elliptical cylinder-plate assembly on the dynamical characteristics in the 1:1 (or, lock-in) synchronization branch is displayed in Fig. 4.7 for a reduced velocity of either $U_r = 7$ or 8. The oscillations of $Y(t)$ and $C_L(t)$ for all three aspect ratios are clearly periodic as is evident on examination of the time series (first column of panels) and the closed curves of the associated phase portraits and Lissajous figures (second and third columns of panels). Moreover, as AR increases from 1 to 1.5, $C_L(t)$ is no longer sinusoidal—the elliptical shape of associated phase portrait C_L-C_L' becomes more irregular, the number of closed loops in the Lissajous curve $Y-C_L$ increases from 1 to 3, and a third-harmonic frequency is present in the power spectrum of $C_L(t)$. These characteristics suggest that the dynamics become more complex with an increase in the aspect ratio. For the largest value of $AR = 2$ studied herein, the complexity of the lock-in regime increases further. This is evident on perusal of Fig. 4.7 (c)— $C_L(t)$

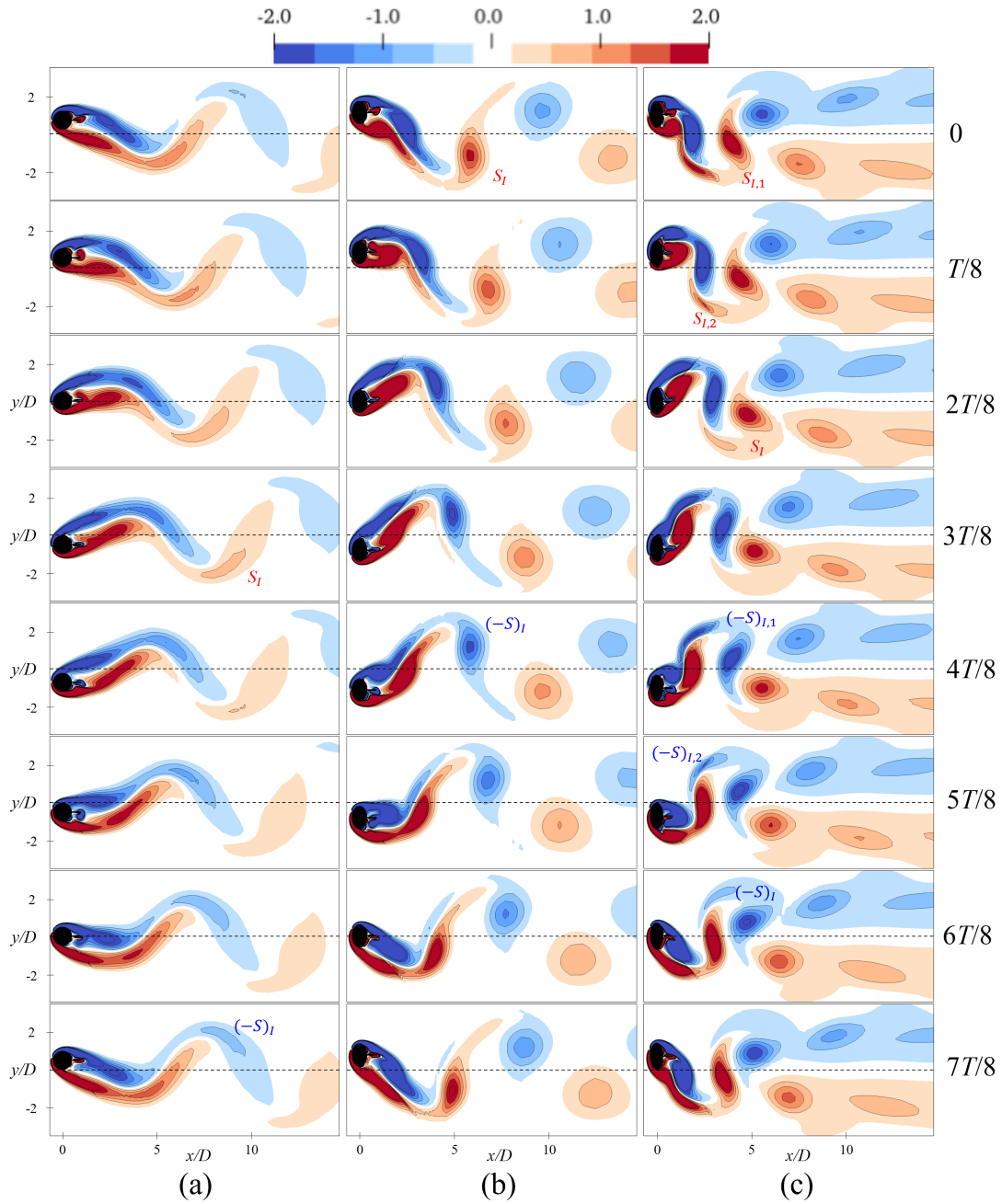


Figure 4.8: Instantaneous vorticity fields in one oscillation cycle T within the 1:1 synchronization branch (viz., lock-in) for an elliptical cylinder-plate assembly with (a) $AR = 1$ and $U_r = 8$; (b) $AR = 1.5$ and $U_r = 8$; and, (c) $AR = 2$ and $U_r = 7$. The “2S” mode is observed for the three cases.

exhibits a more complex temporal waveform and C_L-C_L' and $Y-C_L$ consist of multiple loops, suggesting the emergence of not only a strong third-harmonic frequency but also a weaker fifth-harmonic frequency in the C_L power spectrum. By contrast, the transverse displacement Y is basically not affected by aspect ratio.

Figure 4.8 exhibits the more complex flow dynamics within the lock-in regime with increasing AR . For a circular cylinder-plate assembly (cf. Fig. 4.8 (a)), two counter-rotating elliptically-shaped vortices, consisting of a counter-clockwise positive vortex S_I and a clockwise negative vortex $-S_I$, are shed alternately during one oscillation cycle to form the classical Kármán vortex street downstream of the assembly. For this case, the wake mode is identified as a regular “2S” mode. A similar vortex-shedding pattern is observed for the case $AR = 1.5$ at the same reduced velocity $U_r = 8$ as is evident on examination of Fig. 4.8 (b). However, in this case, the shape of the vortex consists of a core with a long trailing tail when it is shed from the shear layer formed along the cylinder surface and, subsequently, this tail disappears gradually as it evolves downstream to form a circular vortex consisting of only the core region. In Fig. 4.8 (c), the flow pattern becomes even more complex at a larger aspect ratio $AR = 2$. Although there are still two vortices shed alternately over one oscillation cycle, each vortex shed here is composed of two small vortices. More precisely, two connected small vortices $S_{I,1}$ and $S_{I,2}$ are evident at $t = 0$ and $t = T/8$, respectively, which are shed together at $t = 2T/8$ to form a larger swallow-tail-shaped vortex S_I —this vortex subsequently merges into the downstream vortex street. A similar pattern occurs for the negative vortices shed at $t = 4T/8-6T/8$. It stressed that the two opposite-signed parallel vortex streets formed in the wake are unique to the elliptical cylinder-plate assembly with $AR = 2$.

The 1:2 synchronization

Figure 4.9 exhibits the dynamical characteristics associated with the 1:2 synchronization branch for various aspect ratios (namely, $AR = 1, 1.5$ and 2) of an elliptical cylinder-plate assembly at $U_r = 11$. The most striking feature is the asymmetrical characteristics of the transverse force for the elliptical cylinders with non-unity aspect ratios— $C_L(t)$ exhibits two local maxima for each peak value observed in the $Y(t)$ (cf. Figs. 4.9 (bi) and (ci)). The phase portraits C_L-C_L' and Lissajous figures $Y-C_L$ are also asymmetric (cf. Figs. 4.9 (bii), (biii), (cii), and (ciii)). The asymmetry displayed here can be closely associated with distinctive vortex-shedding patterns—this will be explored further in the analysis presented in Fig. 4.10. Furthermore, it is seen that even-multiple harmonics are present in the power spectra of C_L and the second harmonic has a larger power level than other harmonics—indeed, this is the reason for the identification of this branch as a 1:2 synchro-

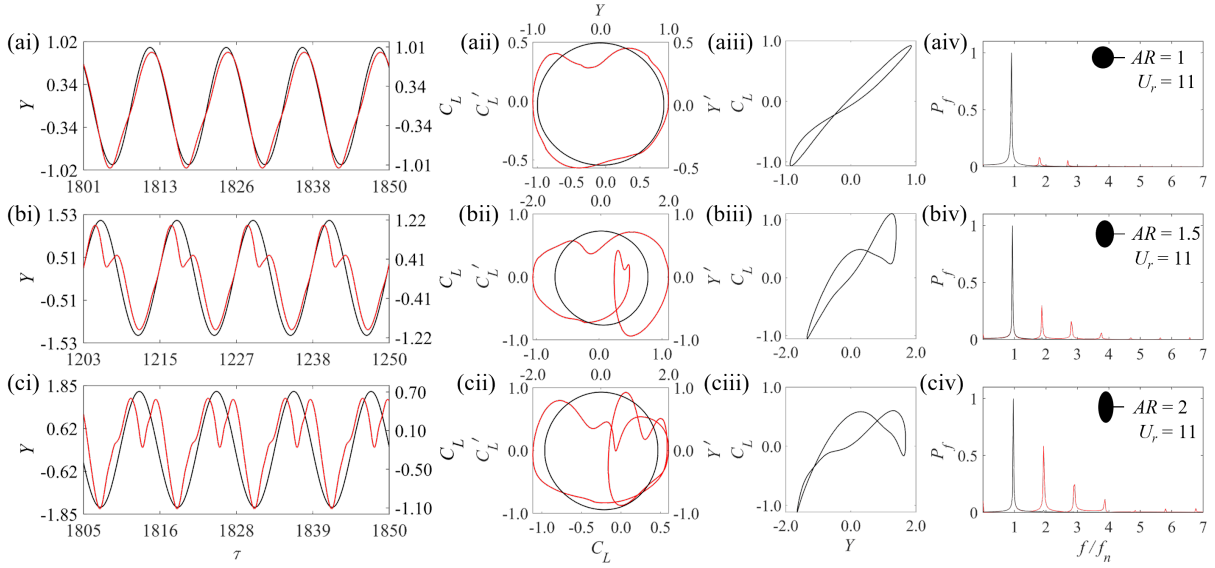


Figure 4.9: Dynamical characteristics in the 1:2 synchronization branch for an elliptical cylinder-plate assembly with (a) $AR = 1$ and $U_r = 11$; (b) $AR = 1.5$ and $U_r = 11$; and, (c) $AR = 2$ and $U_r = 11$. The notations used here are the same as those described in the caption of Fig. 4.7.

nization. Similar to the lock-in regime, an increasing aspect ratio is associated with more complex dynamics in the 1:2 synchronization branch—this is evident on a comparison of the sinusoidal waveform of $C_L(t)$ for $AR = 1$ with the more complex waveforms of $C_L(t)$ for $AR = 1.5$ and 2 and the more complex loop structure in the associated phase portraits.

Compared to the simple “2S” mode of the lock-in regime, the vortex-shedding patterns associated with the 1:2 synchronization branch are generally more complex. As shown in Fig. 4.10 (a), the “2S” mode is repeated twice (viz., “ $2 \times (2S)$ ”, with four vortices are shed in total) over one oscillation cycle for a circular cylinder-plate assembly at $U_r = 11$. As reported in Section 3.4.1, the wake mode in the 1:2 synchronization for a circular cylinder-plate assembly is “T+S” (triplet and singlet) for $U_r = 11.5$. For $AR = 1.5$, the vortex-shedding pattern in the 1:2 synchronization has a similar behavior as that for $AR = 1$ —the wake mode transitions from a “2S” mode to a “T+S” mode with an increasing value of U_r . For example, in Fig. 4.10 (b), the triplet of vortices, namely, $-S_I, -S_{II}, S_I$ (delineated by the box with the black dashed lines), is shed at $t = 3T/8$ and then a single vortex S_{II} is shed at $t = 6T/8$ to form a “T+S” mode at $U_r = 11$. Figs. 4.10 (c)–(e) display the complex vortex-shedding patterns associated with three values of the reduced velocity—namely,

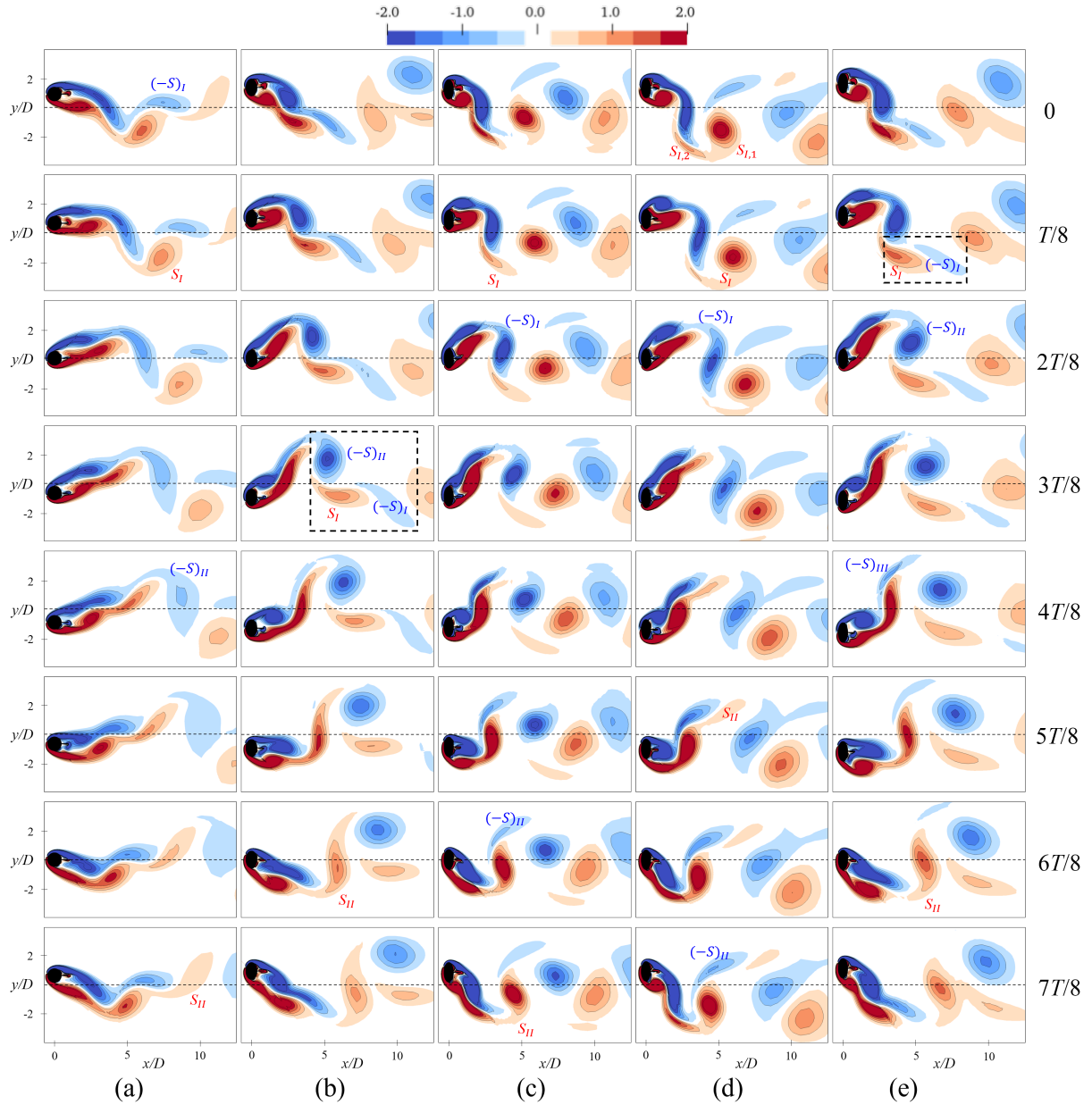


Figure 4.10: Instantaneous vorticity fields in one oscillation cycle within the 1:2 synchronization branch for an elliptical cylinder-plate assembly with (a) $AR = 1$ and $U_r = 11$; (b) $AR = 1.5$ and $U_r = 11$; (c) $AR = 2$ and $U_r = 8$; (d) $AR = 2$ and $U_r = 10$; and, (e) $AR = 2$ and $U_r = 11$. The wake modes are identified as “ $2 \times (2S)$ ”, “ $T+S$ ”, “ $\pm(2S)$ ”, “ $2 \times (2S)$ ” and an irregular mode for the five cases, respectively.

$U_r = 8, 10$ and 11 in the 1:2 synchronization branch for $AR = 2$. At $U_r = 8$, the two “2S” modes shed in one oscillation cycle are not simply a repetition of one another—rather, they are inverses of each other (viz., $(S_I, -S_I)$ and $(-S_{II}, S_{II})$), which suggests a non-alternating vortex-shedding pattern which is identified as a “ $\pm(2S)$ ” mode here. At $U_r = 10$, the wake mode is “ $2 \times (2S)$ ”, and the first primary vortex S_I is composed of two smaller vortices designated as $S_{I,1}$ and $S_{I,2}$. The irregular vortex-shedding pattern at $U_r = 11$ does not belong to any known wake mode. More specifically, one pair of vortices $(S_I, -S_I)$ are shed first, then a single negative vortex $-S_{II}$ is shed, followed by the shedding of another vortex $-S_{III}$ and, finally, a positive vortex S_{II} is shed. Hence, five vortices are shed in total over one oscillation cycle. The shapes of the vortices and/or the vortex-shedding patterns shown in Fig. 4.10 are anti-symmetric and this is consistent with the asymmetry in the dynamical characteristics displayed in Fig. 4.9. Furthermore, the wake modes in the 1:2 synchronization branch are different at different values of the reduced velocity.

The 1:3 synchronization

Figure 4.11 displays the dynamical characteristics associated with the 1:3 synchronization branch. It is noted the reduced velocity associated with the 1:3 synchronization for $AR = 2$ (viz., $U_r = 12$ – 14) is smaller than that for $AR = 1$ and 1.5 ($U_r \geq 19$). In view of this, we display only the dynamical characteristics of the assembly at $U_r = 13$ (rather than $U_r = 19$) for the case of $AR = 2$.

A careful examination of the power spectra of C_L shows that the even harmonics of the fundamental frequency are absent and only the odd harmonics are present. Moreover, the third harmonic in these C_L -power spectra is significantly more prominent than that in the corresponding power spectra for the 1:1 synchronization. For $AR = 1.5$, the C_L power associated with the third harmonic is even larger than that of the fundamental frequency as seen in Fig. 4.11 (biv). This implies that the transverse force here is dominated by the third-harmonic frequency. The corresponding $C_L(t)$ shows the presence of multiple local maxima within every cycle of Y (cf. Fig. 4.11 (bi)), albeit the waveform is still periodic. However, the phase portrait C_L - C_L' shown in Fig. 4.11 (bii) consists of multiple (closed) loops that is suggestive of a quasi-periodic beating [180]. The nonlinear dynamics associated with the 1:3 synchronization branch for $AR = 2$ does not exhibit an increase in complexity, owing to the fact that it corresponds to a smaller reduced velocity of $U_r = 13$.

The vortex-shedding patterns corresponding to the 1:3 synchronization branch are shown in Fig. 4.12. A “ $3 \times (2S)$ ” wake mode (viz., a “2S” mode repeated three times in one oscillation cycle) is identified for the cases of $AR = 1$ and 1.5 at $U_r = 19$ on a careful perusal of Figs. 4.12 (a)–(b). In Fig. 4.12 (c), it is seen that one pair of vortices

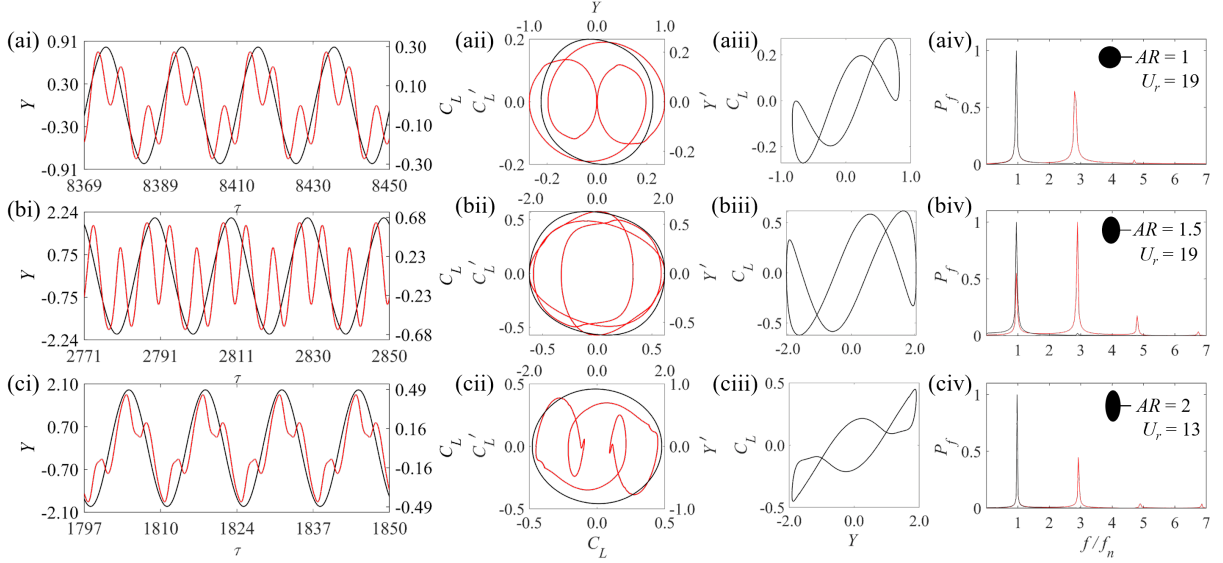


Figure 4.11: Dynamical characteristics in the 1:3 synchronization branch for an elliptical cylinder-plate assembly with (a) $AR = 1$ and $U_r = 19$; (b) $AR = 1.5$ and $U_r = 19$; and, (c) $AR = 2$ and $U_r = 13$. The notations used here are the same as those described in the caption of Fig. 4.7

$(S_I, -S_I)$ are shed together at $t = T/8$, followed by the subsequent shedding of a single vortex $-S_{II}$ at $t = 2T/8$. This combination of vortices forms the so-called “P+S” mode over the first quarter of the oscillation cycle. Moreover, this process repeats again, albeit with opposite signs of the vortices, at $t = 5T/8$ and $6T/8$ in the last quarter of the oscillation cycle. Therefore, the wake mode over one oscillation cycle is identified as “ $2 \times (P+S)$ ” for $AR = 2$ at $U_r = 13$.

Summary

For the elliptical cylinder-plate assembly undergoing a self-limited FIV, increasing the aspect ratios AR will increase the complexity of the flow dynamics associated with the synchronization branches. However, an increasing AR has essentially no effect on the temporal variations in the transverse displacement Y . Furthermore, all the Lissajous plots shown in Figs. 4.7, 4.9 and 4.11 are inclined towards the first and third quadrants of the (Y, C_L) plane—this implies that C_L and Y are in-phase in the various synchronization

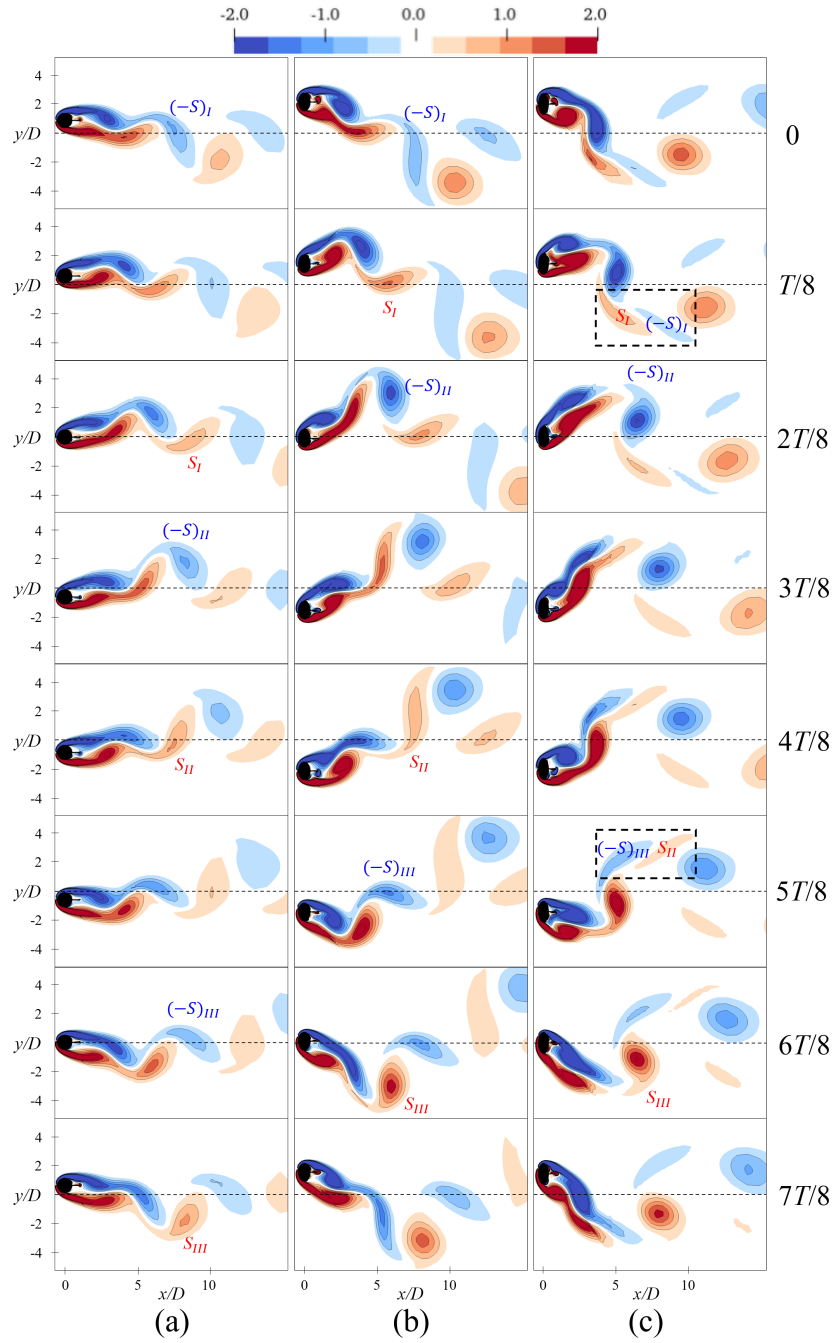


Figure 4.12: Instantaneous vorticity fields in one oscillation cycle within the 1:3 synchronization branch for an elliptical cylinder-plate assembly with (a) $AR = 1$ and $U_r = 19$; (b) $AR = 1.5$ and $U_r = 19$; and, (c) $AR = 2$ and $U_r = 13$. The wake modes are “ $3 \times (2S)$ ”, “ $3 \times (2S)$ ” and “ $2 \times (P+S)$ ”, respectively. 142

branches. This is also supported by the zero phase shift in the oscillations between C_L and Y in Fig. 4.5, except for the 1:3 synchronization for $AR = 1.5$ where ϕ is around 90° —this may be due to the much stronger harmonic components in Fig. 4.11.

The branch identification of the lock-in regime and the 1:2 and 1:3 synchronizations also suggests that the self-limited FIV studied herein is essentially associated with an integrated VIV and galloping response, rather than a pure VIV response.

4.2.4 Aperiodic Oscillation in Non-Synchronization Branch

This section explores the non-synchronization branch in the reduced-velocity range between the synchronization branches, which corresponds to white regions in the amplitude response curves shown in Fig. 4.4, with the exception of the regime close to the lower and upper boundaries of the FIV response. More specifically, the entire range of U_r (viz., $U_r = 6$ –14) is associated with the non-synchronization branch for the case of $AR = 0.75$ (see Fig. 4.4 (a)). For $AR = 1$ and 1.5, the non-synchronization branch occurs primarily between the 1:2 and 1:3 synchronizations, viz., $U_r = 12$ –18 as is evident on a perusal of Figs. 4.4 (b)–(c). A non-synchronization branch does not present for $AR = 2$ as can be seen in Fig. 4.4 (d). From these considerations, it is evident that the non-synchronization branch in the amplitude response can also exist over a large range of U_r —as a result, it is important to investigate the dynamical characteristics corresponding to these regimes.

Analysis of nonlinear dynamical system

Figures. 4.13–4.15 exhibit some statistical quantities in the non-synchronization branch; namely, the power spectra of the transverse coefficient C_L (top panel), as well as the time series, phase portraits and the Poincaré sections of C_L at three representative reduced velocities for $AR = 0.75$, 1 and 1.5.

A perusal of Fig. 4.13 (a) shows that the power spectra of C_L in the non-synchronization branch for an elliptical cylinder-plate assembly with $AR = 0.75$ is simple; namely, it is composed of a primary frequency (largest peak with a value around f_n) and a secondary frequency (lower peak) with a value which increases from f_n to $2f_n$ as U_r increases from 7 to 13. These two frequency components correspond to the horizontal dark region and the oblique lighter region over the reduced-velocity range as is seen in Fig. 4.6 (b). It is this increasing secondary frequency with U_r that results in the absence of a synchronization between the structural oscillations and the vortex shedding in this case. In Figs. 4.13 (bi),

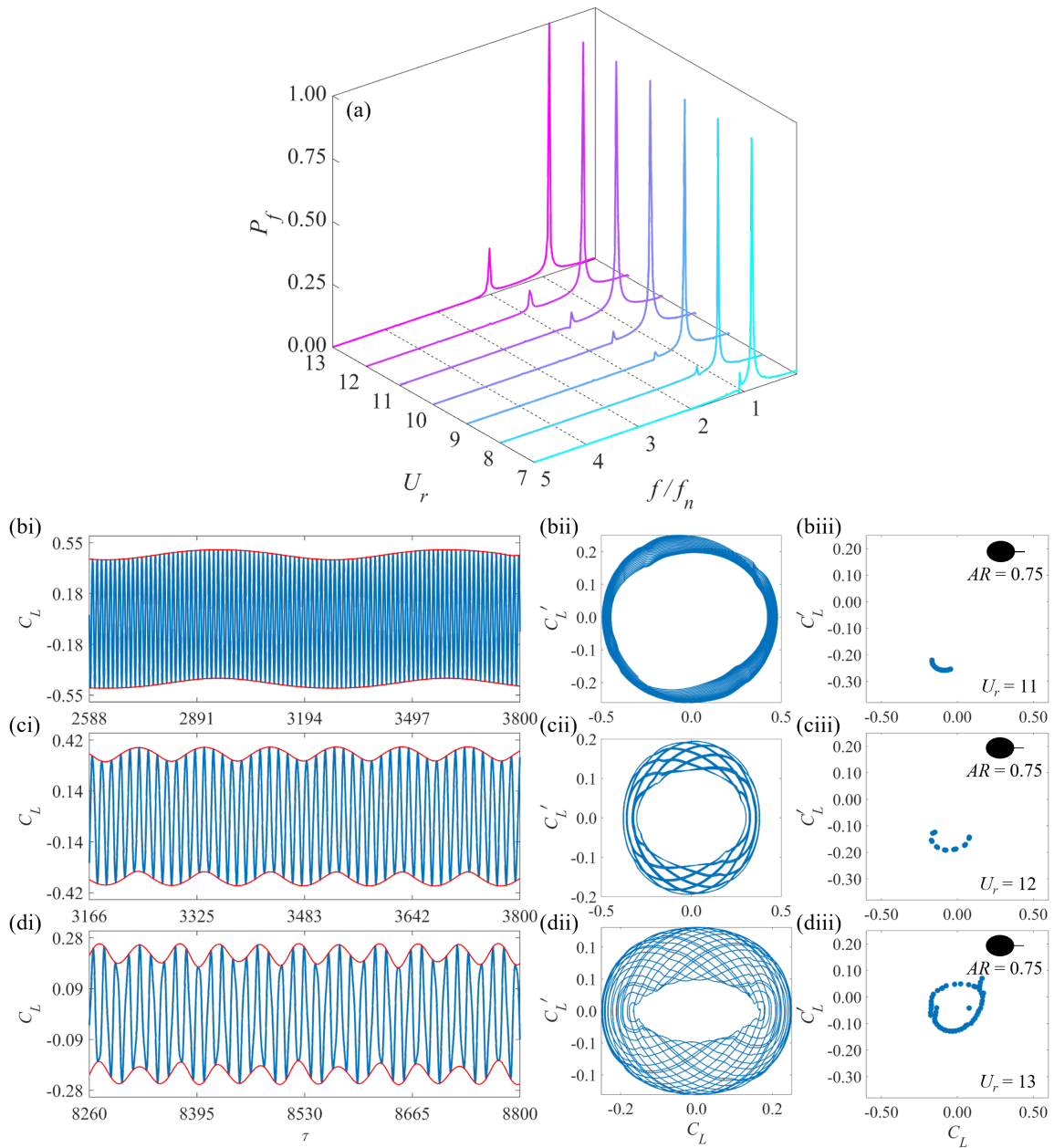


Figure 4.13: Quantities of interest associated with the non-synchronization branch for an elliptical cylinder-plate assembly with $AR = 0.75$. (a) Power spectra (normalized by the maximum power) of C_L over $U_r = 7$ –13. (i) Time series of C_L ; (ii) phase portraits C_L - C'_L ; and, (iii) Poincaré sections at three reduced velocities: namely, (b)–(d) $U_r = 11, 12$ and 13. The amplitude envelopes of the time series are shown as red curves.

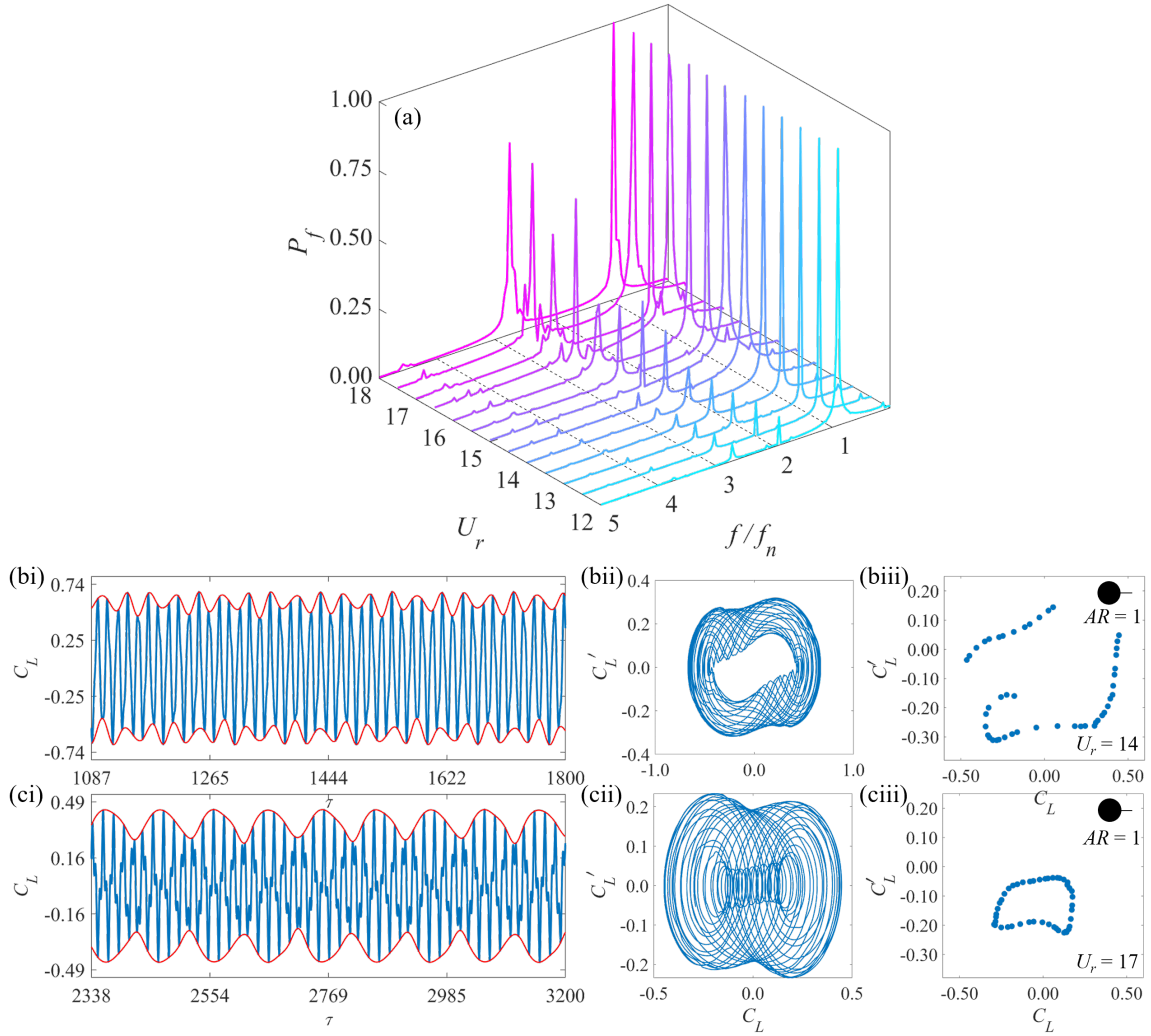


Figure 4.14: Quantities of interest associated with the non-synchronization branch for an elliptical cylinder-plate assembly with $AR = 1$. (a) Power spectra (normalized by the maximum power) of C_L over $U_r = 12$ – 18 . (i) Time series of C_L ; (ii) phase portraits C_L – C_L' ; and, (iii) Poincaré sections at two reduced velocities: namely, (b)–(c) $U_r = 14$ and 17 . The amplitude envelopes of the time series are shown as red curves.

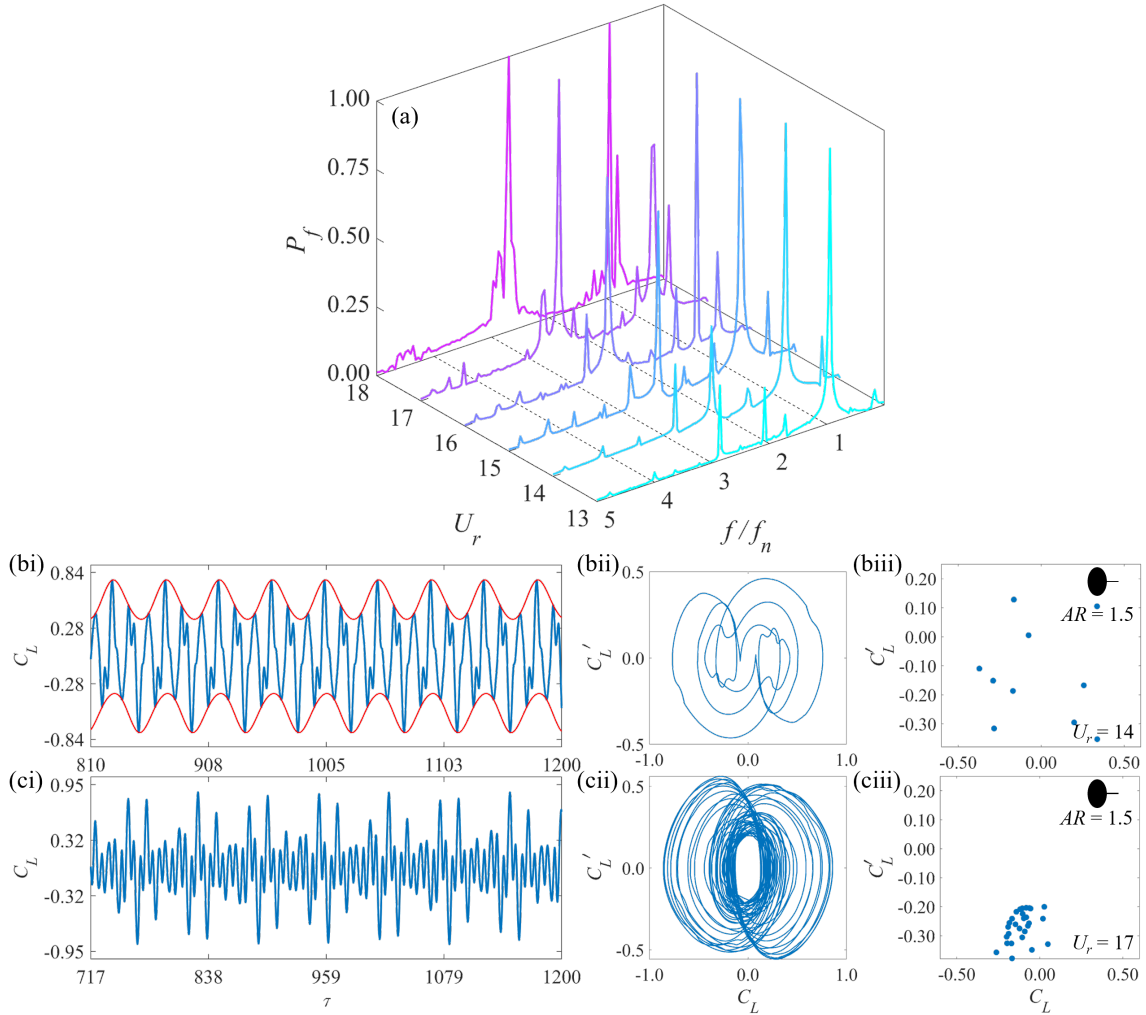


Figure 4.15: Quantities of interest associated with the non-synchronization branch for an elliptical cylinder-plate assembly with $AR = 1.5$. (a) Power spectra (normalized by the maximum power) of C_L over $U_r = 13$ –18. (i) Time series of C_L ; (ii) phase portraits C_L - C'_L ; and, (iii) Poincaré sections at two reduced velocities: namely, (b)–(c) $U_r = 14$ and 17. The amplitude envelopes of the time series are shown as the red curves.

(ci) and (di), the time series of C_L exhibits a beating phenomenon, which is a characteristic feature of the non-synchronization branch. The corresponding phase portrait $C_L-C'_L$ is composed of multiple interleaved orbits, rather than one clear-cut limit cycle as in a synchronization branch. For example, the slow beating in Fig. 4.13 (bi) is reflected in the presence of a wide loop in the corresponding $C_L-C'_L$ plane in Fig. 4.13 (bii). In contrast, the more rapid beating in Figs. 4.13 (ci) and (di) correspond to the donut-shaped closed curves in the phase portraits (see Figs. 4.13 (cii) and (dii)) and in either the partially opened or closed ring of points in the Poincaré sections of C_L evident on examination of Figs. 4.13 (ciii) and (diii), respectively.

Useful information on the topological characteristics of the trajectories in the phase plane can be obtained using Poincaré maps [98]. For example, in Fig. 4.13 (ciii), the Poincaré section for $C_L(t)$ consists of seven point clusters—these correspond to seven periodic-doubling oscillations (viz., the pattern of beating repeats itself over seven oscillation cycles). By contrast, the random distribution of points in the Poincaré sections of $C_L(t)$ exhibited in Figs. 4.13 (biii) and (diii) are indicative of more chaotic (rather than quasi-periodic) motions.

In the non-synchronization branch of the circular cylinder-plate assembly, the power spectra of $C_L(t)$ shown in Fig. 4.14 (a) exhibit a secondary frequency at $f/f_n = 2$ (second harmonic) for $U_r = 12$ (lower end of the non-synchronization branch coinciding roughly with the upper end of the 1:2 synchronization branch)—the power in the second harmonic decreases and that in the third harmonic increases as U_r increases from 12 to 18. Note that $U_r = 18$ is the upper end of the non-synchronization branch which coincides roughly with the lower end (onset) of the 1:3 synchronization branch. In the range of $U_r = 12$ –18, the second and third harmonics are present and all the higher-order harmonics are essentially negligible as seen in Fig. 4.14 (a). At $U_r = 14$, the beating in the $C_L(t)$ is irregular, which leads to a complex set of closed and intersecting loops in the phase portrait and a complex distribution of points in the Poincaré section (see Figs. 4.14 (bii) and (biii), respectively). At $U_r = 17$, the amplitude envelope repeats over a temporal duration of five oscillation cycles—the time variations of C_L are strongly non-sinusoidal and the corresponding phase portrait and Poincaré map are complex and irregular (see Figs. 4.14 (cii) and (ciii), respectively).

The power spectra of $C_L(t)$ for an elliptical cylinder-plate assembly with $AR = 1.5$ is displayed in Fig. 4.15 (a) for $U_r = 13$ –18 associated with the non-synchronization branch. These power spectra are complex, exhibiting multiple frequency peaks—these frequency peaks include harmonics of the fundamental frequency, as well as non-harmonics. At the upper end of the non-synchronization branch ($U_r = 18$), a prominent frequency in the power spectrum of $C_L(t)$ is associated with the third harmonic (viz., $f/f_n = 3$)—the

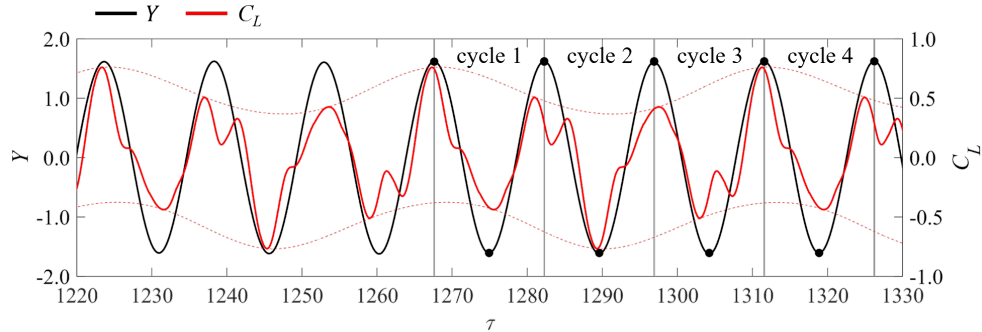


Figure 4.16: Four consecutive oscillation cycles in the time series of Y (black curve) and C_L (red curve) for an elliptical cylinder-plate assembly with $AR = 1.5$ at $U_r = 14$. The red dashed curves delineate the amplitude envelope of C_L .

upper end of the non-synchronization branch coincides approximately with the lower end (onset) of the 1:3 synchronization branch. More precisely, the power level associated with the third harmonic here is comparable to that of the fundamental frequency. Fig. 4.15 (bi) shows the presence of a periodic beating in the $C_L(t)$ at $U_r = 14$ —here, the beating period is three times that of the oscillation period—the phase portrait exhibits three closed and intersecting orbits (see Fig. 4.15 (bii)). However, this highly non-sinusoidal waveform leads to a random point-set topology in the associated Poincaré section displayed in Fig. 4.15 (biii)—interestingly, there are more than three points in this Poincaré section. By contrast, the beating in the time series of C_L at $U_r = 17$ is very irregular and does not yield a well-defined amplitude envelope (see Fig. 4.15 (ci)). Indeed, the temporal oscillations of C_L appear to be chaotic and this is supported by the associated phase portrait and Poincaré section exhibited in Figs. 4.15 (cii) and (ciii), respectively.

Aperiodic wake patterns

The vortex-shedding mode associated with the observed beating of C_L for an elliptical cylinder-plate assembly with $AR = 1.5$ at $U_r = 14$ (in the non-synchronization branch that lies between the 1:2 and 1:3 synchronizations) is investigated here. Using the division method of successive cycles in Section 3.5, four consecutive oscillation cycles (labelled cycle 1, 2, 3, and 4 in Fig. 4.16) have been identified in the time series of Y . Next, a delineation of the amplitude envelope in the $C_L(t)$ demonstrates that the beating pattern in this case repeats after every three oscillation cycles. Fig. 4.17 displays the corresponding instantaneous vorticity fields for the temporal duration of the four cycles.

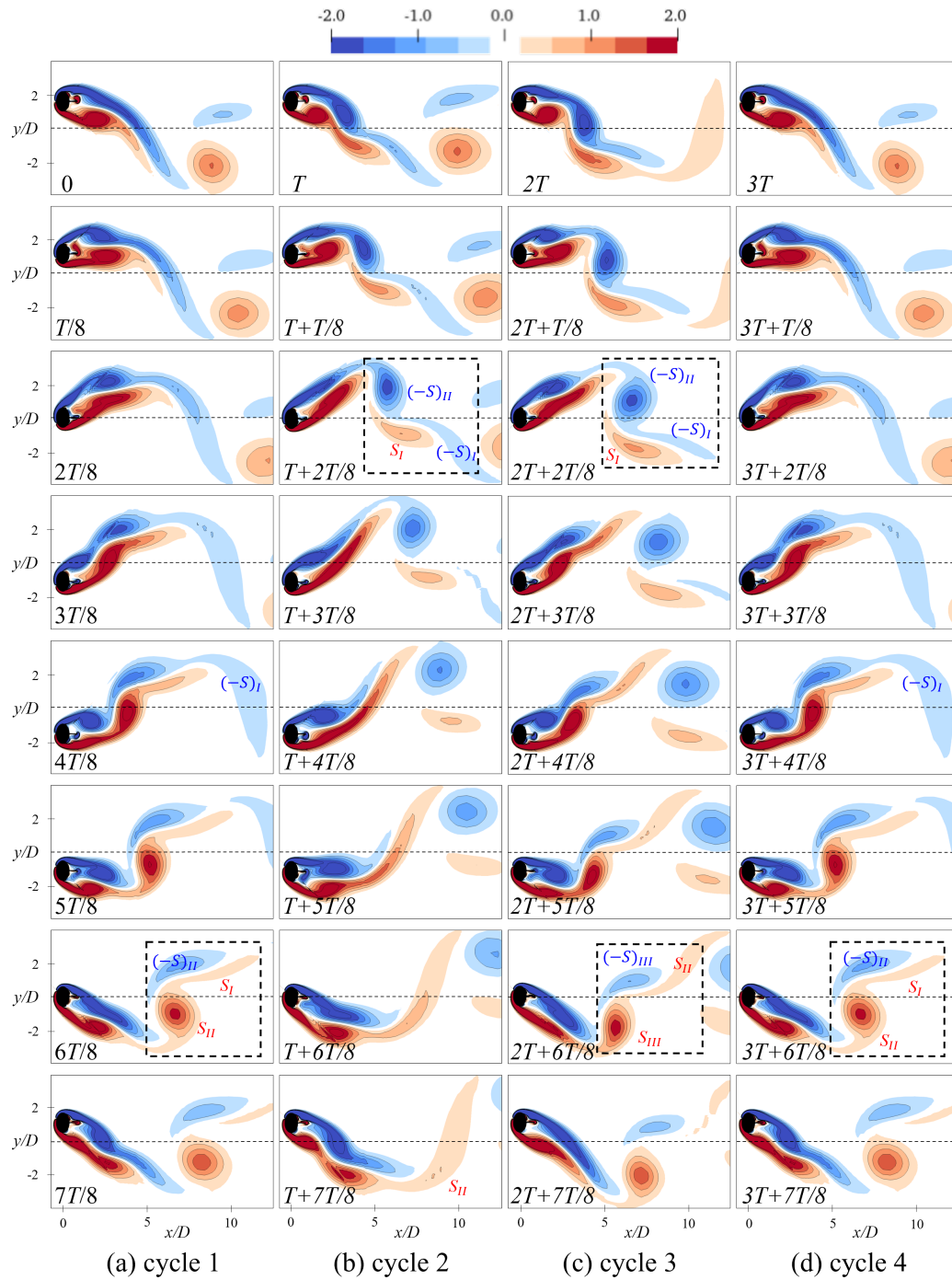


Figure 4.17: Instantaneous vorticity fields over four consecutive oscillation cycles (labelled cycle 1, 2, 3, and 4) used for the vortex-shedding analysis associated with the three-period beating in Fig. 4.16.

A careful perusal of Fig. 4.17 (a) shows that there are four vortices shed in the first cycle—these vortices consist of a single negative vortex $-S_I$ and a group of three vortices S_I , S_{II} , and $-S_{II}$ (delineated within the dashed-lined black box). In consequence, the vortex-shedding pattern is identified as a “T+S” mode. Note that the elongated vortex S_I and the circular vortex S_{II} remain attached to one another as they are shed from the structure. The vortex-shedding pattern in the second cycle is similar to that in the first cycle—more precisely a group of three vortices $-S_I$, $-S_{II}$, and S_I and a single positive vortex S_{II} are shed in the second cycle. Again, two vortices with the same sign in the vortex group (namely, $-S_I$ and $-S_{II}$) are connected to each other as they are shed (initially) from the structure. In marked contrast, the third cycle in Fig. 4.17 (c) is seen to exhibit wake dynamics with greater complexity—six vortices are shed in total. More specifically, these six vortices consist of two distinct and anti-symmetric groups consisting of three vortices each. The vortex-shedding pattern of the fourth cycle is identical to that of the first cycle. This observation is consistent with the 3-period repetitive beating identified previously from a perusal of $C_L(t)$ in Fig. 4.16.

4.3 FIV Occurred in an Unlimited Range of U_r

This section analyzes the unlimited FIV of various elliptical cylinders ($0.5 \leq AR \leq 2$) with a splitter plate of $L_{SP}/D = 0.75$, in terms of the vibration responses, the branching behaviors and the dynamical characteristics in synchronized and unsynchronized regimes. Furthermore, the free oscillation of an elliptical cylinder with a much longer splitter plate of $L_{SP}/D = 2.5$ is discussed.

4.3.1 Vibration Characteristics

Figure 4.18 compares the free oscillation induced on an elliptical cylinder-plate assembly for various aspect ratios ($AR = 0.5-2$) and for two lengths of splitter-plate ($L_{SP}/D = 0.75$ and 2.5)—the quantities of interest displayed here include the maximum amplitude response Y_{max} , the frequency ratio f_Y^*/f_n , and the root-mean-square lift $C_{L,rms}$ and the mean drag $C_{D,mean}$ exerted on the assembly by the fluid. An examination of this figure shows that all the assemblies experience an unlimited FIV in which Y_{max} generally increases with U_r . The analysis in Section 4.2 shows that the FIV mode (viz., whether self-limited or unlimited) is determined primarily by the splitter-plate length. In consequence, in this section we still focus on the influence of aspect ratio on FIV of elliptical cylinder-plate assembly where the fixed splitter-plate length has been chosen to provoke an unlimited FIV.

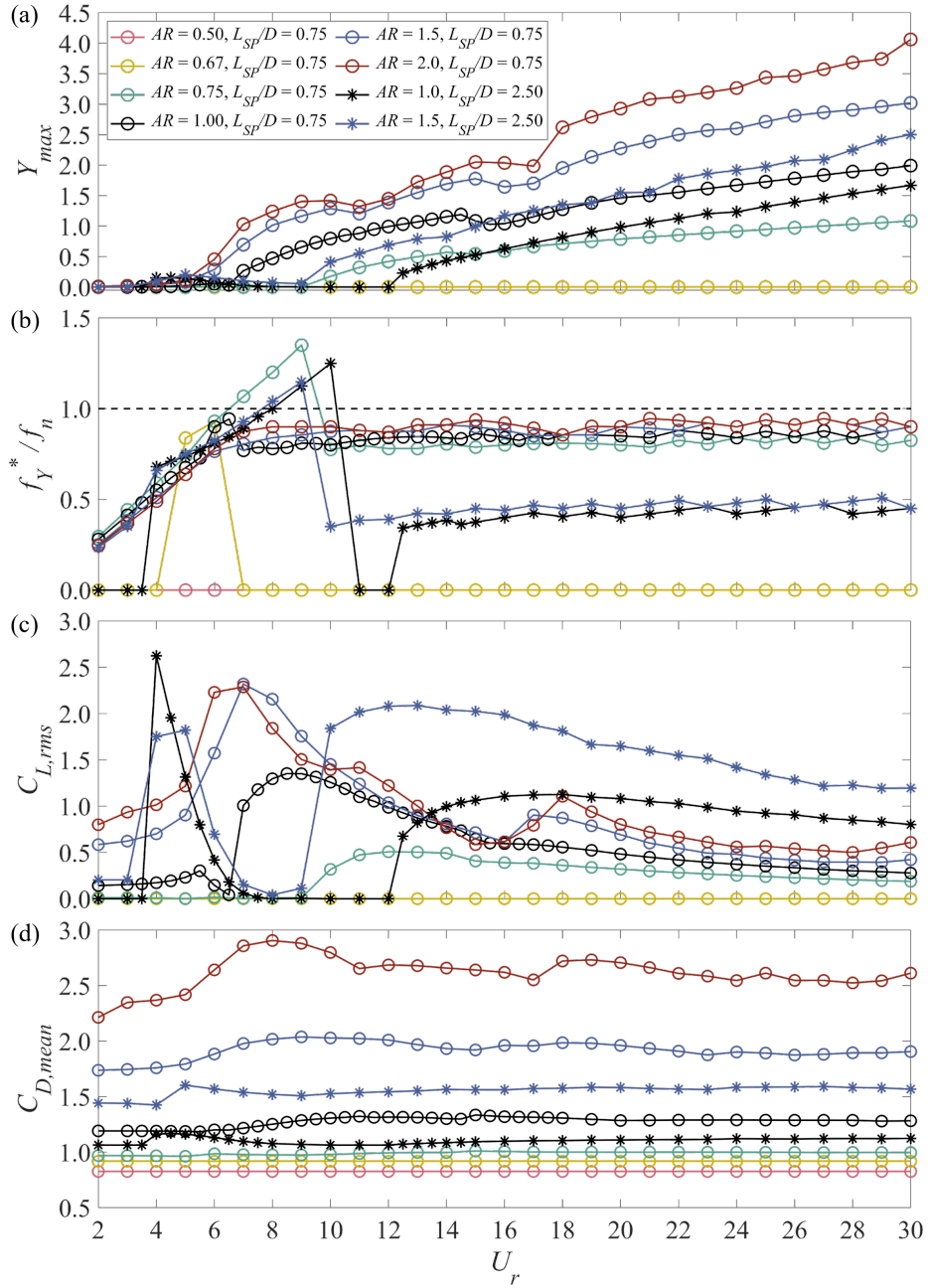


Figure 4.18: Effect of aspect ratio AR ($0.5 \leq AR \leq 2.5$) on the vibration response of an elliptical cylinder-plate assembly with $L_{SP}/D = 0.75$ and 2.5. (a) The maximum transverse displacement Y_{max} ; (b) the frequency ratio f_Y^*/f_n ; (c) the root-mean-square lift coefficient $C_{L,rms}$; and, (d) the mean drag coefficient $C_{D,mean}$ as a function of U_r .

For the assembly with $L_{SP}/D = 0.75$, we have investigated six aspect ratios in the range from 0.5 to 2 (see Fig. 4.18). Similar to the limited FIV, no oscillation occurs in the assembly with the two smallest aspect ratios (viz., $AR = 0.5$ and 0.67)—indeed, the amplitude response, the characteristic oscillation frequency and the lift coefficient have values near zero (see Figs. 4.18 (a)–(c)) and the streamwise drag force is constant with respect to U_r (viz., $C_{D,mean} \approx 0.83$ and 0.92 for $AR = 0.5$ and 0.67 , respectively, on examination of Fig. 4.18 (d)). Even so, the dynamical behavior of the assembly for $AR = 0.5$ slightly differs from that for $AR = 0.67$ —the frequency responses in Fig. 4.18 (b) show that $f_Y^*/f_n \approx 0$ for $AR = 0.5$ over the entire reduced-velocity range $U_r = 2$ – 30 , whereas that for $AR = 0.67$ exhibits a rapid increase to $f_Y^*/f_n \approx 1$ over $U_r = 5$ – 6 .

For aspect ratios $AR \geq 0.75$, an unlimited oscillation can be induced in the elliptical cylinder-plate assembly. An increasing value of AR provokes oscillations in two aspects: namely, the onset of FIV occurs at lower values of U_r (e.g., the onset is $U_r = 9, 6.5, 6$ and 5 for $AR = 0.75, 1, 1.5$ and 2 , respectively) and the maximum transverse displacement increases with AR as is evident on a careful perusal of the amplitude responses in Fig. 4.18 (a). In stark contrast, the influence of the aspect ratio on the frequency response appears to be less obvious—indeed, it can be seen that f_Y^*/f_n varies only over a small range from 0.8 to 0.95 for AR varying from 0.75 to 2 (cf. Fig. 4.18 (b)). In Fig. 4.18 (c), the lift force acting on the assembly attains a maximum value around the onset velocity and gradually decreases with U_r . Moreover, $C_{L,rms}$ is sensitive to the changes in the aspect ratio as evidenced by the lift curves in Fig. 4.18 (c). More specifically, the maximum lift coefficient increases by approximately a factor of three (e.g., from 0.5 to 1.4) as AR increases from 0.75 to 1 . While this increase becomes slower (e.g., from 1.4 to 2.3) for AR from 1 to 2 . Unlike the lift force, the maximum drag force increases proportionally with AR : namely, the maximum value of $C_{D,mean}$ is $1, 1.3, 2$ and 2.6 for $AR = 0.75, 1, 1.5$ and 2 , respectively (cf. Fig. 4.18 (d)). Finally, it is noted that $C_{D,mean}$ is constant over $U_r = 2$ – 30 .

The unlimited FIV response of an elliptical cylinder-plate assembly with a larger plate length $L_{SP}/D = 2.5$ is also exhibited in Fig. 4.18 for $AR = 1$ and 1.5 . The effect of AR on the maximum transverse displacement, the dominant oscillation frequency and fluid forces acting on the assembly are similar to those for $L_{SP}/D = 0.75$. The major difference is the higher onset of FIV (viz., $U_r = 12$ and 9 for $AR = 1$ and 1.5 , respectively) and the lower dominant oscillation frequency ($f_Y^*/f_n = 0.43$ and 0.45 for $AR = 1$ and 1.5 , respectively) for the case $L_{SP}/D = 2.5$. The analysis conducted here implies that increasing AR leads to a slight increase in the f_Y^*/f_n , whereas increasing L_{SP}/D has precisely the opposite effect, namely, that of significantly reducing f_Y^*/f_n .

Following from this analysis and some results reported in Section 4.2, the influence of the aspect ratio of an elliptical cylinder-plate assembly on their self-limited or unlimited

FIV response can be summarized as follows. A self-limited FIV in the assembly increases with AR at least over the range of $AR = 0.75$ – 1.5 . However, the effective reduced-velocity range over which a self-limited FIV occurs is reduced for $AR = 2$. In contrast, for the unlimited FIV in the assembly, both the amplitude of the structural oscillation and the effective reduced-velocity range increase monotonically with AR —this effect is independent of the splitter-plate length provided, of course, the length is large enough to provoke an unlimited FIV response in the assembly.

4.3.2 Branching Behavior

The branching behavior of the unlimited FIV provoked on an elliptical cylinder-plate assembly with $L_{SP}/D = 0.75$ and aspect ratios ranging from 0.75 to 2 are exhibited in Fig. 4.19. The corresponding power spectral density (PSD) isopleths of the transverse displacement Y and the lift coefficient C_L as a function of U_r and the normalized frequency—either f_Y/f_n or f_{C_L}/f_n —are displayed in Figs. 4.20 and 4.21, respectively.

For the oblate ($AR < 1$) elliptical cylinder-plate assembly with $AR = 0.75$, it is seen that only one odd-multiple synchronization is present within the unlimited oscillation range—more specifically, $f_Y^*/f_{C_L}^* = 1:3$ at $U_r = 15$ – 16.5 whose onset is signalled by a “kink” in the amplitude response (delineated by the red box in Fig. 4.19 (a)). As a consequence, this assembly experiences a pure galloping response. The PSD isopleths of Y and C_L exhibit a simple form. More precisely, the dominant frequency in the transverse displacement oscillation occurs at $f_Y/f_n = 0.8$ in the galloping regime (see Fig. 4.20 (b)), whereas the lift coefficient exhibits an evident third-harmonic at $f_{C_L}/f_n = 2.4$ to give a 1:3 synchronization branch. Moreover, the harmonic frequencies in the oscillations of lift coefficient gradually increase to higher order thereafter with U_r as is evident from a perusal of Fig. 4.21 (b). From this behavior, it is reasonable to suggest that a 1:5 synchronization branch may be present in the galloping regime at larger values of the reduced velocity than considered herein.

In comparison to an oblate elliptical cylinder-plate assembly, a circular cylinder-plate assembly exhibits more synchronization branches in the amplitude response that occur over a wider reduced-velocity range. More precisely, these regimes correspond to $f_Y^*/f_{C_L}^* = 1:2$, 1:3 and 1:5 at $U_r = 11$ – 11.5 , 15–20 and 29–30, respectively. The onset of each branch is signalled by a “kink” in the amplitude response as is evident from an examination of Fig. 4.19 (b). Note that there are small oscillations with $Y/D \approx 0.05$ at about $U_r = 6$ —this corresponds to the initial stage of a VIV that has not attained “lock-in” (see Section 3.4). In consequence, the unlimited FIV response of a circular cylinder-plate assembly still consists

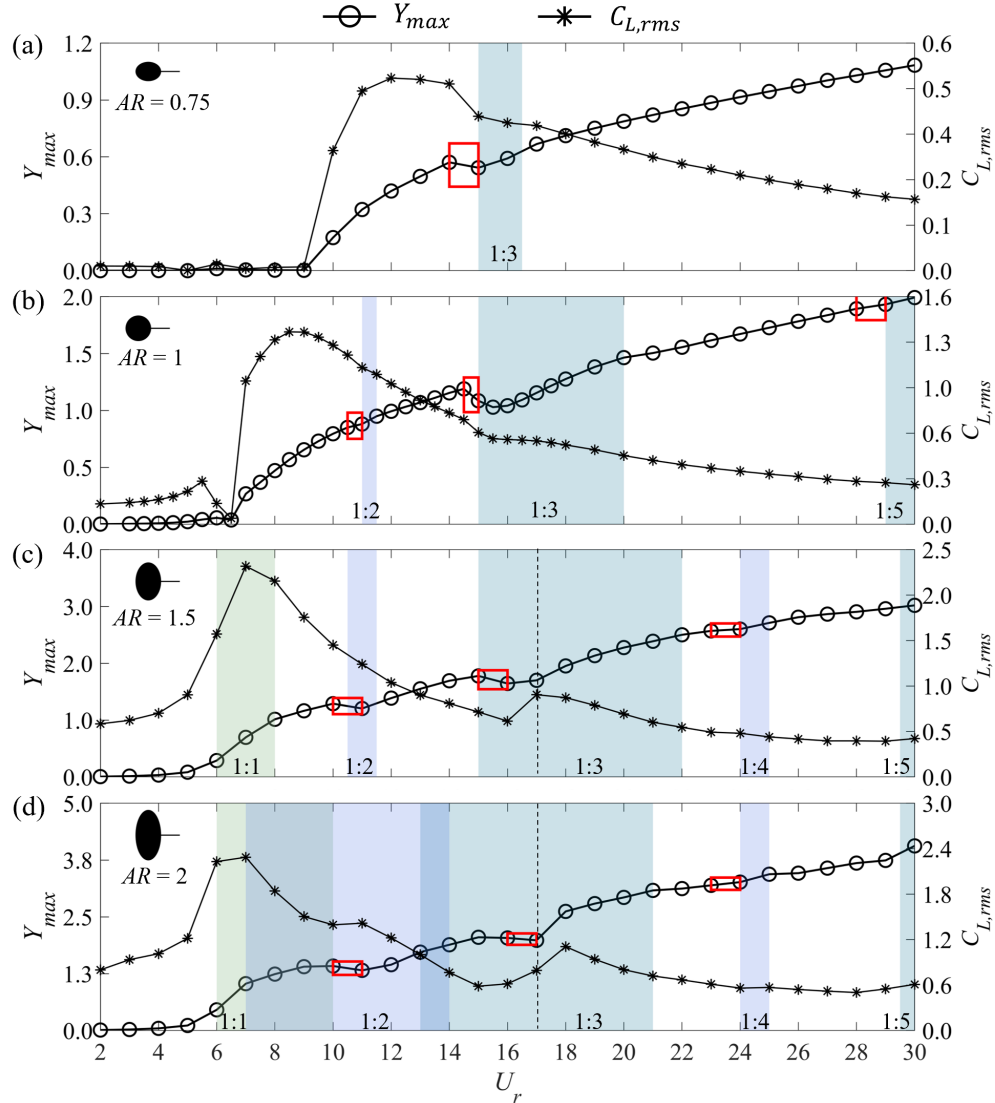


Figure 4.19: Branching behavior of an unlimited FIV response provoked on an elliptical cylinder-plate assembly of various aspect ratios and a fixed splitter-plate length $L_{SP}/D = 0.75$. The maximum transverse displacement Y_{max} (left vertical axis) and the root-mean-square lift coefficient $C_{L,rms}$ (right vertical axis) are plotted as a function of U_r for (a)–(d) $AR = 0.75, 1, 1.5$ and 2 . The synchronization branches are shaded in different colours. “Kinks” in the amplitude response are delineated by red boxes.

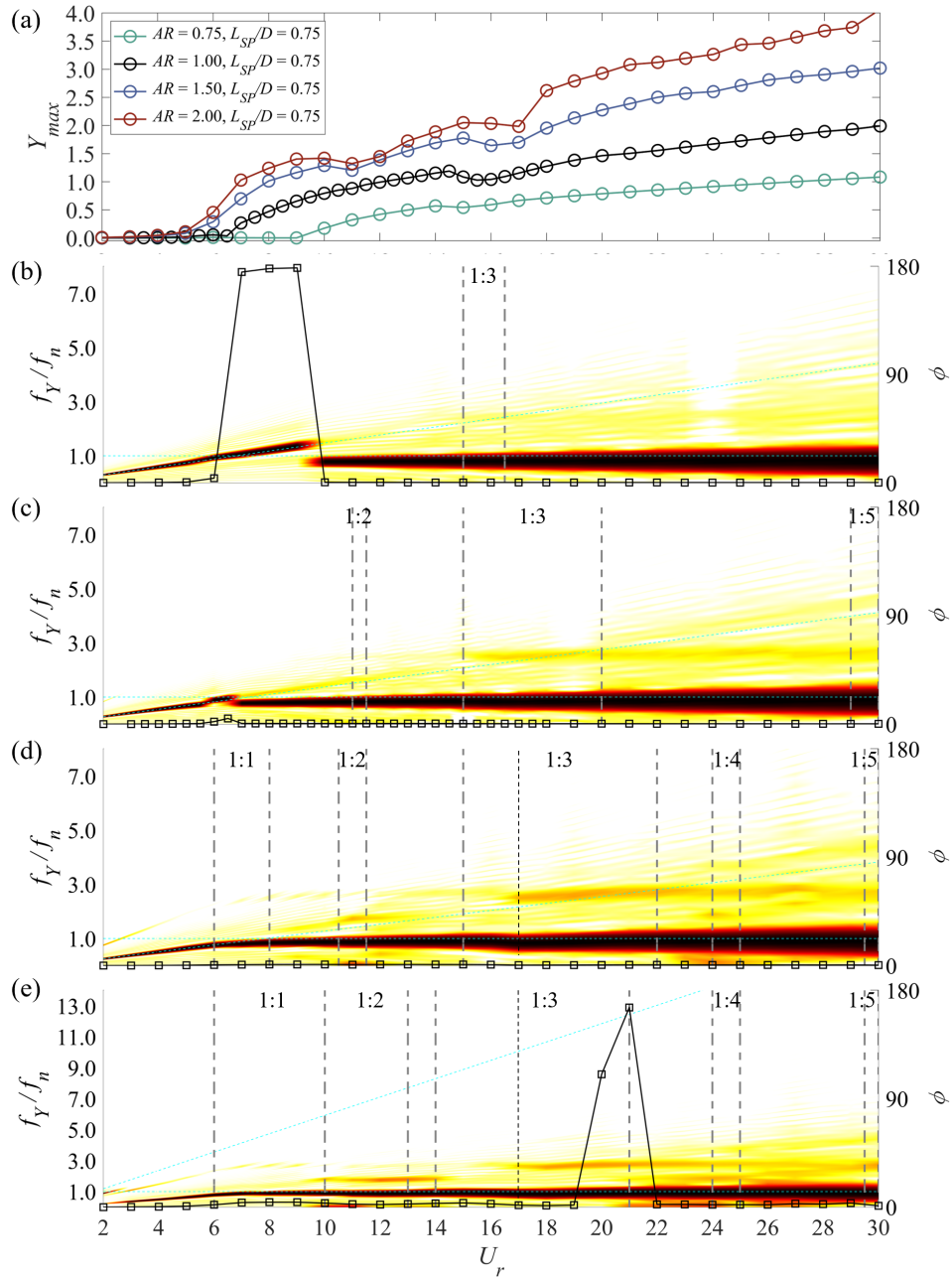


Figure 4.20: (a) The maximum transverse displacement Y_{max} as a function of U_r for an elliptical cylinder-plate assembly with $AR = 0.75-2$ and $L_{SP}/D = 0.75$. PSD (logarithmic scale) of Y exhibited as a function of f_Y/f_n and U_r for (b)–(e) $AR = 0.75, 1, 1.5$ and 2 . Other notations used here are the same as that in Fig. 4.5.

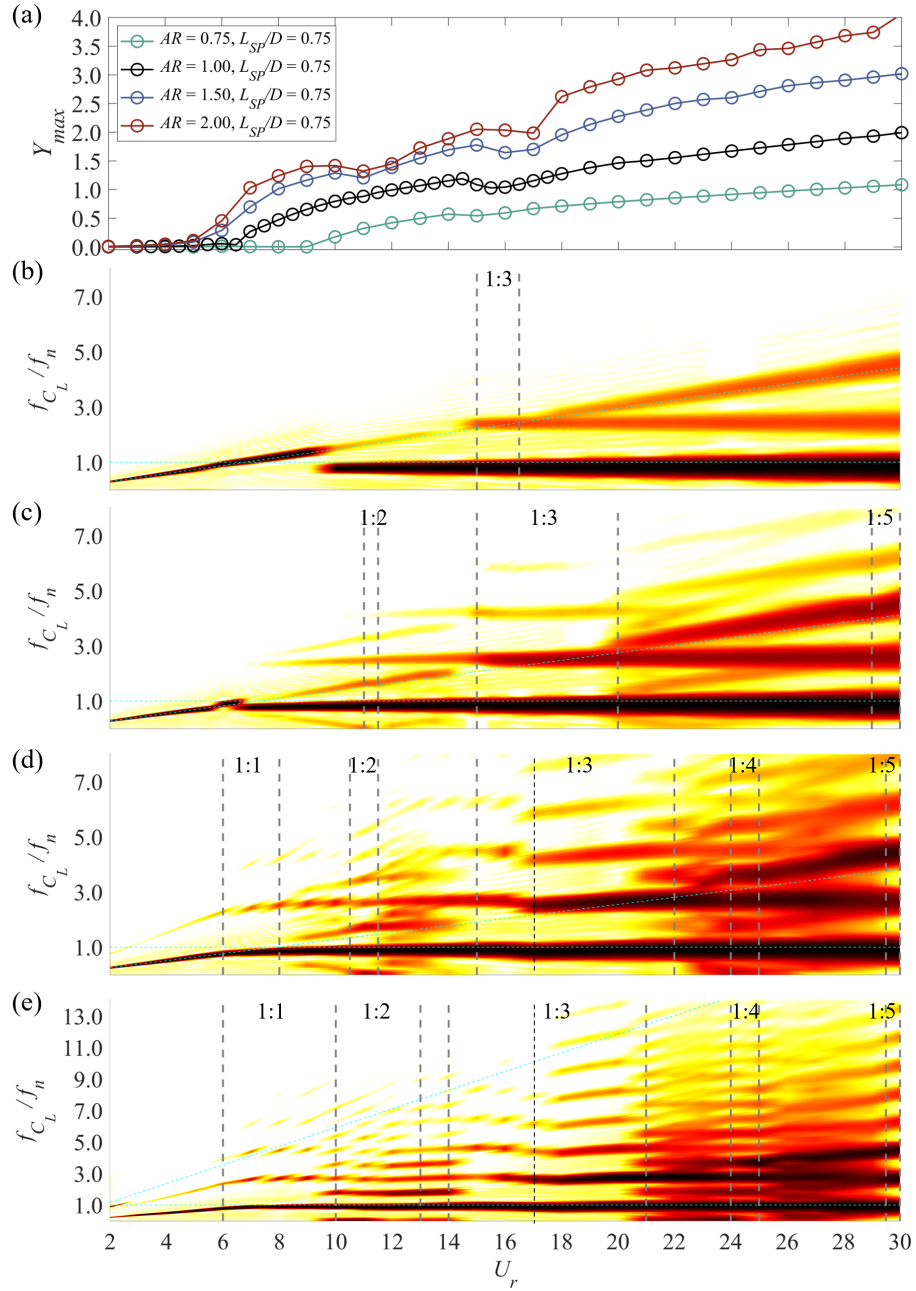


Figure 4.21: (a) The normalized amplitude responses and (b)–(e) PSD of C_L for $AR = 0.75$ – 2 and $L_{SP}/D = 0.75$. Other notations used here are the same as that in Fig. 4.5.

primarily of galloping. In addition to the fundamental frequency of $f_Y^*/f_n \approx 0.85$, a third harmonic gradually emerges at $U_r \geq 16$ in the power spectrum of Y as is evident in Fig. 4.20 (c). In contrast, the C_L power spectrum exhibits a more complex harmonic structure—only odd harmonics are present in the odd (1:3 and 1:5) synchronization branches, whereas both odd and even harmonics are present in the even (1:2) synchronization branch.

For a prolate ($AR > 1$) elliptical cylinder-plate assembly with aspect ratios of $AR = 1.5$ and 2, the most striking branching characteristic is that a 1:1 synchronization branch (i.e., “lock-in”) corresponding to the VIV regime is present at a lower value of the reduced velocity. This branch is succeeded at larger values of U_r by several high-order synchronization branches with $f_Y^*/f_{C_L}^* = 1:2, 1:3, 1:4$ and 1:5 in the galloping regime. Consequently, these assemblies experience an integrated VIV and galloping response. As is evident from Fig. 4.19 (c), the five synchronization branches are separated from each other. Furthermore, the onset of the 1:2, 1:3 and 1:4 synchronization branches is signalled by a “kink” in the amplitude response. For the assembly with $AR = 2$ shown in Fig. 4.19 (d), the first three synchronization branches are integrated with one another without any clear-cut boundaries between them (viz., $f_Y^*/f_{C_L}^* = 1:1, 1:2$ and 1:3 at $U_r = 6-7, 10-13$ and 14–21 respectively). Consequently, two transition regions are present, namely, $U_r = 7-10$ between 1:1 and 1:2 synchronizations and $U_r = 13-14$ between 1:2 and 1:3 synchronizations. These transition regimes are identified by their vortex-shedding patterns which will be discussed in greater detail in Section 4.3.3.

Another interesting branching behavior for a prolate ($AR > 1$) elliptical cylinder-plate assembly is that the 1:3 synchronization branch appears to be further split into two parts. The first sub-branch— $U_r = 15-17$ for $AR = 1.5$ and $U_r = 14-17$ for $AR = 2$ —is characterized by three properties, namely, a near constant maximum transverse displacement Y_{max} as a function of U_r , the presence of a single frequency in the Y power spectrum, and the existence of a number of weaker and lower-order harmonic components in the C_L power spectrum. In marked contrast, the second sub-branch (viz., $U_r = 17-22$ for $AR = 1.5$ and $U_r = 17-21$ for $AR = 2$) is characterized by an increase in the Y_{max} as a function of U_r , the presence of a third harmonic in the Y power spectrum, and the existence of stronger and higher-order harmonic components in the C_L power spectrum. The subdivision of the 1:3 synchronization branch is closely associated with the transition in the vortex-shedding patterns in this regime—this will be investigated in greater detail in Section 4.3.3.

4.3.3 Periodic Oscillation in Synchronization Branch

This section investigates the influence of aspect ratio on the dynamical characteristics and the vortex-shedding models within the synchronization branches in the amplitude response

of an elliptical cylinder-plate assembly. To this purpose, we analyze the behavior of the oscillatory time series of the transverse displacement $Y(t)$ and lift coefficient $C_L(t)$.

“Lock-in” regime

Figure 4.22 compares the dynamic characteristics and vortex-shedding patterns in the 1:1 synchronization branch for an elliptical cylinder-plate assembly with $AR = 1.5$ and 2 at $U_r = 6$, as well as in the transition regime that occurs between the 1:1 and 1:2 synchronization branches for the assembly with $AR = 2$ at $U_r = 7$ –8. As shown in Figs. 4.22 (a)–(c), the transverse displacement time series $Y(t)$ consists of a periodic sinusoidal variation with one fundamental frequency—this is reflected in the presence of a circular limit cycle in the Y - Y' phase plane. Increasing the value of AR results in a non-sinusoidal waveform for the $C_L(t)$ and this manifestation is associated with the more complex shapes of the phase portraits of $C_L(t)$ (red curve in Fig. 4.22 (bii) for $AR = 2$ at $U_r = 6$). Moreover, the increasing number of harmonic components present in the power spectra of $C_L(t)$ with increasing AR and/or U_r (cf. Figs. 4.22 (aiv), (biv), and (civ)) are reflected in the increasing complexity of the corresponding Lissajous figures that exhibit increasingly complex loop structures with increasing AR (cf. Figs. 4.22 (aiii) and (biii) for $AR = 1.5$ and 2, at $U_r = 6$) and/or U_r (cf. Figs. 4.22 (biii) and (ciii) at $U_r = 6$ and 8, for $AR = 2$). In the transition regime between the 1:1 and 1:2 synchronization branches for $AR = 2$ at $U_r = 8$, the temporal waveform of $C_L(t)$ is noticeably non-sinusoidal owing to the presence of a larger number of stronger harmonics in the corresponding power spectrum.

A careful inspection of Figs. 4.22 (d) and (e) shows that the vortex-shedding pattern associated with the 1:1 synchronization branch is a “2S” wake mode consisting two counter-rotating vortices (S_I and $-S_I$) that are shed alternately during one oscillation cycle. Furthermore, the vortex shape is strongly dependent on the aspect ratio; namely, the elliptically-shaped vortices are shed for $AR = 1.5$, whereas the vortices shed for $AR = 2$ consist of a vortex core with a trailing “tail” (marked using a black circle in Fig. 4.22 (e)).

In the transition regime between the 1:1 and 1:2 synchronization branches for $AR = 2$, the vortex shedding exhibits some new characteristic features. In Fig. 4.22 (f) for $AR = 2$ and $U_r = 7$, it is evident that a large positive vortex S_I is first shed at $t = 0$ (beginning of an oscillation cycle of period T), followed by the shedding of a small slender vortex with the same sign (designated here as T_I) at $t = T/4$ —this vortex appears to be the tail of the next positive vortex. A similar vortex-shedding pattern occurs in the next half oscillation, except that the shed vortices have a negative sign ($-S_I$ and $-T_I$). The wake flow dynamics exhibited in Fig. 4.22 (g) for $AR = 2$ and $U_r = 8$ is different—the vortex-shedding pattern here involves a large vortex and a small “tail” vortex with the opposite sign that are shed

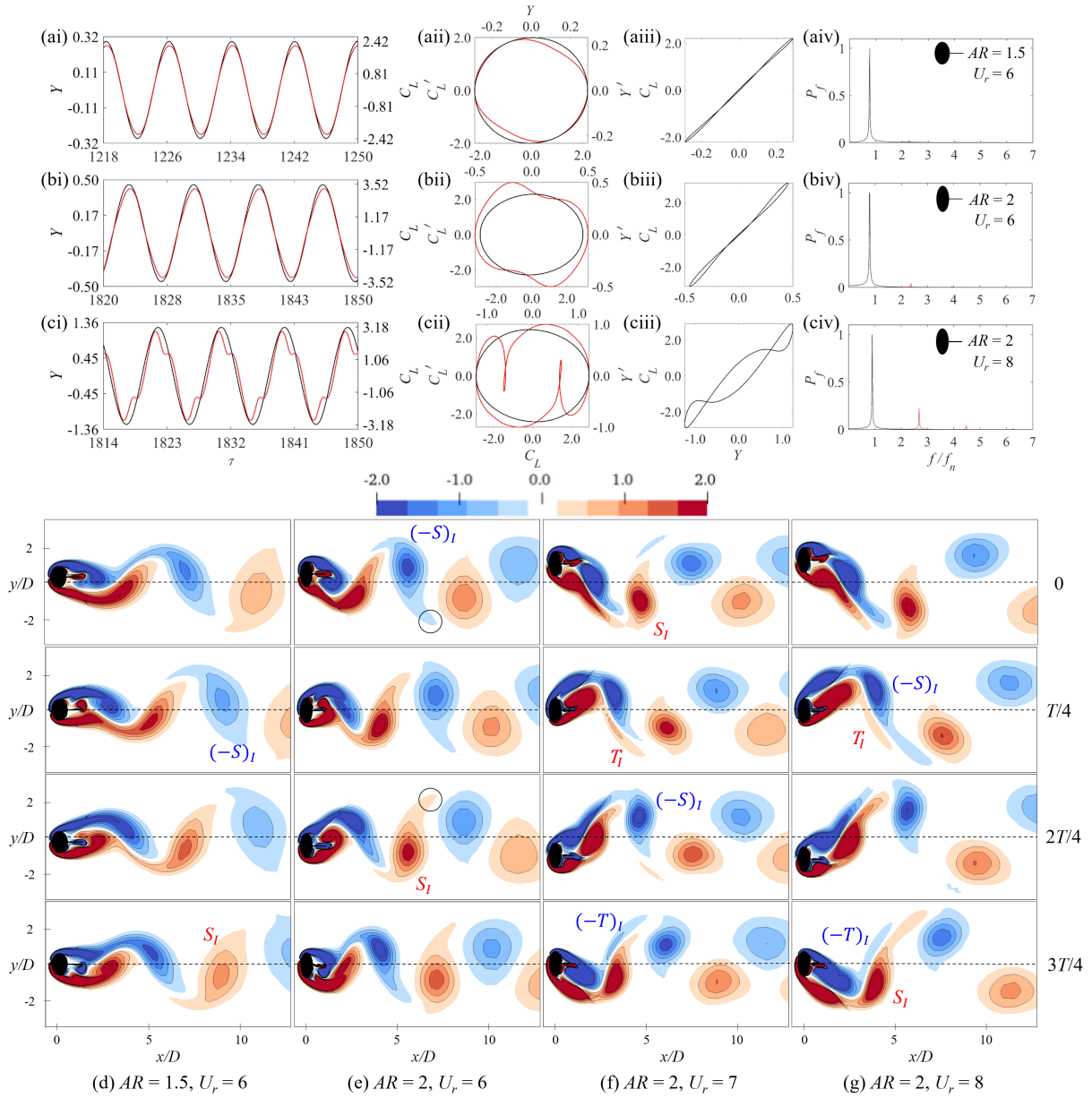


Figure 4.22: Dynamical characteristics of the “lock-in” regime for an elliptical cylinder-plate assembly with (a) $AR = 1.5$ and (b) $AR = 2$ at $U_r = 6$ and of the transition regime between the 1:1 and 1:2 synchronizations for (c) $AR = 2$ at $U_r = 8$. The evolution of instantaneous vorticity fields during one oscillation cycle T is displayed for (d) $AR = 1.5$ at $U_r = 6$; (e) $AR = 2$ at $U_r = 6$; (f) $AR = 2$ at $U_r = 7$; and, (g) $AR = 2$ at $U_r = 8$. The “2S” and “quasi-2S” modes are identified in the “lock-in” and transition regimes, respectively.

together as a pair—more precisely, $(-S_I, T_I)$ and $(S_I, -T_I)$ are shed in one oscillation cycle. Moreover, the large vortices $-S_I$ and S_I are not elliptically shaped as those in Fig. 4.22 (f), but instead have a long tail. This dramatic change in the vortex-shedding pattern is only due to the marginally greater value of the reduced velocity $U_r = 8$ in Fig. 4.22 (g). It is evident that in the transition regime, four vortices are shed in total in each oscillation cycle—these vortices have the characteristic vortex-tail structural pattern where the “tail” vortex is smaller and possesses a weaker vorticity than that of the primary vortex. In view of this, we identify the wake mode in the transition regime as a “quasi-2S” mode.

Odd-multiple synchronization in the galloping regime

Figures 4.23–4.24 display the dynamical characteristics and wake modes associated with the 1:3 synchronization branch for elliptical cylinder-plate assembly with aspect ratios in the range $AR = 0.75$ –2. In particular, two representative values of the reduced velocity (i.e., $U_r = 16$ and 20) are selected for $AR = 1.5$ and 2, which correspond to the two sub-branches of the 1:3 synchronization branch.

To begin, we study the influence of the aspect ratio on the 1:3 synchronization branch at $U_r = 16$. As evident from an inspection of Figs. 4.23 (a)–(c) and (e), increasing AR from 0.75 to 2 results in a more complex time variation in $C_L(t)$, a more irregular phase portrait of $C_L-C'_L$, and in the presence of a stronger third harmonic in the power spectrum of C_L . In marked contrast, increasing the aspect ratio of the assembly has little influence on the comparable characteristics for the transverse displacement $Y(t)$. The corresponding vortex-shedding patterns are displayed in Figs. 4.24 (a)–(d). A perusal of these figures shows that for all values of the aspect ratio studied herein, the vortex-shedding pattern of the 1:3 synchronization branch corresponds to a “ $3 \times (2S)$ ” wake mode. However, we note that some of the vortices shed from the assembly transition from an oblong shape (for $AR \leq 1$) to a more elongated shape (for $AR > 1$). More precisely, with increasing AR , the vortices S_{II} and $-S_{III}$ (marked by the black box in Figs. 4.24 (c) and (d)) shed from the assembly for $AR = 1.5$ and 2 become more slender and sinuous with increasing AR .

Next, we investigate the influence of the reduced velocity for the elliptical cylinder-plate assembly with $AR = 1.5$ and 2. As is evident on examination of Figs. 4.23 (d) and (f), increasing U_r from 16 to 20 results in the emergence of a strong third harmonic (with an amplitude comparable to that of the fundamental frequency) in the power spectrum of C_L . As a result, the corresponding $C_L(t)$ is characterized by multiple peaks of various amplitudes and the associated phase portrait $C_L-C'_L$ exhibits a complex loop structure with the various loops intersecting with one another. A careful inspection of Fig. 4.24 (e) shows that the vortex-shedding pattern adheres to a “ $3 \times (2S)$ ” wake mode—however, the

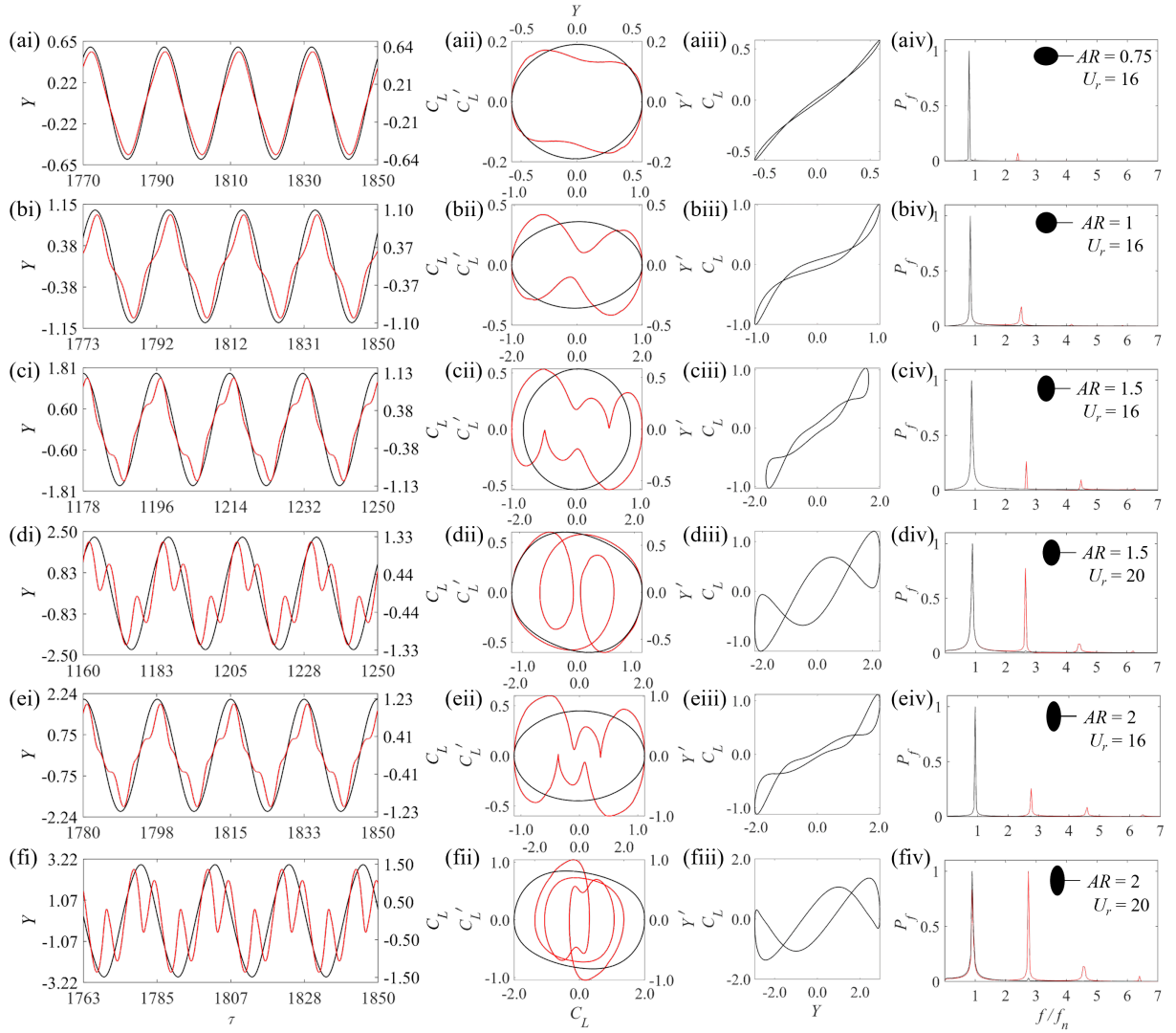


Figure 4.23: Dynamical characteristics of the 1:3 synchronization branch for an elliptical cylinder-plate assembly with (a) $AR = 0.75$, (b) $AR = 1$, (c, d) $AR = 1.5$, and (e, f) $AR = 2$ at two values of reduced velocity (viz., $U_r = 16$ and 20).

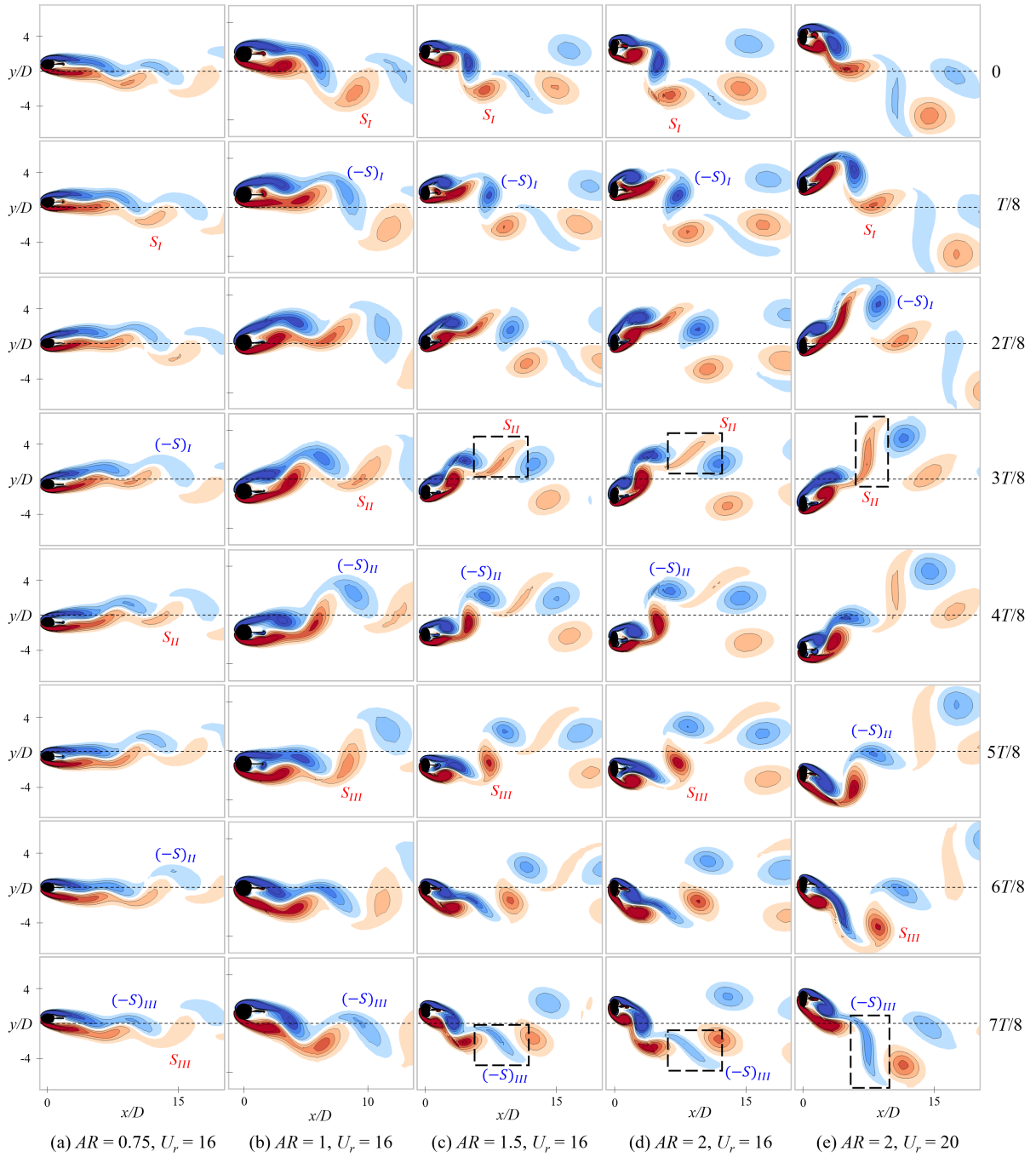


Figure 4.24: Instantaneous vorticity field over one oscillation cycle T in the 1:3 synchronization branch for an elliptical cylinder-plate assembly with (a) $AR = 0.75$, (b) $AR = 1$, (c) $AR = 1.5$ and (d, e) $AR = 2$ at $U_r = 16$ and 20 . The 1:3 synchronization branch is associated with a “ $3 \times (2S)$ ” mode. 162

vortices here are more strongly oriented in the “vertical” direction and consist of larger and more slender vortices (S_{II} , $-S_{III}$) owing to the larger value of the reduced velocity.

The vortex-shedding pattern associated with an elliptical cylinder-plate assembly reflects the nature of the oscillatory response of the structure. To this point, the maximum transverse displacement increases significantly with AR for a given fixed reduced velocity (e.g., $Y_{max}/D = 0.6, 1, 1.6$ and 2 for $AR = 0.75, 1, 1.5$ and 2 , respectively, at $U_r = 16$). This is probably due to the shedding of more slender vortices at the larger values of the aspect ratio—these vortices are shed when near the maximum and minimum of the transverse displacement in each oscillation cycle (viz., the vortex S_{II} is shed at $t = 3T/8$ just before the occurrence of the positive peak and the vortex $-S_{III}$ is shed at $t = 7T/8$ just before the occurrence of the negative peak in the oscillation cycle in Fig. 4.24 (e)). Furthermore, the value of Y_{max} is almost constant in the first sub-branch of the 1:3 synchronization, whereas Y_{max} increases with U_r in the second sub-branch. This is true for an elliptical cylinder-plate assembly with $AR = 1.5$ and 2 . This can be explained as follows. For these two aspect ratios, the orientation of the slender vortices shed by the assembly transitions from an oblique orientation to an almost vertical orientation (viz., parallel to the transverse direction) as the reduced velocity increases. The near constant value of Y_{max} (in the first sub-branch) will accordingly begin to increase with U_r after a critical value of the reduced velocity has been exceeded. This occurs at $U_r = 17$ for $AR = 1.5$ and 2 . As a result, the 1:3 synchronization branch is divided into two characteristic sub-branches as noted previously.

Figure 4.25 exhibits the dynamical characteristics of the 1:5 synchronization branch for the elliptical cylinder-plate assembly with various aspect ratios. It is seen that for the C_L power spectrum, the fifth harmonic is significant and the seventh harmonic is evident—this more complex power spectrum is associated with the more complex temporal variations in $C_L(t)$ and the more complex system of loops in the associated phase portrait $C_L-C'_L$. An increase in AR has a similar effect on the dynamical characteristics in the 1:5 synchronization branch as those in the 1:3 synchronization branch described above. Correspondingly, the wake mode is identified as “ $5 \times (2S)$ ”.

Even-multiple synchronization in the galloping regime

Figures 4.26–4.27 present the 1:2 and 1:4 synchronization branches for an elliptical cylinder-plate assembly with $AR = 1, 1.5$ and 2 at $U_r = 11$ and $U_r = 24$. These figures also exhibit the transition regime between the 1:2 and 1:3 synchronizations branches for $AR = 2$ at $U_r = 13$ – 14 . The most remarkable aspect of an even-multiple synchronization is that, in contrast to anti-symmetric odd-multiple synchronization branches described above, the

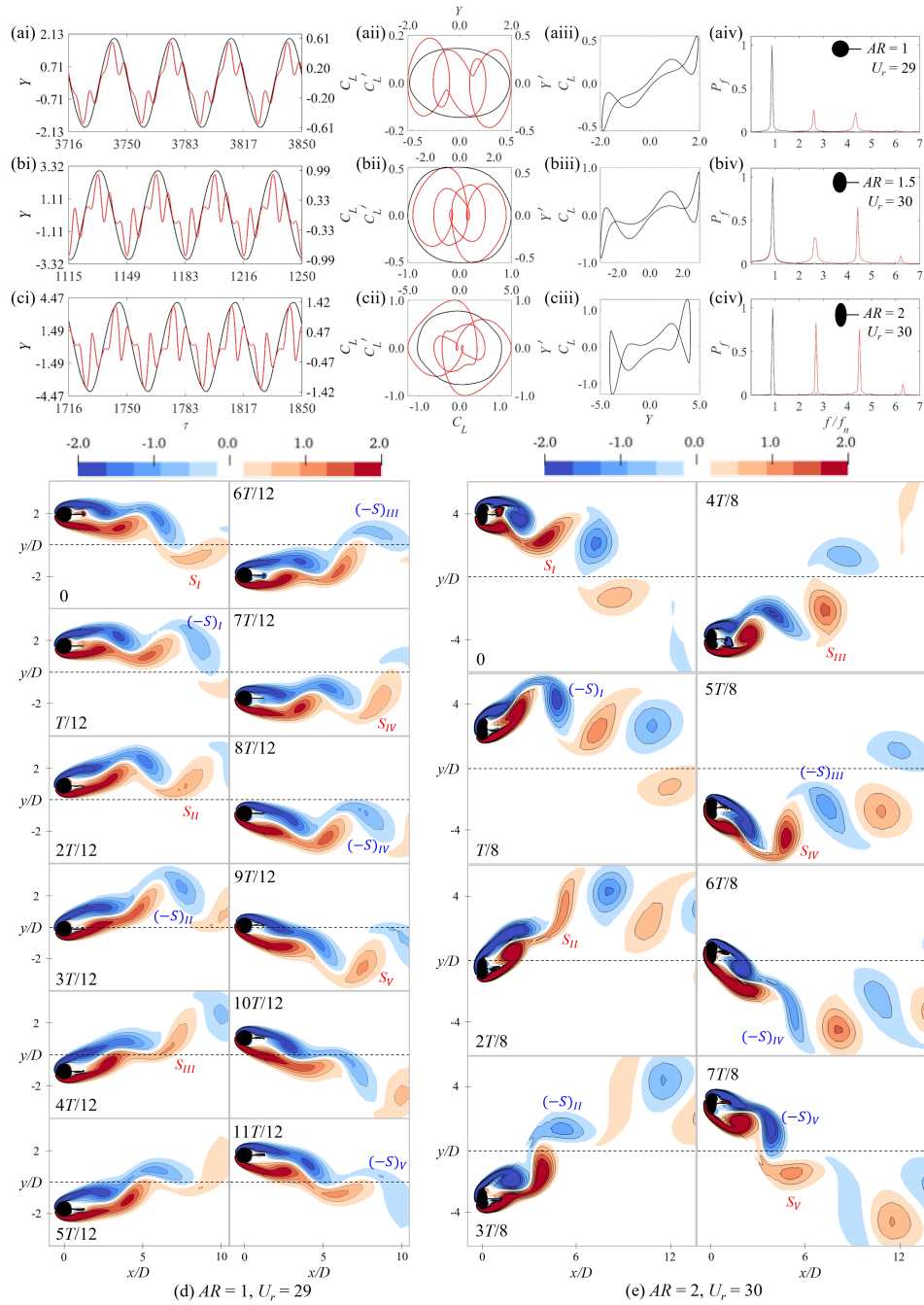


Figure 4.25: Dynamical characteristics of the 1:5 synchronization branch for an elliptical cylinder-plate assembly with (a)–(c) $AR = 1, 1.5$ and 2 at $U_r = 29$ and 30 . The vortex-shedding pattern over one oscillation cycle T is exhibited in (d)–(e) where a “ $5 \times (2S)$ ” mode is identified.

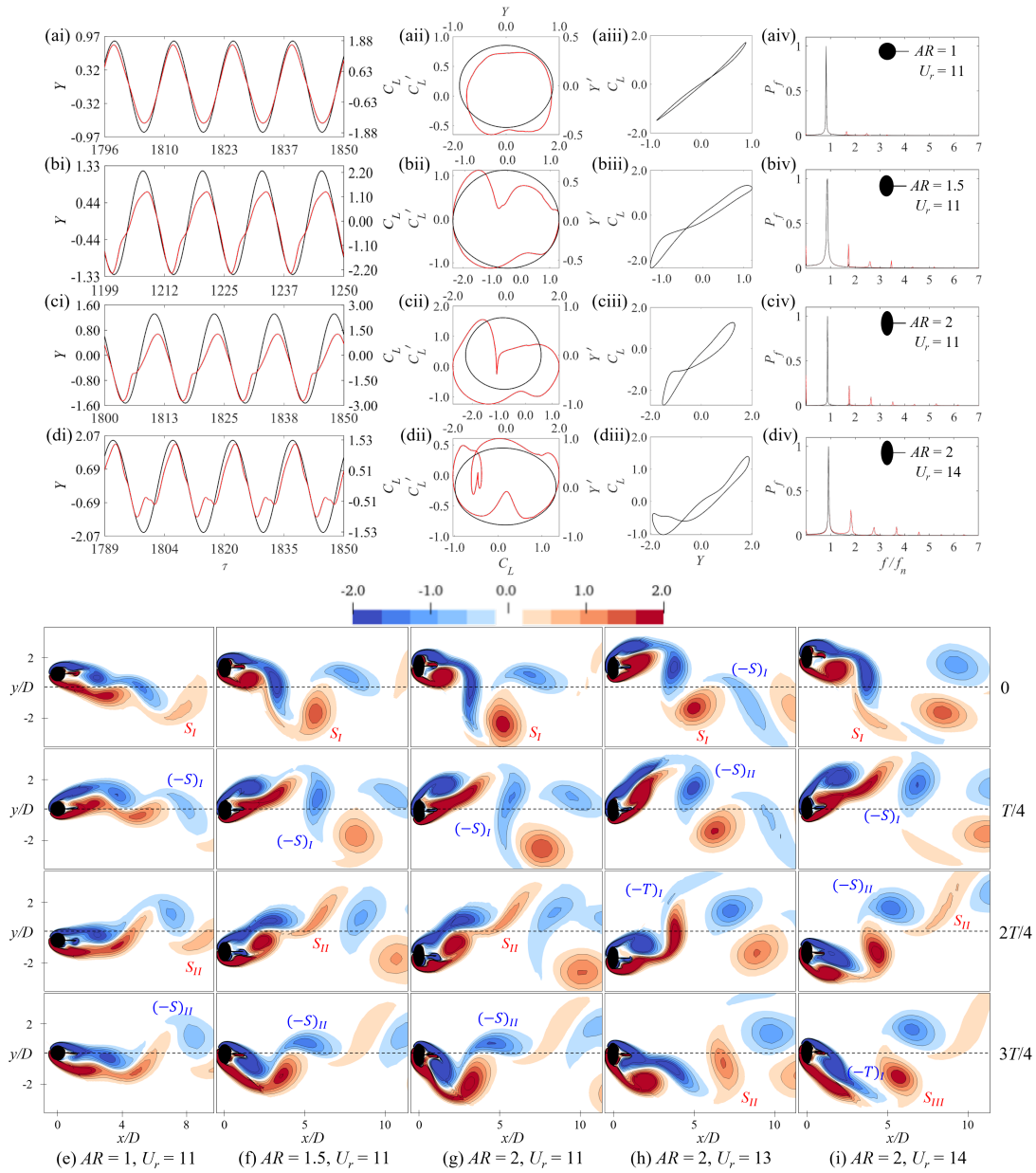


Figure 4.26: Dynamical characteristics of the 1:2 synchronization branch for an elliptical cylinder-plate assembly with (a)–(c) $AR = 1, 1.5$ and 2 at $U_r = 11$. The transition regime between the 1:2 and 1:3 synchronizations for the assembly with (d) $AR = 2$ at $U_r = 14$. Instantaneous vorticity field during one oscillation cycle for (e)–(g) $AR = 1, 1.5$ and 2 at $U_r = 11$; and, $AR = 2$ at (h)–(i) $U_r = 13$ and 14 . The “ $2 \times (2S)$ ” and “quasi- $2 \times (2S)$ ” modes are supported by the 1:2 synchronization and the transition regime, respectively.

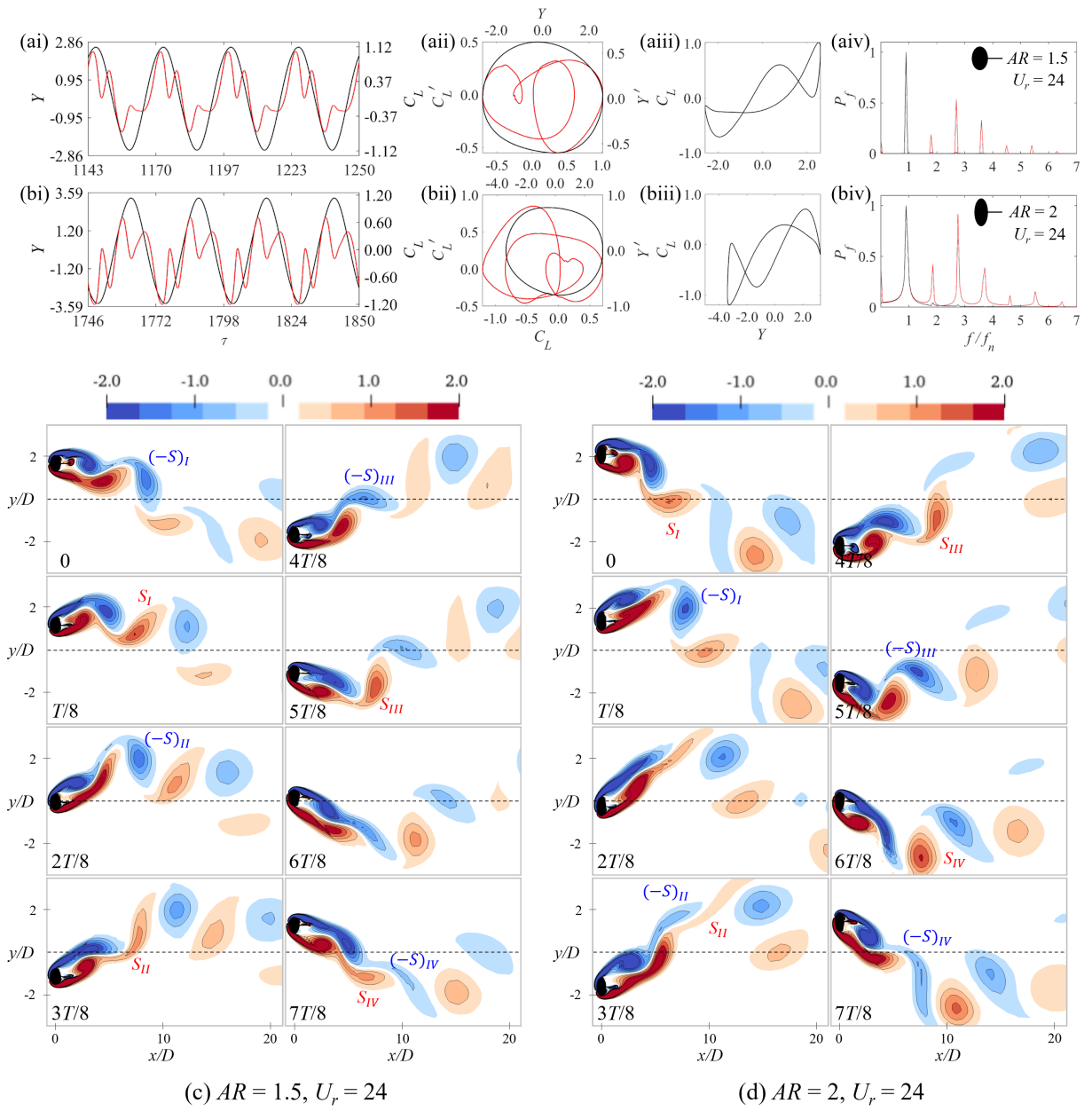


Figure 4.27: Dynamical characteristics of the 1:4 synchronization branch for an elliptical cylinder-plate assembly with (a)–(b) $AR = 1.5$ and 2 at $U_r = 24$ (c)–(d) Instantaneous vorticity field during one oscillation cycle T . The 1:4 synchronization branch supports a “ $4 \times (2S)$ ” mode.

characteristic plots of the lift coefficient and flow patterns are asymmetric. This is evident from the asymmetric $C_L(t)$ about the $C_L = 0$ line, the asymmetric phase-plane portraits $C_L-C'_L$, and the asymmetric Lissajous figures $Y-C_L$ about the origin. Other aspects of the dynamical characteristics and flow dynamics of the even-multiple synchronizations are similar to those described in the odd-multiple synchronizations. For example, increasing AR produces higher and stronger harmonic frequency components in the power spectrum of $C_L(t)$, but has a negligible effect in that of the transverse displacement. In addition, the vortex-shedding modes for the 1:2 and 1:4 synchronization branches are “ $2 \times (2S)$ ” (see Figs. 4.26 (e)–(g)) and “ $4 \times (2S)$ ” (see Figs. 4.27 (c)–(d)), respectively.

The transition regime between the 1:2 and 1:3 synchronizations for an elliptical cylinder-plate assembly with $AR = 2$ occurs over $U_r = 13$ – 14 —this is determined following a careful analysis of the shape and number of vortices shed over one oscillation cycle. More precisely, at $U_r = 13$, a “ $2S$ ” mode (vortices S_I and $-S_I$) is observed in the first part of the oscillation cycle. In the second part, an unusual flow pattern occurs: namely, the negative vortex $-S_{II}$ is followed by a same-signed “tail” vortex ($-T_I$) and, subsequently, this is accompanied by the shedding of a positive vortex S_{II} (see Fig. 4.26 (h)). Consequently, five vortices are shed during one oscillation cycle at $U_r = 13$. This number is midway between the four vortices (i.e., “ $2 \times (2S)$ ”) shed in the 1:2 synchronization branch and the six vortices (i.e., “ $3 \times (2S)$ ”) shed in the 1:3 synchronization branch. At $U_r = 14$, the “ $2S$ ” wake mode is shed twice in the first part of the oscillation cycle, which is followed in the second part by the shedding of a positive elliptically-shaped vortex S_{III} and a negative tail vortex $-T_I$ (see Fig. 4.26 (i)). Although the total number of vortices shed during one oscillation cycle here is six, the vorticity associated with the last vortex is smaller than that in the 1:3 synchronization branch—so, the transition branch occurs at $U_r = 14$.

In summary, the synchronization branch between the structural oscillation and the vortex shedding from the elliptical cylinder-plate assembly exhibit highly periodic dynamical characteristics—these can be either anti-symmetric (odd-multiple synchronizations) or asymmetric (even-multiple synchronizations). For an unlimited FIV of the amplitude response of an elliptical cylinder-plate assembly, the vortex shedding in a synchronization branch generally conforms to an “ $n \times (2S)$ ” wake mode where n is the ratio of the vortex-shedding to the vibration frequency. The vortices in this wake mode are alternately shed from one side of the assembly to the other. However, it is noted that “tail” vortices can occur in the transition regime between two synchronization branches. In marked contrast, the wake modes observed in the synchronization branches of a self-limited FIV of an elliptical cylinder-plate assembly are generally more complex (e.g., “ $T+S$ ”, “ $P+S$ ” in Section 4.2) compared to those observed in an unlimited FIV of the assembly.

4.3.4 Aperiodic Behavior in Non-Synchronization Branch

In Fig. 4.19, it is evident that there exist regions between the synchronization branches in the amplitude response of an elliptical cylinder-plate assembly. These regions correspond to the non-synchronization branches in the galloping regime. For $AR \leq 1.5$, the non-synchronization branches account for a considerable proportion in the amplitude response—the reduced-velocity range associated with these branches is comparable to or even greater than that for the synchronization branches.

Figure 4.28 displays the power spectra of the lift coefficient C_L for reduced velocities in the range $6 \leq U_r \leq 30$ for an elliptical cylinder-plate assembly with various aspect ratios ($AR = 0.75-2$). These power spectra provide a comparison of the frequency content of the C_L power spectra associated with the synchronization (colored lines) and non-synchronization (black lines) branches in the galloping regime. First, the assembly with larger aspect ratio is associated with power spectra with a more complex frequency structure—this observation applies in both the synchronization and non-synchronization branches. Second, the frequency content is composed of a fundamental frequency and a number of odd (e.g., third and fifth) harmonics in the odd-synchronization branches (e.g., 1:1, 1:3, and 1:5). In contrast, both even and odd (e.g., second, third, fourth and fifth) harmonics of the fundamental frequency are present in the even-synchronization branches (e.g., 1:2, 1:4). Additionally, the C_L power spectra of the synchronization branch are essentially invariant (unchanged) as a function of U_r . In stark contrast, the C_L power spectra varies with U_r in the non-synchronization branch—ever higher-order harmonics emerge with increasing U_r as is evident on a careful perusal of Figs. 4.28 (a) and (b).

The harmonics in the C_L power spectra in two successive synchronization branches are seen to evolve in the non-synchronization branch lying between these two branches (viz., a particular harmonic in the C_L power spectrum for the lower-order synchronization transitions to an associated harmonic in that for the next higher-order synchronization in the intervening non-synchronization branch). For example, in an elliptical cylinder-plate assembly with $AR = 1.5$ shown in Fig. 4.28 (c), the fundamental frequency in the C_L power spectrum of the 1:1 synchronization branch evolves smoothly through the non-synchronization branch at $U_r = 9-10$ (see the single grey dashed line) to give the associated second harmonic in the C_L power spectrum of the 1:2 synchronization branch. Furthermore, the second and third harmonics in the C_L power spectrum of the 1:3 synchronization branch appears to both contribute to an associated harmonic in that of the 1:4 and 1:5 synchronization branches as it undergoes a smooth transition in the frequency content of the power spectra associated with the intervening non-synchronization branches (see the pair of dashed grey lines in Fig. 4.28 (c)). In marked contrast, for an elliptical cylinder-

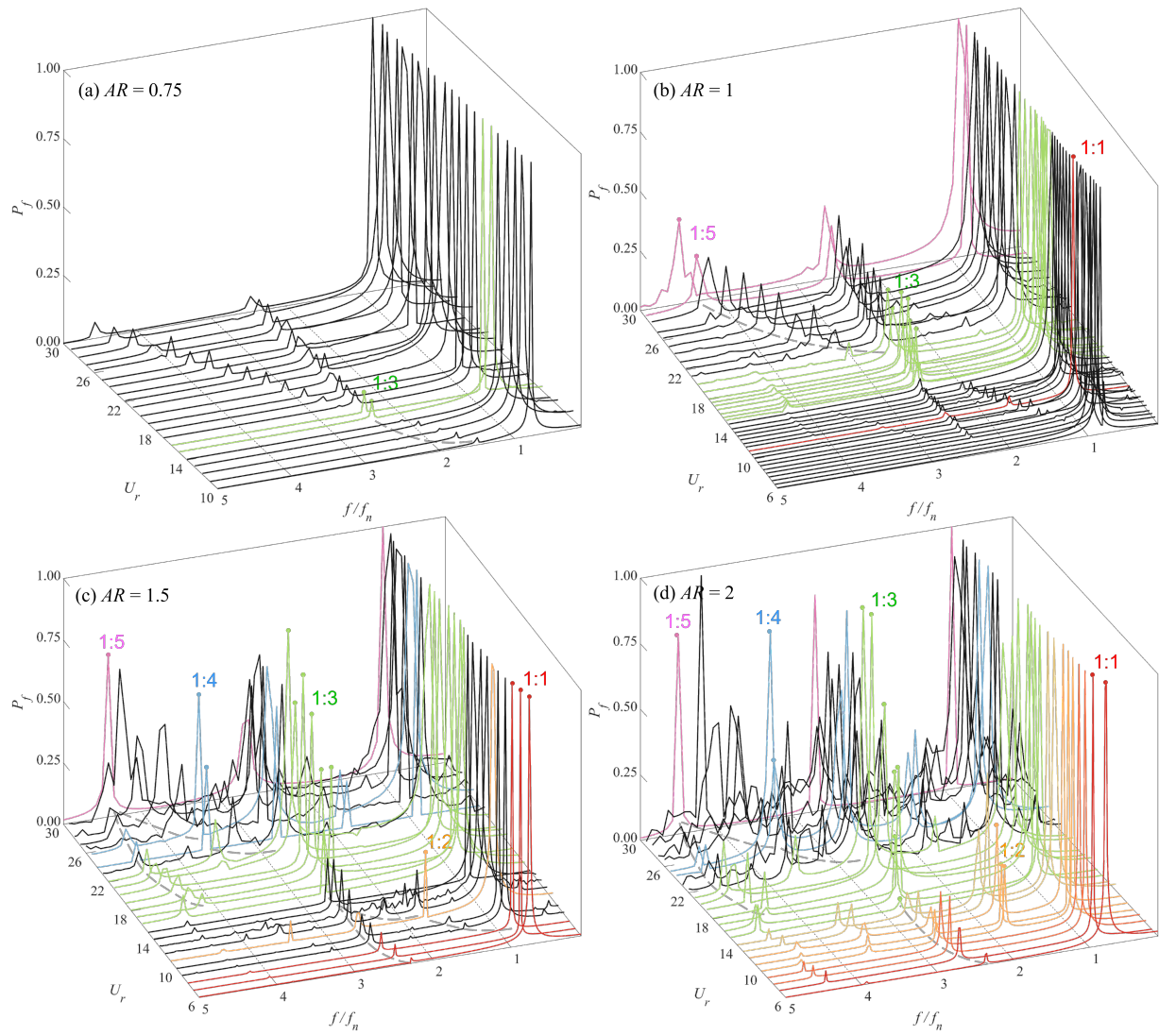


Figure 4.28: The normalized power spectra of the lift coefficient C_L for reduced velocities in the range from 6 to 30 for an elliptical cylinder-plate assembly with (a)–(d) $AR = 0.75$, 1, 1.5 and 2.

plate assembly with $AR = 2$ displayed in Fig. 4.28 (d), there is no non-synchronization branch between the 1:1, 1:2 and 1:3 synchronization branches.

The preceding analysis demonstrates that the frequencies in the C_L power spectrum corresponding to a non-synchronization branch are not necessarily harmonics of a fundamental frequency—these frequencies are a signature of the underlying aperiodic dynamics in the branch. The typical phenomenon associated with aperiodic dynamics is the presence of an amplitude modulation (or “beating”) in the $C_L(t)$. Fig. 4.29 provides an example of the aperiodic characteristics of the lift coefficient in the non-synchronization branch—the signature of the aperiodic dynamics is evident in the $C_L(t)$, the phase portrait $C_L-C'_L$ and the Poincaré section for elliptical cylinder-plate assembly with various aspect ratios and at a number of representative reduced velocities. Indeed, it is seen that the $C_L(t)$ exhibit complex variations over a number of scales, the phase-plane portrait $C_L-C'_L$ consists of multiple overlapping and intersecting loops, and the Poincaré section is composed of a complex point set (rather than simply a single point)—these characteristics are indicative of the highly aperiodic nature of the dynamics in the non-synchronization branch.

A few cases shown in Fig. 4.29 exhibit a quasi-periodic dynamical behavior (e.g., a period-doubling oscillation). For example, the dynamics shown in Fig. 4.29 (c) corresponds to a period-3 beating for the amplitude of C_L as is evident on inspection of the trajectory in the phase-space portrait $C_L-C'_L$ (similar to that seen in the periodic oscillations in the synchronization branch) and of the presence of three clusters of points in the corresponding Poincaré section. The dynamics displayed in Fig. 4.29 (d) is also a period-3 oscillation as evidenced by the fact that the $C_L(t)$ repeats every three oscillation cycles. In comparison to the C_L time series exhibited in Fig. 4.29 (c), the corresponding time series in Fig. 4.29 (d) is substantially more complex—indeed, the dynamics here corresponds to a larger value of the aspect ratio (i.e., $AR = 1.5$) and of the reduced velocity (i.e., $U_r = 23$). The greater complexity in the time series for this case is reflected also in the greater complexity in the associated phase-plane portrait $C_L-C'_L$ and in a greater number of point clusters in the associated Poincaré section. The example shown Fig. 4.29 (f) is a period-5 oscillation. The C_L time series here exhibits temporal variations on multiple time scales. The remaining examples in Fig. 4.29 are associated with aperiodic dynamics which can manifest a symmetric beating (e.g., Figs. 4.29 (ai) and (bi)), a non-symmetric beating (e.g., Fig. 4.29 (ei)), or a completely irregular beating without a clear-cut (discernible) amplitude envelope (e.g., Fig. 4.29 (gi)). An increasing value of the aspect ratio and/or the reduced velocity is associated with a more nonlinear dynamics in the non-synchronization branch.

Figure 4.30 displays the flow pattern over a number of consecutive oscillation cycles for an elliptical cylinder-plate assembly with $L_{SP}/D = 0.75$ and $AR = 1.5$ at $U_r = 28$. This flow pattern corresponds to a period-5 oscillation. An inspection of this pattern shows that

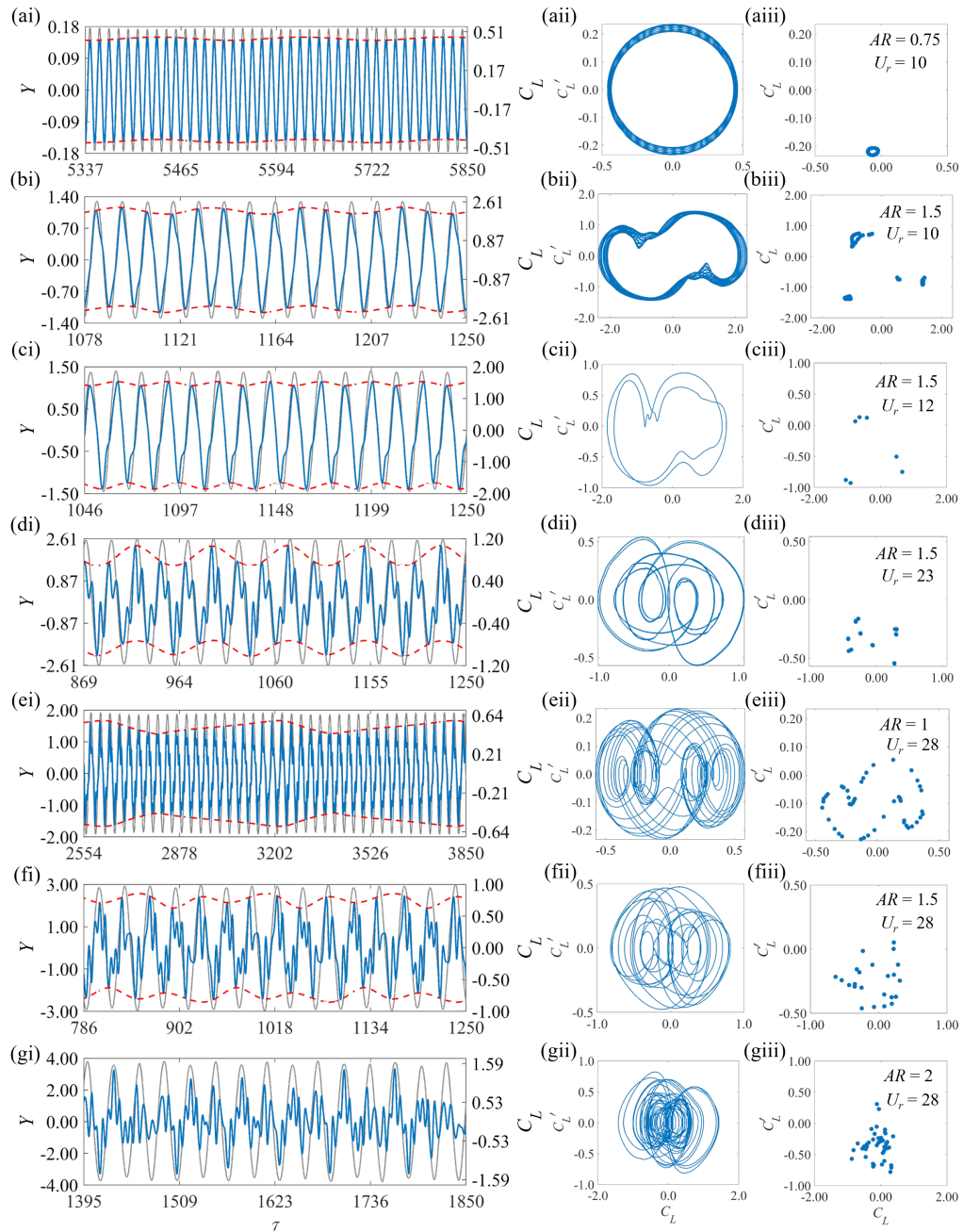


Figure 4.29: Dynamical characteristics in the non-synchronization branches of an elliptical cylinder-plate assembly with $L_{SP}/D = 0.75$. The dynamical characteristics consist of (i) the time series of Y (grey lines) and C_L (blue lines); (ii) phase portrait C_L - C'_L ; and, (iii) Poincaré section. The red dashed lines delineate the amplitude envelope of $C_L(t)$.

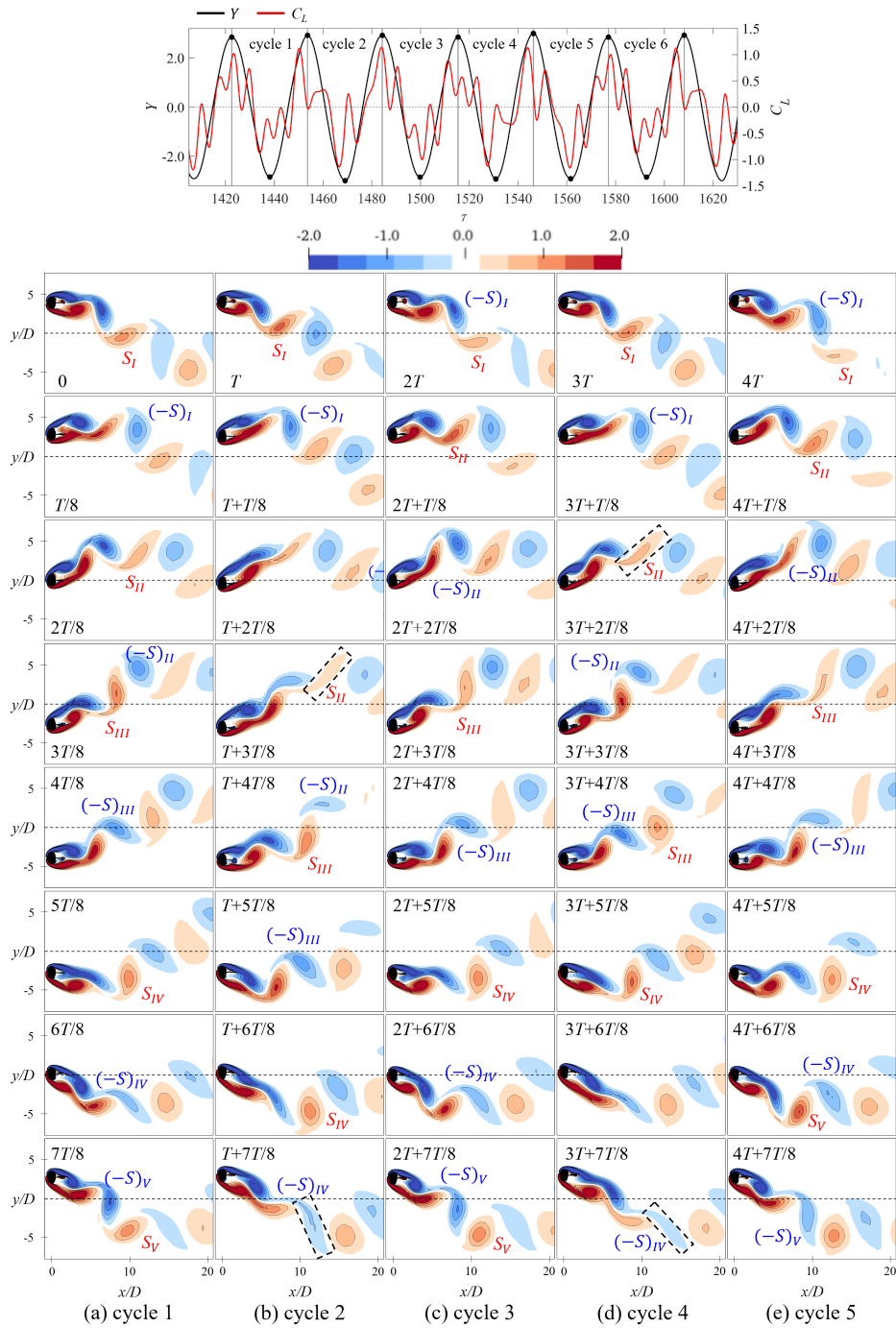


Figure 4.30: The instantaneous vorticity field over five consecutive oscillation cycles for an elliptical cylinder-plate assembly with $L_{SP}/D = 0.75$ and $AR = 1.5$ at $U_r = 28$. This is a period-5 oscillation.

the vortex shedding corresponds to an “ $n \times (2S)$ ” wake mode. At $U_r = 28$, which is located in the non-synchronization branch between the 1:4 and 1:5 synchronization branches, n can have a value of either four (cycles 2 and 4) or five (cycles 1, 3 and 5). A few non-elliptically-shaped vortices are present during the vortex-shedding process (e.g., the elongated vortices delineated within the black box). The wake mode in cycle 6 (not shown here) is identical to that of cycle 1—this implies that a period-5 oscillation is associated with this vortex-shedding pattern.

4.3.5 Elliptical Cylinder-Plate Assembly with a Longer Splitter-Plate

Sections 4.3.2–4.3.4 focus on how the aspect ratio of an elliptical cylinder-plate assembly affects the dynamical characteristics of the assembly’s unlimited FIV response. In accordance to Chapter 3, a longer splitter-plate can provoke a VIV and galloping response on a cylinder-plate assembly at small and large values of the reduced velocity, respectively. In this section, we focus on the dynamic characteristics associated with an elliptical cylinder-plate assembly with $AR = 1$ and 1.5, but with a longer splitter-plate of $L_{SP}/D = 2.5$.

Figure 4.31 shows a comparison of the branching behavior of an elliptical cylinder-plate assembly with $L_{SP}/D = 2.5$ for aspect ratios of 1 and 1.5. As shown in Fig. 4.31 (a), a “lock-in” regime and three consecutive odd-multiple (i.e., 1:3, 1:5 and 1:7) synchronization branches that about one another in the galloping regime are observed for $AR = 1$. In addition, two special branches—the still branch (grey) and initial galloping branch (pink)—are identified based on their unique dynamical characteristics (viz., the steady-state dynamics of structure and flow for the former and the presence of wake meandering for the latter). The corresponding PSDs of f_Y/f_n and f_{C_L}/f_n exhibit a simple frequency structure. When AR is increased from 1 to 1.5, the elliptical cylinder-plate assembly still exhibits a clear-cut separation in the VIV and galloping responses. However, the branching behavior of the amplitude response is significantly different as is evident from an examination of Fig. 4.31 (b). First, two even-multiple (i.e., 1:4 and 1:6) synchronization branches, with narrow reduced-velocity ranges, are present in the amplitude response at about $U_r = 14$ and 24. The 1:3 synchronization branch is absent for $AR = 1.5$. Furthermore, the synchronization branches in this case are separated from each other. Second, the still and initial galloping branches that are specific to the assembly with a longer splitter-plate, are absent. The corresponding PSDs of f_Y/f_n and f_{C_L}/f_n are more complex than those for $AR = 1$, including stronger and higher-order harmonic components in the spectrum.

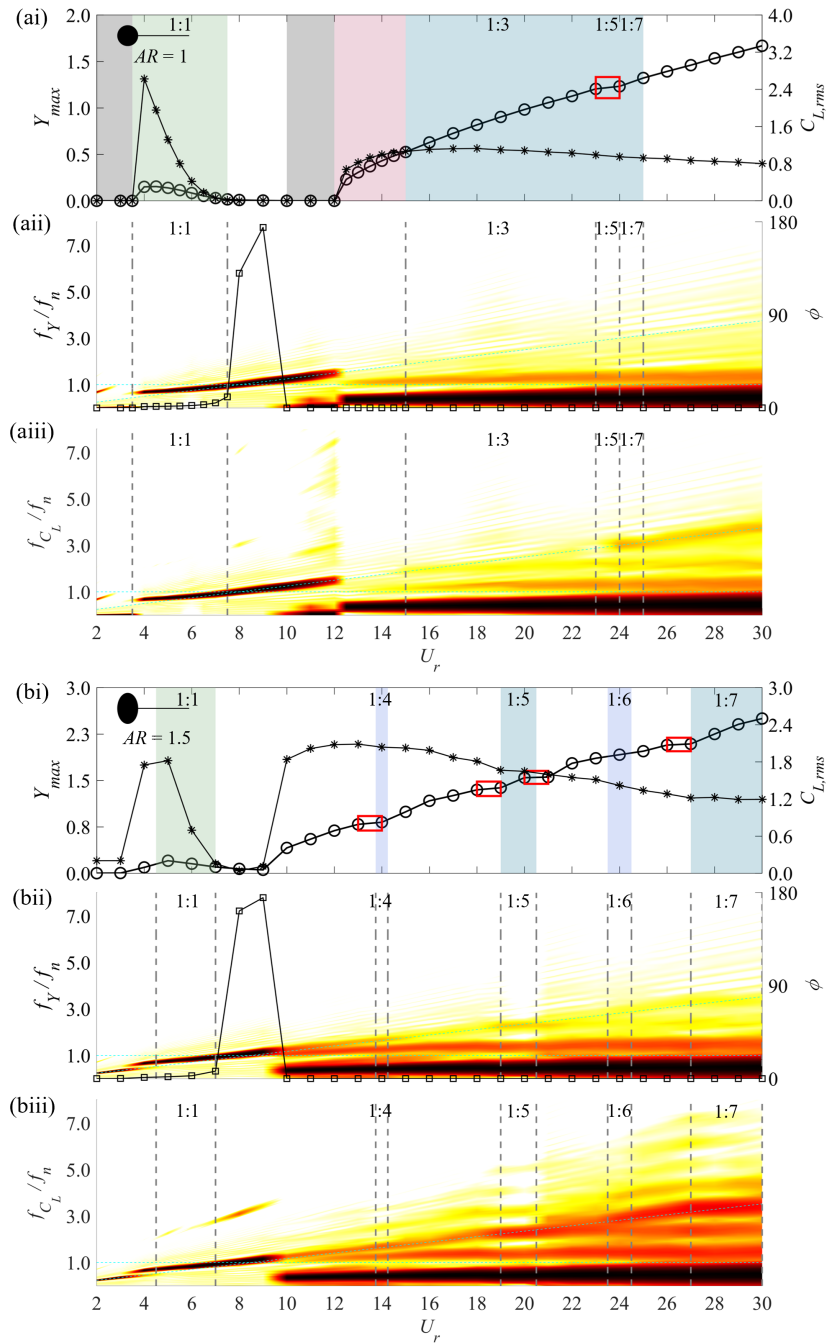


Figure 4.31: The unlimited FIV of an elliptical cylinder-plate assembly with $L_{SP}/D = 2.5$ for (a) $AR = 1$ and (b) 1.5, in terms of the branching behavior of amplitude response and PSD of Y and C_L . Other notations used here are the same as those in Figs. 4.19–4.21.

4.4 Mechanism Analysis

This section discusses some aspects related to the physical mechanisms underpinning certain interesting (unusual) dynamical characteristics of an elliptical cylinder-plate assembly described above.

Figures 4.32–4.33 display in the (AR, U_r) plane the branching behavior and wake mode of the elliptical cylinder-plate assembly experiencing the limited ($LSP/D = 0.5$) and unlimited ($LSP/D = 0.75$) FIV. The black solid lines circle the effective range for FIV responses, while the outside region represents the steady-state regimes. The synchronized branches are shaded in different colors, and the unsynchronized regimes are in white. As shown, a larger aspect ratio does not alter the nature of the dynamic response induced on an elliptical cylinder-plate assembly. The nature of the dynamic response is determined primarily by the length of the splitter-plate (e.g., a self-limited FIV response is provoked for an assembly with $LSP/D = 0.5$, an unlimited integrated VIV-galloping response appears for $LSP/D = 0.75$, and a separated VIV and unlimited galloping response is provoked for $LSP/D = 2.5$). However, larger values of AR affect the branching behavior of the amplitude response and the corresponding vortex-shedding pattern due to the significant increase in the complexity of the frequency content in the power spectrum of the lift coefficient. In some sense, a simultaneous increase in both AR and U_r can achieve the same effect with respect to the FIV response of an elliptical cylinder-plate assembly.

4.4.1 Why does an elliptical cylinder-plate assembly with $AR = 2$ and $LSP/D = 0.5$ have a narrow FIV range?

The reduced-velocity range over which the limited FIV of an elliptical cylinder-plate assembly occurs increases with AR (at least over the range of $AR = 0.75$ – 1.5). However, when the aspect ratio is 2, this trend reverses—the effective U_r range becomes smaller by a factor of roughly three compared to that for $AR = 1.5$.

To understand why this happens, we conduct a re-analysis of the branching behavior in this assembly. Two limiting cases shown in Fig. 4.4, namely, the smallest and largest values of the aspect ratio for which FIV occurs in the assembly (viz., $AR = 0.75$ and $AR = 2$), exhibit a significantly narrower range of FIV response. Moreover, only a non-synchronization and a synchronization branch are observed in the amplitude response for $AR = 0.75$ and 2, respectively. In stark contrast, the branching behavior for $AR = 1$ and 1.5 includes both synchronization and non-synchronization branches in their amplitude responses, leading to a wider range of FIV for these cases. This suggests that the significantly reduced FIV range

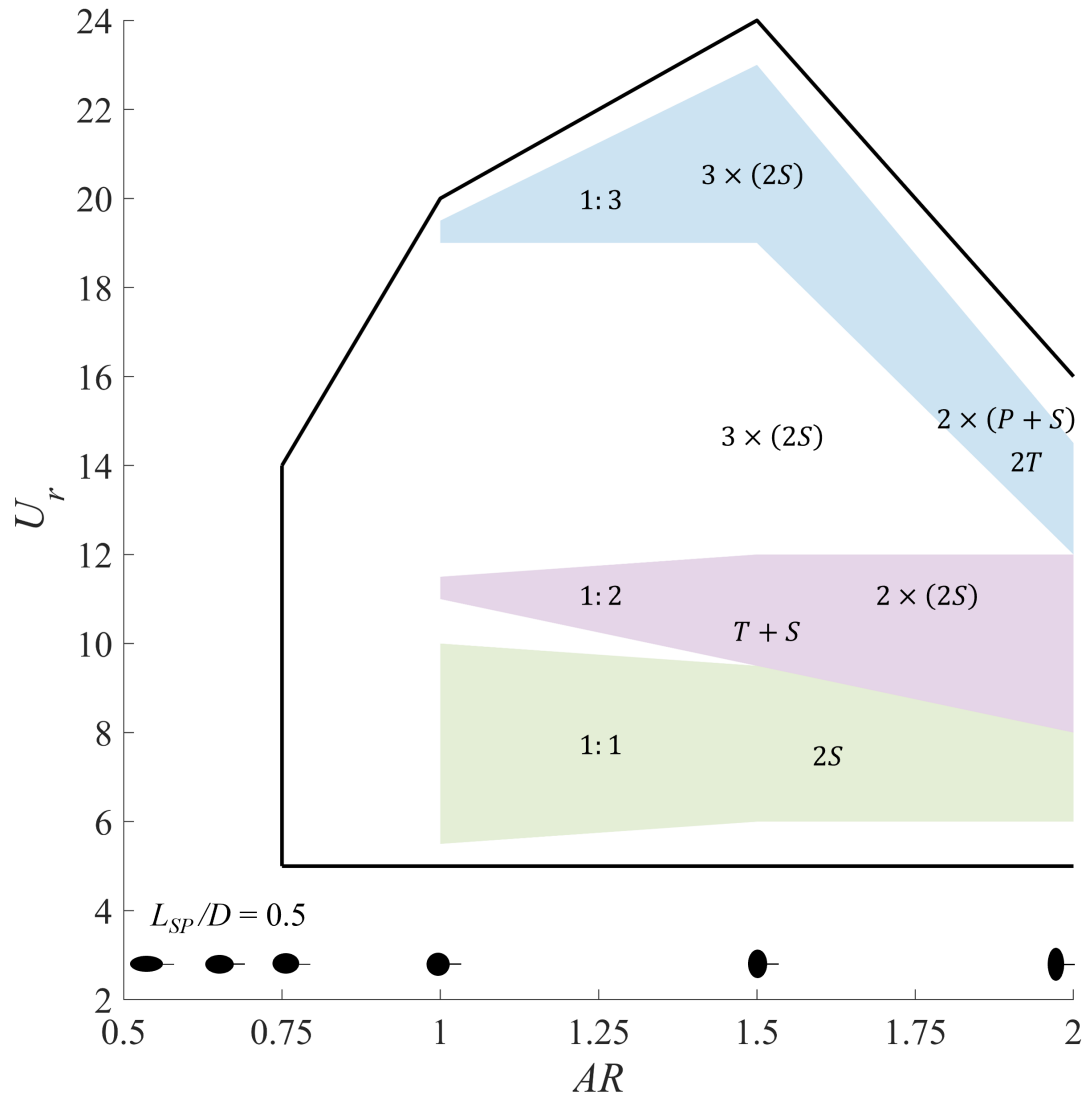


Figure 4.32: The branching behavior and wake mode for an elliptical cylinder-plate assembly with $L_{SP}/D = 0.5$ in the (AR, U_r) plane. The assembly's FIV response occurs over a limited U_r range.

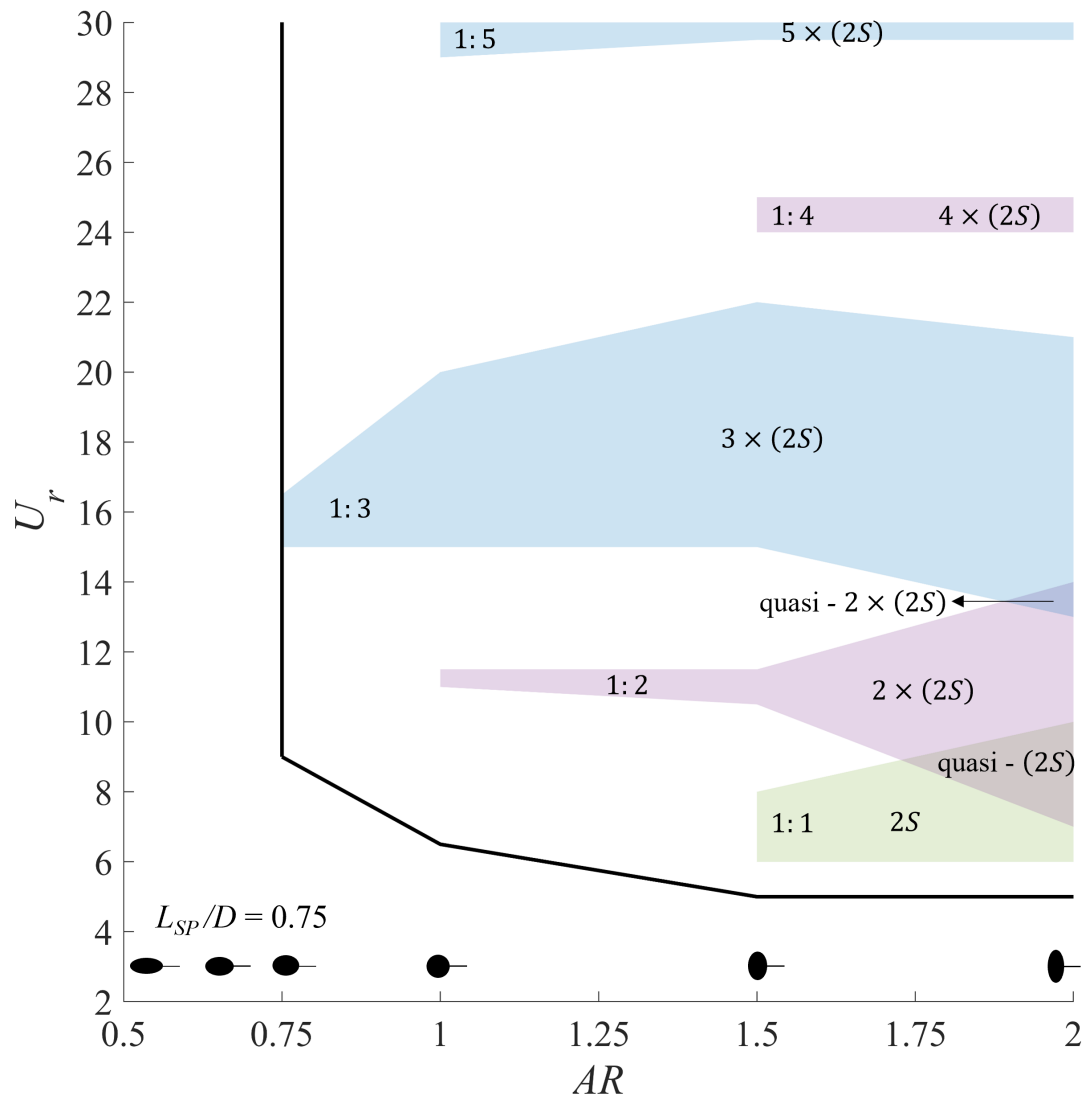


Figure 4.33: The branching behavior and wake mode of an elliptical cylinder-plate assembly with $L_{SP}/D = 0.75$ in the (AR, U_r) plane. The assembly's FIV response occurs over an unlimited U_r range.

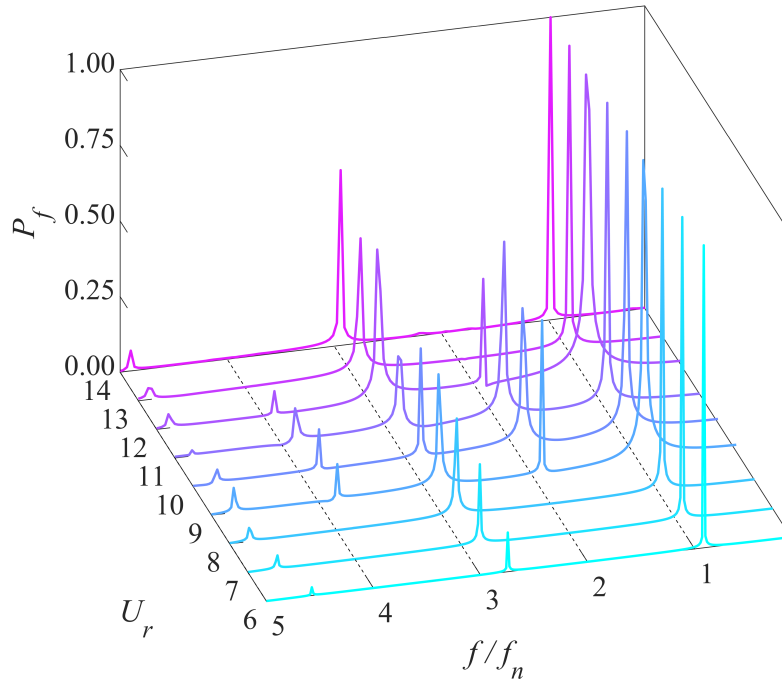


Figure 4.34: Power spectra of C_L obtained from an elliptical cylinder-plate assembly with $AR = 2$ and $L_{SP}/D = 0.5$ for $U_r = 6$ –14.

for $AR = 2$ may be due to the absence of a non-synchronization branch. Fig. 4.34 supports this hypothesis—all the frequency peaks in the C_L -power spectra for $AR = 2$ are aligned with one another over $U_r = 6$ –14. The contiguity of the three synchronization branches (viz., 1:1, 1:2, and 1:3) with no intervening non-synchronization branch between any of them and the alignment of the frequency peaks in the associated C_L -power spectra across the range of reduced velocities associated with these three branches result in a monotonic increase in the amplitude response observed for $AR = 2$.

The analysis here provides a clearer understanding of the role of synchronization and non-synchronization branches in the amplitude response of an elliptical cylinder-plate assembly experiencing a limited FIV response. In the synchronization branch, the dynamics of the structure and flow are periodic and strongly correlated with one another. Furthermore, the number of vortices shed over one oscillation cycle is an integral multiple of two (even). All these factors act together to enhance the FIV response of the assembly. In contrast, in the non-synchronization branch, there is less correlation in the dynamics of the structure and flow and the vortices shed from the assembly are more random, lead-

ing to more irregular wake modes. From this perspective, the non-synchronization branch appears to play the role of a transitional branch in the switch from a lower-order to a higher-order synchronization branch in the amplitude response. In this passage, the amplitude response may change slope or even decrease with increasing U_r (viz., the response is not necessarily monotonic). Furthermore, the non-synchronization branch (if one exists) serves to extend the effective U_r range over which the FIV response occurs. It is noted that increasing the aspect ratio from 0.75 to 2 tends to promote synchronization, while suppresses non-synchronization. Finally, the self-limited nature of the FIV response for the elliptical cylinder-plate assembly studied herein is due to the fixed splitter-plate length $L_{SP}/D = 0.5$. It is expected that a longer plate length will provoke a non-limited (galloping-dominated) FIV response.

4.4.2 Why is FIV inhibited in the elliptical cylinder-plate assembly with $AR < 0.75$?

The numerical simulations conducted herein suggest that there exists a critical value of aspect ratio $(AR)_{cri}$ (more precisely, $0.67 < (AR)_{cri} \leq 0.75$ for $Re = 100$ with $L_{SP}/D = 0.5$) below which an elliptical cylinder-plate assembly undergoes no oscillation. Therefore, a natural question is: why can't FIV be provoked in an elliptical cylinder-plate assembly with an aspect ratio less than $(AR)_{cri}$?

To address this question, we examine the flow dynamics surrounding an elastically-mounted elliptical cylinder-plate assembly. Our numerical simulations demonstrate that the structural oscillation is not induced in the assembly for $AR = 0.5$ and 0.67 . Even so, we note that these cases are associated with different wake patterns. For $AR = 0.5$, the assembly does not oscillate and the surrounding flow does not exhibit any dynamics on an examination of Figs. 4.35 (ai) and (bi). However, for $AR = 0.67$, the assembly undergoes oscillations with a very small amplitude (viz., $Y_{max} \approx 0.002D$), accompanied by alternative vortex shedding in the wake (see Figs. 4.35 (aii) and (bii)). For larger values of $AR = 0.75$ and 1 , the assembly exhibits a clear-cut FIV with a more evident vortex shedding.

A careful examination of the near wake shows that the structural oscillation is highly correlated with the location of the flow separation. Figs. 4.35 (c) and (d) compare the zoomed-in instantaneous vorticity fields around an elliptical cylinder-plate assembly for various aspect ratios at times $t = 3T/8$ and $t = 7T/8$, respectively. The points, designated as A and B , identify the separation points of flow from the surface of the elliptical cylinder—these points are seen to move gradually towards the leading edge (viz., windward side) of the assembly with increasing AR , owing to the fact that the major axis (larger dimension)

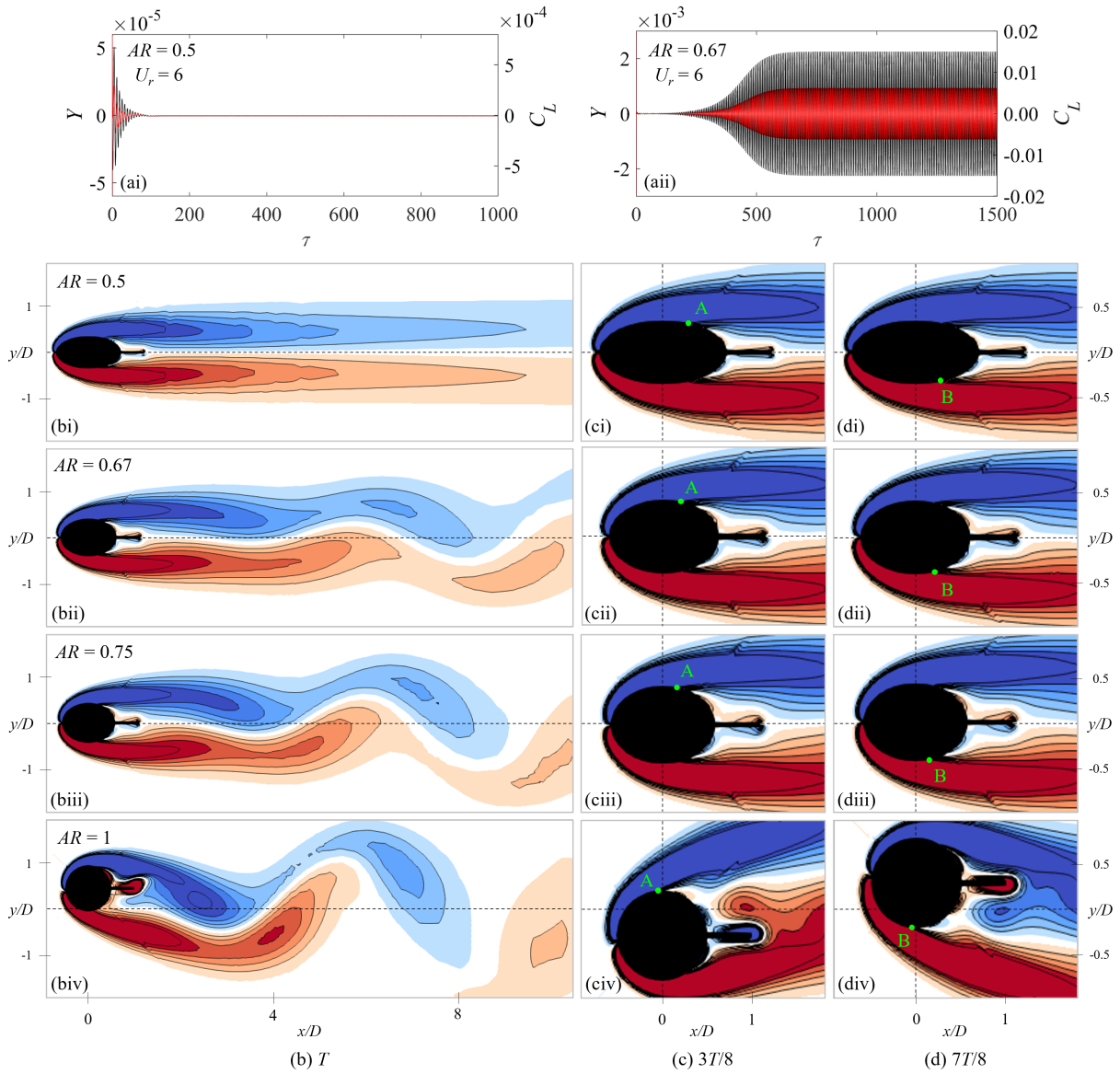


Figure 4.35: A comparison of the structural oscillations and the flow surrounding the elliptical cylinder-plate assembly with $AR = 0.5-1$ and $L_{SP}/D = 0.5$ at $U_r = 6$. (a) Time series of Y (black) and C_L (red) for $AR = 0.5$ (left panel) and $AR = 0.67$ (right panel). (b) The flow patterns surrounding the assembly at time $t = T$ for (i)–(iv) $AR = 0.5, 0.67, 0.75$ and 1 . Zoomed-in view of the instantaneous vorticity field around the assembly at times (c) $t = 3T/8$ and (d) $t = 7T/8$ for (i)–(iv) $AR = 0.5, 0.67, 0.75$ and 1 .

of the elliptical cylinder is along the transverse direction. From these considerations, it seems that the earlier the flow separation occurs, the greater is the susceptibility for the assembly to undergo FIV (all other factors remain the same such as U_r and L_{SP}/D). This explains why an elliptical cylinder-plate assembly with an aspect ratio less than a certain critical value cannot experience oscillatory motions.

As noted earlier in Section 2.1.2, Zhao *et al.* [192] interpreted the amplified VIV response of an elliptical cylinder with a large aspect ratio as the consequence of a reduced afterbody for such geometry. This is similar to the explanation provided here in the context of an elliptical cylinder-plate assembly. The main difference is that for the assembly, the effect of aspect ratio is related to the change in the position of the flow separation point, rather than the size of afterbody (which is difficult to define precisely for an elliptical cylinder-plate assembly).

4.5 Chapter Summary

In this chapter, both the limited and unlimited FIV responses of an elliptical cylinder-plate assembly are investigated using numerical simulation at $Re = 100$, with a mass ratio of 10 and zero structural damping ratio. The aspect ratio AR and the splitter-plate length L_{SP} affect the dynamical characteristics of the free oscillation of an elliptical cylinder-plate assembly.

First, the elliptical ratio AR determines whether an oscillation can be triggered in the assembly—a critical value for $0.67 < (AR)_{cri} < 0.75$ is required for this to occur at $Re = 100$. Because if the minor axis of elliptical cylinder (oriented in the transverse direction) is too short, the flow separation point occurs too far back on the windward surface of the elliptical cylinder to provoke an oscillatory motion. Second, the splitter-plate length L_{SP} determines primarily the nature of the FIV response that can be induced on the assembly (*viz.*, whether the response is limited or unlimited in terms of the reduced-velocity range).

For $L_{SP}/D = 0.5$, the FIV response of the elliptical cylinder-plate assembly occurs in a limited reduced-velocity range. From the viewpoint of structural vibration, no oscillation is induced on the assembly with an aspect ratio smaller than the critical value ($0.67 < (AR)_{cri} < 0.75$ at $Re = 100$). Increasing the value of aspect ratio to $0.75 \leq AR \leq 1.5$, the assembly's FIV is significantly amplified, not only occurring over a wider U_r range (e.g., $U_r = 6\text{--}14$ for $AR = 0.75$ and $U_r = 6\text{--}24$ for $AR = 1.5$) but also displaying a larger maximum transverse displacement (e.g., $Y_{max} = 0.36D$ for $AR = 0.75$ and $Y_{max} = 2D$ for

$AR = 1.5$). However, the assembly with a larger aspect ratio of $AR = 2$ exhibits FIV over a narrow U_r range of $U_r = 6$ – 16 due to the absence of non-synchronization branch in the amplitude response.

By contrast, the elliptical ratio has only a limited impact on the branching behavior in the amplitude response—no synchronization for $AR = 0.75$, and three synchronizations (with $f_Y^*/f_{C_L}^* = 1:1, 1:2$ and $1:3$) for $AR = 1$ – 2 . The self-limited FIV of assembly is thus identified as an integrated VIV and galloping. In general, increasing AR leads to an increase in the complexity of dynamical characteristics observed in the synchronization branch. For example, although a classical “2S” mode is identified in the 1:1 synchronization branch (lock-in regime), the shape of vortex becomes more complex for larger AR —an elliptically-shaped vortex is shed in the wake for $AR = 1$, a vortex with a tail is present for $AR = 1.5$, and a signature swallow-tailed vortex and a parallel vortex street are observed for $AR = 2$. The 1:2 synchronization is associated with asymmetric wake modes (e.g., “ $2 \times (2S)$ ”, “T+S”, “ $\pm(2S)$ ”) or irregular wake patterns depending on AR . In the 1:3 synchronization, the vortex shedding again exhibits a regular and alternating pattern (e.g., “ $3 \times (2S)$ ” and “ $2 \times (P+S)$ ” wake modes).

The non-synchronization branch is characterized by the aperiodic and highly-nonlinear flow dynamics (e.g., beating and chaotic oscillations of the lift coefficient C_L), in which the structure oscillation and the vortex shedding are not correlated with one another. In fact, the non-synchronization branch functions as a transition in the passage from a lower-order to a higher-order synchronization branch in the amplitude response and leads to an increased reduced-velocity range for FIV in the elliptical cylinder-plate assembly.

For $L_{SP}/D = 0.75$ and 2.5 , the FIV response of the elliptical cylinder-plate assembly occurs in an unlimited reduced-velocity range. In this case, a larger AR always provokes a stronger unlimited FIV response through a reduction of the onset velocity and a concomitant increase the vibration amplitude.

For branching behavior, increasing AR results in the generation of more synchronization branches in the amplitude response (e.g., $AR = 0.75$ has a 1:3 synchronization branch; $AR = 1$ is associated with 1:2, 1:3 and 1:5 synchronization branches; and, $AR = 1.5$ and 2 have corresponding 1:1, 1:2, 1:3, 1:4 and 1:5 synchronization branches). Accordingly, an unlimited FIV response can transition from a galloping-dominated to an integrated VIV-galloping response. In particular, transition regimes are present between the 1:1 and 1:2 and between the 1:2 and 1:3 synchronization branches in the amplitude response for an elliptical cylinder-plate assembly with $AR = 2$.

A regular alternating vortex-shedding pattern is observed in the various synchronization branches of the response—the pattern is associated with an “ $n \times (2S)$ ” wake mode for a 1: n

synchronization branch. However, the shape of the vortices that are shed from the assembly are affected by the aspect ratio AR and the reduced velocity U_r . For example, increasing AR results in the shedding of slender vortices at times corresponding to the amplitude maxima of the transverse displacement. Furthermore, increasing U_r results in a more vertical orientation (viz., oriented more strongly in the transverse direction) in the vortices that are shed from the assembly. This leads to a subdivision of the 1:3 synchronization branches for assembly with $AR = 1.5$ and 2. In addition, a “quasi-2S” mode and a “quasi-2×(2S)” wake mode are present in the transition regimes (viz., the regime between the 1:1 and 1:2 synchronization branches and between the 1:2 and 1:3 synchronization branches). The vortices shed in the transition regime consist of a combination of a primary elliptically-shaped vortex and a secondary weaker “tail”-shaped vortex. The number of vortices shed in the transition regime is between those of the two synchronization branches that bracket it on either side. By contrast, the non-synchronization branch is characterized by aperiodic oscillations (e.g., amplitude modulation of $C_L(t)$) and the period-doubling oscillation associated with the vortex-shedding pattern marking the transition from a lower-order to a higher-order synchronization branch.

Chapter 5

GA–Optimized Nonlinear Grey-Box Model for FIV

5.1 Problem Description

It is known that the coupled wake-oscillator model includes two differential equations, namely, the structure equation in terms of vibrating displacement (Y) and the fluid equation in terms of lift coefficient (C_L) or wake rotation angle (θ). Besides the independent variables, the equation system also has various undetermined parameters. As a consequence, determining appropriate model parameters (viz., model identification) is crucially important to the application of phenomenological models to predict the FIV phenomenon.

In previous studies, the model parameters are often decided through experimental data or engineering experience. For example, the undetermined coefficients in the original Facchinetti model (Eqs. (5.3)–(5.4)) can be directly determined from the stationary tests (e.g., $m^* = 250$, $\zeta = 0.0031$, $St = 0.2$, $C_{L0} = 0.3$, $C_D = 2.0$ for Reynolds number in the sub-critical range 300–150,000) and the forced-oscillation tests (e.g., $\epsilon = 0.3$, $A = 12$), or calculated from given parameters (e.g., $\gamma = C_D/(4\pi St)$, $\delta = 1/(StU_r)$). Similarly, the newly introduced parameters related to the θ -based wake oscillator in the original Mannini model [97], such as the size of wake lamina, can be evaluated by means of the flow visualization. To be specific, the two new physical parameters are expressed as a function of St , f_m and h^* , viz., $\zeta_f = 4\sqrt{2}St^2h^*f_m/\pi$ and $\bar{l}^* = 1/8\pi St^2h^*$, where $h^* = 1.8$ is determined by the definition of wake oscillator for rectangular cylinder with a side ratio of 1.5.

However, the experiment- and experience-based determination of model parameters has some inherent deficiencies. First, the parameter without clear physical meaning is often

estimated by fitting to the experimental data (such as ϵ and A of the original Facchinetti model), which means the resulted parameter works only for the specific experimental condition. Second, not all physical parameters can be easily derived from measurements. For example, Mannini *et al.* [97] mentioned that the Magnus effect coefficient f_m for a sharp-edged body was questionable and not straightforward, so they calibrated f_m based on experimental data. Third, the instantaneous flow visualization is not always available and the parameter value is somewhat arbitrary and subjective depending on the researcher.

In this chapter, we first improve the two kinds of wake-oscillator models based on the lift coefficient C_L and the wake angular displacement θ . Then, a genetic algorithm (GA) enhanced grey-box nonlinear model estimation framework is proposed to evaluate the free parameters of wake-oscillator model. This data-driven methodology to determine model parameters is verified under two different scenarios, namely, the VIV of a circular cylinder and the galloping of a circular cylinder-plate assembly with $L_{SP}/D = 0.75$. The estimation data used here is from the simulation dataset in Chapter 3.

5.2 Improved Mathematical Model

5.2.1 Improved Wake-Oscillator Model Based on C_L

Original Facchinetti model

As mentioned in Chapter 2.4, one of the most popular wake-oscillator models that apply the aerodynamic force coefficient as fluid variable is the coupled model proposed by Facchinetti *et al.* [39] in 2004 (called as Facchinetti model hereafter). This mathematical model applies the basic Van der Pol kernel to describe the transverse VIV of a circular cylinder in stationary uniform flow (see Fig. 5.1).

The structure oscillator and wake oscillator are respectively expressed in the following dimensional forms:

$$m\ddot{y} + c\dot{y} + ky = \frac{1}{2}\rho U^2 D C_L, \quad (5.1)$$

$$\ddot{q} + \varepsilon\omega_{vs} (q^2 - 1) \dot{q} + \omega_{vs}^2 q = \frac{A}{D}\ddot{y}. \quad (5.2)$$

In Eq. (5.1), the total mass $m = m_{osc} + m_a$ takes into account both the structure mass m_{osc} and the fluid-added mass $m_a = \frac{C_a \rho \pi D^2}{4}$ (where $C_a = 1$ for circular cylinder). Similarly, the structure damping $c = c_{sys} + c_f$ includes both the viscous damping c_{sys} and the fluid-added

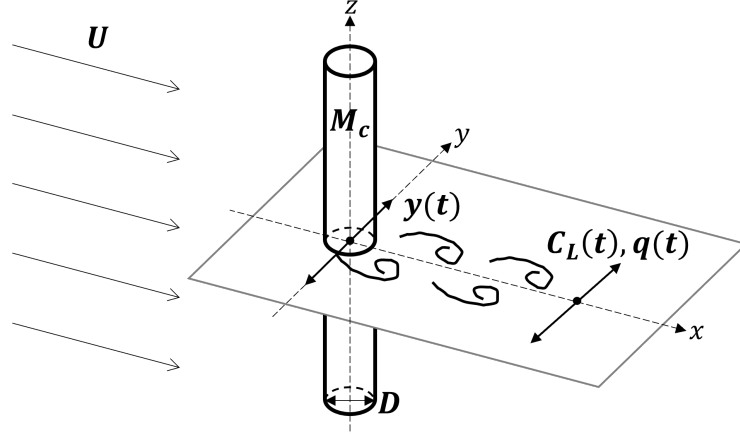


Figure 5.1: A schematic model of an elastically mounted circular cylinder undergoing the cross-flow VIV due to the aerodynamic fluid force acting on the oscillating body.

damping $c_f = \gamma \omega_{vs} \rho D^2$ (where the coefficient γ , also called the stall parameter, is related to the drag coefficient through $\gamma = \frac{C_D}{4\pi St}$). Other quantities include the stiffness k , the fluid density ρ , the free-stream velocity U , the cylinder diameter D , the lift coefficient C_L and the transverse displacement y , velocity \dot{y} , acceleration \ddot{y} of the oscillating body. It should be noted that Facchinetti model is a two-dimensional model, so all mass, damping and stiffness parameters are defined per unit length. In Eq. (5.2), the generalized fluid variable q can be any physical quantity that characterizes the fluctuation of near wake theoretically, which is still related to the lift coefficient in Facchinetti model by $q = 2 \frac{C_L}{C_{L0}}$ (where C_{L0} is the reference lift coefficient observed on a fixed circular cylinder subjected to vortex shedding). The forcing term expressed as acceleration coupling models the effects of the structural motion on the surrounding fluid. Other quantities include the vortex-shedding angular frequency $\omega_{vs} = \frac{2\pi St U}{D}$ and two constant parameters ϵ and A .

The corresponding non-dimensional dynamical system can be written as:

$$\ddot{Y} + \left(2\xi\delta + \frac{\gamma}{m^*}\right) \dot{Y} + \delta^2 Y = \frac{1}{8\pi^2 St^2 m^*} \frac{C_{L0}}{2} q, \quad (5.3)$$

$$\ddot{q} + \epsilon(q^2 - 1)\dot{q} + q = A\ddot{Y}. \quad (5.4)$$

The overdot in Eqs. (5.3)–(5.4) refers to the derivative with respect to the dimensionless time $\tau = \omega_{vs} t$. Other dimensionless terms include the dimensionless displacement $Y = \frac{y}{D}$, the structural mass ratio $m^* = \frac{m}{\rho D^2}$, the structural damping ratio $\xi = \frac{c_{sys}}{2\omega_n m}$ with ω_n being the structural natural angular frequency $\omega_n = \sqrt{\frac{k}{m_s + m_a}}$, and the frequency ratio $\delta = \frac{\omega_n}{\omega_{vs}}$.

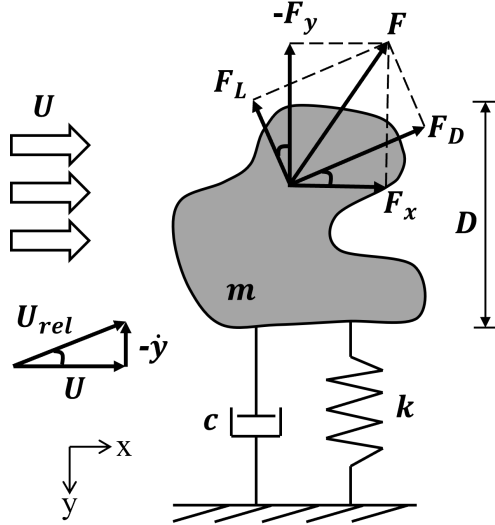


Figure 5.2: A schematic of a bluff body experiencing transverse galloping.

In order to adapt to the numerical results under various flow speeds, the non-dimensional expressions with respect to the frequency ratio δ are first reformulated in terms of the reduced velocity $U_r = \frac{U}{f_n D}$ by $\delta = \frac{1}{StU_r}$, so Eq. (5.3) becomes:

$$\ddot{Y} + \left(\frac{2\xi}{StU_r} + \frac{\gamma}{m^*} \right) \dot{Y} + \frac{1}{St^2 U_r^2} Y = \frac{1}{8\pi^2 St^2 m^*} \frac{C_{L0}}{2} q. \quad (5.5)$$

Improved Facchinetti model

The original Facchinetti model can only predict the VIV of circular cylinder but cannot describe the galloping-type oscillation of other shapes, because it does not include the relevant physics. As reviewed in Chapter 2.4.3, the quasi-steady theory is a common analytical tool to calculate the fluid force causing galloping. In Fig. 5.2, the aerodynamic force in the transverse direction F_y can be calculated by projecting the lift and drag (measured in the static wind-tunnel tests on a stationary body under various incidence angles α) along y -axis. The quasi-steady transverse force coefficient C_L^{QS} is therefore a function of α , and of $\alpha \approx \tan\alpha = \dot{y}/U$ (assuming the body's velocity \dot{y} is much smaller than that of the incoming flow U).

On this basis, Parkinson and Smith [118] employed a seventh-order polynomial to ap-

proximate C_L^{QS} over the pertinent range of α , which has the following dimensional form:

$$C_L^{QS} = A_1 \left(\frac{\dot{y}}{U} \right) + A_3 \left(\frac{\dot{y}}{U} \right)^3 + A_5 \left(\frac{\dot{y}}{U} \right)^5 + A_7 \left(\frac{\dot{y}}{U} \right)^7, \quad (5.6)$$

where A_i ($i = 1, 3, 5, 7$) are fitting coefficients of odd polynomial terms depending on the Reynolds number. The corresponding dimensionless form reads:

$$C_L^{QS} = A_1 (2\pi St) \dot{Y} + A_3 (2\pi St)^3 \dot{Y}^3 + A_5 (2\pi St)^5 \dot{Y}^5 + A_7 (2\pi St)^7 \dot{Y}^7. \quad (5.7)$$

This approximation for $C_L^{QS}(\alpha)$ was then incorporated as a forcing term in the governing equation of a linear mass–spring–damper to form the single-equation analytical model for the pure galloping oscillation.

From above discussions, the most straightforward way to include both VIV and galloping in a wake-oscillator model is to simply superimpose the two aerodynamic force components inducing VIV and galloping in a linear fashion [32, 159]. Therefore, the forcing term in Eq. (5.1) should be of $(C_L + C_L^{QS})$. The new motion equation of structure has the following dimensionless form:

$$\ddot{Y} + \frac{2\xi}{StU_r} \dot{Y} + \frac{1}{St^2U_r^2} Y = \frac{1}{8\pi^2 St^2 m^*} \left[\frac{C_{L0}}{2} q + A_1 (2\pi St) \dot{Y} + \dots + A_7 (2\pi St)^7 \dot{Y}^7 \right]. \quad (5.8)$$

It should be noted that the seventh-order polynomial expression of C_L^{QS} in Eq. (5.8) also includes even terms, viz. $C_L^{QS} = \sum_{i=1}^7 A_i (2\pi St)^i \dot{Y}^i$, which is more generalized than the odd-only approximation. Moreover, the stall term (viz., the fluid-added damping term $\gamma \dot{Y}/m^*$) in the structure equation of original Facchinetti model (Eq. (5.3)) is implicitly incorporated in the term of \dot{Y} on the right hand side and the effect of γ is represented by a constant coefficient A_1 . The wake oscillator (Eq. (5.4)) is also modified by including an extra velocity coupling as the forcing term, which reads:

$$\ddot{q} + \varepsilon (q^2 - 1) \dot{q} + q = B_1 \ddot{Y} + B_2 \dot{Y}, \quad (5.9)$$

where B_i ($i = 1, 2$) is fitting coefficient.

In order to directly use the numerical results (viz., the time sequences of displacement Y and lift coefficient C_L) in Chapters 3–4, the wake variable q in Eqs. (5.8)–(5.9) needs to be converted to the lift coefficient C_L through $q = 2C_L/C_{L0}$. The modified dynamical system consists of the following two ordinary differential equations (ODE):

$$\ddot{Y} + \frac{2\xi}{StU_r} \dot{Y} + \frac{1}{St^2U_r^2} Y = \frac{1}{8\pi^2 St^2 m^*} \left[C_L + A_1 (2\pi St) \dot{Y} + \dots + A_7 (2\pi St)^7 \dot{Y}^7 \right], \quad (5.10)$$

$$\ddot{C}_L + \varepsilon \left(\frac{4}{C_{L0}^2} C_L^2 - 1 \right) \dot{C}_L + C_L = B_1 \ddot{Y} + B_2 \dot{Y}. \quad (5.11)$$

As shown, the coupled wake-oscillator model after multiple measures of improvement (Eqs. (5.10)–(5.11)) is now explicitly formulated with respect to Y and C_L .

5.2.2 Improved Wake-Oscillator Model Based on θ

In addition to taking the instantaneous lift coefficient as the fluid variable, another major class of wake oscillator is based on the wake rotation angle θ (see Chapter 2.4.2). A representative is the coupled wake-oscillator model for FIV of a rectangular cylinder proposed by Mannini *et al.* [97] in 2018 (called as Mannini model hereafter) with the following dimensional form:

$$m\ddot{y} + c_{sys}\dot{y} + ky = \frac{1}{2}\rho U^2 D \left(C_L + C_L^{QS} \right), \quad (5.12)$$

$$\bar{I}\ddot{\theta} - \bar{C} \left(1 - \frac{4f_m^2}{C_{L0}^2} \theta^2 \right) \dot{\theta} + \bar{k}\theta = \frac{\bar{I}}{\bar{l}}\ddot{y} + \frac{\bar{k}}{U}\dot{y}. \quad (5.13)$$

As shown, the forcing term in Eq. (5.12) is composed of two parts, namely, the aerodynamic lift inducing VIV:

$$C_L = f_m \left(\theta - \frac{\dot{y}}{U} \right), \quad (5.14)$$

and the quasi-steady lift inducing galloping:

$$C_L^{QS} = A_1 \frac{\dot{y}}{U} + A_3 \left(\frac{\dot{y}}{U} \right)^3 + A_5 \left(\frac{\dot{y}}{U} \right)^5 + A_7 \left(\frac{\dot{y}}{U} \right)^7. \quad (5.15)$$

The model parameter f_m is related to the Magnus effect and can be determined from experimental tests on a rotating cylinder [159]. C_{L0} represents the amplitude of fluctuating lift coefficient due to vortex shedding on a stationary body. Other aerodynamic parameters in Eq. (5.13) depend on the definition of wake oscillator, such as the moment of inertia \bar{I} , the fluid damping \bar{C} , the spring constant \bar{k} and the half length of wake lamina \bar{l} . Moreover, the oscillating mass m , the structural damping c_{sys} and the system stiffness k are defined per unit length for a two-dimensional model.

Mannini *et al.* [97] normalized Eqs. (5.12)–(5.13) using the dimensionless quantities proposed in earlier θ -based wake-oscillator models [160, 159], such as the dimensionless time $\tau = \omega_n t$, the frequency ratio $\delta = \frac{\omega_n}{\omega_{vs}}$, etc. To be consistent with the C_L -based model in Section 5.2.1, the non-dimensional formulation of Mannini model is re-derived

here by using the dimensionless definitions in Eqs. (5.10)–(5.11). In addition, some new dimensionless quantities are introduced to fit the wake oscillator with respect to the angular displacement of wake lamina θ . Those are the damping ratio of wake oscillator $\zeta_f = \frac{\bar{C}}{2\omega_{vs}\bar{l}}$, the non-dimensional half length of wake lamina $\bar{l}^* = \bar{l}/D$ and the vortex shedding frequency $\omega_{vs} = \frac{2\pi StU}{D} = \sqrt{\frac{\bar{k}}{\bar{l}}}$. As a consequence, the dimensionless system of the second-order differential equations are expressed as:

$$\ddot{Y} + \frac{2\xi}{StU_r}\dot{Y} + \frac{1}{St^2U_r^2}Y = \frac{1}{8\pi^2St^2m^*} \left[f_m\theta + A_1(2\pi St)\dot{Y} + \dots + A_7(2\pi St)^7\dot{Y}^7 \right], \quad (5.16)$$

$$\ddot{\theta} - 2\zeta_f \left(1 - \frac{4f_m^2}{C_{L0}^2}\theta^2 \right) \dot{\theta} + \theta = \frac{1}{\bar{l}^*}\ddot{Y} + 2\pi St\dot{Y}. \quad (5.17)$$

As shown, the second term of C_L (viz., $-f_m\dot{y}/U$ in Eq. (5.14)) is included in the constant coefficient A_1 and does not appear explicitly in Eq. (5.16). Here we also add even terms in the polynomial approximation of C_L^{QS} .

Finally, the fluid variable θ also needs to be converted into C_L through Eq. (5.14). The resulting differential equations are:

$$\ddot{Y} + \frac{2\xi}{StU_r}\dot{Y} + \frac{1}{St^2U_r^2}Y = \frac{1}{8\pi^2St^2m^*} \left[C_L + A_1(2\pi St)\dot{Y} + \dots + A_7(2\pi St)^7\dot{Y}^7 \right], \quad (5.18)$$

$$\begin{aligned} \ddot{C}_L + 2\zeta_f \left(\frac{4}{C_{L0}^2}C_L^2 - 1 \right) \dot{C}_L + C_L + M = -2\pi f_m St \ddot{Y} + f_m \left(\frac{1}{\bar{l}^*} + 4\pi\zeta_f St \right) \ddot{Y} - \frac{64\pi^3\zeta_f f_m^3 St^3}{C_{L0}^2} \ddot{Y}\dot{Y}^2, \\ \text{where, } M = \frac{16\pi\zeta_f f_m St}{C_{L0}^2} \left(\ddot{Y}C_L^2 + 2\dot{Y}\dot{C}_L C_L \right) + \frac{32\pi^2\zeta_f f_m^2 St^2}{C_{L0}^2} \left(2\ddot{Y}\dot{Y}C_L + \dot{Y}^2\dot{C}_L \right). \end{aligned} \quad (5.19)$$

It can be seen that the C_L -based model and the θ -based model have identical structure oscillators (Eqs. (5.10) and (5.18)). However, the latter has a much more complex wake oscillator by comparing Eq. (5.19) to Eq. (5.11). To be specific, a big mixing part of Y , C_L as well as their first and second derivatives appears on the left hand side (denoted by M) to provide four extra nonlinear terms. In addition, the forcing term on the right hand side also displays a complicated composition of \ddot{Y} , \ddot{Y} and $\ddot{Y}\dot{Y}^2$.

5.3 GA–Optimized Nonlinear Grey-Box Model

This section proposes a genetic algorithm optimized nonlinear grey-box model to estimate the parameters of the nonlinear dynamical systems described in Section 5.2 (viz., the improved Facchinetti model and Mannini model).

As the name suggests, the grey-box identification technique (also called semi-physical modeling) is used for the system with a priori knowledge, viz., some internal physics of how the dynamical system works is known, but some model parameters must be determined empirically. From this perspective, the grey-box model combines the black-box model (built on statistical information without any prior knowledge) and the white-box model (built on first principles). In our case, the coupled wake-oscillator models consisting of two differential equations are constructed based on the physical insights into the FIV response, accompanied by some unknown parameters—this is a perfect scenario to utilize the grey-box technique for model identification.

5.3.1 The State-Space Model

The first step is to construct the nonlinear state-space model based on the differential equations, which has the following general representation:

$$\dot{\mathbf{x}} = f(\mathbf{x}, \mathbf{u}, \mathbf{H}), \quad (5.20)$$

$$\mathbf{y} = g(\mathbf{x}, \mathbf{u}, \mathbf{H}), \quad (5.21)$$

where \mathbf{x} , \mathbf{u} , \mathbf{y} and \mathbf{H} represent the state, input, output and parameter vectors, respectively. The functions f and g can have any parameterization. Note that the coupled wake-oscillator models in Section 5.2 are related to the time series modelling without any exogenous input signals (viz., $\mathbf{u} = 0$) and has two outputs of displacement and lift coefficient (viz., $\mathbf{y} = [y_1(t) \ y_2(t)]^T = [Y(t) \ C_L(t)]^T$) that the model seeks to predict. The state and parameter vectors can be different for different wake-oscillator models.

The improved Facchinetti model (Eqs. (5.10)–(5.11)) gives the following state-space structure in terms of the state response and output response:

$$\dot{\mathbf{x}}(t) = \begin{bmatrix} \dot{x}_1(t) \\ \dot{x}_2(t) \\ \dot{x}_3(t) \\ \dot{x}_4(t) \end{bmatrix} = \begin{bmatrix} x_2(t) \\ \frac{1}{8\pi^2 S t^2 m^*} [x_3(t) + C_L^{QS}] - \frac{2\xi}{StU_r} x_2(t) - \frac{1}{St^2 U_r^2} x_1(t) \\ x_4(t) \\ B_1 \dot{x}_2(t) + B_2 x_2(t) - \varepsilon \left(\frac{4}{C_{L0}^2} x_3^2(t) - 1 \right) x_4(t) - x_3(t) \end{bmatrix}, \quad (5.22)$$

$$\mathbf{y}(t) = \begin{bmatrix} y_1(t) \\ y_2(t) \end{bmatrix} = \begin{bmatrix} x_1(t) \\ x_3(t) \end{bmatrix}. \quad (5.23)$$

The state vector includes four states:

$$\mathbf{x} = [x_1(t) \ x_2(t) \ x_3(t) \ x_4(t)]^T = [Y(t) \ \dot{Y}(t) \ C_L(t) \ \dot{C}_L(t)]^T. \quad (5.24)$$

C_L^{QS} is the intermediate variable:

$$C_L^{QS} = \sum_{i=1}^7 A_i (2\pi St)^i x_2^i(t). \quad (5.25)$$

The parameter vector include fifteen parameters:

$$\mathbf{H} = [m^* \ \xi \ U_r \ C_{L0} \ St \ \varepsilon \ A_1 \ A_2 \ A_3 \ A_4 \ A_5 \ A_6 \ A_7 \ B_1 \ B_2]^T. \quad (5.26)$$

The state-space formulation describing the fluid-structure dynamics from the improved Mannini model (Eqs. (5.18)–(5.19)) takes the following form (with the same output response as Eq. (5.23)):

$$\dot{\mathbf{x}}(t) = \begin{bmatrix} \dot{x}_1(t) \\ \dot{x}_2(t) \\ \dot{x}_3(t) \\ \dot{x}_4(t) \\ \dot{x}_5(t) \end{bmatrix} = \begin{bmatrix} x_2(t) \\ \frac{1}{8\pi^2 St^2 m^*} \left(x_4(t) + C_L^{QS} \right) - \frac{2\xi}{St U_r} x_2(t) - \frac{1}{St^2 U_r^2} x_1(t) \\ \frac{1}{8\pi^2 St^2 m^*} \left(x_5(t) + \dot{C}_L^{QS} \right) - \frac{2\xi}{St U_r} x_3(t) - \frac{1}{St^2 U_r^2} x_2(t) \\ x_5(t) \\ -2\pi f_m St \dot{x}_3(t) + f_m \left(\frac{1}{\bar{l}^*} + 4\pi \zeta_f St \right) x_3(t) - \frac{64\pi^3 \zeta_f f_m^3 St^3}{C_{L0}^2} x_3(t) x_2^2(t) \\ -2\zeta_f \left(\frac{4}{C_{L0}^2} x_4^2(t) - 1 \right) x_5(t) - x_4(t) - M \end{bmatrix}. \quad (5.27)$$

The corresponding state vector includes five states:

$$\mathbf{x} = [x_1(t) \ x_2(t) \ x_3(t) \ x_4(t) \ x_5(t)]^T = \left[Y(t) \ \dot{Y}(t) \ \ddot{Y}(t) \ C_L(t) \ \dot{C}_L(t) \right]^T. \quad (5.28)$$

Three intermediate variables are defined:

$$M = \frac{16\pi \zeta_f f_m St}{C_{L0}^2} [x_3(t) x_4^2(t) + 2x_2(t) x_4(t) x_5(t)] + \frac{32\pi^2 \zeta_f f_m^2 St^2}{C_{L0}^2} [2x_2(t) x_3(t) x_4(t) + x_2^2(t) x_5(t)],$$

$$C_L^{QS} = \sum_{i=1}^7 A_i (2\pi St)^i x_2^i(t),$$

$$C_L^{\dot{QS}} = x_3(t) \sum_{i=1}^7 i A_i (2\pi St)^i x_2^{i-1}(t). \quad (5.29)$$

The parameter vector also includes fifteen parameters:

$$\mathbf{H} = [m^* \ \xi \ U_r \ C_{L0} \ St \ f_m \ \bar{l}^* \ \zeta_f \ A_1 \ A_2 \ A_3 \ A_4 \ A_5 \ A_6 \ A_7]^T. \quad (5.30)$$

In our case, above explicit state-space models are programmed into the C MEX files in MATLAB to improve the execution speed, which specifies how to update the states (*compute_dx* function) and compute the outputs (*compute_y* function). Then, the C MEX files are compiled to feed as the model structure during the grey-box estimation procedure.

5.3.2 Model Parameter Estimation

The MATLAB System Identification Toolbox™ is utilized to estimate the model parameters, which is generally a two-step procedure. First, the MATLAB function *idnlgrey* is used to create an initial nonlinear grey-box model (a time-continuous system). Second, the MATLAB function *nlgreyest* is used to identify the unknown parameters based on the estimation data. The detailed simulation and estimation techniques used in this section are described below, which are determined after a lot of trial and error.

Simulation method

The above ODE systems have the similar structure with the Van der Pol oscillator, which is a stiff problem—the solution being sought varies slowly, but there are nearby solutions that vary rapidly, so the numerical method must take small steps to obtain satisfactory results. In order to numerically integrate the stiff equation in a high efficiency in MATLAB, instead of using the standard ODE solver *ode45* we apply the function *ode15s* [138, 139], a variable-step and variable-order solver based on the numerical differentiation formulas of orders 1 to 5, to solve the state-space equations derived in Section 5.3.1. The remaining simulation settings use the default values, such as the absolute error tolerance of 1e-6 and the relative error tolerance of 1e-3.

Loss function

The loss function (or cost function) is a function of the error between the model output and the estimation dataset, which will be minimized to determine the optimal parameters during the process of estimation.

Without considering the effects of regularization, output weight or error thresholds, the present grey-box model uses a purely quadratic loss function with the following form:

$$Loss = \frac{1}{N} \sum_{i=1}^N e_Y(i) + e_{C_L}(i), \quad (5.31)$$

where N is the number of data samples in the estimation data; e represents the error vector between the estimation data and model output (with hat operator), viz., $e_Y = Y - \hat{Y}$, $e_{C_L} = C_L - \hat{C}_L$. As shown, the loss function has the same expression with the mean squared error (MSE).

The Trust-Region-Reflective Newton algorithm (*lsqnonlin*) from MATLAB's Optimization Toolbox™ is used to implicitly compute the sum of squares of all error components in Eq. (5.31) and find a local minimum *Loss* using the nonlinear least-squares search method. As a consequence, the best-fitting model parameters can be estimated by iteratively varying the parameter vector H so as to minimize the loss function. More information about the *lsqnonlin* function can be found in [31, 83].

In the context of parameter estimation, the gradient refers to the derivative of the explicitly given loss function (viz., the error vector between model output and estimation data) with respect to the free parameters to be estimated, which can be calculated by numerically perturbing the unknown parameters and measuring their effects on the simulation error. The gradient computation uses the default methods, such as the differencing scheme (randomly choose from forward, backward or central approximation), the size of minimum (1.49e-10) and maximum (infinite) perturbations of unknown parameters, etc.

Evaluation of model performance

The normalized root mean squared error (NRMSE) between the model response and the estimation data is expressed as:

$$NRMSE = \frac{\sqrt{\frac{1}{N} \sum_{i=1}^N |y(i) - \hat{y}(i)|^2}}{\sigma} = \frac{\|y - \hat{y}\|_2}{\|y - \bar{y}\|_2}, \quad (5.32)$$

where $\|\bullet\|_2$ indicates the 2-norm of a vector; y is the estimation data; \hat{y} is the output of estimated model; $\bar{y} = \frac{1}{N} \sum_{i=1}^N y(i)$ is the mean of y . As shown, the root mean squared error (RMSE) is normalized by the standard derivation $\sigma = \sqrt{\frac{\sum_{i=1}^N |y(i) - \bar{y}(i)|^2}{N}}$.

To quantitatively assess the quality of the identified model, the NRMSE fitness value (in percentage) is used in the present grey-box model, as defined by:

$$fit = 100 \left(1 - \frac{\|y - \hat{y}\|_2}{\|y - \bar{y}\|_2} \right). \quad (5.33)$$

The *fit* varies between -Inf (bad fit) to 100 (perfect fit).

5.3.3 Parameter optimization based on genetic algorithm

When invoking *idnlgrey*, in addition to specifying the MEX-file storing the model structure and the related techniques, it is also necessary to give the initial conditions including the initial values of model parameters and states. The initial states are identical to the state response of the first sample in the estimation data. And in our case, the states are fixed to their initial values during the model identification procedure. The initial parameters, by contrast, are often difficult to determine, especially if involving non-physical parameters such as A_1 to A_7 in Eqs. (5.26) and (5.30). Most importantly, the optimization routines for estimating the model parameters can even fail if poor starting values are provided [91]. Therefore, the computationally heavy task of parameter estimation should start with reasonable initial guesses of parameters.

In order to find an optimum set of model parameters, the genetic algorithm (GA) is integrated into the construction of nonlinear grey-box model. The genetic algorithm is a stochastic global search method for solving optimization problem built up on the basis of natural genetics, imitating the process that drives the natural biological evolution. Applying the principle of survival of the fittest, GA repeatedly modifies a population of potential individuals to produce successively better approximations to a solution. At each generation, GA selects individuals from the current population to be parents according to their level of fitness in the problem domain and uses them to produce children for the next generation by applying some genetic operators borrowed from natural genetics. Over successive generations, the population of individuals evolves to be better suited to the environment than the initial population, just as in natural adaptation.

The Genetic Algorithm Toolbox, a public MATLAB package developed by the Department of Automatic Control and Systems Engineering of the University of Sheffield [29, 28], is utilized here for the optimization of model parameters. The premise to use GA is to specify the necessary arguments, mainly referring to the data structure and the genetic properties. The former includes the number of parameters to be estimated N_{var} , the number of individuals in a population N_{ind} (viz., population size) and the binary length of individual parameter L_{ind} . The latter involves the generation gap rate $R_{gap} \leq 1$ (viz., the entire population is not reproduced in each generation), the crossover rate p_x , the mutation rate p_m and the maximum number of iterations. Table 5.1 shows the settings used in the present GA optimization problem. Note that the binary scheme is used inside the GA generational loop, while the objective value and fitness value have a phenotype representation (in real value).

The major GA optimization procedure is described as follows:

Table 5.1: Optimization properties of genetic algorithm.

NO.	Properties	Method or Value
1	Number of free parameters (N_{var})	4-12
2	Population size (N_{ind})	10
3	Binary length of individual (L_{ind})	15
4	Selection method	stochastic universal sampling
5	Generation gap (R_{gap})	0.9
6	Crossover method	single-point
7	Crossover rate (P_x)	0.7
8	Mutation rate (P_m)	0.01
9	Maximum iterations	15

1. Create an initial uniformly-distributed random binary population using the routine *crtpb* and return a matrix of dimension $N_{ind} \times (N_{var} \times L_{ind})$. Note that each row corresponds to a particular individual that represents a set of values of parameters in our case.
2. Evaluate the objective values for each individual in the initial population, which returns a real-valued column vector of length N_{ind} . It should be noted that a complete procedure of grey-box estimation for wake-oscillator model is integrated in the calculation of objective value.
3. Assign the non-negative fitness to the individuals using the routine *ranking* and return a same-dimensional vector as Step 2. It is critical to note that the individuals with smaller objective value will receive higher fitness.
4. **Selection operator:** select a given number of individuals from the current population as parents according to their fitness, using the routine *select* with stochastic universal sampling. The more suited to the “environment” the individual is, the more likely it will be chosen to form children (survival of the fittest). The returned matrix has a dimension of $(R_{gap} \times N_{ind}) \times (N_{var} \times L_{ind})$.
5. **Crossover operator:** the single-point crossover [100] (swap one gene between two selected individuals) is implemented to recombine pairs of parents at given probability (p_x) to produce new offspring, using the routine *recombin*. The returned matrix has the same dimension as that in the Step 4.

6. **Mutation operator:** the mutation applies random changes to individual parents at given probability (p_m) to produce new offspring using the routine *mut*, with same-dimensional matrix returned.
7. Duplicate the best individual (with the highest fitness value) in the current generation to ensure its size equals to N_{ind} (viz., fitness-based re-insertion) and calculate the objective values of the reinserted offspring generation, using the routine *reins*.
8. Repeat Steps 3–8 until the given maximum iterations are reached.

The objective function of GA optimization is defined as the sum of NRMSE of two outputs ($Y(t)$ and $C_L(t)$) from the wake-oscillator model. The evolution of the objective value as a function of iterations in one GA optimization procedure is described in Fig. 5.3. Although the mean NRMSE of each generation shows a high fluctuation, the minimum NRMSE remains almost unchanged after three generations, implying that the maximum fifteen iterations should be enough for a successful process of GA optimization.

As a consequence, an optimal group of model parameters can be obtained by using the grey-box estimation procedure. Fig. 5.4 gives the complete flowchart of the GA-optimized grey-box estimation framework. This entails writing a MATLAB program that applies the Genetic Algorithm Toolbox™ and the System Identification Toolbox™.

5.4 Results and Discussions

Using the proposed GA-optimized grey-box estimation framework, the identification of the coupled wake-oscillator models based on lift coefficient and wake rotation angle is performed in this section, in terms of the VIV of a circular cylinder and the FIV of a circular cylinder-plate assembly. The estimation data comes from the comprehensive simulation database established in Chapter 3, which is downsampled to run at a sample time of 0.1 s.

5.4.1 Configuration of Model Parameters

The parameter vectors for above two types of models (see Eqs. (5.26) and (5.30)) include all the candidate parameters that can be estimated by grey-box identification. However, the state of model parameters can be either free, or fixed to a non-zero value, or fixed to zero.

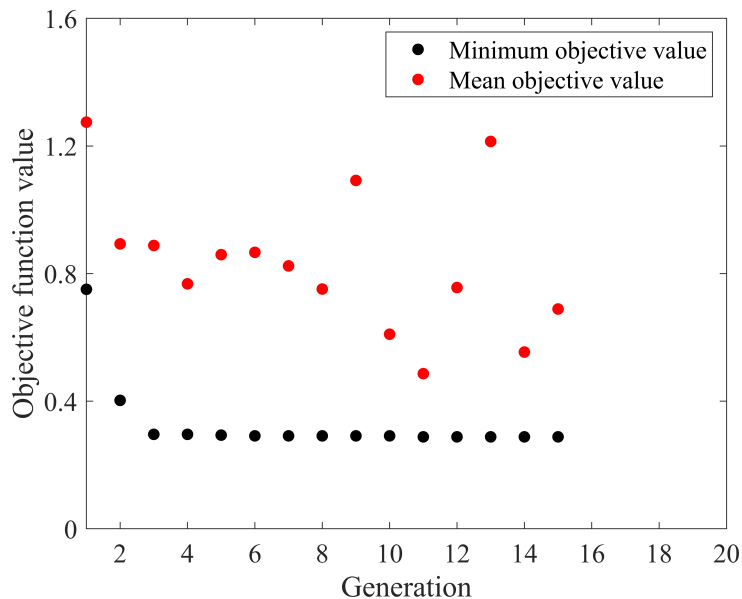


Figure 5.3: The evolution of minimum and mean objective values as a function of iterations in one optimization procedure of genetic algorithm.

The estimation dataset is obtained at a mass ratio of 10 and zero structural damping. According to this, the values of model parameters m^* and ζ can be derived and keep fixed during the grey-box identification. It should be noted that the definition of mass ratio for simulation data is $m_{CFD}^* = \frac{4m}{\pi\rho D^2}$, which is slightly different from that of the wake-oscillator model $m_{wom}^* = \frac{m}{\rho D^2}$. Therefore, the mass ratio should be fixed to $m^* = 7.854$ during model estimation. The structural damping ratio ζ is still fixed to zero. Another fixed parameter U_r is also consistent with the estimation data.

The state of parameter determines the model structure because the parameter always be zero removes the corresponding term from the differential equations. Therefore, in order to obtain the optimal model structure, various combinations of free parameters are tested in this section.

When configuring fixed and free parameters, some constraints must be taken into consideration. For C_L -based wake-oscillator model (Eq. (5.26)), except for the three fixed parameters (m^* , ζ and U_r), there are two more constraints: (i) the physical parameters C_{L0} , St and ϵ are always positive and free to estimate; (ii) B_1 and B_2 cannot be fixed to zero at the same time to ensure the right hand side of fluid equation is not zero. For θ -based wake-oscillator model (Eq. (5.30)), five parameters have definite physical meaning,

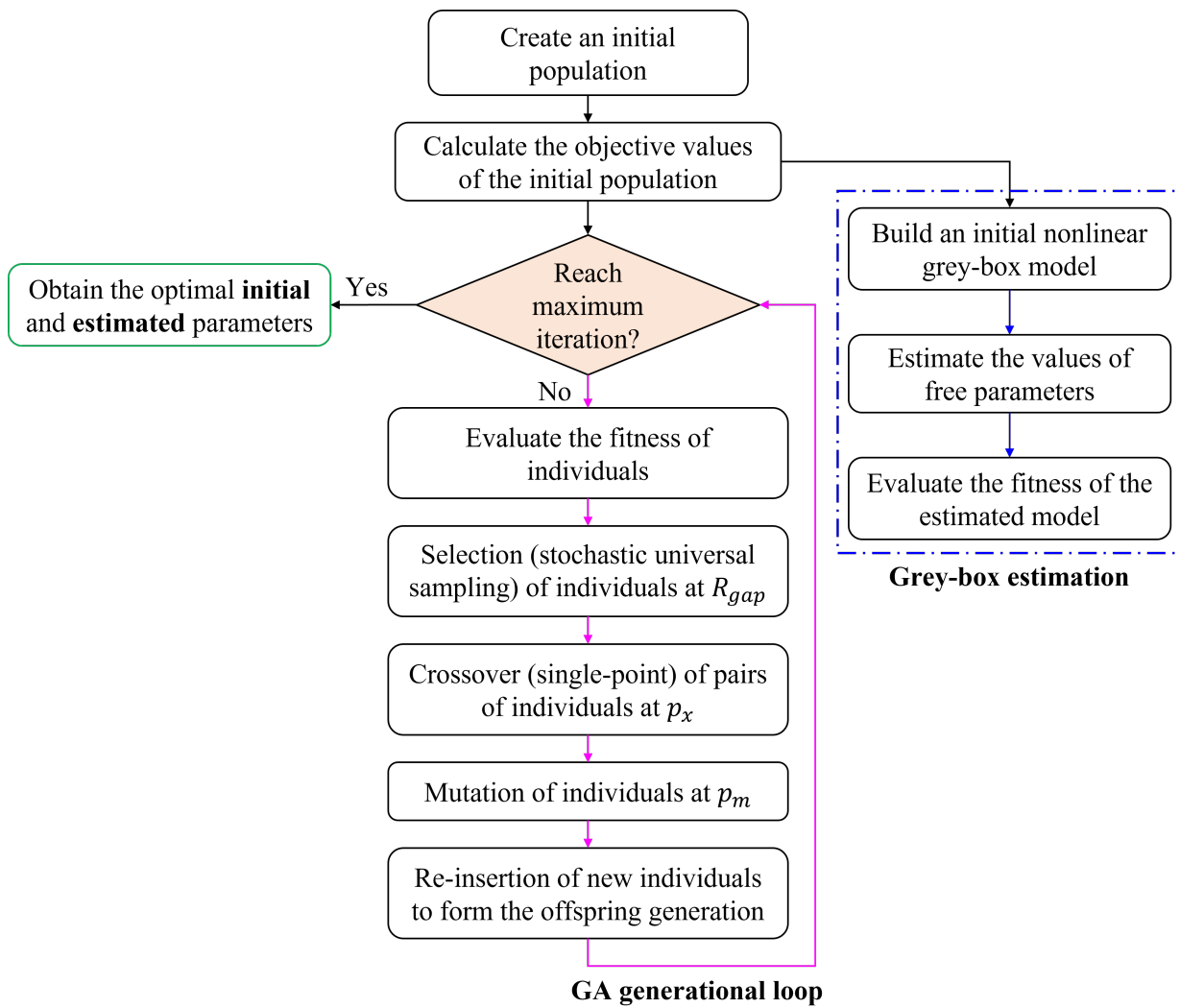


Figure 5.4: Flow chart of the GA-optimized grey-box estimation framework.

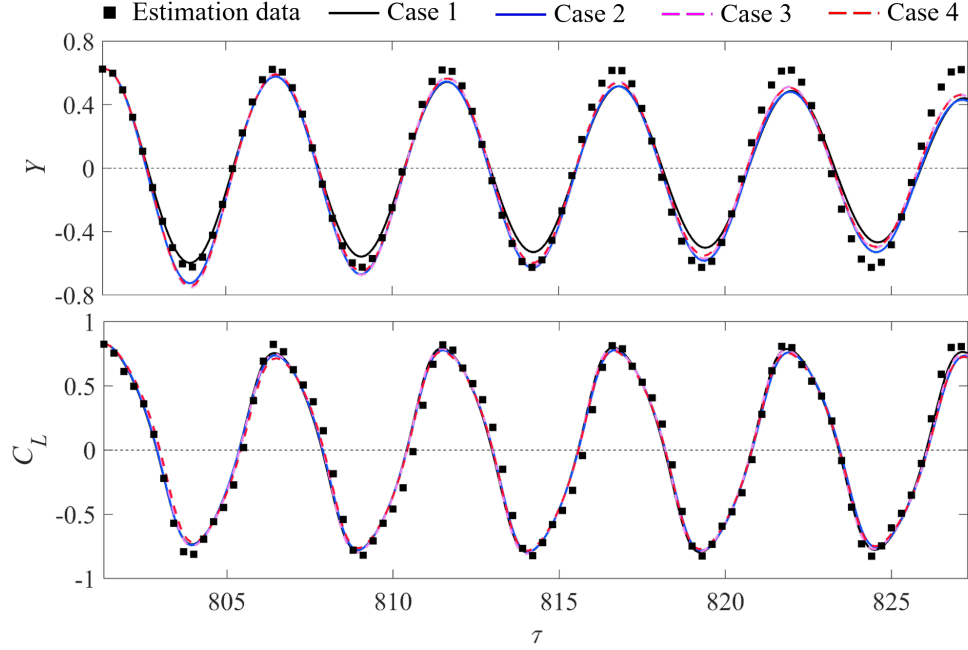


Figure 5.5: Time series of Y and C_L for VIV of circular cylinder at $U_r = 5$. The C_L -based model is identified when various even polynomial terms are free to estimate: Case 1—no even polynomial coefficient; Case 2— A_2 ; Case 3— A_2 and A_4 ; Case 4— A_2 , A_4 and A_6 .

namely, C_{L0} , St , ζ_f , f_m and \bar{l}^* , which are always free to estimate. With the exception of f_m , the other four parameters are always positive. As a consequence, the adjustable free parameters of θ -based model are polynomial coefficients A_1 to A_7 .

As mentioned in Section 5.2, the inclusion of both odd and even polynomial terms on the right-hand-side of Y -ODE is a more generalized form of the typical QS model (only with the odd terms). However, it is still unclear of the influencing mechanism of these terms on the solution of the coupled ODE system. Therefore, a preliminary test is first to be carried out to determine if it is necessary to consider the even terms.

Figures 5.5–5.6 compare the simulation data and the grey-box model outputs in terms of $Y(t)$ and $C_L(t)$ for VIV of a circular cylinder at $U_r = 5$. Cases 1–4 are obtained by including various combinations of even-order polynomial terms (viz. $A_i(2\pi St)^i \dot{Y}^i$ where $i = 2, 4, 6$) in the right hand side of Y -ODE for the C_L -based model, while Cases 5–8 considers the superposition of the first-order polynomial and various even terms. As shown in Fig. 5.5, the inclusion of only even terms, regardless of their number or order, will lead to an asymmetric time history of Y , which is inconsistent with the physics as

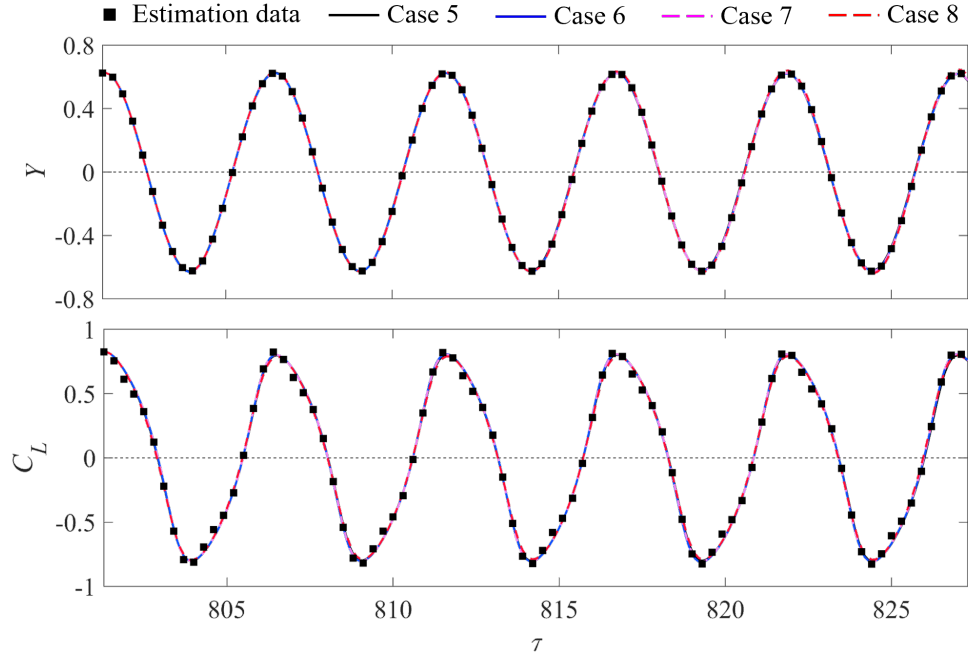


Figure 5.6: Time series of Y and C_L for VIV of circular cylinder at $U_r = 5$. The C_L -based grey-box model is estimated when various odd and even polynomial terms are free to estimate: Case 5— A_1 ; Case 6— A_1 and A_2 ; Case 7— A_1 , A_2 and A_4 ; Case 8— A_1 , A_2 , A_4 and A_6 .

described by Parkinson and Smith [118]. By contrast, adding an odd term like the first-order polynomial $A_1(2\pi St)\dot{Y}$ is a cure for this problem. Fig. 5.6 demonstrates that the estimated model can reach very high accuracy of 99% fitness for $Y(t)$ and 95% fitness for $C_L(t)$, with either only odd term (Case 5) or the combination of odd and even terms (Case 6–8). As a consequence, containing the odd polynomials seems to be necessary to generate the physical outputs, while the even term, apparently, does not help much to improve the model performance but increase the model complexity. All these preliminary results are considered when configuring various combinations of model parameters. Table 5.2 gives several representative combinations of parameters for the two types of wake-oscillator models.

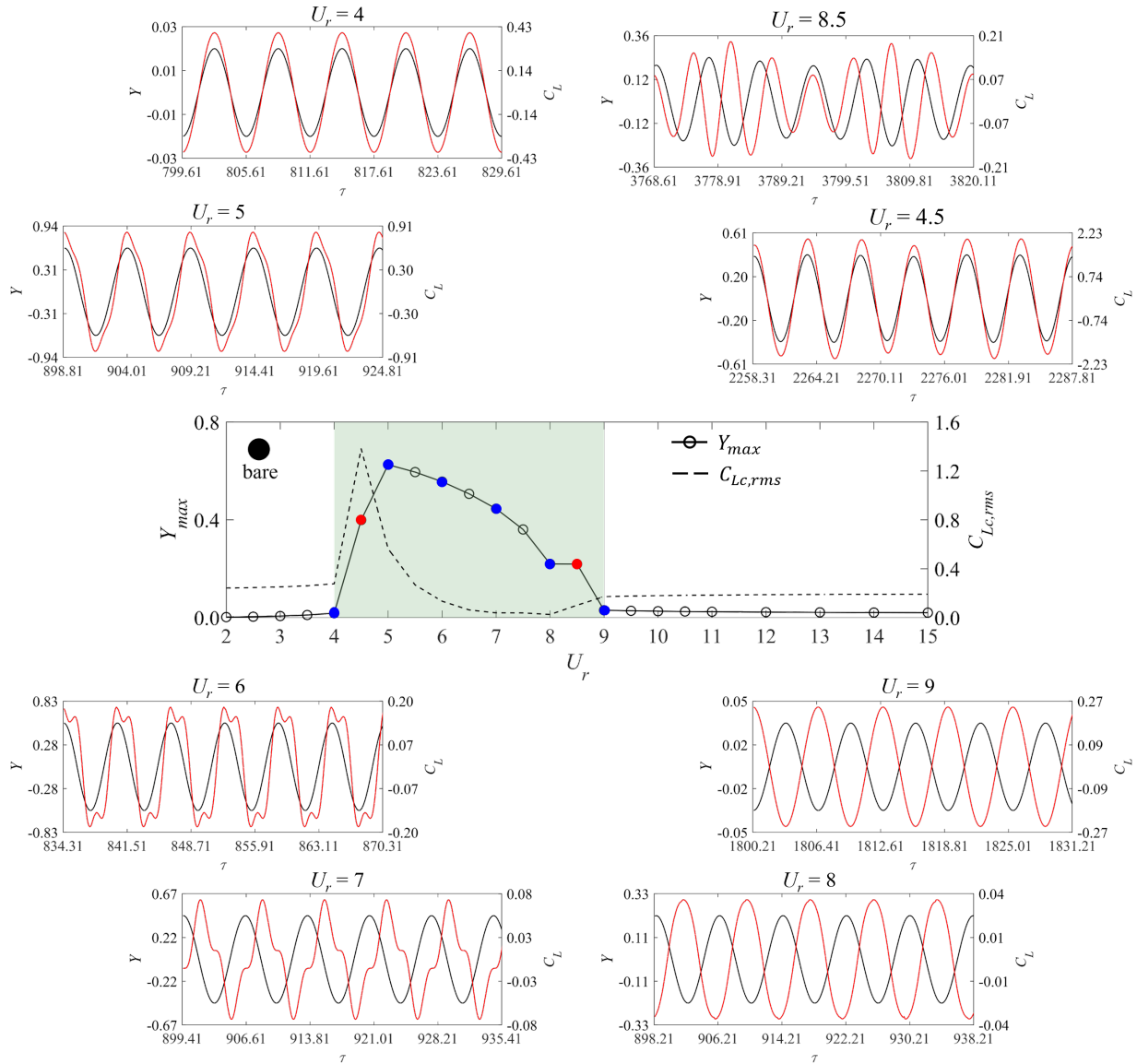


Figure 5.7: The VIV response of a circular cylinder in terms of the transverse displacement and lift coefficient as a function of U_r , surrounded by the time series of Y (black) and C_L (red) at eight representative values of U_r . Note that the periodic and beating oscillations are respectively marked by blue and red points in the amplitude response.

Table 5.2: Configurations of parameters for the wake-oscillator models based on C_L (Case 1-X) and θ (Case 2-X). 1–fixed to zero, 0–free.

Cases	A_1	A_2	A_3	A_4	A_5	A_6	A_7	B_1	B_2
1-1	0	1	1	1	1	1	1	0	1
1-2	0	1	1	1	1	1	1	0	0
1-3	0	1	0	1	1	1	1	0	0
1-4	0	1	0	1	0	1	0	0	0
1-5	0	0	1	1	1	1	1	0	0
1-6	0	1	0	1	1	1	1	0	1
1-7	0	1	0	1	0	1	0	0	1
2-1	0	1	1	1	1	1	1	/	/
2-2	0	1	0	1	1	1	1	/	/
2-3	0	1	0	1	0	1	1	/	/
2-4	0	1	0	1	0	1	0	/	/
2-5	0	0	1	1	1	1	1	/	/

5.4.2 VIV of a Circular Cylinder

The first simulation dataset involves the pure VIV of a circular cylinder, which occurs at $U_r = 4-9$. As shown in Fig. 5.7, the time histories of Y and C_L at eight representative values of U_r are selected as estimation data to identify the free parameters of the C_L -based and θ -based wake-oscillator models using the GA-optimized grey-box framework. It should be noted that the oscillations of the two cases at top right display the beating phenomenon, namely, $U_r = 4.5$ near the onset and $U_r = 8.5$ near the end velocity. While other cases are characterized by the highly-periodic oscillations.

Structure of C_L -based wake oscillator model

First, we compare the acceleration coupling (with B_1 as a free parameter, viz. Case 1-1) and the velocity–acceleration coupling (with B_1 and B_2 as free parameters, viz. Case 1-2) in the C_L differential equation. Fig. 5.8 displays the periodic oscillations in the time series of Y and C_L for the VIV response of a circular cylinder at $U_r = 6$. The estimation data indicates that $Y(t)$ is characterized by the sinusoidal waves, for which both two cases show quite high accuracy of more than 99%. By contrast, the $C_L(t)$ curve is deformed around the locations of maximum and minimum and displays a double peak phenomenon, which

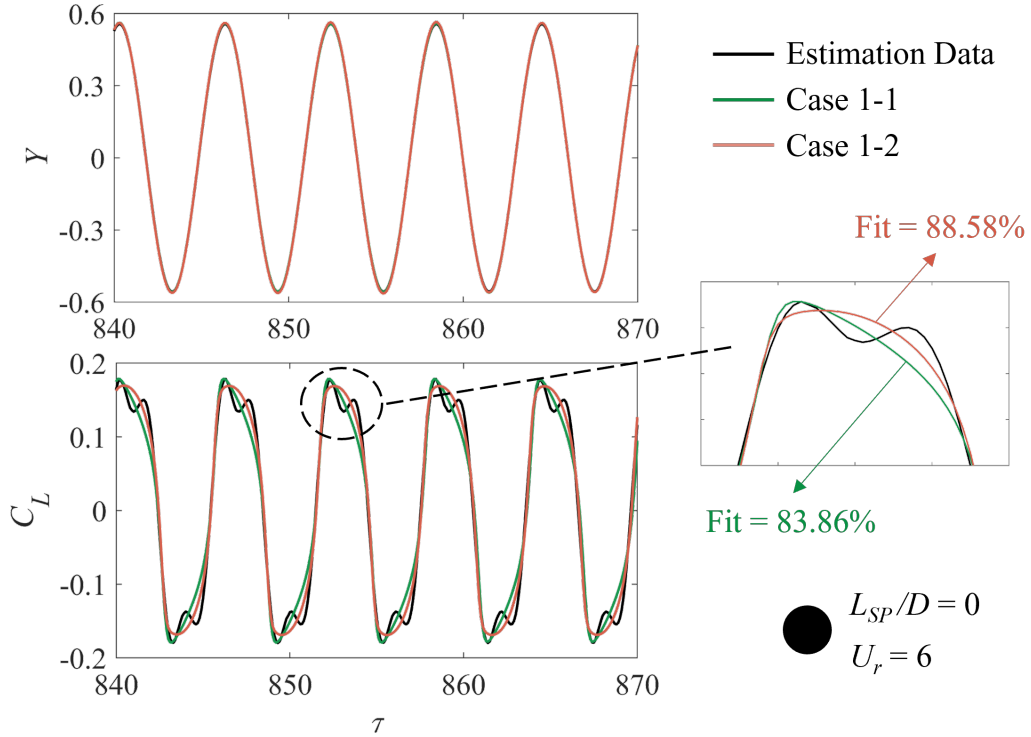


Figure 5.8: The time series of Y and C_L for VIV of a circular cylinder at $U_r = 6$ from estimation data and C_L -based wake-oscillator models. For Case 1-1, the estimated parameters are $C_{L0} = 0.1894$, $St = 0.1590$, $\epsilon = 2.6422$, $A_1 = 0.3976$ and $B_1 = 0.1737$. For Case 1-2, the estimated parameters are $C_{L0} = 0.0818$, $St = 0.1591$, $\epsilon = 0.7283$, $A_1 = 0.4380$, $B_1 = -0.3356$ and $B_2 = 0.8748$.

is more difficult to fit using the mathematical model. As a consequence, the fitness of both cases decreases to less than 90%. Even so, Case 1-2 has a higher fitness value of 88.58% than that of Case 1-1 (83.86%), which is due to the inclusion of the velocity coupling with coefficient B_2 in the C_L -ODE. Moreover, the velocity-acceleration coupling seems to exhibit some advantages in the quasi-periodic oscillations, which is particularly evident on a careful perusal of Fig. 5.9. As mentioned above, the oscillations in $Y(t)$ and $C_L(t)$ have a beating phenomenon at $U_r = 4.5$. In this case, the prediction accuracy of Case 1-2 for the two signals are respectively 96.52% and 92.76%, which is much better than the highest precision (88.18% and 84.51%) that the Case 1-1 can reach with reasonable parameters. In addition to the non-sinusoidal oscillation or beating oscillation, the C_L -based wake oscillator model with B_1 and B_2 is superior to that with only B_1 at various

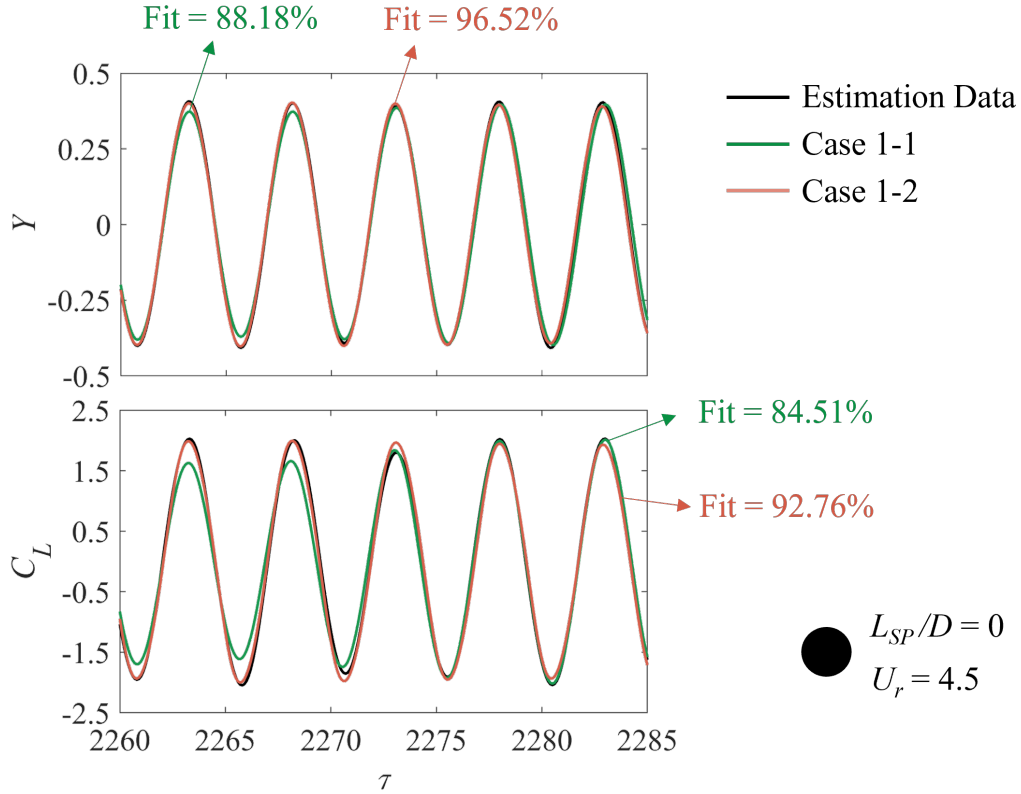


Figure 5.9: The time series of Y and C_L for VIV of a circular cylinder at $U_r = 4.5$ from estimation data and C_L -based wake-oscillator models. For Case 1-1, the estimated parameters are $C_{L0} = 0.6$, $St = 0.1607$, $\epsilon = 0$, $A_1 = 0.2458$ and $B_1 = 1.8165$. For Case 1-2, the estimated parameters are $C_{L0} = 0.5715$, $St = 0.1589$, $\epsilon = 0.016$, $A_1 = 0.7711$, $B_1 = 1.8253$ and $B_2 = 1.1840$.

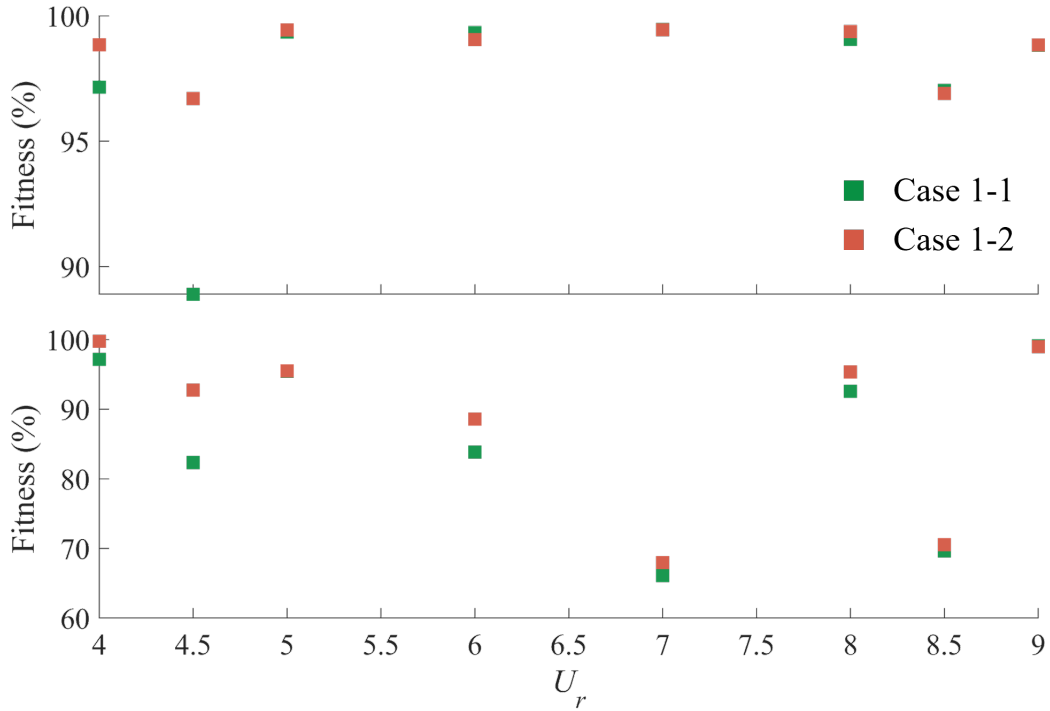


Figure 5.10: Fitness of $Y(t)$ (top) and $C_L(t)$ (bottom) from Case 1-1 and Case 1-2 for VIV of a circular cylinder at different reduced velocities.

values of reduced velocity. As indicated in Fig. 5.10, the orange square (Case 1-1) is generally located above the green square (Case 1-2) for the prediction of $Y(t)$ and $C_L(t)$.

Second, we focus on the forcing term of Y -ODE to determine how many odd-order polynomial terms of \dot{Y} should be reserved for the accuracy of model prediction. As mentioned in Section 5.2.1, the classical quasi-steady theory applies a seventh-order polynomial fitting with four odd-terms of \dot{Y} (viz., $A_i(2\pi St)^i \dot{Y}^i$ where $i = 1, 3, 5, 7$) included, which corresponds to the Case 1-4 in Table 5.2. However, the inclusion of more high-order polynomials means the theoretical model becomes increasingly complex and thus is difficult to popularize and use in a large amount. Therefore, some simpler structures are investigated here, such as that with the first-order polynomial forcing term (viz., Case 1-2), as well as with the first- and third-order polynomial forcing terms (viz., Case 1-3).

A comparison between above three cases is given for either the periodic and non-sinusoidal oscillations at $U_r = 6$ and 7 (see Table 5.3), or the quasi-periodic oscillations at $U_r = 4.5$ and 8.5 (see Table 5.4), in terms of the estimated values of free parameters and the

Table 5.3: Estimated C_L -based wake oscillator model with different odd polynomial terms. The estimation data is associated with the VIV of a circular cylinder at $U_r = 6$ and 7.

Parameter	Case 1-2	Case 1-3	Case 1-4	Case 1-2	Case 1-3	Case 1-4
U_r	6	6	6	7	7	7
C_{L0}	0.0818	0.0958	0.1039	0.0376	0.0380	0.0355
St	0.1591	0.1591	0.1591	0.1593	0.1592	0.1592
ϵ	0.7283	0.9697	1.1290	0.4070	0.4742	0.4232
A_1	0.4380	0.0870	6.3447	0.3559	-0.0477	-1.2229
A_3	/	1.3787	-131.44	/	3.4486	61.9098
A_5	/	/	762.42	/	/	-586.26
A_7	/	/	-1287.10	/	/	1564.50
B_1	-0.3356	-0.2779	-0.2322	-0.0481	-0.0506	-0.0555
B_2	0.8748	0.8014	0.7182	-0.0375	-0.0376	-0.0401
Fit_Y (%)	99.42	99.45	98.75	99.45	99.46	99.42
Fit_{C_L} (%)	88.49	88.64	88.44	67.96	68.21	68.02

Table 5.4: Estimated C_L -based wake oscillator model with different odd polynomial terms. The estimation data is associated with the VIV of a circular cylinder at $U_r = 4.5$ and 8.5.

Parameter	Case 1-2	Case 1-3	Case 1-4	Case 1-2	Case 1-3	Case 1-4
U_r	4.5	4.5	4.5	8.5	8.5	8.5
C_{L0}	0.5585	0.4914	1.6016	0.1335	0.1336	0.1364
St	0.1589	0.1590	0.1590	0.1587	0.1586	0.1587
ϵ	0.0161	0.0128	0.1325	0.8314	0.8320	0.8026
A_1	0.7676	0.3696	-0.0085	0.2323	-0.0688	-1.1706
A_3	/	2.1455	-125.60	/	15.001	-90.9856
A_5	/	/	1423.40	/	/	19683.78
A_7	/	/	-3570.83	/	/	-514776.9
B_1	1.8255	1.8093	1.8034	-0.0171	-0.0166	0.0050
B_2	1.2289	1.2681	0.5452	-0.0274	-0.0237	-0.0310
Fit_Y (%)	96.70	97.07	95.93	96.91	96.64	95.97
Fit_{C_L} (%)	92.76	92.77	92.04	70.55	70.28	70.03

corresponding fitness of $Y(t)$ and $C_L(t)$. Comparing Case 1-2 with Case 1-3, it can be found that the value of A_1 is greatly reduced due to the appearance of A_3 , while other parameters (viz., C_{L0} , St , ϵ , A_1 and B_2) not change too much. But the inclusion of the third-order polynomial term $A_3(2\pi St)^3 Y^3$ does not obviously promote the model prediction. In fact, the fitness value from Case 1-3 is only slightly higher than that from Case 1-2. If further increasing the number of odd polynomials, such as Case 1-4 with A_1 , A_3 , A_5 and A_7 , the prediction accuracy of the C_L -based wake oscillator model would, unexpectedly, decrease to a certain degree, especially for the instantaneous vibration displacement $Y(t)$.

It is worth mentioning that based on the author's experience, it is more difficult to apply a successful GA-optimized grey-box identification procedure on Case 1-4, not only because it has more (nice) free parameters to estimate, but also because the reasonable variation ranges of the non-physical coefficients (A_1 , A_3 , A_5 and A_7) are unclear, which can only be determined by sufficient replicates of estimation tests. It is certain that there are some tricks to help evaluate the optimal model parameters. For example, many results in this section demonstrate that the estimated value of St remains almost unchanged among different reduced velocities and model structures, which is also a measure of an efficient estimation procedure. As a consequence, the Strouhal number can be fixed to a constant value to reduce the difficulty in estimating a complex model. The results of Case 1-4 shown in Tables 5.3–5.4 are the optimal estimate after many attempts and obtained by fixing St . Based on this, we may reasonably conclude that the forcing term of four odd polynomials has no beneficial effect on the model prediction. It should be noted that we don't rule out the possibility that a better set of parameters may be existential for Case 1-4. However, it is not cost-efficient to make massive estimations just for the possible small accuracy increase.

Third, we analyze the contribution made by the even (second-order) polynomial term $A_2(2\pi St)^2 \dot{Y}^2$ to the model prediction. Table 5.5 compares the estimated model parameters and fitness of Case 1-2 and Case 1-5 at four representative values of reduced velocity. Obviously, the two cases have nearly the same prediction accuracy at different U_r . At $U_r = 7$, Case 1-5 leads to a higher value of Fit_Y (99.28%) but a smaller value of Fit_{C_L} (68.17%), so the total NRMSE of the two outputs is still very close to that of Case 1-2. Moreover, the value of A_2 is an order of magnitude lower than the value of A_1 .

From above analysis, Case 1-2 can be considered as the optimal structure of C_L -based wake oscillator model to predict the VIV response of a circular cylinder. The estimated values of six free parameters (viz., C_{L0} , St , ϵ , A_1 , B_1 and B_2) are plotted with respect to the reduced velocity in Fig. 5.11. It should be noted that the optimal parameter can vary in a certain range and end up with the almost identical model accuracy. So the variation ranges of parameters at each value of U_r are also marked with the error bar in Fig. 5.11.

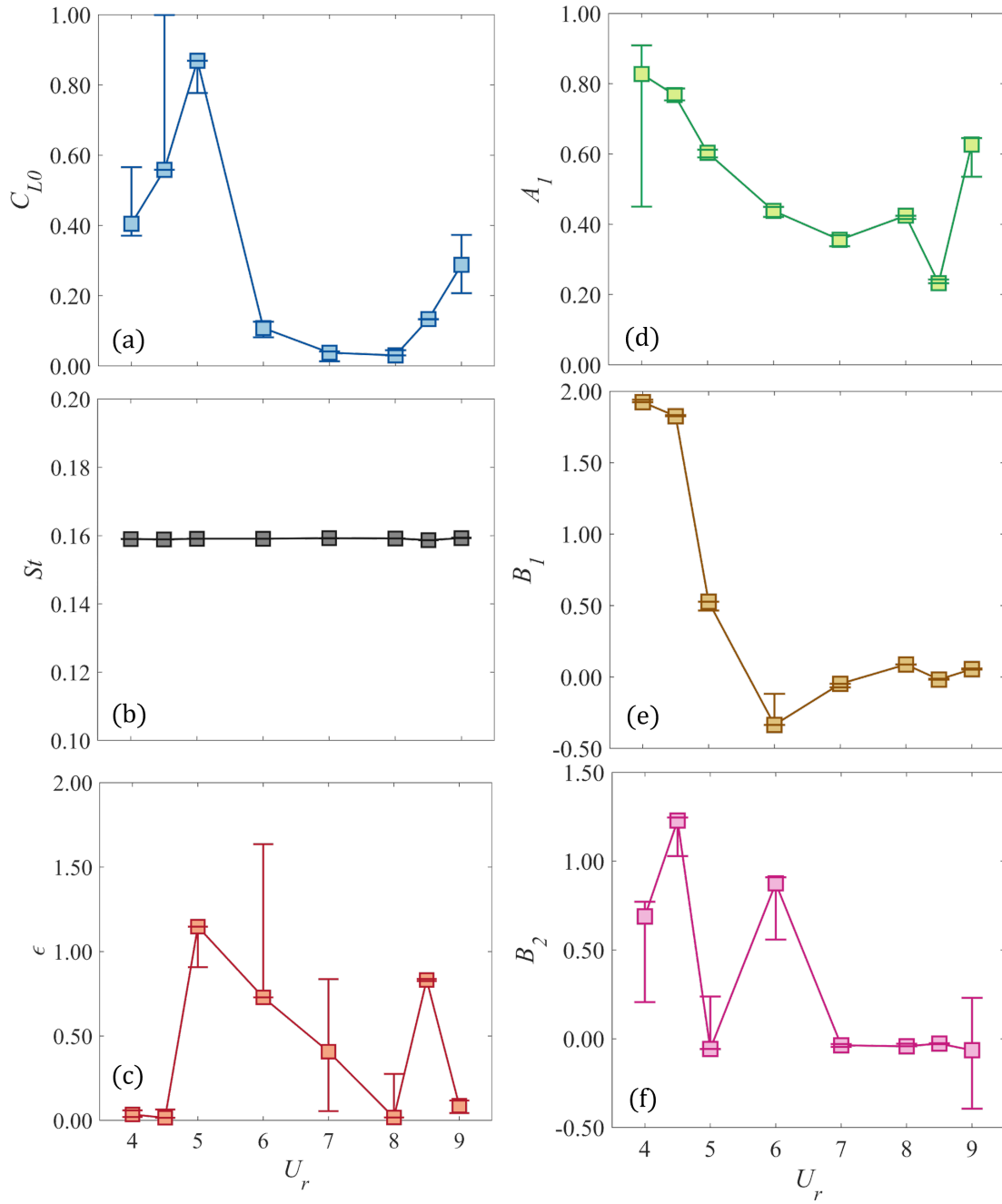


Figure 5.11: Estimated parameters of C_L -based wake oscillator model with an optimal structure for VIV of circular cylinder. (a)–(f) represent C_{L0} , St , ϵ , A_1 , B_1 and B_2 as a function of U_r .

Table 5.5: Estimated parameters for C_L -based wake oscillator model with (Case 1-2) and without (Case 1-5) the second-order polynomial term. The estimation data is associated with the quasi-periodic oscillation for VIV of a circular cylinder at $U_r = 6, 7, 4.5$ and 8.5 .

Parameter	Case 1-2	Case 1-5	Case 1-2	Case 1-5	Case 1-2	Case 1-5	Case 1-2	Case 1-5
U_r	6	6	7	7	4.5	4.5	8.5	8.5
C_{L0}	0.0818	0.0904	0.0376	0.0215	0.5585	0.8488	0.1335	0.1337
St	0.1591	0.1591	0.1593	0.1593	0.1589	0.1589	0.1587	0.1587
ϵ	0.7283	0.8593	0.4070	0.1291	0.0161	0.0336	0.8314	0.8341
A_1	0.4380	0.4373	0.3559	0.4109	0.7676	0.7951	0.2323	0.2388
A_2	/	0.0392	/	0.0585	/	-0.1158	/	-0.0252
B_1	-0.3356	-0.3027	-0.0481	-0.0746	1.8255	1.8257	-0.0171	-0.0151
B_2	0.8748	0.8272	-0.0375	-0.0488	1.2289	1.0644	-0.0274	-0.0255
Fit_Y (%)	99.42	99.38	96.91	99.28	96.70	96.32	96.91	96.85
Fit_{C_L} (%)	88.49	88.63	70.55	68.17	92.76	92.74	70.55	70.51

The first thing to note is that all model parameters, except the Strouhal number St , display an optimum value varying with U_r . By contrast, St is a constant value of about 0.159 over $U_r = 4-9$, which is coincidentally very close to the value of St (around 0.16) for the flow over a stationary circular cylinder from the simulation data (see Section 5.4.3 for more details). In other words, the estimated St in this section, although estimated within a wide range, can always perfectly match the physical value. This consistency also proves that the grey-box estimation procedure here is physically reasonable. Another physical parameter C_{L0} represents the lift coefficient acting on a stationary circular cylinder due to the vortex shedding. Instead of fixed to a constant value, C_{L0} displays a trend similar to that of the root-mean-square of instantaneous lift coefficient $C_{Lc,rms}$ as a function of U_r (see the dashed line in Fig. 5.7), which is also a theoretical basis for the rationality of model estimation. The variations of A_1 and B_1 have something in common with that of C_{L0} , for example, they generally decrease with U_r and then slightly increase when approaching the end velocity of VIV (see Figs. 5.11 (d)–(e)). Moreover, the optimal values of above four parameters do not vary much at the same reduced velocity, except to say that when close to the two boundaries of VIV regime (e.g., the error bar of C_{L0} and A_1 becomes visible at $U_r = 4, 4.5$ and 9). By contrast, a careful perusal of Figs. 5.11 (c) and (f) shows that the ϵ and B_2 do not have a clear-cut smooth trend with U_r , and their optimum values vary in a wide range at multiple reduced velocities within the VIV regime.

Table 5.6: Estimated parameters of θ -based wake oscillator model with various combinations of even and odd polynomial terms. The estimation data is associated with the non-sinusoidal periodic oscillation for VIV of a circular cylinder at $U_r = 6$ and 7.

Parameter	Case 2-1	Case 2-2	Case 2-5	Case 2-1	Case 2-2	Case 2-5
U_r	6	6	6	7	7	7
C_{L0}	0.1649	0.1640	0.1638	0.0531	0.0568	0.0544
St	0.1591	0.1590	0.1591	0.1593	0.1593	0.1593
ζ_f	0.9362	0.8946	0.9063	0.6947	0.4479	0.6960
f_m	0.0688	0.0684	0.0717	-0.0039	-0.0211	-0.0040
\bar{l}^*	0.7272	0.7653	0.8113	0.8892	1.5950	0.9914
A_1	0.4654	2.4406	0.4654	0.3244	1.9201	0.3287
A_2	/	/	0.0705	/	/	0.0888
A_3	/	-8.0755	/	/	-12.89	/
Fit_Y (%)	99.33	98.72	99.40	99.23	98.79	99.12
Fit_{C_L} (%)	88.78	88.23	88.57	66.05	66.25	65.93

Structure of θ -based wake oscillator model

For θ -based wake oscillator model, three new physical parameters, viz., ζ_f (equivalent to the Van der Pol constant ϵ in the C_L -based model to a certain extent), f_m and \bar{l}^* , are introduced to form a fairly complicated forcing term of C_L -ODE, which replaces the velocity–acceleration coupling with coefficients B_1 and B_2 in the C_L -based model. Therefore, only the polynomial terms involving A_1 to A_7 that included in the Y -ODE needs a discussion here.

Similarly, we first analyze the influence of odd polynomial terms through a comparison of three cases, namely, Case 2-1 (with A_1), Case 2-2 (with A_1, A_3) and Case 2-4 (with A_1, A_3, A_5, A_7) in Table 5.2. For VIV of a circular cylinder, we still focus on the model prediction of the non-sinusoidal periodic oscillations at $U_r = 6$ and 7, as well as the quasi-periodic oscillations at $U_r = 4.5$ and 8.5. Tables 5.6–5.7 list the estimated parameters and the fitness values of Case 2-1 and Case 2-2. As shown, the inclusion of the third-order polynomial term $A_3(2\pi St)^3 \dot{Y}^3$ does not cause significant changes in other model parameters except A_1 . To be specific, the value of A_1 experiences either a more than five times increase at $U_r = 6$ and 7, or a slight increase at $U_r = 4.5$ and 8.5, accompanied by a negative value of A_3 . In addition, there is roughly an equal prediction accuracy of Case 2-1 and Case 2-2 at different values of reduced velocity. As for the Case 2-4 with the

Table 5.7: Estimated parameters of θ -based wake oscillator model with various combinations of even and odd polynomial terms. The estimation data is associated with the quasi-periodic oscillation for VIV of a circular cylinder at $U_r = 4.5$ and 8.5.

Parameter	Case 2-1	Case 2-2	Case 2-5	Case 2-1	Case 2-2	Case 2-5
U_r	4.5	4.5	4.5	8.5	8.5	8.5
C_{L0}	0.5989	0.5887	0.4514	0.1350	0.1348	0.1342
St	0.1589	0.1589	0.1591	0.1586	0.1586	0.1586
ζ_f	0.0150	0.0139	0.0109	0.4121	0.4138	0.4084
f_m	1.0888	1.0607	1.4086	-0.0447	-0.0408	-0.0427
\bar{l}^*	0.4997	0.4933	0.5770	1.6200	1.5918	1.9222
A_1	0.7035	0.8855	0.6236	0.2252	0.3038	0.2173
A_2	/	/	-0.9337	/	/	0.0294
A_3	/	-0.8600		/	-4.2169	/
Fit_Y (%)	96.69	96.79	96.69	96.76	96.64	96.76
Fit_{C_L} (%)	92.47	92.53	92.04	70.82	70.79	70.77

most odd polynomial terms, no effective or successful grey-box estimation procedure can be conducted on such a complex structure after several attempts. Furthermore, the VIV response of circular cylinder mainly involves a simpler (viz., quasi-sinusoidal temporal series of lift coefficient) structural oscillation at low reduced velocity—for this case including too many odd polynomials will considerably increase the model complexity but not improve the accuracy. All these demonstrate that including the first-order polynomial term (viz., Case 2-1) is sufficient for a θ -based wake oscillator model to predict the pure VIV of a circular cylinder well. This conclusion is similar to that for a C_L -based model.

On the basis of above discussion, we further investigate the addition of an even (second-order) polynomial term to the Y -ODE of the θ -based model, viz. Case 2-5 in Table 5.2. As shown in Tables 5.6–5.7, the estimated value of A_2 can be either a quite small positive with an order of 0.01 (e.g., $A_2 = 0.07, 0.08$ and 0.03 at $U_r = 6, 7$ and 8.5 respectively) or a negative (e.g., $A_2 = -0.93$ at $U_r = 4.5$). But, nevertheless, the addition of A_2 has little effect on the values of other parameters. Most importantly, the Cases 2-1 and 2-5 have almost identical accuracy for $Y(t)$ and $C_L(t)$ —this means the inclusion of $A_2(2\pi St)^2 \dot{Y}^2$ in the Y -ODE is not necessary.

Above analysis on the influence of odd and even polynomial terms indicates that in addition to the inherent five physical parameters (viz., C_{L0} , St , ζ_f , f_m and \bar{l}^*), the optimal θ -based wake oscillator model should include the first-order polynomial $A_1(2\pi St)\dot{Y}$ in the

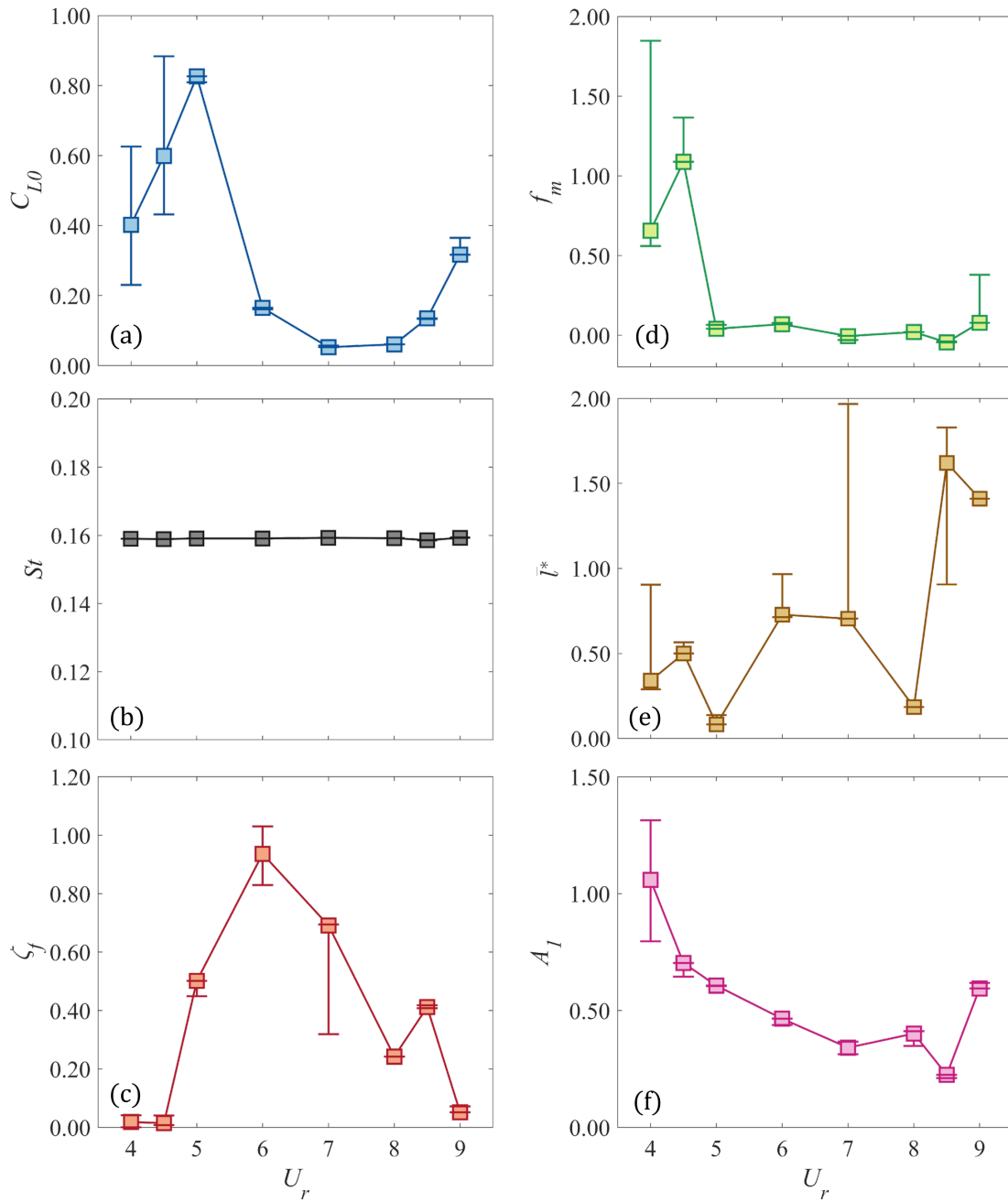


Figure 5.12: Estimated parameters of θ -based wake oscillator model with an optimal structure for VIV of circular cylinder. (a)–(f) represent C_{L0} , St , ζ_f , f_m , \bar{l}^* and A_1 as a function of U_r .

right hand side of Y -ODE, in order to predict the pure VIV of a circular cylinder. As a consequence, it includes six free parameters in total as that of the optimal C_L -based model (viz., Case 1-2). The estimated parameters are also plotted as a function of U_r in Fig. 5.12.

Similar to Figs. 5.11 (a)–(b), the model estimation procedure here is also meaningful for two reasons: (i) the Strouhal number St is fixed at 0.16 for different reduced velocities; (ii) the variation of C_{L0} with U_r basically follows the trend of the instantaneous lift coefficient $C_{Lc,rms}$. The damping ratio of fluid ζ_f in the θ -based model is equivalent to the Van der Pol constant ϵ in the C_L -based model to a certain extent, so their plots display similar patterns (see Fig. 5.11 (c) and Fig. 5.12 (c)). Such analogy is also true for the coefficient A_1 of the first-order polynomial (see Fig. 5.11 (d) and Fig. 5.12 (f)). As shown in Fig. 5.12 (d), the parameter related to the Magnus effect f_m has a quite small value of order 0.01 except near the onset of VIV. By contrast, the parameter measuring the size of the oscillating near-weak region \bar{l}^* shows a more random variation with U_r . And its optimal value can vary within a wide range at multiple reduced velocities in the VIV regime (see Fig. 5.12 (e)).

A careful perusal of Fig. 5.12 shows that the parameters C_{L0} , St and A_1 are always estimated to the same value for each U_r (viz., with very narrow error bar) except near the VIV onset. However, the optimal values of other three parameters ζ_f , f_m and \bar{l}^* have a wide variation range with visible error bars, and their different combinations can reach almost the same model accuracy. This presents challenges for the grey-box estimation of the θ -based wake oscillator model. By contrast, the C_L -based model shows an easier estimation procedure because it only has one parameter with higher uncertainty—that is the Van der Pol constant ϵ , as is evident in Fig. 5.11.

5.4.3 Galloping of a Circular Cylinder-Plate Assembly

This case study involves the pure galloping of a circular cylinder-plate assembly with $L_{SP}/D = 0.75$. As shown in Fig. 5.13, eleven representative values of reduced velocity are selected from various response regimes, including the 1:2 ($U_r = 11$), 1:3 ($U_r = 15, 17, 19$) and 1:5 ($U_r = 29$) synchronization branches, as well as the non-synchronization branches ($U_r = 9, 13, 21, 23, 25$ and 27). The corresponding time series of Y and C_L are also plotted in Fig. 5.13, with the top six representing the quasi-periodic oscillations of non-synchronization and the bottom five representing the periodic oscillations of synchronization.

In contrast to the pure VIV of circular cylinder, the galloping response is always associated with more complex structural oscillations and vortex-shedding patterns, as indicated

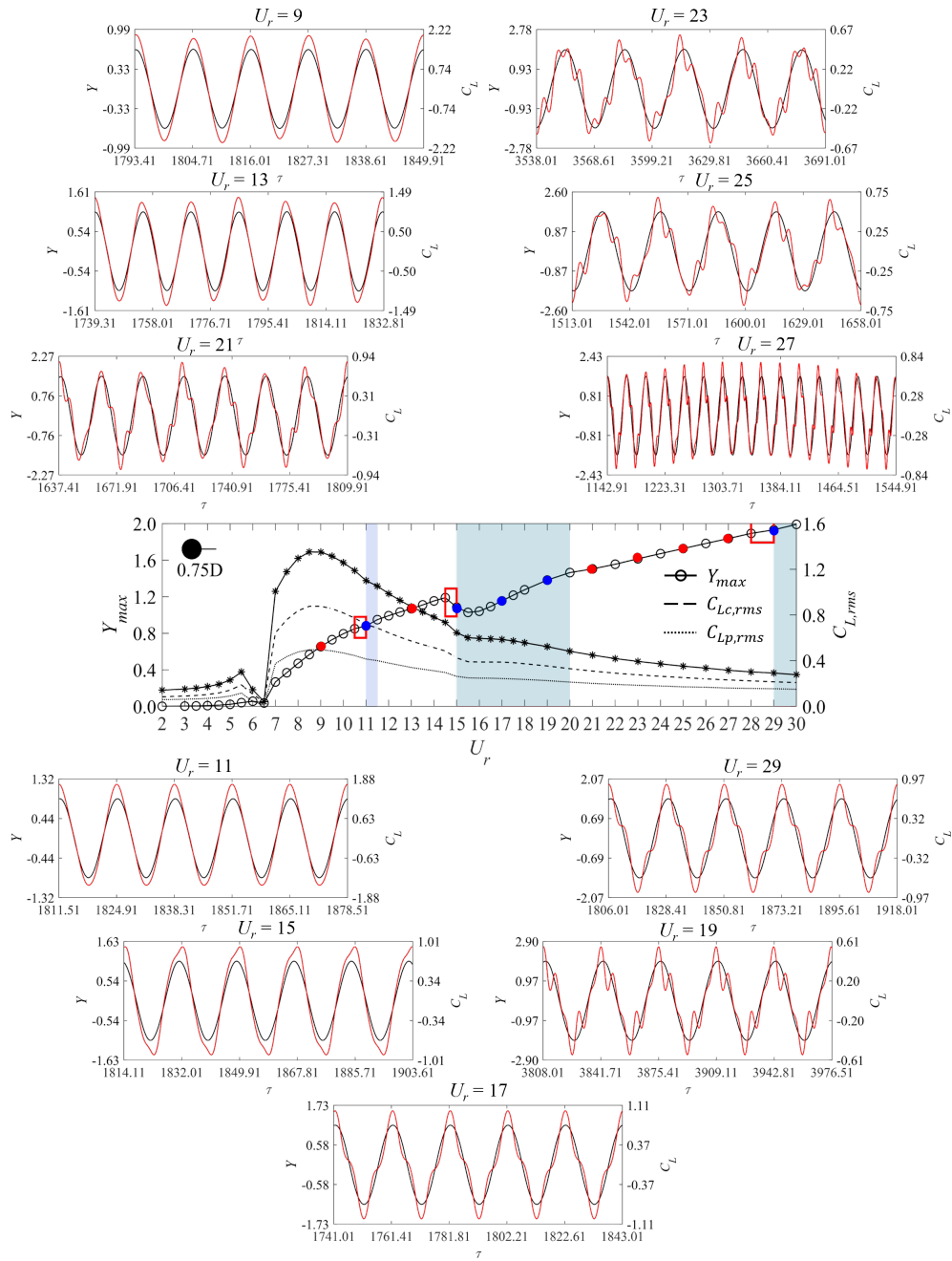


Figure 5.13: The galloping response of a circular cylinder-plate assembly with $L_{SP}/D = 0.75$ in terms of Y and C_L as a function of U_r , surrounded by $Y(t)$ (black) and $C_L(t)$ (red) at eleven representative values of U_r . The periodic and beating oscillations are respectively marked by blue and red points in the amplitude response.

Table 5.8: Estimated parameters for C_L -based wake oscillator model with (Case 1-2) and without (Case 1-5) the second-order polynomial term. The estimation data is associated with the quasi-periodic oscillation for VIV of a circular cylinder at $U_r = 9, 25, 27$ and 29 .

Parameter	Case 1-1	Case 1-2	Case 1-1	Case 1-2	Case 1-1	Case 1-2	Case 1-1	Case 1-2
U_r	9	9	25	25	27	27	29	29
C_{L0}	2.0897	1.8753	0.0197	0.0331	0.1123	0.1184	0.1041	0.0975
St	0.1554	0.1553	0.1570	0.1570	0.1569	0.1569	0.1570	0.1570
ϵ	0.0203	0.0221	0.0001	0.0002	0.0008	0.0009	0.0042	0.0035
A_1	0.2728	0.2479	0.0458	0.0198	0.0329	0.0260	0.0378	0.0156
B_1	-6.5843	-6.5910	-5.6211	-5.6120	-5.5736	-5.5733	-5.4993	-5.5020
B_2	/	0.0149	/	0.0254	/	0.0068	/	0.0209
Fit_Y (%)	97.94	97.27	98.27	98.26	98.42	98.42	98.25	98.26
Fit_{C_L} (%)	95.50	95.53	65.80	65.86	63.95	63.96	62.02	62.06

by the more severely distorted time trajectories of C_L at much higher reduced velocities in Fig. 5.13. Due to this, the prediction of galloping using wake oscillator model is theoretically more challenging than that of pure VIV.

Structure of C_L -based wake oscillator model

For C_L -based wake oscillator model, the first thing is still to determine whether it is necessary to include the velocity-coupling $B_2\dot{Y}$ as a forcing term in the C_L -ODE. Table 5.8 compares the model performance of Case 1-1 and Case 1-2 at four values of reduced velocity, which represent both the oscillation with beating phenomenon ($U_r = 9, 25$ and 27) and the highly periodic oscillation ($U_r = 29$). According to the discussions in Section 5.4.2, the term $B_2\dot{Y}$ might improve the model accuracy if C_L displays a non-sinusoidal time history, so here we focus more on the higher values of U_r where the non-sinusoidal oscillations can occur. As indicated, the inclusion of B_2 has little effect on either the values of other parameters or the fitness of Y and C_L . In addition, the estimated B_2 is quite small with an order of 0.01, which means the velocity coupling has a limited influence on the model prediction. Therefore, B_2 can be set to be zero during the model estimation.

In order to determine a reasonable forcing term of Y -ODE, the influence of various odd polynomial terms $A_i(2\pi St)^i\dot{Y}^i$ is then investigated by comparing three cases, viz., Case

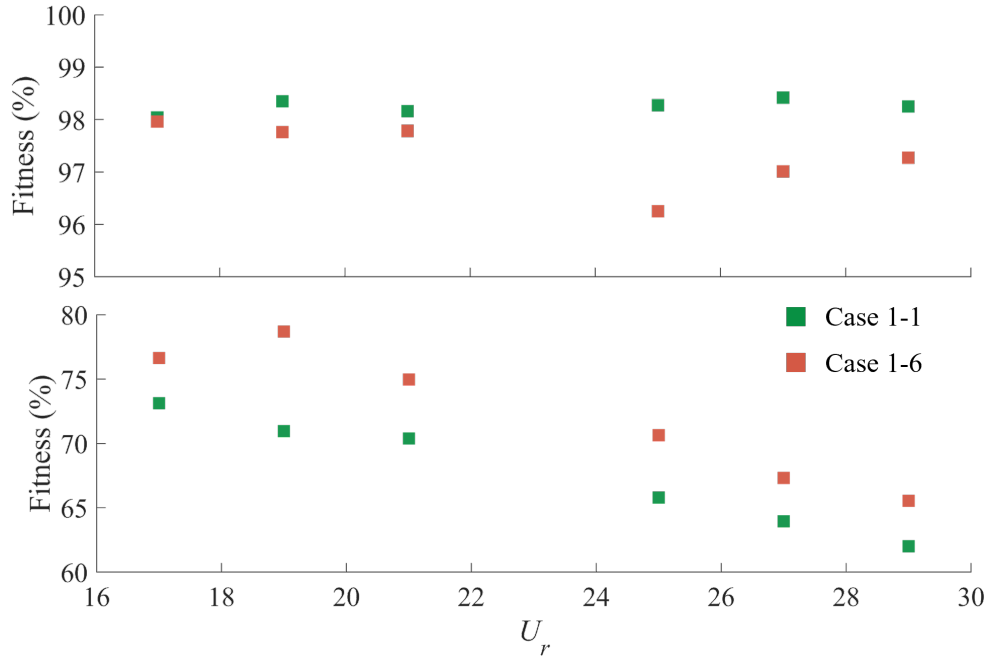


Figure 5.14: Fitness of $Y(t)$ (top) and $C_L(t)$ (bottom) from Case 1-1 and Case 1-6 for galloping of a circular cylinder-plate assembly at larger reduced velocity.

1-1 ($i = 1$), Case 1-6 ($i = 1, 3$) and Case 1-7 ($i = 1, 3, 5, 7$) in Table 5.2. Among them, only B_1 is free to estimate to provide an acceleration coupling term in the C_L -ODE.

Figure 5.14 compares the fitness values of $Y(t)$ and $C_L(t)$ from Case 1-1 and Case 1-6 at higher values of U_r . As shown, both cases can obtain a much higher accuracy in predicting the oscillation of Y (more than 96%) comparing to that of C_L (around 60%-80%), which is due to the severe distortion of $C_L(t)$ at larger U_r . Moreover, Case 1-6 obviously performs better than Case 1-1 for the prediction of $C_L(t)$, while a little bit worse than Case 1-1 for $Y(t)$. Overall, including both the first- and third-order polynomial terms has a positive effect on the performance of C_L -based wake oscillator model.

Another thing worth noting is that in the process of model estimation, we find the Case 1-1 seems unable to find a reasonable solution at certain values of U_r . For example, Table 5.9 lists three unsuccessful predictions of Case 1-1 at $U_r = 13$. Although $Y(t)$ and $C_L(t)$ have a high accuracy up over 90%, the corresponding model parameters can be unreasonable. To be specific, the C_{L0} of Solution 1 has an unrealistic high value of 6.2751. If the variation range of C_{L0} is prescribed as 0–0.7 during estimation, the optimal value of ϵ would be unrealistic small to reach the same accuracy as Solutions 2–3. In fact, we cannot

Table 5.9: Estimated parameters and fitness of $Y(t)$ and $C_L(t)$ at $U_r = 13$. Invalid solutions from Case 1-1 (Solutions 1–3) and Case 1-2 (Solution 4), as well as a valid solution from Case 1-6 (Solution 5). The unreasonable parameter is marked in box.

Parameter	Solution 1	Solution 2	Solution 3	Solution 4	Solution 5
C_{L0}	6.2751	0.7000	0.3447	4.2737	0.6149
St	0.1564	0.1564	0.1564	0.1564	0.1564
ϵ	0.0310	1.62×10^{-9}	3.65×10^{-6}	0.0627	0.0078
A_1	0.0829	0.1257	0.1396	0.1137	-0.1375
A_3	/	/	/	/	2.2103
B_1	-6.0007	-5.9917	-5.9757	-5.9888	-5.9692
B_2	/	/	/	-0.0578	/
Fit_Y (%)	98.55	98.64	98.31	98.61	98.48
Fit_{C_L} (%)	94.06	93.91	93.39	94.33	93.92

find a reasonable set of parameters at $U_r = 13$ using Case 1-1 after many failed attempts. And this tricky problem cannot be fixed by adding a free parameter of B_2 , as indicated by Solution 4 still with a high value of $C_{L0} = 4.2737$ using Case 1-2. However, the inclusion of two odd polynomial terms has the potential to solve this problem as Solution 5 from Case 1-6. As a consequence, the C_L -based wake oscillator model should contain at least $A_1(2\pi St)\dot{Y}$ and $A_3(2\pi St)^3\dot{Y}^3$ in the Y -ODE in order to give a meaningful prediction of galloping response.

We further investigate whether the model results would be more accurate by adding more odd polynomial terms, viz., Case 1-7 with A_1 , A_3 , A_5 and A_7 as free parameters. Figs. 5.15–5.16 compare the estimation data with the model results from Cases 1-1, 1-6 and 1-7, in terms of the oscillations of $Y(t)$ and $C_L(t)$ at $U_r = 19$ and 29. As shown, the three cases show a very good agreement with the estimation data for the prediction of $Y(t)$ with sine waveform. In addition, the Case 1-7 substantially improves the model performance to predict $C_L(t)$ with either a slight ($U_r = 19$) or a severe ($U_r = 29$) deformation, because the inclusion of more odd polynomial terms can help to capture the local variations of C_L trajectories with time. By contrast, Cases 1-1 and 1-6 can only produce the rough trend of $C_L(t)$. From this perspective, it is necessary to include the free parameters A_1 , A_3 , A_5 and A_7 in the C_L -based wake oscillator model for a better prediction of galloping response.

The effect of the even polynomial term on the model prediction can be negligible, similar to that for the VIV of a circular cylinder. In addition, considering that the structure of Case 1-7 already has eight free parameters to estimate, the forcing term $A_2(2\pi St)^2\dot{Y}^2$ will

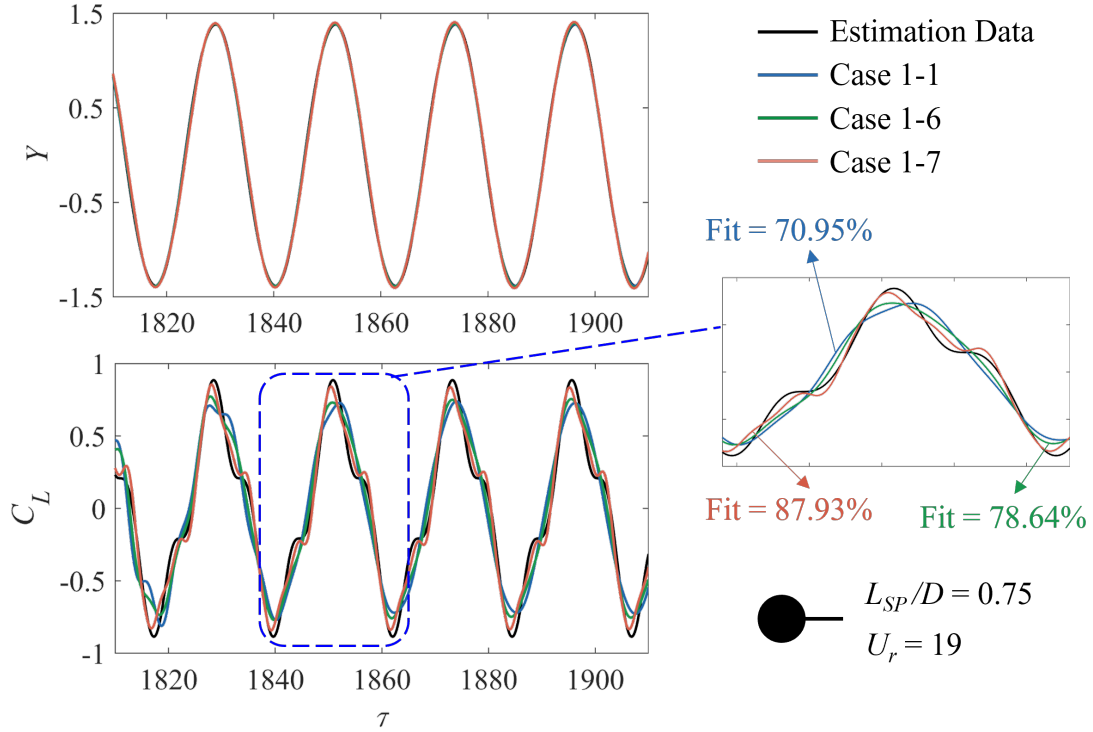


Figure 5.15: The time series of Y and C_L for galloping of a circular cylinder-plate assembly with $L_{SP}/D = 0.75$ at $U_r = 19$ from estimation data and C_L -based wake-oscillator models. For Case 1-1, the estimated parameters are $C_{L0} = 0.1553$, $St = 0.1563$, $\epsilon = 0.0007$, $A_1 = 0.0682$ and $B_1 = -6.1186$. For Case 1-6, the estimated parameters are $C_{L0} = 0.2073$, $St = 0.1563$, $\epsilon = 0.0025$, $A_1 = -0.8891$, $A_3 = 8.7814$ and $B_1 = -6.0558$. For Case 1-7, the estimated parameters are $C_{L0} = 0.3375$, $St = 0.1563$, $\epsilon = 0.0184$, $A_1 = 0.9373$, $A_3 = -163.4914$, $A_5 = 2572.8800$, $A_7 = -10073.8521$ and $B_1 = -5.5171$.

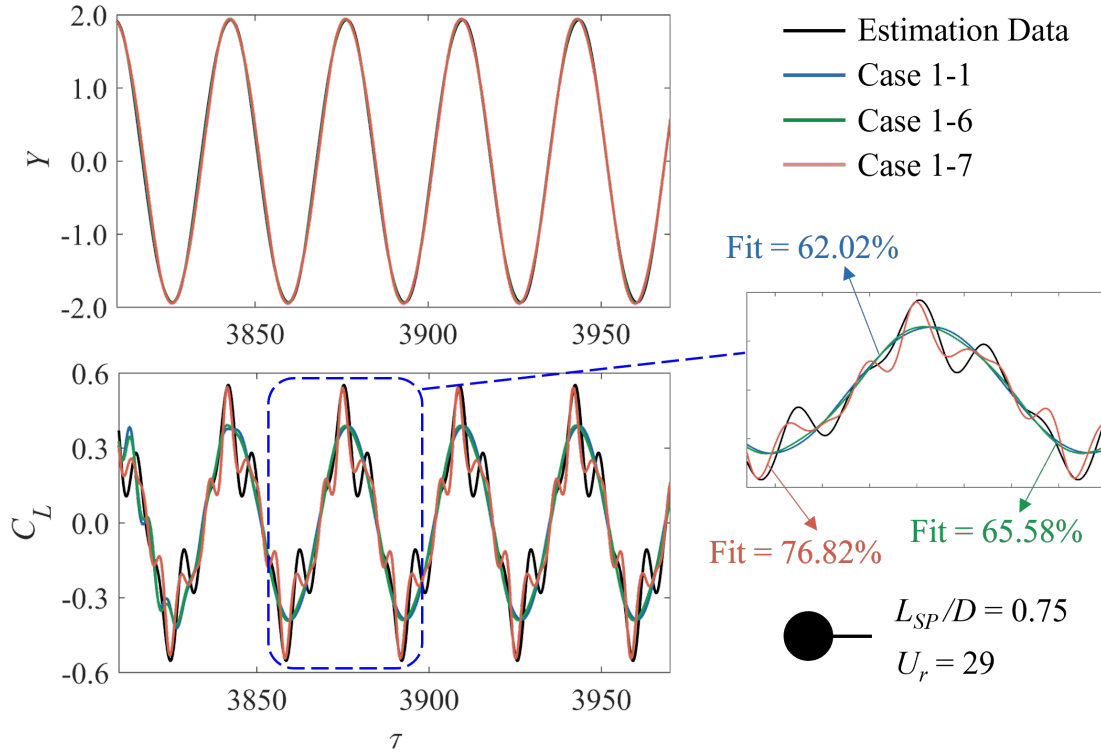


Figure 5.16: The time series of Y and C_L for galloping of a circular cylinder-plate assembly with $L_{SP}/D = 0.75$ at $U_r = 29$ from estimation data and C_L -based wake-oscillator models. For Case 1-1, the estimated parameters are $C_{L0} = 0.1041$, $St = 0.1570$, $\epsilon = 0.0042$, $A_1 = 0.0378$ and $B_1 = -5.4993$. For Case 1-6, the estimated parameters are $C_{L0} = 0.2884$, $St = 0.1570$, $\epsilon = 0.0474$, $A_1 = -0.4622$, $A_3 = 5.1627$ and $B_1 = -5.4442$. For Case 1-7, the estimated parameters are $C_{L0} = 0.0492$, $St = 0.1570$, $\epsilon = 0.0010$, $A_1 = -1.1962$, $A_3 = -49.2549$, $A_5 = 1495.0582$, $A_7 = -8154.3825$ and $B_1 = -4.9050$.

not be included in the Y -ODE to avoid the model getting too complicated.

From above analysis, the C_L -based wake oscillator model has the optimal structure of Case 1-7 to predict the pure galloping response of a cylinder-plate assembly with $L_{SP}/D = 0.75$, which considers a seventh-order odd polynomial forcing term in the Y -ODE and an acceleration coupling term in the C_L -ODE. The variations of the eight free parameters with respect to U_r are described in Fig. 5.17. It can be seen that the Strouhal number St still has a constant value of around 0.156 for different reduced velocities. The value of C_{L0} decreases from 2 to 0.1 over $U_r = 9$ –30, which basically follows the trend of the root-mean-square of lift coefficient on the assembly $C_{L,rms}$ in Fig. 5.13. These features prove the rationality of the grey-box estimation procedure here. For galloping response, the Van der Pol constant ϵ is less than 0.15. Once entering the 1:3 synchronization ($U_r \geq 15$), the value of ϵ becomes much smaller of around 0.01–0.02. Conversely, the coefficient associated with the acceleration coupling B_1 generally increases with U_r within the range from -7 to -4. In Figs. 5.17 (e)–(h), the four coefficients of odd polynomial terms have more random estimated values. But the sure thing is that A_1 and A_5 are always positive, while A_3 and A_7 are always negative, which is consistent with some previous studies [58].

Structure of θ -based wake oscillator model

For the θ -based wake oscillator model, the main point of the discussion is how many polynomial terms should be contained in the right hand side of Y -ODE. Here we still ignore the minimal influence of even polynomial terms based on previous experience.

Figure 5.18 compares the θ -based wake oscillator model with various combinations of odd polynomial terms $A_i(2\pi St)^i \dot{Y}^i$ (viz., Case 2-1 with $i = 1$, Case 2-2 with $i = 1, 3$, Case 2-3 with $i = 1, 3, 5$ and Case 2-4 with $i = 1, 3, 5, 7$) and the estimation data in terms of the time history of C_L at two representative values of reduced velocity, viz., $U_r = 19$ and $U_r = 29$. As shown, the model results of Cases 2-1 and 2-2 are quite similar with a nearly the same accuracy of about $Fit_{C_L} = 73\%$ at $U_r = 19$ and $Fit_{C_L} = 67\%$ at $U_r = 29$ —this means the third-order polynomial has an obvious contribution to the estimated model. While if further adding the fifth-order polynomial in the forcing term of Y -ODE, the fitness values of C_L are significantly increased to $Fit_{C_L} = 86\%$ at $U_r = 19$ and $Fit_{C_L} = 83\%$ at $U_r = 29$, as indicated by the green curves in Fig. 5.18. However, applying all four odd polynomial terms in Case 2-4 achieves very similar prediction accuracy with that of Case 2-3, maybe with a slight increase of about 1%, but this is at the expense of model complexity with nine free parameters to estimate. From this perspective, Case 2-3 with three (first-, third- and fifth-order) odd polynomial terms should be the optimal structure for a θ -based wake oscillator model to predict the galloping response well. In this

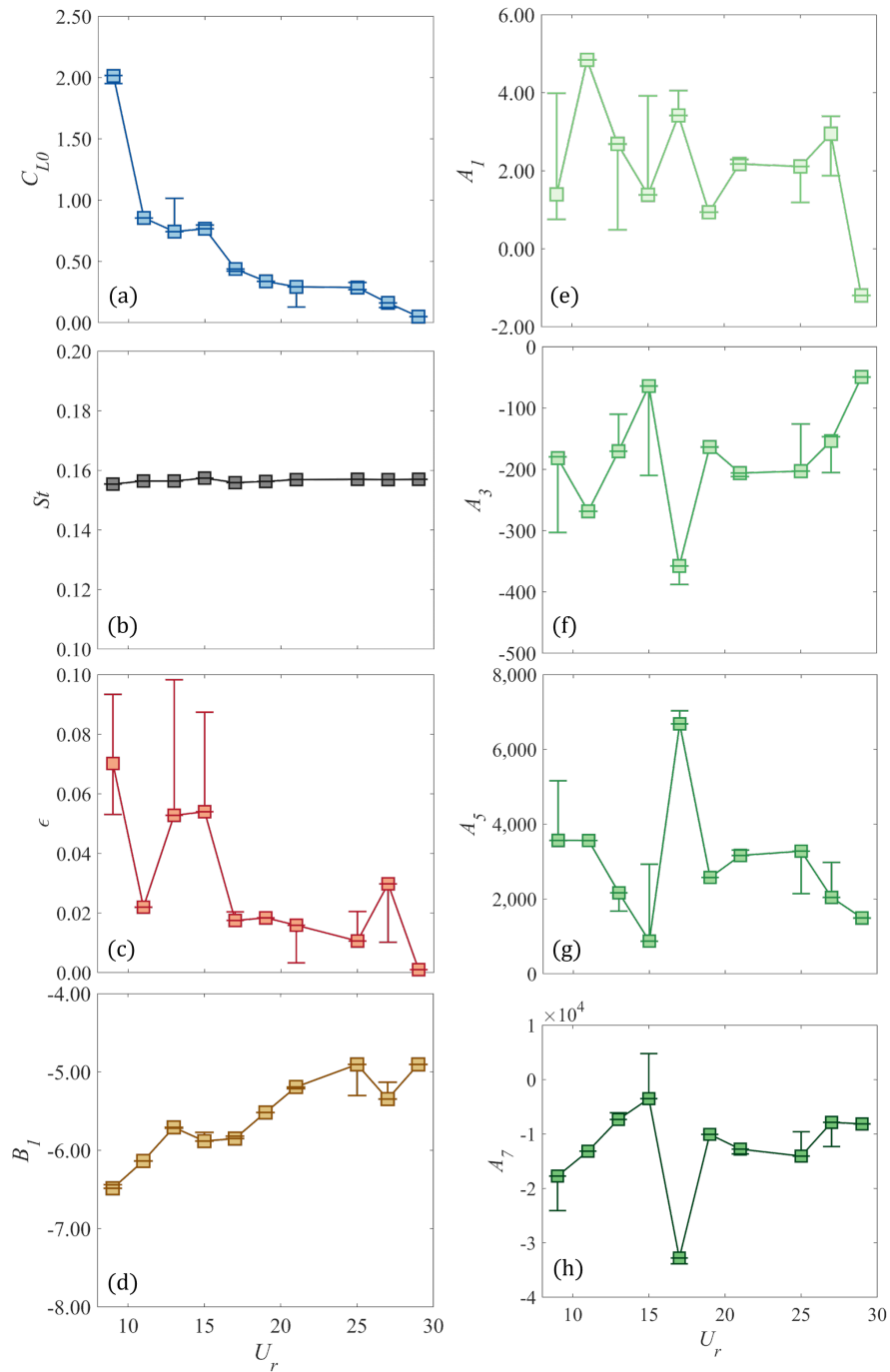


Figure 5.17: Estimated parameters of C_L -based wake oscillator model with optimal structure for the galloping of circular cylinder-plate assembly. (a)–(h) represent C_{L0} , St , ϵ , A_1 , A_3 , A_5 , A_7 and B_1 as a function of U_r .

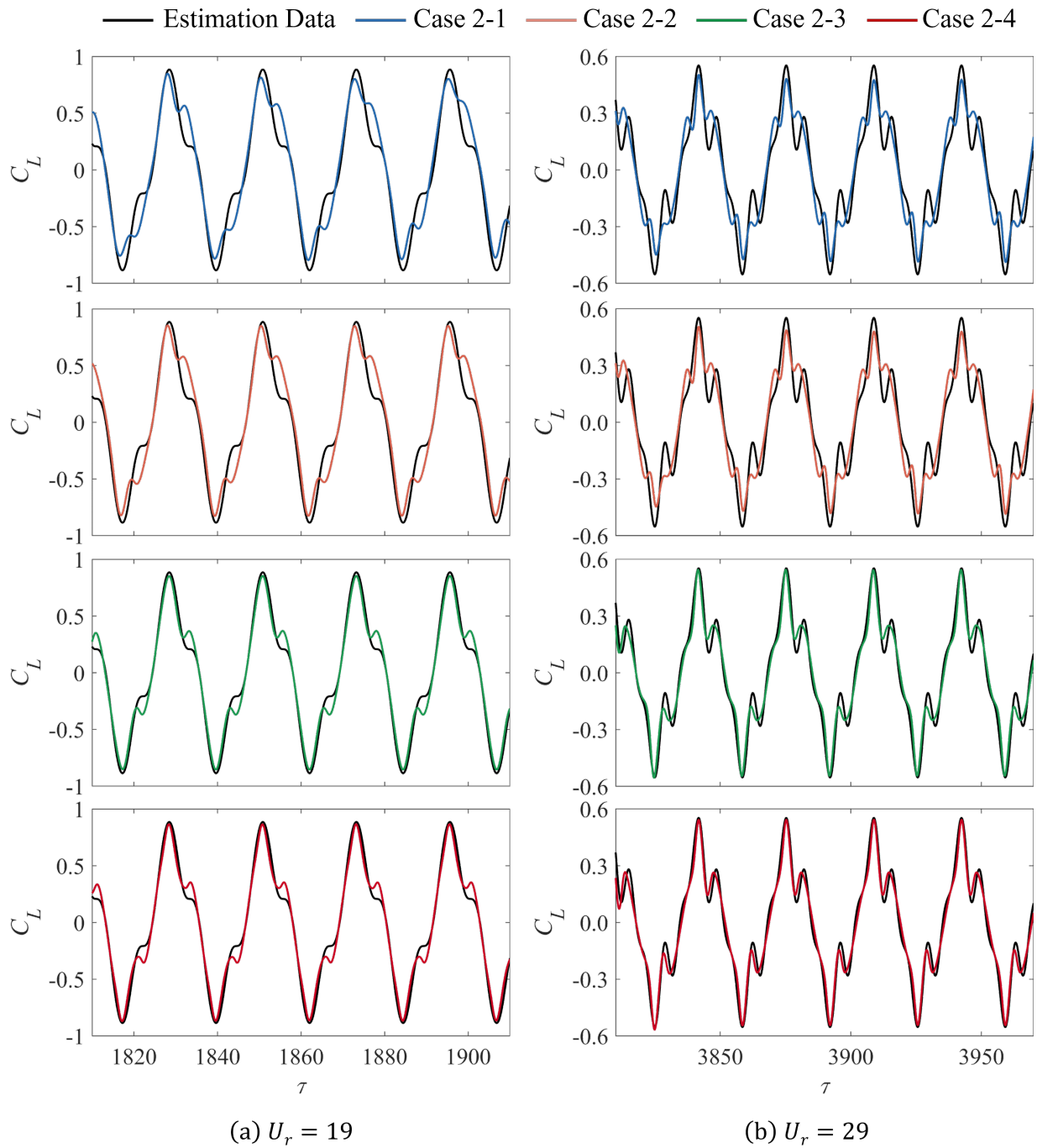


Figure 5.18: Time history of C_L from estimation data and estimated wake-oscillator models (Cases 2-1, 2-2, 2-3 and 2-4) at (a) $U_r = 19$ and (b) $U_r = 29$.

Table 5.10: Fitness value of Y (columns 2–3) and C_L (columns 4–5) associated with the VIV of circular cylinder from the best-structured C_L -based (Case 1-2) and θ -based (Case 2-1) wake oscillator models.

U_r	Case 1-2	Case 2-1	Case 1-2	Case 2-1
4	98.85	98.42	99.77	99.59
4.5	96.70	96.69	92.76	92.47
5	99.44	99.41	95.50	94.66
6	99.21	99.33	88.52	88.78
7	99.45	99.42	67.96	66.01
8	99.37	99.30	95.35	90.34
8.5	96.91	96.76	70.55	70.82
9	98.84	99.01	99.00	99.12

case, the model has eight free parameters like that of the C_L -based wake oscillator model (viz., Case 1-7).

The variation of the estimated values of model parameters with respect to U_r is given in Fig. 5.19. Again, the value of St is fixed at around 0.156, and the C_{L0} generally decreases with U_r as the lift coefficient acting on a moving assembly (see $C_{L,rms}$ in Fig. 5.13). By contrast, other three physical parameters (ζ_f , f_m and \bar{l}^*) don't display clear-cut patterns. Moreover, when including three odd polynomial terms, A_1 and A_5 are always negative but A_3 is positive.

5.4.4 A Further Discussion

In this section, some interesting phenomena displayed during the model estimation using the grey-box framework are further discussed.

First, the best-structured wake oscillator models based on C_L and θ are compared in terms of their potentials to predict VIV and galloping responses. As shown in Table 5.10, for the simpler VIV of a circular cylinder, the optimal structures of the two models include six free parameters to estimate, and they can basically achieve the same prediction accuracy. Moreover, the optimal C_L -based model can give some advantages in predicting the time history of C_L (e.g., $Fit_{C_L} = 95.35\%$ for Case 1-2 and $Fit_{C_L} = 90.34\%$ for Case 2-1 at $U_r = 8$). By contrast, for the complex galloping response of cylinder-plate assembly, the optimal model structures have eight free parameters. And the wake oscillator model based

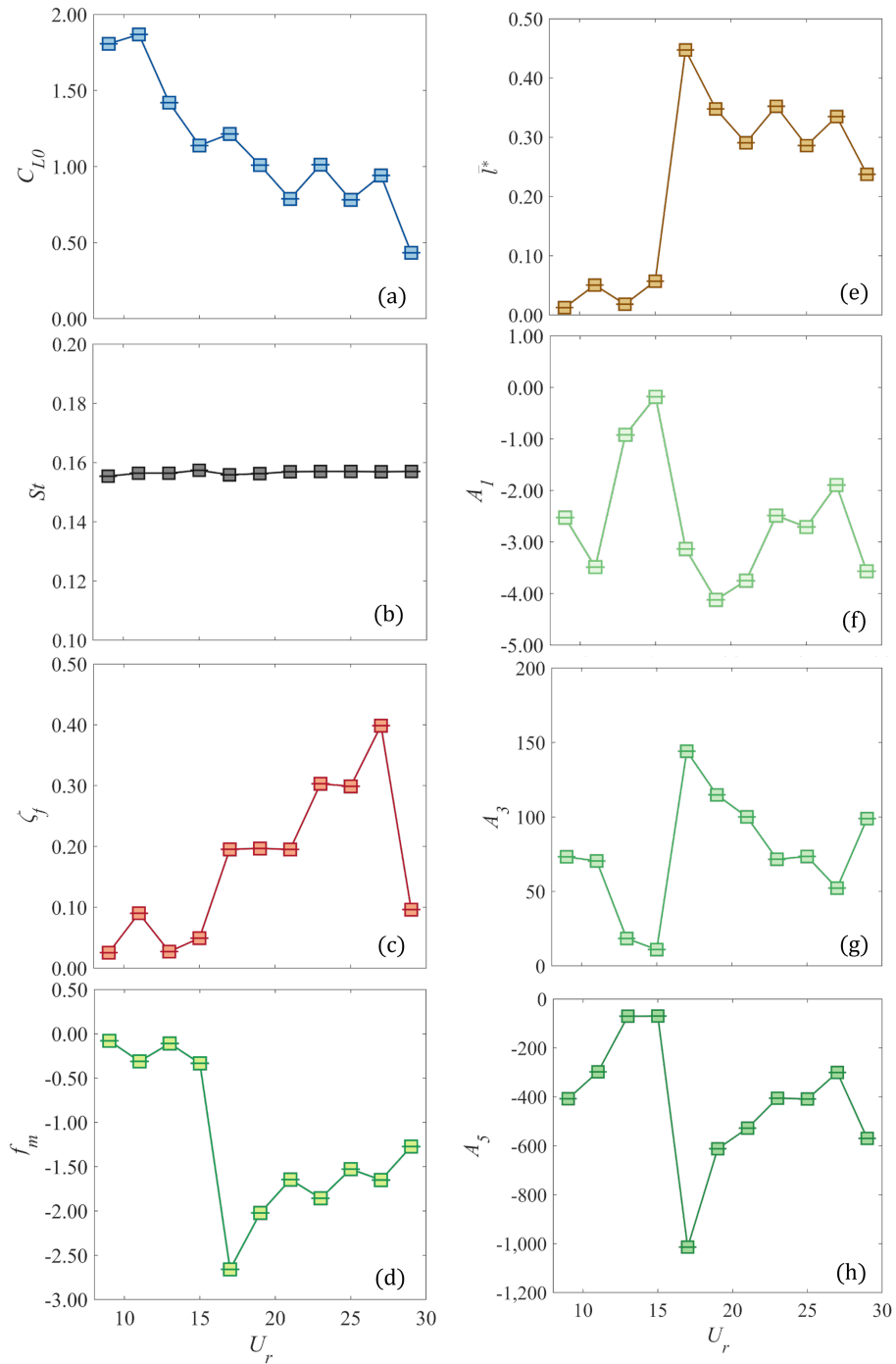


Figure 5.19: Estimated parameters of θ -based wake oscillator model with optimal structure for the galloping of circular cylinder-plate assembly. (a)–(h) represent C_{L0} , St , ζ_f , f_m , \bar{l}^* , A_1 , A_3 and A_5 as a function of U_r . 225

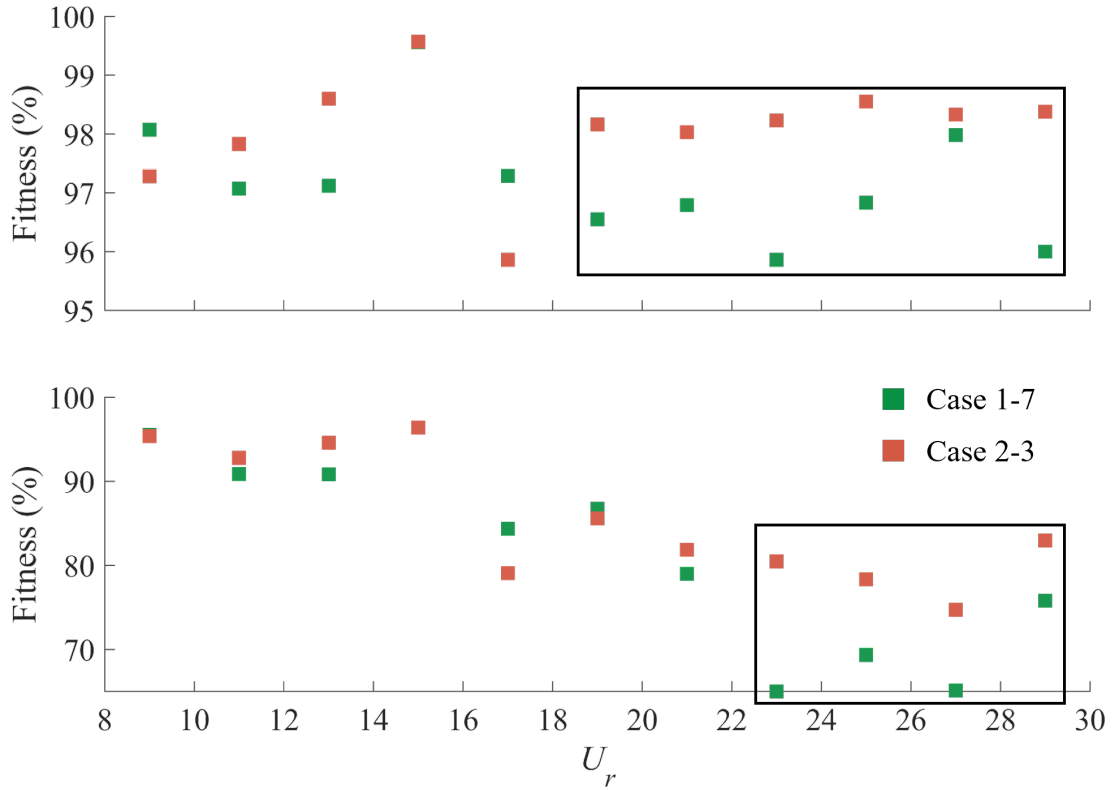


Figure 5.20: Fitness value of Y (up) and C_L (bottom) associated with the galloping of a circular cylinder-plate assembly with $L_{SP}/D = 0.75$ from the best-structured C_L -based (Case 1-7) and θ -based (Case 2-3) wake oscillator models.

on θ obviously reaches higher precision for the prediction of $Y(t)$ and $C_L(t)$, especially at larger values of reduced velocities (marked by the black box in Fig. 5.20). This finding may indicate that more physical parameters contained in the θ -based wake oscillator model are helpful in predicting the galloping response.

Second, we focus on the fixed Strouhal number during model estimation. Figs. 5.21–5.22 show the time history of lift coefficient acting on a stationary circular cylinder and a stationary cylinder-plate assembly with $L_{SP}/D = 0.75$, associated with the flow patterns around the fixed structure over one oscillation cycle of C_L . According to the vortex-shedding frequency, the Strouhal number is found to be $St = 0.16$ for $L_{SP} = 0$ and $St = 0.147$ for $L_{SP}/D = 0.75$ —this is consistent with the large-amplitude but low-frequency galloping response. The periodic variations of instantaneous vorticity fields also indicate

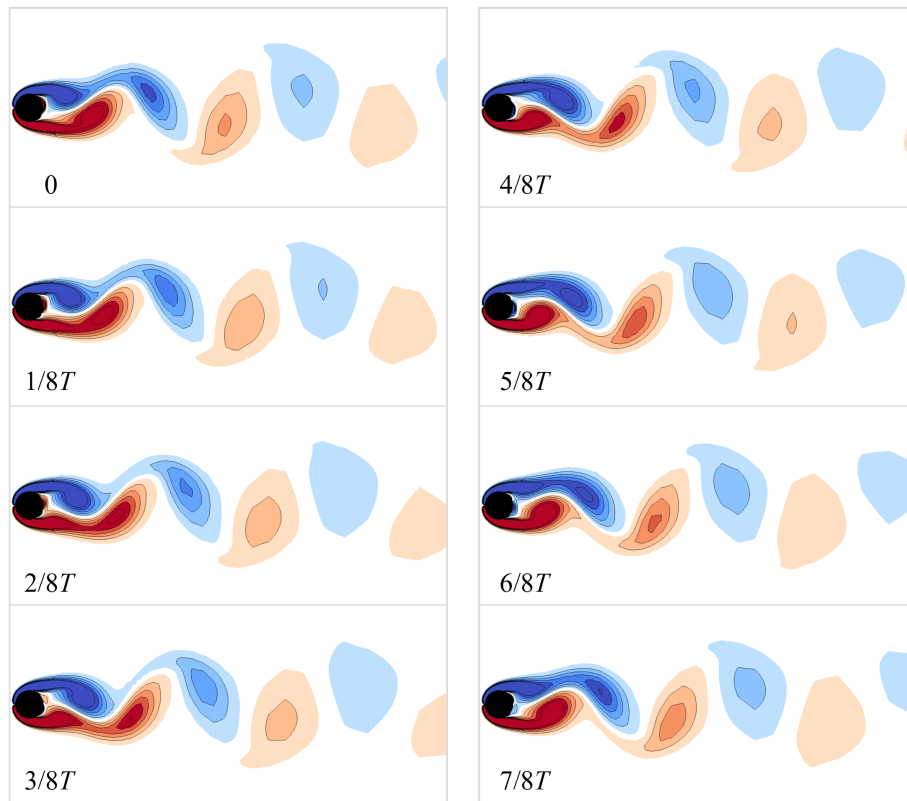
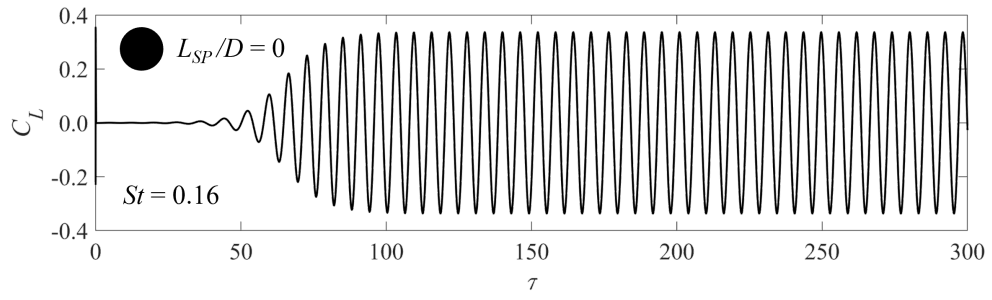


Figure 5.21: Time history of lift coefficient and instantaneous vorticity field of a stationary circular cylinder at $Re = 100$.

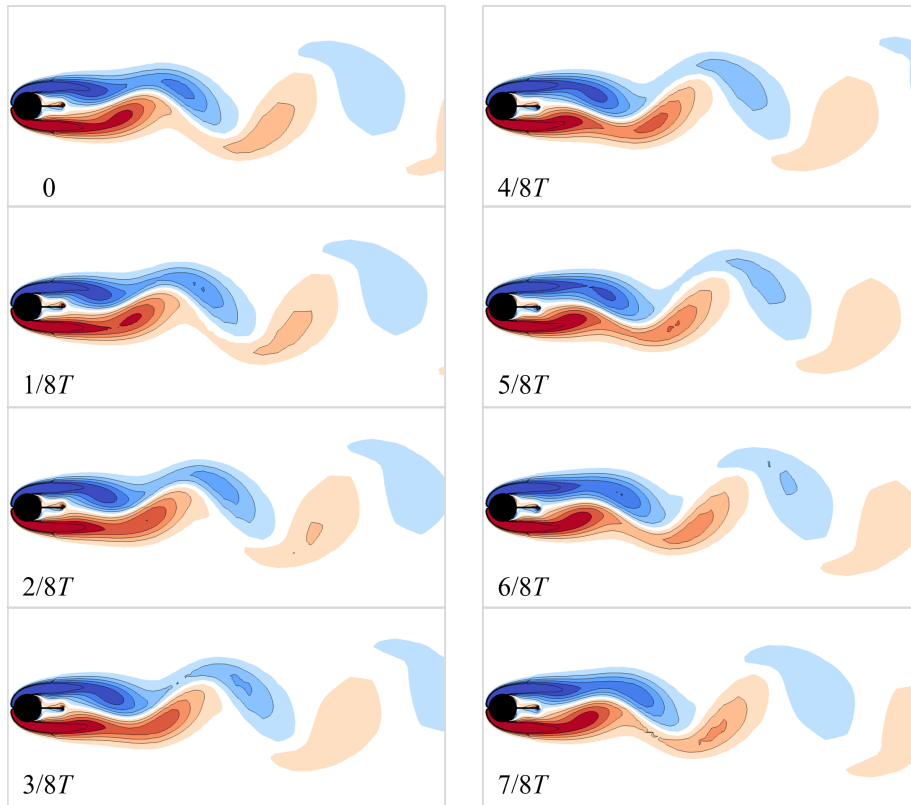
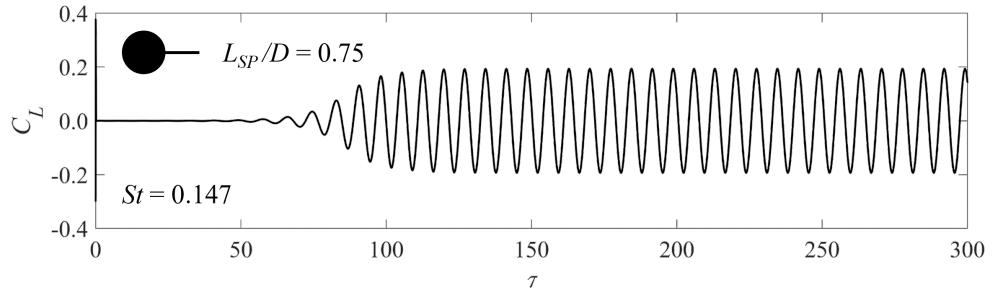


Figure 5.22: Time history of lift coefficient and instantaneous vorticity field of a stationary circular cylinder-plate assembly with $L_{SP}/D = 0.75$ at $Re = 100$.

that the near-wake flow behind a cylinder-plate assembly is characterized by the elongated boundary layers and slower vortex shedding.

As mentioned in Section 5.4.2, for VIV of a circular cylinder, the estimated Strouhal number $St = 0.159$ is consistent with the vortex shedding frequency from simulation for flow over a stationary circular cylinder, which justifies the wake-oscillator models based on C_L and θ . Likewise, for galloping of a circular cylinder-plate assembly, the Strouhal number of wake-oscillator model is estimated to be a slightly smaller value of 0.156—this does not agree with $St = 0.147$ from numerical simulations. The inconsistency of St may indicate that the model estimation may not very physically reasonable. In fact, we have tried to control the value of St to be fixed at 0.147 during estimation, but the corresponding fitness of Y and C_L can only reach about 80%.

To the author’s knowledge, the relatively poor performance of the wake-oscillator model in predicting the galloping response may be relevant with the intrinsic defects of the quasi-steady assumption. In other words, a higher order polynomial approximation may not be able to model the fluid force responsible for the galloping precisely. As a consequence, the complex oscillations of Y and C_L at larger reduced velocities might be less predictable using the wake-oscillator model.

5.5 Chapter Summary

In this chapter, the coupled wake-oscillator models to predict the FIV response are investigated from the perspective of model identification and parameter estimation, based on the simulation data for the VIV and galloping responses at $Re = 100$.

First, the classical wake-oscillator models based on the lift coefficient C_L and wake angular displacement θ are improved from multiple aspects. To be specific, the C_L -based VIV model is extended to predict the galloping response by including the quasi-steady galloping force in the structure equation. Here, a generalized polynomial approximation with both even and odd terms is applied to model the driving force of galloping. Moreover, both the acceleration coupling and velocity coupling are added in the fluid equation. In order to directly use the simulation data with time history of lift coefficient C_L , the wake-oscillator model is reformulated by converting the implicit fluid variables (e.g., q for the C_L -based model and θ for the θ -based model) into the explicit C_L . Based on above model structures, a genetic algorithm enhanced nonlinear grey-box framework is proposed to estimate the free parameters.

The proposed framework is verified by two scenarios, namely, VIV of a circular cylinder and galloping of a circular cylinder-plate assembly with $L_{SP}/D = 0.75$, focusing on the optimal structures of various wake-oscillator models. For the simpler VIV, the best-structured model has six free parameters to estimate, viz., C_{L0} , St , ϵ , A_1 , B_1 , B_2 for a C_L -based model, and C_{L0} , St , ζ_f , f_m , \bar{l}^* , A_1 for a θ -based model. In other words, the first-order polynomial term $A_1(2\pi St Y)$ is enough for a wake-oscillator model to predict the VIV response. For the complex galloping, more high-order polynomial terms are necessary in the optimal model, which has eight free parameters, viz., C_{L0} , St , ϵ , A_1 , A_3 , A_5 , A_7 , B_1 for a C_L -based model and C_{L0} , St , ζ_f , f_m , \bar{l}^* , A_1 , A_3 , A_5 for a θ -based model. Note that the even polynomial terms lead to non-symmetrical time series and have extremely weak effect on the model prediction.

Comparing the C_L -based and θ -based wake oscillator models, it can be found that the latter displays a better performance in predicting the galloping response, which may be due to the fact that it has more (five) physical parameters. However, the estimated Strouhal number $St = 0.156$ of wake-oscillator models is higher than that from simulation ($St = 0.147$), which could be associated with the inherent defect of the quasi-steady assumption to model the fluid flow for galloping.

Chapter 6

Conclusions and Future Works

This thesis focuses on the transverse FIV response of an elastically-supported cylinder-plate assembly. For one thing, extensive full-order numerical simulations are carried out to systematically investigate the influence of the geometrical shape (viz., the length of splitter plate and the aspect ratio of cylinder) and the reduced velocity on the assembly's FIV from different aspects. On this basis, a complete simulation database is established, which allows for all aspects of the FIV response of a cylinder-plate assembly to be covered. For another, a genetic algorithm optimized nonlinear grey-box framework is proposed to estimate the free parameters of the improved wake-oscillator models for the FIV phenomenon, which is verified by the simulation dataset regarding to the VIV and galloping responses. The conclusions are summarized as follows.

The two dimensional laminar flow over an elastically-supported circular cylinder-plate assembly with $m^* = 10$ and $\zeta = 0$ is simulated at $Re = 100$, involving extensive spans of the splitter-plate length $L_{SP}/D = 0-4$ and reduced velocity $U_r = 2-30$. The research has found that an increase in the L_{SP} would substantially affect nearly every aspect of the assembly's FIV response, including the structural vibrations, the branching behaviors, the flow dynamics and the nonlinear dynamical features.

1. For $L_{SP}/D \leq 0.5$, a self-limited FIV, either a pure VIV ($L_{SP}/D = 0.25$) or an integrated VIV-galloping ($L_{SP}/D = 0.5$) is induced on the assembly. Using the classical VIV of a circular cylinder as a reference, the former shows a 1.5 times larger lock-in range, whereas the latter has a three times wider U_r -range with a low-frequency oscillation. For $0.75 \leq L_{SP}/D < 4$, an unlimited FIV is triggered on the assembly—this consists of a steadily increasing vibration amplitude in the

galloping regime that is preceded by a VIV regime. As L_{SP} increases, the two regimes become increasingly separated from strongly-overlapped to no overlap. Moreover, the structural vibration and flow dynamics are affected more by the lift forces on the circular cylinder and on the splitter-plate, respectively.

2. Both even- and odd-multiple synchronization branches are supported by the assembly, which appear successively in increasing order, viz., $f_Y^* : f_{C_L}^* = 1:n$ where $n = 1, 2, 3$, and so forth. If the highest harmonic of C_L -spectrum is larger than that of Y -spectrum, the synchronization starts with a (step, slow-growth or decrease) “kink” in the amplitude response. For $L_{SP}/D \geq 2.5$, two new branches are identified: (i) the initial galloping branch associated with wake meandering occurs immediately after the galloping onset; (ii) the still branch characterized by the stationary assembly and steady flow appears due to the complete uncoupling of upper and lower shear layers. Based on branching behaviors, the assemblies are categorized into five groups.
3. The beating phenomenon occurred near the VIV boundaries is categorized into five distinct types based on the relationship between local frequency, f_n and f_{St} , while that occurred in the non-synchronized galloping regime is elucidated from a global perspective (e.g., periodicity and symmetry). Moreover, three nonlinear oscillations are identified based on their limit cycles and Poincaré sections. The Type-I nonlinearity characterized by the donut-shaped orbits corresponds to a period-doubling oscillation. The Type-II nonlinearity exhibiting wide limit cycles composed of numerous closed loops corresponds to a long-period beating. The Type-III nonlinearity associated with disordered phase-plane portraits corresponds to a chaotic oscillation.
4. The synchronization branch is accompanied by cyclical vortex-shedding modes with elliptical vortices, such as the classical “2S” mode for 1:1 synchronization, the regular “ $n \times (2S)$ ” mode for higher-order odd synchronizations and more complex modes (e.g., “T+S”, “P+S”) for higher-order even synchronizations. By contrast, the non-synchronization branch is associated with non-periodic wake modes that consisting of irregular vortices, such as the newly observed right-angled vortex S_A and crescent-shaped vortex S_B , which leads to strong nonlinear dynamical characteristics.

The synergy effect of the aspect ratio of cylinder (AR) and the splitter-plate length (L_{SP}) on the FIV of an elliptical cylinder-plate assembly is numerically investigated by the simulations under same conditions, which involves various combinations of AR (0.5, 0.67, 0.75, 1, 1.5 and 2) and L_{SP}/D (0.5, 0.75 and 2.5).

1. Each geometrical factor stresses on different aspects in influencing the assembly's FIV. The aspect ratio determines whether a FIV can be induced in the assembly—a critical value of $0.67 < AR_{cri} < 0.75$ is required for this to occur at $Re = 100$, because the flow separation point on the windward surface of a horizontal ellipse is too far back to provoke an oscillatory motion. For a triggered FIV ($AR > AR_{cri}$), the splitter-plate length determines its fundamental vibration mode to be limited ($L_{SP}/D = 0.5$) or unlimited ($L_{SP}/D = 0.75$ and 2.5), while changing AR only has an impact on the vibration level.
2. As AR increases, the self-limited FIV is significantly amplified for $0.75 \leq AR \leq 1.5$ but weakened for $AR = 2$. The former is associated with a wider effective U_r range (e.g., $U_r = 6\text{--}14$ for $AR = 0.75$ and $U_r = 6\text{--}24$ for $AR = 1.5$) and a larger maximum vibration amplitude (e.g., $Y_{max} = 0.36D$ for $AR = 0.75$ and $Y_{max} = 2D$ for $AR = 1.5$). While the latter occurs over a narrower range $U_r = 6\text{--}16$ owing to the absence of non-synchronization branch in the amplitude response. By contrast, a larger AR always enhances the FIV that occurred in an unlimited U_r range by reducing its onset velocity and increasing its vibration amplitude.
3. According to the identified synchronization branch with $f_Y^*/f_{C_L}^* = 1 : n$, the assembly's self-limited FIV is an integrated VIV and galloping response—no synchronization for $AR = 0.75$ and three synchronizations ($n = 1, 2, 3$) for $AR = 1\text{--}2$, while the unlimited FIV transitions from a pure galloping ($n = 3$ for $AR = 0.75$; $n = 2, 3, 5$ for $AR = 1$) to an integrated VIV-galloping ($n = 1, 2, 3, 4, 5$ for $AR = 1.5\text{--}2$) with increasing AR . In addition, the non-synchronization regime functions as a transition in the passage from lower- to higher-order synchronizations and leads to a wider effective U_r range with FIV response.
4. The complexity of flow dynamics is also increased with AR . For the self-limited FIV, the 2S mode of lock-in is associated with more complex vortex shapes—elliptically-shaped vortex for $AR = 1$, vortex with a tail for $AR = 1.5$ and swallow-tailed vortex for $AR = 2$, while the wake modes in the high-order synchronizations can be either anti-symmetric (e.g., “ $3 \times (2S)$ ” and “ $2 \times (P+S)$ ” in the 1:3 synchronization) or non-symmetric (e.g., “ $2 \times (2S)$ ”, “T+S”, “ $\pm(2S)$ ” in the 1:2 synchronization). For the unlimited FIV, the $1 : n$ synchronization branch is associated with regular “ $n \times (2S)$ ” mode. But some particular flow dynamics can induce special branching behaviors. For example, the slender vortices oriented more in the transverse direction lead to the subdivision of 1:3 synchronization for $AR = 1.5$ and 2 . The “quasi-2S” and “quasi- $2 \times (2S)$ ” wake modes consisting of a primary elliptical vortex and a secondary tail vortex lead to the transition regimes between synchronizations.

Last, the FIV response is investigated using the mathematical models, which are identified by a genetic algorithm optimized nonlinear grey-box estimation framework. The optimal model structures to predict different FIV responses are discussed based on the simulation dataset of the cylinder-plate assembly obtained above.

1. The previous coupled wake-oscillator models based on lift coefficient C_L and wake angular displacement θ are improved from multiple aspects. For C_L -based model, the quasi-steady fluid force is included in the Y -ODE to give it ability to predict VIV and galloping, and both acceleration and velocity coupling terms are added in the C_L -ODE. Moreover, the seventh-order polynomial approximation from QS theory includes both even and odd terms to give a more generalized expression of galloping force. Most importantly, the fluid variable is converted into the explicit lift coefficient from the implicit lift (q) in C_L -based model or from the wake rotation angle in θ -based model, in order to directly use the time history of C_L in the simulation dataset.
2. Based on the improved wake-oscillator models, a nonlinear grey-box estimation framework is proposed to determine the free model parameters. The integration of genetic algorithm into the proposed framework effectively optimizes the model parameters. The rationality is verified by applying the GA-optimized grey-box model to the prediction of both VIV and galloping responses.
3. For the VIV of a circular cylinder, the acceleration-velocity coupling (for C_L -based model) and the first-order polynomial approximation $A_1(2\pi St)\dot{Y}$ (for C_L - and θ -based models) can accurately predict the time series of Y and C_L . Therefore, the optimal model structures include six free parameters, which are C_{L0} , St , ϵ , A_1 , B_1 , B_2 for a C_L -based model, and C_{L0} , St , ζ_f , f_m , \bar{l}^* , A_1 for a θ -based model. The two models can achieve similar accuracy in the prediction of VIV. Moreover, the estimated Strouhal number $S_t = 0.16$ is consistent with that from simulations.
4. For the galloping of a circular cylinder-plate assembly with $L_{SP}/D = 0.75$, more high-order polynomial terms are necessary to predict the severely distorted waveform in the oscillation of C_L . To be specific, eight free parameters are included in the optimal C_L -based model (viz., C_{L0} , St , ϵ , A_1 , A_3 , A_5 , A_7 , B_1) and θ -based model (viz., C_{L0} , St , ζ_f , f_m , \bar{l}^* , A_1 , A_3 , A_5). The θ -based model shows a better performance in predicting galloping, probably because it has more (five) physical parameters. In addition, the inconsistency of the estimated $S_t = 0.156$ and the simulated $St = 0.147$ may be due to the inherent defects of the QS assumption to model the galloping fore.

It should be noted that the conclusions summarized above can provide the guidance for the engineering application of cylinder-plate assembly, such as fluid energy harvester. For example, the effect of aspect ratio on the amplitude response can help to design an optimal elliptical cylinder, while the effect of splitter-plate length can be used to generate an optimal power curve, following which the assembly can reach high power generation.

In the future, the FIV response of a cylinder-plate assembly can be investigated from the following aspects.

1. The effect of Reynolds number on the assembly's FIV can be studied by carrying out high- Re and 3D numerical simulations, which can be verified by experimental data.
2. The GA-optimized nonlinear grey-box model can be combined with the actuator-line model (ALM) and the existing CFD solver (e.g. OpenFOAM) to develop a reduced-order simulation tool for the FIV response.
3. The cylinder-plate can have different structure features, such as replacing the smooth cylinder with prismatic body, or replacing the rigid plate with flexible plate.
4. The prediction of FIV can be investigated using deep learning (DL) methods. For example, one possible strategy [109] is to use the DL-based reduced order model (ROM) to first reduce the full-order CFD dataset using some reduced-order algorithms (e.g. proper orthogonal decomposition) and then learn the dynamics from the reduced dataset using some neural networks (e.g. long short-term memory neural network).

References

- [1] Hyung Taek Ahn and Yannis Kallinderis. Strongly coupled flow/structure interactions with a geometrically conservative ALE scheme on general hybrid meshes. *Journal of Computational Physics*, 219(2):671–696, 2006.
- [2] Huseyin Akilli, Besir Sahin, and N Filiz Tumen. Suppression of vortex shedding of circular cylinder in shallow water by a splitter plate. *Flow Measurement and Instrumentation*, 16(4):211–219, 2005.
- [3] Helmi Al-Jamal and Charles Dalton. Vortex induced vibrations using large eddy simulation at a moderate Reynolds number. *Journal of Fluids and Structures*, 19(1):73–92, 2004.
- [4] G Alonso and J Meseguer. A parametric study of the galloping stability of two-dimensional triangular cross-section bodies. *Journal of Wind Engineering and Industrial Aerodynamics*, 94(4):241–253, 2006.
- [5] G Alonso, J Meseguer, and I Pérez-Grande. Galloping instabilities of two-dimensional triangular cross-section bodies. *Experiments in Fluids*, 38:789–795, 2005.
- [6] G Alonso, J Meseguer, and I Pérez-Grande. Galloping stability of triangular cross-sectional bodies: a systematic approach. *Journal of Wind Engineering and Industrial Aerodynamics*, 95(9-11):928–940, 2007.
- [7] G Alonso, Alfredo Sanz-Lobera, and J Meseguer. Hysteresis phenomena in transverse galloping of triangular cross-section bodies. *Journal of Fluids and Structures*, 33:243–251, 2012.
- [8] EA Anderson and AA Szewczyk. Effects of a splitter plate on the near wake of a circular cylinder in 2 and 3-dimensional flow configurations. *Experiments in Fluids*, 23(2):161–174, 1997.

- [9] CJ Apelt, GS West, and Albin A Szewczyk. The effects of wake splitter plates on the flow past a circular cylinder in the range $104 < r < 5 \times 10^4$. *Journal of Fluid Mechanics*, 61(1):187–198, 1973.
- [10] Perumal Dharmaraj Arumuga, Gundavarapu VS Kumar, and Anoop K Dass. Lattice Boltzmann simulation of flow over a circular cylinder at moderate Reynolds numbers. *Thermal Science*, 18(4):1235–1246, 2014.
- [11] Gustavo RS Assi and Peter W Bearman. Transverse galloping of circular cylinders fitted with solid and slotted splitter plates. *Journal of Fluids and Structures*, 54:263–280, 2015.
- [12] Gustavo RS Assi, PW Bearman, and N Kitney. Low drag solutions for suppressing vortex-induced vibration of circular cylinders. *Journal of Fluids and Structures*, 25(4):666–675, 2009.
- [13] MH Bahmani and MH Akbari. Effects of mass and damping ratios on VIV of a circular cylinder. *Ocean Engineering*, 37(5-6):511–519, 2010.
- [14] Xu Bai and Wei Qin. Using vortex strength wake oscillator in modelling of vortex induced vibrations in two degrees of freedom. *European Journal of Mechanics-B/Fluids*, 48:165–173, 2014.
- [15] Yan Bao, Dai Zhou, and Jiahuang Tu. Flow interference between a stationary cylinder and an elastically mounted cylinder arranged in proximity. *Journal of Fluids and Structures*, 27(8):1425–1446, 2011.
- [16] Antonio Barrero-Gil, A Sanz-Andres, and Miquel Roura. Transverse galloping at low Reynolds numbers. *Journal of Fluids and Structures*, 25(7):1236–1242, 2009.
- [17] PW Bearman. Circular cylinder wakes and vortex-induced vibrations. *Journal of Fluids and Structures*, 27(5-6):648–658, 2011.
- [18] PW Bearman, IS Gartshore, DJ Maull, and GV Parkinson. Experiments on flow-induced vibration of a square-section cylinder. *Journal of Fluids and Structures*, 1(1):19–34, 1987.
- [19] Michael M Bernitsas, Kamaldev Raghavan, Y Ben-Simon, and EMH Garcia. VI-VACE (Vortex Induced Vibration Aquatic Clean Energy): A new concept in generation of clean and renewable energy from fluid flow. *Journal of offshore mechanics and Arctic engineering*, 130(4), 2008.

- [20] K Yusuf Billah and Robert H Scanlan. Resonance, Tacoma Narrows bridge failure, and undergraduate physics textbooks. *American Journal of Physics*, 59(2):118–124, 1991.
- [21] Garrett Birkhoff. Formation of vortex streets. *Journal of Applied Physics*, 24(1):98–103, 1953.
- [22] Richard Evelyn Donohue Bishop and AY Hassan. The lift and drag forces on a circular cylinder oscillating in a flowing fluid. *Proceedings of the Royal Society of London. Series A. Mathematical and Physical Sciences*, 277(1368):51–75, 1964.
- [23] Robert D Blevins. *Flow-induced vibration*. Van Nostrand Reinhold Company, 1977.
- [24] Iman Borazjani and Fotis Sotiropoulos. Vortex-induced vibrations of two cylinders in tandem arrangement in the proximity-wake interference region. *Journal of Fluid Mechanics*, 621:321–364, 2009.
- [25] Rémi Bourguet and David Lo Jacono. Flow-induced vibrations of a rotating cylinder. *Journal of Fluid Mechanics*, 740:342–380, 2014.
- [26] Cong Chen, Claudio Mannini, Gianni Bartoli, and Klaus Thiele. Wake oscillator modeling the combined instability of vortex induced vibration and galloping for a 2:1 rectangular cylinder. *Journal of Fluids and Structures*, 110:103530, 2022.
- [27] Guang Chen, Xi-Feng Liang, Xiao-Bai Li, Dan Zhou, and Fue-sang Lien. Numerical investigation of vortex induced vibration effects on the heat transfer for various aspect ratios ellipse cylinder. *International Journal of Thermal Sciences*, 170:107138, 2021.
- [28] AJ Chipperfield and PJ Fleming. The MATLAB genetic algorithm toolbox. *IEE Colloquium on Applied Control Techniques Using MATLAB*, 1995.
- [29] AJ Chipperfield, PJ Fleming, H Pohlheim, and CM Fonseca. A genetic algorithm toolbox for MATLAB. In *Proc. International Conference on Systems Engineering, Coventry, UK*, volume 6, 1994.
- [30] John Michael Cimbala and S Garg. Flow in the wake of a freely rotatable cylinder with splitter plate. *AIAA Journal*, 29(6):1001–1003, 1991.
- [31] Thomas F Coleman and Yuying Li. An interior trust region approach for nonlinear minimization subject to bounds. *SIAM Journal on optimization*, 6(2):418–445, 1996.

- [32] Robert M Corless and GV Parkinson. A model of the combined effects of vortex-induced oscillation and galloping. *Journal of Fluids and Structures*, 2(3):203–220, 1988.
- [33] Zhendong Cui, Ming Zhao, Bin Teng, and Liang Cheng. Two-dimensional numerical study of vortex-induced vibration and galloping of square and rectangular cylinders in steady flow. *Ocean Engineering*, 106:189–206, 2015.
- [34] Nihar B Darbhamulla and Rajneesh Bhardwaj. Flow-induced vibrations of circular cylinder in tandem arrangement with D-section cylinder at low Reynolds number. *Physics of Fluids*, 33(5):053606, 2021.
- [35] Behzad Ghadiri Dehkordi and Hamed Hourri Jafari. On the suppression of vortex shedding from circular cylinders using detached short splitter-plates. *Journal of Fluids Engineering*, 132(4), 2010.
- [36] JP Den Hartog. Transmission line vibration due to sleet. *Transactions of the American Institute of Electrical Engineers*, 51(4):1074–1076, 1932.
- [37] YM Desai, AH Shah, and N Popplewell. Galloping analysis for two-degree-of-freedom oscillator. *Journal of Engineering Mechanics*, 116(12):2583–2602, 1990.
- [38] Dániel Dorogi and László Baranyi. Identification of upper branch for vortex-induced vibration of a circular cylinder at $Re = 300$. *Journal of Fluids and Structures*, 98:103135, 2020.
- [39] Matteo Luca Facchinetti, Emmanuel De Langre, and Francis Biolley. Coupling of structure and wake oscillators in vortex-induced vibrations. *Journal of Fluids and structures*, 19(2):123–140, 2004.
- [40] Mark A Feero, Ahmed M Naguib, and Manoochehr M Koochesfahani. Influence of geometry on the galloping instability of rectangular cylinders in the Reynolds number range 1,000–10,000. *Journal of Fluids and Structures*, 94:102881, 2020.
- [41] CC Feng. *The measurement of vortex induced effects in flow past stationary and oscillating circular and D-section cylinders*. PhD thesis, University of British Columbia, 1968.
- [42] Zhipeng Feng, Naibin Jiang, Fenggang Zang, Yixiong Zhang, Xuan Huang, and Wanjun Wu. Nonlinear characteristics analysis of vortex-induced vibration for a three-dimensional flexible tube. *Communications in Nonlinear Science and Numerical Simulation*, 34:1–11, 2016.

- [43] K Foo, YY Liang, Chee Keong Tan, and GA Fimbres Weihs. Coupled effects of circular and elliptical feed spacers under forced-slip on viscous dissipation and mass transfer enhancement based on CFD. *Journal of Membrane Science*, 637:119599, 2021.
- [44] K Foo, YY Liang, and GA Fimbres Weihs. CFD study of the effect of SWM feed spacer geometry on mass transfer enhancement driven by forced transient slip velocity. *Journal of Membrane Science*, 597:117643, 2020.
- [45] M Funakawa. Excitation mechanism of elastically supported circular cylinder in the flow. *Bulletin of the Japan Society of Mechanical Engineering*, 36(285):303–312, 1970.
- [46] Gunnar K Furnes and Kristian Sørensen. Flow induced vibrations modeled by coupled non-linear oscillators. In *The Seventeenth International Offshore and Polar Engineering Conference*. OnePetro, 2007.
- [47] Rene D Gabbai and Haym Benaroya. An overview of modeling and experiments of vortex-induced vibration of circular cylinders. *Journal of Sound and Vibration*, 282(3-5):575–616, 2005.
- [48] Guang-zhong Gao and Le-dong Zhu. Nonlinear mathematical model of unsteady galloping force on a rectangular 2: 1 cylinder. *Journal of Fluids and Structures*, 70:47–71, 2017.
- [49] Guangzhong Gao and Ledong Zhu. Measurement and verification of unsteady galloping force on a rectangular 2: 1 cylinder. *Journal of Wind Engineering and Industrial Aerodynamics*, 157:76–94, 2016.
- [50] Guangzhong Gao, Ledong Zhu, Jiawu Li, and Wanshui Han. Modelling nonlinear aerodynamic damping during transverse aerodynamic instabilities for slender rectangular prisms with typical side ratios. *Journal of Wind Engineering and Industrial Aerodynamics*, 197:104064, 2020.
- [51] Fei Ge, Xu Long, Lei Wang, and YouShi Hong. Flow-induced vibrations of long circular cylinders modeled by coupled nonlinear oscillators. *Science in China Series G: Physics, Mechanics and Astronomy*, 52(7):1086–1093, 2009.
- [52] R Govardhan and CHK1789246 Williamson. Modes of vortex formation and frequency response of a freely vibrating cylinder. *Journal of Fluid Mechanics*, 420:85–130, 2000.

- [53] OM Griffin, RA Skop, and GH Koopmann. The vortex-excited resonant vibrations of circular cylinders. *Journal of Sound and Vibration*, 31(2):235–IN3, 1973.
- [54] Owen M Griffin, Richard A Skop, and Steven E Ramberg. The resonant, vortex-excited vibrations of structures and cable systems. In *Offshore Technology Conference*. OnePetro, 1975.
- [55] Martin D Griffith, David Lo Jacono, John Sheridan, and Justin S Leontini. Flow-induced vibration of two cylinders in tandem and staggered arrangements. *Journal of Fluid Mechanics*, 833:98–130, 2017.
- [56] Ffi Gu, JS Wang, XQ Qiao, and Zhen Huang. Pressure distribution, fluctuating forces and vortex shedding behavior of circular cylinder with rotatable splitter plates. *Journal of Fluids and Structures*, 28:263–278, 2012.
- [57] MZ Guan and RK Jaiman. Flow-induced vibration of two side-by-side square cylinders with combined translational motions. *Journal of Fluids and Structures*, 69:265–292, 2017.
- [58] Peng Han, Pascal Hémon, Guang Pan, and Emmanuel de Langre. Nonlinear modeling of combined galloping and vortex-induced vibration of square sections under flow. *Nonlinear Dynamics*, 103:3113–3125, 2021.
- [59] Xiangxi Han, Wei Lin, Xiaojun Zhang, Youhong Tang, and Chengbi Zhao. Two degree of freedom flow-induced vibration of cylindrical structures in marine environments: Frequency ratio effects. *Journal of Marine Science and Technology*, 21(3):479–492, 2016.
- [60] Ronald T Hartlen and Iain G Currie. Lift-oscillator model of vortex-induced vibration. *Journal of the Engineering Mechanics Division*, 96(5):577–591, 1970.
- [61] Seyyed M Hasheminejad and Miad Jarrahi. Numerical simulation of two dimensional vortex-induced vibrations of an elliptic cylinder at low Reynolds numbers. *Computers & Fluids*, 107:25–42, 2015.
- [62] Mingzhe He and John HG Macdonald. An analytical solution for the galloping stability of a 3 degree-of-freedom system based on quasi-steady theory. *Journal of Fluids and Structures*, 60:23–36, 2016.
- [63] Gang Hu, Kam-Tim Tse, and Kenny CS Kwok. Enhanced performance of wind energy harvester by aerodynamic treatment of a square prism. *Applied Physics Letters*, 108(12):123901, 2016.

- [64] Gang Hu, Kam Tim Tse, Minghai Wei, Rashid Naseer, Abdessattar Abdelkefi, and Kenny CS Kwok. Experimental investigation on the efficiency of circular cylinder-based wind energy harvester with different rod-shaped attachments. *Applied Energy*, 226:682–689, 2018.
- [65] Jong-Yeon Hwang and Kyung-Soo Yang. Drag reduction on a circular cylinder using dual detached splitter plates. *Journal of Wind Engineering and Industrial Aerodynamics*, 95(7):551–564, 2007.
- [66] Jong-Yeon Hwang, Kyung-Soo Yang, and Seung-Han Sun. Reduction of flow-induced forces on a circular cylinder using a detached splitter plate. *Physics of Fluids*, 15(8):2433–2436, 2003.
- [67] N.A. Jauvtis and Charles H.K. Williamson. The effect of two degrees of freedom on vortex-induced vibration at low mass and damping. *Journal of Fluid Mechanics*, 509:23–62, 2004.
- [68] A Joly, S Etienne, and D Pelletier. Galloping of square cylinders in cross-flow at low Reynolds numbers. *Journal of Fluids and Structures*, 28:232–243, 2012.
- [69] Kathleen F Jones. Coupled vertical and horizontal galloping. *Journal of engineering mechanics*, 118(1):92–107, 1992.
- [70] Hiromasa Kawai. A discrete vortex analysis of flow around a vibrating cylinder with a splitter plate. *Journal of Wind Engineering and Industrial Aerodynamics*, 35:259–273, 1990.
- [71] A Khalak and Charles H.K. Williamson. Dynamics of a hydroelastic cylinder with very low mass and damping. *Journal of Fluids and Structures*, 10(5):455–472, 1996.
- [72] A Khalak and Charles H.K. Williamson. Fluid forces and dynamics of a hydroelastic structure with very low mass and damping. *Journal of Fluids and Structures*, 11(8):973–982, 1997.
- [73] Asif Khalak and Charles HK Williamson. Motions, forces and mode transitions in vortex-induced vibrations at low mass-damping. *Journal of fluids and Structures*, 13(7-8):813–851, 1999.
- [74] Efstathios Konstantinidis, Jisheng Zhao, Justin Leontini, D Lo Jacono, and John Sheridan. Phase dynamics of effective drag and lift components in vortex-induced vibration at low mass-damping. *Journal of Fluids and Structures*, 96:103028, 2020.

- [75] Kiyoungh Kwon and Haecheon Choi. Control of laminar vortex shedding behind a circular cylinder using splitter plates. *Physics of Fluids*, 8(2):479–486, 1996.
- [76] R Landl. A mathematical model for vortex-excited vibrations of bluff bodies. *Journal of Sound and Vibration*, 42(2):219–234, 1975.
- [77] Yun Zhi Law and Rajeev Kumar Jaiman. Wake stabilization mechanism of low-drag suppression devices for vortex-induced vibration. *Journal of Fluids and Structures*, 70:428–449, 2017.
- [78] Jinmo Lee and Donghyun You. Study of vortex-shedding-induced vibration of a flexible splitter plate behind a cylinder. *Physics of Fluids*, 25(11):110811, 2013.
- [79] Justin S Leontini, MD Griffith, D Lo Jacono, and John Sheridan. The flow-induced vibration of an elliptical cross-section at varying angles of attack. *Journal of Fluids and Structures*, 78:356–373, 2018.
- [80] Justin Scott Leontini, Mark Christopher Thompson, and Kerry Hourigan. The beginning of branching behaviour of vortex-induced vibration during two-dimensional flow. *Journal of Fluids and Structures*, 22(6-7):857–864, 2006.
- [81] Tian Li and Takeshi Ishihara. Numerical study on vortex-induced vibration of circular cylinder with two-degree-of-freedom and geometrical nonlinear system. *Journal of Fluids and Structures*, 107:103415, 2021.
- [82] Tian Li, Jiye Zhang, and Weihua Zhang. Nonlinear characteristics of vortex-induced vibration at low Reynolds number. *Communications in Nonlinear Science and Numerical Simulation*, 16(7):2753–2771, 2011.
- [83] Y Li and TF Coleman. On the convergence of reflective newton methods for large-scale nonlinear minimization subject to bounds. *Mathematical Programming*, 67(2):189–224, 1994.
- [84] Shengping Liang, Jiasong Wang, and Zhongming Hu. VIV and galloping response of a circular cylinder with rigid detached splitter plates. *Ocean Engineering*, 162:176–186, 2018.
- [85] John H Lienhard et al. *Synopsis of lift, drag, and vortex frequency data for rigid circular cylinders*, volume 300. Technical Extension Service, Washington State University Pullman, WA, 1966.

- [86] Lin Lu, Xiao-ling Guo, Guo-qiang Tang, Ming-ming Liu, Chuan-qi Chen, and Zhi-hua Xie. Numerical investigation of flow-induced rotary oscillation of circular cylinder with rigid splitter plate. *Physics of Fluids*, 28(9):093604, 2016.
- [87] SC Luo, YT Chew, and YT Ng. Hysteresis phenomenon in the galloping oscillation of a square cylinder. *Journal of Fluids and Structures*, 18(1):103–118, 2003.
- [88] Angelo Luongo and Giuseppe Piccardo. Linear instability mechanisms for coupled translational galloping. *Journal of Sound and Vibration*, 288(4-5):1027–1047, 2005.
- [89] Yanfang Lv, Liping Sun, Michael M Bernitsas, and Hai Sun. A comprehensive review of nonlinear oscillators in hydrokinetic energy harnessing using flow-induced vibrations. *Renewable and Sustainable Energy Reviews*, 150:111388, 2021.
- [90] Xiaoqing Ma and Shengxi Zhou. A review of flow-induced vibration energy harvesters. *Energy Conversion and Management*, 254:115223, 2022.
- [91] BP MacLeod, DK Fork, B Lam, and CP Berlinguette. Calorimetry under non-ideal conditions using system identification. *Journal of Thermal Analysis and Calorimetry*, 138(5):3139–3157, 2019.
- [92] C Mannini, AM Marra, and G Bartoli. VIV-galloping instability of rectangular cylinders: Review and new experiments. *Journal of Wind Engineering and Industrial Aerodynamics*, 132:109–124, 2014.
- [93] Claudio Mannini. Incorporation of turbulence in a nonlinear wake-oscillator model for the prediction of unsteady galloping response. *Journal of Wind Engineering and Industrial Aerodynamics*, 200:104141, 2020.
- [94] Claudio Mannini, Antonino M Marra, and Gianni Bartoli. Experimental investigation on VIV-galloping interaction of a rectangular 3: 2 cylinder. *Meccanica*, 50(3):841–853, 2015.
- [95] Claudio Mannini, Antonino Maria Marra, Tommaso Massai, and Gianni Bartoli. Interference of vortex-induced vibration and transverse galloping for a rectangular cylinder. *Journal of Fluids and Structures*, 66:403–423, 2016.
- [96] Claudio Mannini, Tommaso Massai, ANTONINO Marra, Gianni Bartoli, et al. Modelling the interaction of VIV and galloping for rectangular cylinders. In *Proceedings of the 14th International Conference on Wind Engineering*, pages 1–20. International Association for Wind Engineering-IAWE, 2015.

- [97] Claudio Mannini, Tommaso Massai, and Antonino Maria Marra. Modeling the interference of vortex-induced vibration and galloping for a slender rectangular prism. *Journal of Sound and Vibration*, 419:493–509, 2018.
- [98] Karthik Menon and Rajat Mittal. On the initiation and sustenance of flow-induced vibration of cylinders: Insights from force partitioning. *Journal of Fluid Mechanics*, 907, 2021.
- [99] J Meseguer, A Sanz-Andrés, and G Alonso. Determination of maximum mechanical energy efficiency in energy galloping systems. *Journal of Engineering Mechanics*, 141(1):04014101, 2015.
- [100] Seyedali Mirjalili and Seyedali Mirjalili. Genetic algorithm. *Evolutionary Algorithms and Neural Networks: Theory and Applications*, pages 43–55, 2019.
- [101] S Mittal. Effect of a “slip” splitter plate on vortex shedding from a cylinder. *Physics of fluids*, 15(3):817–820, 2003.
- [102] Sanjay Mittal. Free vibrations of a cylinder: 3-D computations at $Re = 1000$. *Journal of Fluids and Structures*, 41:109–118, 2013.
- [103] Y Modarres-Sadeghi, F Chasparis, MS Triantafyllou, M Tognarelli, and P Beynet. Chaotic response is a generic feature of vortex-induced vibrations of flexible risers. *Journal of Sound and Vibration*, 330(11):2565–2579, 2011.
- [104] Tomomichi Nakamura, Shigehiko Kaneko, Fumio Inada, Minoru Kato, Kunihiko Ishihara, Takashi Nishihara, Njuki W Mureithi, and Mikael A Langthjem. *Flow-induced vibrations: Classifications and lessons from practical experiences*. Butterworth-Heinemann, 2013.
- [105] Y Nakamura, K Hirata, and T Urabe. Galloping of rectangular cylinders in the presence of a splitter plate. *Journal of Fluids and Structures*, 5(5):521–549, 1991.
- [106] Yh Nakamura, K Hirata, and K Kashima. Galloping of a circular cylinder in the presence of a splitter plate. *Journal of fluids and structures*, 8(4):355–365, 1994.
- [107] K Narendran, K Murali, and V Sundar. Vortex-induced vibrations of elastically mounted circular cylinder at Re of the $O(105)$. *Journal of Fluids and Structures*, 54:503–521, 2015.

- [108] Navrose, V Yogeswaran, Subhankar Sen, and Sanjay Mittal. Free vibrations of an elliptic cylinder at low Reynolds numbers. *Journal of Fluids and Structures*, 51:55–67, 2014.
- [109] Anastasiia Nazvanova, Muk Chen Ong, and Guang Yin. A data-driven reduced-order model based on long short-term memory neural network for vortex-induced vibrations of a circular cylinder. *Physics of Fluids*, 35(6), 2023.
- [110] András Nemes, Jisheng Zhao, David Lo Jacono, and John Sheridan. The interaction between flow-induced vibration mechanisms of a square cylinder with varying angles of attack. *Journal of Fluid Mechanics*, 710:102–130, 2012.
- [111] M. E. J. Newman and M. Girvan. Finding and evaluating community structure in networks. *Phys. Rev. E.*, 69:026113, 2004.
- [112] YT Ng, SC Luo, and YT Chew. On using high-order polynomial curve fits in the quasi-steady theory for square-cylinder galloping. *Journal of fluids and structures*, 20(1):141–146, 2005.
- [113] Christoffer Norberg. Flow around rectangular cylinders: pressure forces and wake frequencies. *Journal of wind engineering and industrial aerodynamics*, 49(1-3):187–196, 1993.
- [114] RHM Ogink and AV Metrikine. A wake oscillator with frequency dependent coupling for the modeling of vortex-induced vibration. *Journal of sound and vibration*, 329(26):5452–5473, 2010.
- [115] Shigehira Ozono. Flow control of vortex shedding by a short splitter plate asymmetrically arranged downstream of a cylinder. *Physics of Fluids*, 11(10):2928–2934, 1999.
- [116] G Parkinson and D Bouclin. Hydroelastic oscillations of square cylinders. In *Proceedings of the International Research Seminar on Safety of Structures under Dynamic Loading, Trondheim, Norway*, pages 25–30, 1977.
- [117] GV Parkinson and NPH Brooks. On the aeroelastic instability of bluff cylinders. *Journal of Applied Mechanics*, 1961.
- [118] GV Parkinson and JD Smith. The square prism as an aeroelastic non-linear oscillator. *The Quarterly Journal of Mechanics and Applied Mathematics*, 17(2):225–239, 1964.

- [119] GV Parkinson and PP Sullivan. Galloping response of towers. *Journal of Wind Engineering and Industrial Aerodynamics*, 4(3-4):253–260, 1979.
- [120] GV Parkinson and MA Wawzonek. Some considerations of combined effects of galloping and vortex resonance. *Journal of Wind Engineering and Industrial Aerodynamics*, 8(1-2):135–143, 1981.
- [121] Giuseppe Piccardo, Luisa Carlotta Pagnini, and Federica Tubino. Some research perspectives in galloping phenomena: critical conditions and post-critical behavior. *Continuum Mechanics and Thermodynamics*, 27:261–285, 2015.
- [122] Antoine Placzek, Jean-François Sigrist, and Aziz Hamdouni. Numerical simulation of an oscillating cylinder in a cross-flow at low Reynolds number: Forced and free oscillations. *Computers & Fluids*, 38(1):80–100, 2009.
- [123] Andrey Postnikov, Ekaterina Pavlovskaya, and Marian Wiercigroch. 2DOF CFD calibrated wake oscillator model to investigate vortex-induced vibrations. *International Journal of Mechanical Sciences*, 127:176–190, 2017.
- [124] TK Prasanth and Sanjay Mittal. Vortex-induced vibrations of a circular cylinder at low Reynolds numbers. *Journal of Fluid Mechanics*, 594:463–491, 2008.
- [125] U. Raghavan, R. Albert, and S. Kumara. Near linear time algorithm to detect community structures in large-scale networks. *Phys. Rev E.*, 76:036106, 2007.
- [126] John William Strutt Baron Rayleigh. *The theory of sound*, volume 2. Macmillan, 1896.
- [127] Anatol Roshko. Experiments on the flow past a circular cylinder at very high Reynolds number. *Journal of fluid mechanics*, 10(3):345–356, 1961.
- [128] Ali Bakhshandeh Rostami and Mohammadmehdi Armandei. Renewable energy harvesting by vortex-induced motions: Review and benchmarking of technologies. *Renewable and Sustainable Energy Reviews*, 70:193–214, 2017.
- [129] Tulsi Ram Sahu, Mohd Furquan, Yash Jaiswal, and Sanjay Mittal. Flow-induced vibration of a circular cylinder with rigid splitter plate. *Journal of Fluids and Structures*, 89:244–256, 2019.
- [130] Günter Schewe. On the force fluctuations acting on a circular cylinder in crossflow from subcritical up to transcritical Reynolds numbers. *Journal of fluid mechanics*, 133:265–285, 1983.

- [131] Christopher Scruton and Anthony Ray Flint. Wind-excited oscillations of structures. *Proceedings of the Institution of Civil Engineers*, 27(4):673–702, 1964.
- [132] Subhankar Sen. Wake modes of a freely vibrating square cylinder. *Physics of Fluids*, 34(5):053601, 2022.
- [133] Subhankar Sen and Sanjay Mittal. Free vibration of a square cylinder at low Reynolds numbers. *Journal of Fluids and Structures*, 27(5-6):875–884, 2011.
- [134] Subhankar Sen and Sanjay Mittal. Effect of mass ratio on free vibrations of a square cylinder at low Reynolds numbers. *Journal of Fluids and Structures*, 54:661–678, 2015.
- [135] Subhankar Sen and Sanjay Mittal. Free vibrations of a square cylinder of varying mass ratios. *Procedia Engineering*, 144:34–42, 2016.
- [136] Banafsheh Seyed-Aghazadeh, Daniel W Carlson, and Yahya Modarres-Sadeghi. Vortex-induced vibration and galloping of prisms with triangular cross-sections. *Journal of Fluid Mechanics*, 817:590–618, 2017.
- [137] Mohammad Abu Shahzer, Mohammad Athar Khan, Syed Fahad Anwer, Saleem Anwar Khan, Mohammad Shoaib Khan, Abdullah Algethami, and Mishal Alsehli. A comprehensive investigation of vortex-induced vibrations and flow-induced rotation of an elliptic cylinder. *Physics of Fluids*, 34(3):033605, 2022.
- [138] Lawrence F Shampine and Mark W Reichelt. The matlab ode suite. *SIAM journal on scientific computing*, 18(1):1–22, 1997.
- [139] Lawrence F Shampine, Mark W Reichelt, and Jacek A Kierzenka. Solving index-1 DAEs in MATLAB and Simulink. *SIAM review*, 41(3):538–552, 1999.
- [140] Nan Shao, Jijian Lian, Fang Liu, Xiang Yan, and Peiyao Li. Experimental investigation of flow induced motion and energy conversion for triangular prism. *Energy*, 194:116865, 2020.
- [141] S Shukla, RN Govardhan, and JH Arakeri. Dynamics of a flexible splitter plate in the wake of a circular cylinder. *Journal of Fluids and Structures*, 41:127–134, 2013.
- [142] Emil Simiu and DongHun Yeo. *Wind effects on structures: Modern structural design for wind*. John Wiley & Sons, 2019.

- [143] SP Singh and S Mittal. Vortex-induced oscillations at low Reynolds numbers: Hysteresis and vortex-shedding modes. *Journal of Fluids and Structures*, 20(8):1085–1104, 2005.
- [144] RA Skop and OM Griffin. A model for the vortex-excited resonant response of bluff cylinders. *Journal of Sound and Vibration*, 27(2):225–233, 1973.
- [145] RA Skop and OM Griffin. On a theory for the vortex-excited oscillations of flexible cylindrical structures. *Journal of Sound and Vibration*, 41(3):263–274, 1975.
- [146] RA Skop and G Luo. An inverse-direct method for predicting the vortex-induced vibrations of cylinders in uniform and nonuniform flows. *Journal of Fluids and Structures*, 15(6):867–884, 2001.
- [147] Richard A Skop and Sathish Balasubramanian. A new twist on an old model for vortex-excited vibrations. *Journal of Fluids and Structures*, 11(4):395–412, 1997.
- [148] Jie Song, Gang Hu, KT Tse, SW Li, and KCS Kwok. Performance of a circular cylinder piezoelectric wind energy harvester fitted with a splitter plate. *Applied Physics Letters*, 111(22):223903, 2017.
- [149] Kumar Sourav and Subhankar Sen. Transition of VIV-only motion of a square cylinder to combined VIV and galloping at low Reynolds numbers. *Ocean Engineering*, 187:106208, 2019.
- [150] Narakorn Srinil and Hossein Zanganeh. Modelling of coupled cross-flow/in-line vortex-induced vibrations using double duffing and Van der Pol oscillators. *Ocean Engineering*, 53:83–97, 2012.
- [151] Brad Stappenbelt. Splitter-plate wake stabilisation and low aspect ratio cylinder flow-induced vibration mitigation. *International Journal of Offshore and Polar Engineering*, 20(03), 2010.
- [152] Steven H Strogatz. *Nonlinear Dynamics and Chaos: With Applications to Physics, Biology, Chemistry, and Engineering*. CRC Press, Boca Raton, Florida, 2018.
- [153] Yi Su, Jin Di, Shaopeng Li, Bin Jian, and Jun Liu. Buffeting response prediction of long-span bridges based on different wind tunnel test techniques. *Applied Sciences*, 12(6):3171, 2022.

- [154] Xu Sun, C Steve Suh, Ze-Hua Ye, and Bo Yu. Dynamics of a circular cylinder with an attached splitter plate in laminar flow: A transition from vortex-induced vibration to galloping. *Physics of Fluids*, 32(2):027104, 2020.
- [155] Y Tamura. Model of vortex induced oscillation of circular cylinder. In *Proceedings of the 5th Symposium on Wind Effects on Structures, Tokyo, Japan*, pages 199–206, 1978.
- [156] Y Tamura. Vortex induced vibration of circular cylinder (Part I Wake oscillator model). *Trans Archit Inst Jpn*, 266:87–95, 1978.
- [157] Y. Tamura. Vortex induced vibration of circular cylinder: Part II Model of vortex induced vibration. *Transactions of the Architectural Institute of Japan*, 280:67—77, 1979.
- [158] Y Tamura and A Amano. Mathematical model for vortex-induced oscillations of continuous systems with circular cross section. *Journal of Wind Engineering and Industrial Aerodynamics*, 14(1-3):431–442, 1983.
- [159] Y Tamura and K Shimada. A mathematical model for the transverse oscillations of square cylinders. In *Proc. of International Conference on Flow Induced Vibrations, Bowness-Windermere, England*, pages 12–14, 1987.
- [160] Yukio TAMURA. Wake-oscillator model of vortex-induced oscillation of circular cylinder. *Journal of Wind Engineering*, 1981(10):13–24, 1981.
- [161] Yukio Tamura. Mathematical models for understanding phenomena: Vortex-induced vibrations. *Japan Architectural Review*, 3(4):398–422, 2020.
- [162] Zhaolie Tang and Benmou Zhou. The effect of mass ratio and spring stiffness on flow-induced vibration of a square cylinder at different incidence angles. *Ocean Engineering*, 198:106975, 2020.
- [163] Vortex Bladeless Technology. Vertical wind turbines @ONLINE. <https://www.tubewaysolar.at/english/vertical-wind-turbines/>, 2021.
- [164] Balth Van Der Pol and Jan Van Der Mark. The heartbeat considered as a relaxation oscillation, and an electrical model of the heart. *The London, Edinburgh, and Dublin Philosophical Magazine and Journal of Science*, 6(38):763–775, 1928.
- [165] J Kim Vandiver. Damping parameters for flow-induced vibration. *Journal of fluids and structures*, 35:105–119, 2012.

- [166] C. Vehlow, T. Reinhardt, and D. Weiskopf. Visualizing fuzzy overlapping communities in networks. *IEEE Trans. Vis. Comput. Graph.*, 19:2486–2495, 2013.
- [167] Hui Wan, Jeffrey A DesRoches, Anthony N Palazotto, and Soumya S Patnaik. Vortex-induced vibration of elliptic cylinders and the suppression using mixed-convection. *Journal of Fluids and Structures*, 103:103297, 2021.
- [168] Juan BV Wanderley, Sergio H Sphaier, and Carlos Levi. A two-dimensional numerical investigation of the hysteresis effect on vortex induced vibration on an elastically mounted rigid cylinder. *Journal of Offshore Mechanics and Arctic Engineering*, 134(2), 2012.
- [169] Chenglei Wang, Hui Tang, Fei Duan, and CM Simon. Control of wakes and vortex-induced vibrations of a single circular cylinder using synthetic jets. *Journal of Fluids and Structures*, 60:160–179, 2016.
- [170] Enhao Wang, Wanhai Xu, Xifeng Gao, Liqin Liu, Qing Xiao, and Kiran Ramesh. The effect of cubic stiffness nonlinearity on the vortex-induced vibration of a circular cylinder at low Reynolds numbers. *Ocean Engineering*, 173:12–27, 2019.
- [171] Huakun Wang, Qiu Zhai, and Kaixiao Chen. Vortex-induced vibrations of an elliptic cylinder with both transverse and rotational degrees of freedom. *Journal of Fluids and Structures*, 84:36–55, 2019.
- [172] Huakun Wang, Dongliang Zhao, Wenyu Yang, and Guoliang Yu. Numerical investigation on flow-induced vibration of a triangular cylinder at a low Reynolds number. *Fluid Dynamics Research*, 47(1):015501, 2014.
- [173] Junlei Wang, Linfeng Geng, Lin Ding, Hongjun Zhu, and Daniil Yurchenko. The state-of-the-art review on energy harvesting from flow-induced vibrations. *Applied Energy*, 267:114902, 2020.
- [174] RHJ Willden and JMR Graham. Three distinct response regimes for the transverse vortex-induced vibrations of circular cylinders at low Reynolds numbers. *Journal of Fluids and Structures*, 22(6-7):885–895, 2006.
- [175] Charles HK Williamson and Anatol Roshko. Vortex formation in the wake of an oscillating cylinder. *Journal of fluids and structures*, 2(4):355–381, 1988.
- [176] J Wu, YL Qiu, C Shu, and N Zhao. Flow control of a circular cylinder by using an attached flexible filament. *Physics of Fluids*, 26(10):103601, 2014.

- [177] Ying Wu, Zhi Cheng, Ryley McConkey, Fue-Sang Lien, and Eugene Yee. Modelling of flow-induced vibration of bluff bodies: A comprehensive survey and future prospects. *Energies*, 15(22):8719, 2022.
- [178] Ying Wu, Fue Sang Lien, and Eugene Yee. Self-limited flow-induced vibration of an elliptic cylinder with a splitter-plate attachment at low Reynolds number. *Journal of fluids and structures*, 2023.
- [179] Ying Wu, Fue Sang Lien, Eugene Yee, and Guang Chen. Flow-induced vibration of cylinder-plate assembly at low Reynolds number: Branching behavior. *Physics of Fluids (submitted for publication)*, 2022.
- [180] Ying Wu, Fue Sang Lien, Eugene Yee, and Guang Chen. Nonlinear analysis of the flow-induced vibration of a circular cylinder with a splitter-plate attachment. *Communications in Nonlinear Science and Numerical Simulation (submitted for publication)*, 2022.
- [181] Ying Wu, Fue Sang Lien, Eugene Yee, and Guang Chen. Numerical investigation of flow-induced vibration for cylinder-plate assembly at low Reynolds number. *Fluids*, 8(118):1–21, 2023.
- [182] Bin Xu, Hao Wang, Yilin Deng, Xi Shen, Linlin Geng, Keyang Liu, and Desheng Zhang. Nonlinear vortex dynamic analysis of flow-induced vibration of a flexible splitter plate attached to a square cylinder. *Ocean Engineering*, 264:112433, 2022.
- [183] John C Xu, Mihir Sen, and Mohamed Gad-el Hak. Low-Reynolds number flow over a rotatable cylinder-splitter plate body. *Physics of Fluids A: Fluid Dynamics*, 2(11):1925–1927, 1990.
- [184] Jun-ling Xu and Ren-qing Zhu. Numerical simulation of VIV for an elastic cylinder mounted on the spring supports with low mass-ratio. *Journal of Marine Science and Application*, 8(3):237–245, 2009.
- [185] Wanhai Xu, Ankang Cheng, Yexuan Ma, and Xifeng Gao. Multi-mode flow-induced vibrations of two side-by-side slender flexible cylinders in a uniform flow. *Marine Structures*, 57:219–236, 2018.
- [186] Haiyan Yu and Mingjie Zhang. Effects of side ratio on energy harvesting from transverse galloping of a rectangular cylinder. *Energy*, 226:120420, 2021.

- [187] Baoshou Zhang, Zhaoyong Mao, Baowei Song, Wenjun Ding, and Wenlong Tian. Numerical investigation on effect of damping-ratio and mass-ratio on energy harnessing of a square cylinder in FIM. *Energy*, 144:218–231, 2018.
- [188] Baoshou Zhang, Keh-Han Wang, Baowei Song, Zhaoyong Mao, and Wenlong Tian. Numerical investigation on the effect of the cross-sectional aspect ratio of a rectangular cylinder in FIM on hydrokinetic energy conversion. *Energy*, 165:949–964, 2018.
- [189] Jun Zhang, Guobin Xu, Fang Liu, Jijian Lian, and Xiang Yan. Experimental investigation on the flow induced vibration of an equilateral triangle prism in water. *Applied Ocean Research*, 61:92–100, 2016.
- [190] Mingjie Zhang, Ole Øiseth, and Fuyou Xu. Laminar flow-induced vibration of a three-degree-of-freedom circular cylinder with an attached splitter plate. *Physics of Fluids*, 33(11):113605, 2021.
- [191] Mingjie Zhang, Xu Wang, and Ole Øiseth. Torsional vibration of a circular cylinder with an attached splitter plate in laminar flow. *Ocean Engineering*, 236:109514, 2021.
- [192] Jisheng Zhao, Kerry Hourigan, and Mark C Thompson. Dynamic response of elliptical cylinders undergoing transverse flow-induced vibration. *Journal of Fluids and Structures*, 89:123–131, 2019.
- [193] Jisheng Zhao, Kerry Hourigan, and Mark C Thompson. An experimental investigation of flow-induced vibration of high-side-ratio rectangular cylinders. *Journal of Fluids and Structures*, 91:102580, 2019.
- [194] Jisheng Zhao, Justin Leontini, David Lo Jacono, and John Sheridan. The effect of mass ratio on the structural response of a freely vibrating square cylinder oriented at different angles of attack. *Journal of Fluids and Structures*, 86:200–212, 2019.
- [195] Jisheng Zhao, Justin S Leontini, David Lo Jacono, and John Sheridan. Fluid–structure interaction of a square cylinder at different angles of attack. *Journal of Fluid Mechanics*, 747:688–721, 2014.
- [196] Jisheng Zhao, Justin S Leontini, David Lo Jacono, and John Sheridan. Chaotic vortex induced vibrations. *Physics of Fluids*, 26(12):121702, 2014.
- [197] Ming Zhao. Flow induced vibration of two rigidly coupled circular cylinders in tandem and side-by-side arrangements at a low Reynolds number of 150. *Physics of Fluids*, 25(12):123601, 2013.

- [198] Ming Zhao, Liang Cheng, and Tongming Zhou. Numerical simulation of vortex-induced vibration of a square cylinder at a low Reynolds number. *Physics of Fluids*, 25(2):023603, 2013.
- [199] Hongjun Zhu, Guomin Li, and Junlei Wang. Flow-induced vibration of a circular cylinder with splitter plates placed upstream and downstream individually and simultaneously. *Applied Ocean Research*, 97:102084, 2020.
- [200] Hongjun Zhu, Tao Tang, Mahbub Alam, Jinze Song, and Tongming Zhou. Flow-induced rotation of a circular cylinder with a detached splitter plate and its bifurcation behavior. *Applied Ocean Research*, 122:103150, 2022.
- [201] Hongjun Zhu, Tao Tang, Yun Gao, Tongming Zhou, and Junlei Wang. Flow-induced vibration of a trapezoidal cylinder placed at typical flow orientations. *Journal of Fluids and Structures*, 103:103291, 2021.
- [202] Hongjun Zhu, Tao Tang, Tongming Zhou, Mingjin Cai, Oleg Gaidai, and Junlei Wang. High performance energy harvesting from flow-induced vibrations in trapezoidal oscillators. *Energy*, 236:121484, 2021.
- [203] Hongjun Zhu, Ying Zhao, and Tongming Zhou. Numerical investigation of the vortex-induced vibration of an elliptic cylinder free-to-rotate about its center. *Journal of Fluids and Structures*, 83:133–155, 2018.

APPENDICES

Appendix A

Publications During PhD

In the following publications, the author of this thesis is shown in bold, the corresponding author is marked with a superscript asterisk *.

1. **Wu, Y.***, Lien, F. S., Yee, E., Chen, G. (2023). Flow-induced vibration of a cylinder-plate assembly in laminar flow: Branching behavior. *Physics of Fluids*, 35(5).
2. **Wu, Y.***, Lien, F. S., Yee, E., Chen, G. (2023). Numerical investigation of flow-induced vibration for cylinder-plate assembly at low Reynolds number. *Fluids*, 8(4), 118.
3. **Wu, Y.**, Cheng, Z., McConkey, R., Lien, F. S.*, Yee, E. (2022). Modelling of Flow-Induced Vibration of Bluff Bodies: A Comprehensive Survey and Future Prospects. *Energies*, 15(22), 8719.
4. **Wu, Y.***, Lien, F. S., Yee, E. (2023). Nonlinear analysis of the flow-induced vibration of a circular cylinder with a splitter-plate attachment. Submitted to *Communications in Nonlinear Science and Numerical Simulation* (in March 2023) Accepted.
5. **Wu, Y.***, Lien, F. S., Yee, E. (2023). Flow-induced vibration of an elliptic cylinder with a splitter-plate attachment at low-Reynolds number: Self-limited oscillations. Submitted to *Journal of Fluids and Structures* (in Apr 2023) under review.
6. **Wu, Y.***, Lien, F. S., Yee, E. (2023). Effect of aspect ratio on the unlimited flow-induced vibration of an elliptical cylinder-plate assembly in laminar flow. Submitted to *Physical Review Fluids* (in June 2023) under review.
7. Chen, G.*, Fu, C., Xu, B.*, **Wu, Y.**, Lien, F. S., Yee, E. (2022). Internal mixing air-assisted spray nozzle for large droplets: Experimental measurements and numerical simulations. *Journal of Aerosol Science*, 165, 106035.